IN-02
8497
249P

NASA Contractor Report 195301

An Experimental Study of the Flowfield on a Semispan Rectangular Wing With a Simulated Glaze Ice Accretion

Abdollah Khodadoust
University of Illinois
Urbana, Illinois 61801

April 1994

Prepared for
Lewis Research Center
Under Grant NAG3–1134

National Aeronautics and
Space Administration

(NASA-CR-195301) AN EXPERIMENTAL STUDY OF THE FLOWFIELD ON A SEMISPAN RECTANGULAR WING WITH A SIMULATED GLAZE ICE ACCRETION Ph.D. Thesis, 1993 Final Report (Illinois Univ.) 249 p

N94-32475

Unclas

G3/02 0008497

AN EXPERIMENTAL STUDY OF THE FLOWFIELD ON A SEMISPAN RECTANGULAR WING WITH A SIMULATED GLAZE ICE ACCRETION

BY

ABDOLLAH KHODADOUST

ORIGINAL CONTAINS
COLOR ILLUSTRATIONS

ABSTRACT

Wind-tunnel experiments were conducted in order to study the effect of a simulated glaze ice accretion on the flowfield of a semispan, reflection-plane, rectangular wing at Re = 1.5 million and M = 0.12. A laser Doppler velocimeter was used to map the flowfield on the upper surface of the model in both the clean and iced configurations at $\alpha = 0$, 4, and 8 degrees angle of attack.

At low angles of attack, the massive separation bubble aft of the leading edge ice horn was found to behave in a manner similar to laminar separation bubbles. At $\alpha = 0°$ and 4°, the locations of transition and reattachment, as deduced from momentum thickness distributions, were found to be in good agreement with transition and reattachment locations in laminar separation bubbles. These values at y/b = 0.470, the centerline measurement location, matched well with data obtained on a similar but 2-D model. The measured velocity profiles on the iced wing compared reasonably with the predicted profiles from Navier-Stokes computatuions.

The iced-induced separation bubble was also found to have features similar to the recirculating region aft of rearward-facing steps. At $\alpha = 0°$ and 4°, reverse flow magnitudes and turbulence intensity levels were typical of those found in the recirculating region aft of rearward-facing steps. The calculated separation streamline aft of the ice horn at $\alpha = 4°$, y/b = 0.470 coincided with the locus of the maximum Reynolds normal stress. The maximum Reynolds normal stress peaked at two locations along the separation streamline. The location of the first peak-value coincided with the transition location, as deduced from the momentum thickness distributions. The location of the second peak was just upstream of reattachment, in good agreement with measurements of flows over similar obstacles. The

PRECEDING PAGE BLANK NOT FILMED

intermittency factor in the vicinity of reattachment at $\alpha = 4°$, $y/b = 0.470$, revealed the time-dependent nature of the reattachment process.

The size and extent of the separation bubble were found to be a function of angle of attack and the spanwise location. Three dimensional effects were found to be strongest at $\alpha = 8°$. The calculated separation and stagnation streamlines were found to vary little with spanwise location at $\alpha = 0°$. The calculated separation streamlines at $\alpha = 4°$ revealed that the bubble was largest near the centerline measurement plane, whereas the tip-induced vortex flow and the model root-tunnel wall boundary-layer interaction reduced the size of the bubble. These effects were found to be most dramatic at $\alpha = 8°$.

TABLE OF CONTENTS

CHAPTER PAGE

LIST OF SYMBOLS viii

I INTRODUCTION 1

II REVIEW OF LITERATURE 7
2.1. Iced Wing, Iced Airfoil Aerodynamics - Early Research 7
2.2. Iced Wing, Iced Airfoil Aerodynamics - Recent Research 8
2.2.1. Experimental Research - Two-Dimensional Flowfields 9
2.2.2. Computational Research - Two-Dimensional Flowfields 16
2.2.3. Experimental Research - Three-Dimensional Flowfields 20
2.2.4. Computational Research - Three-Dimensional Flowfields 23
2.3. Research Related to Iced-Wing Aerodynamics 25
2.3.1. Laminar Separation Bubbles 25
2.3.2. Rearward-Facing Steps 29
2.4. Present Research 30

III EXPERIMENTAL SETUP 32
3.1. Experimental Facilities and Ancillary Equipment 32
3.1.1 Wind Tunnel 32
3.1.2 Model 33
3.2. Measurement Technique 34
3.2.1. Laser Doppler Velocimetery: Operating Principles 34
3.2.2. Transmitting and Receiving Optics 35
3.2.3. Data Acquisition Hardware and Software 38
3.2.3.1. Frequency Shifting and Downmixing 38
3.2.3.2. Signal Conditioning 40
3.2.3.3. Computation of Particle Transit Time 43
3.2.3.4. Data Reduction, Analysis and Storage 45
3.3. Seeding 47
3.4. Alignment and Traverse Equipment 48
3.4.1. Model and Tunnel Coordinate System 49

3.4.2. Traverse Mechanism 49
3.4.3. Alignment Procedure 51
3.4.4. Measurement Locations 52
3.5. Error Analysis 54
3.5.1. Systematic Uncertainty 54
3.5.2. Clock Resolution 57
3.5.3. Fringe Bias 59
3.5.4. Velocity Bias 62
3.5.5. Spatial Resolution and Gradient Bias 69
3.5.6. Statistical Uncertainty 72

IV RESULTS AND DISCUSSION 74
4.1. Empty Test Section(Model not Mounted in Tunnel) 74
4.2. LDV Measurements - Clean Wing 75
4.2.1. Pressure Distribution on the Wing Centerline 75
4.2.2. Comparison with Computation 76
4.2.3. Evolution of (u)- and (w)-Velocities Normal to the Finite Wing's Surface 80
4.3. LDV Measurements - Iced Wing 86
4.3.1. Comparison with Earlier Measurements 86
4.3.2. Comparison with Navier-Stokes Calculations 90
4.3.2.1. Comparison at y/b=0.470 90
4.3.2.2. Comparison at y/b=0.175 and y/b=0.819 92
4.3.3. Mean Measurement Results 93
4.3.3.1. Evolution of Flow Normal to the Wing Surface 94
4.3.3.1.1. Profiles Upstream of the Separation Bubble ... 94
4.3.3.1.2. Profiles Inside of the Separation Bubble 95
4.3.3.1.3. Profiles Downstream of the Separation Bubble 96
4.3.3.2. Evolution of Flow in the Streamwise Direction 98
4.3.3.2.1. Stagnation and Separation Streamlines 98
4.3.3.2.2. Boundary Layer Thicknesses 99
4.3.3.2.3. Transition and Reattachment 100
4.3.3.3. Evolution of Flow in the Spanwise Direction 102
4.3.3.4. Reynolds Number Effects 104
4.3.3.5. Time-Dependent Measurement Results 105
4.3.3.5.1. Histogram Distributions 106
4.3.3.5.2. Turbulence Intensities 108
4.3.3.5.3. Reynolds Normal Stresses 109

V SUMMARY, CONCLUSIONS AND RECOMMENDATIONS 111
5.1. Summary and Conclusion 111
5.1.1. Clean Wing 112
5.1.2. Iced Wing 112
5.1.2.1. Comparison with Other Measurements and Theory . 112

5.1.2.2. Mean Measurement Results 113
5.1.2.3. Turbulence Quantities 115
5.2. Recommendations 116

REFERENCES **119**

FIGURES **132**

APPENDIX 1 EQUATIONS USED FOR CALCULATION OF VARIOUS FLOW MOMENTS 232
APPENDIX 2 MEAN VELOCITY PROFILES FROM LDV MEASUREMENTS ON THE CLEAN RECTANGULAR WING 234
APPENDIX 3 COMPARISON OF SPLIT HOT-FILM MEASUREMENTS WITH LDV MEASUREMENTS ON THE ICED RECTANGULAR WING 242

VITA 244

LIST OF SYMBOLS

b	Wing span, in. (m)
c	Wing chord, in. (m)
C_D	Drag Coefficient, $D/(0.5\rho U^2_\infty S)$
C_L	Lift coefficient, $L/(0.5\rho U^2_\infty S)$
C_P	Pressure coefficient, $(p-p_\infty)/(0.5\rho U^2_\infty S)$
d_{bw}	Diameter of the beam waist, μm
d_f	Fringe spacing, μm
d_{mv}	Diameter of the measurement volume, μm
f	Doppler frequency, MHz
f_s	Frequency shift, MHz
l_{mv}	Length of the measurement volume, μm
M	Mach number
N_T	Total number of fringes in the measurement volume
N_f	Number of fringes required for valid measurement
P	Probability of particle detection
Re	Reynolds number based on the chord, $(\rho U_\infty c)/\mu$
T_N	Time for N-cycle measurement, μs
T_{N_c}	Time for comparison-cycle measurement, μs
u	Mean velocity in the streamwise direction, ft/sec (m/s)
U_∞	Tunnel speed, ft/sec (m/sec)
u'	Fluctuating component of velocity in the x-direction, ft/sec (m/s)
v	Mean velocity in the spanwise direction, ft/sec (m/s)
w	Mean velocity in the vertical direction, ft/sec (m/s)
Δy	Distance between beam focus and measurement volume, mm

Greek Symbols

α	Wing geometric angle of attack, deg.
γ_P	Intermittency factor
δ	Boundary layer thickness, in. (mm)
δ^*	Boundary layer displacement thickness, in. (mm)
e_{bias}	Bias error

$\theta/2$	Half-angle of coincidence laser beams, deg.
θ	Boundary layer momentum thickness, in. (mm)
λ	Laser wavelength, nm
σ_n	Standard deviation due to the processor clock count
ϕ	Angle between the velocity vector and normal to the fringes

CHAPTER I

INTRODUCTION

Airframe or structural ice accretion continues to be one of the most serious aviation hazards faced by the pilot. A statistical study of aircraft icing accidents[1] has revealed that 803 icing-related aircraft accidents were reported between 1975 and 1988. Sixty-eight percent of the reported accidents were due to deterioration of in-flight performance induced by structural ice accretion during cruise and landing phases of flight. Of all the airframe icing accidents, almost half involved fatalities. Right along with thunderstorms, structural or airframe ice accretion is one of the pilot's worst environmental enemies. Understanding the performance penalties associated with in-flight icing can be used to enhance future aircraft design, and therefore increase the flight safety margin.

The primary cause of in-flight ice accretion has been attributed to the presence of super-cooled water droplets in the air[2]. In this meta-stable state, the water droplets can stay in liquid form down to temperatures well below freezing. These droplets freeze either if the temperature is further lowered or if a nucleus is provided around which ice can form. The surfaces of an aircraft moving through a cloud of super-cooled water droplets provide such icing nuclei. Small aircraft components such as the pitot tubes, antennas and empennage deflect less air than the larger, more blunt components. The smaller components, therefore, have a higher collection efficiency and collect more ice compared to the larger surfaces for a given accretion time.

Once the accretion process begins, ice builds up quickly and the effect is an increased aircraft weight. Far more important, however, is the disturbance of the

boundary layer over the aerodynamic surfaces, Fig. 1. The wings are the primary source of lift and a major contributor to drag. Interruption of the boundary layer flow over the wings causes a deterioration of the wing aerodynamic performance with possible catastrophic consequences in terms of aircraft performance and controllability.

During an encounter with super-cooled droplets, depending on the liquid water content, air temperature, and aircraft velocity, two different forms of ice accretion on the wings may be expected. A sketch of the two forms of accretion, called rime and glaze, is shown in Fig. 2. The conditions under which each type of ice formation may be expected are summarized in Table 1. While rime ice has a fairly streamlined shape and causes some performance degradation, the glaze ice shape with its characteristic large protrusions causes a gross distortion of the wing geometry. The result is an undesirable change in the airflow pattern over the wing surface which ultimately leads to a drastic reduction in lift performance, and an increase in drag. The performance penalties due to glaze ice accretion are therefore more severe. As a result, the recent analytical and experimental iced-airfoil and iced-wing studies have focused on the glaze ice formation.

The glaze ice accretion on an airfoil leading edge creates a large region of flow separation aft of the ice horns on the upper and lower airfoil surfaces. At low angles of attack, the separated flow on the suction side of the airfoil reattaches to the surface. The separation bubble, bound from the top by the separated shear layer and from the bottom by the airfoil, is characterized by a region of recirculating fluid. Downstream of reattachment, the shear layer begins to grow next to the wall in a normal sense. At higher angles of attack, but far lower than the clean-wing stall angle, the separated shear layer fails to reattach to the airfoil and an early stall condition exists. The earlier onset of stall, due to the presence of the ice shape, manifests itself in the form of a reduction in maximum lift, increase in drag and an adverse change in pitching moment. These effects are shown qualitatively in Fig. 3 for a typical wing.

TABLE 1. ICE FORMATION[3]		
Ice Shape	Rime	Glaze
Liquid Water Content(LWC)	Low	High
Air Temperature	Low	Near Freezing
Flight Velocity	Low	High
Freezing Fraction	One	Less Than One
Droplets Freeze	On Impact	Flow On Surface
Ice Color	White, Opaque	Clear
Ice Density	< 1 gm/cc	1 gm /cc

Bragg[3] has cited two approaches to minimizing or eliminating the aircraft icing problem. The first method involves prevention of ice accretion (anti-icing) or periodic removal of ice from the aircraft surfaces (de-icing). Installation and design of complex mechanical or thermal systems as an add-on to the existing components achieve this purpose. The second method which Bragg has cited takes advantage of the proper design of the aircraft component to minimize the adverse effects of ice accretion. Such a component therefore would prohibit ice formation or force the ice formation into a geometrical shape which would be least likely to have an adverse effect on the aerodynamic performance of that component.

De-icing and anti-icing methods are usually expensive. They require bulky equipment which is costly to maintain and requires an external power source. These disadvantages hinder their installation and operation in small general aviation aircraft. Operation of such equipment on larger transport and business-class aircraft has not entirely excluded this class of aircraft from claiming a large share of icing-related accidents. According to Cole and Sand[1], 42 percent of the 803 icing-related accidents reported between 1975 and 1988 involved business and commercial flights while aircraft utilized for personal use claimed 58 percent of the accidents.

Indeed, a better approach would be to reduce the adverse effects of ice formation through proper aerodynamic design of the aircraft lift and control surfaces. Both commercial and private aircraft, in addition to remotely piloted vehicles and missiles would benefit from such an improvement in design. Once the performance penalties associated with icing are well understood, component design may be improved. Such a task requires the well-coordinated efforts of both the experimental and computational community. The computational branch utilizes well-known numerical methods to understand the flowfield of an iced component. The experimental branch, through detailed measurements, gains insight of the flow physics while at the same time it provides a means of verification and code calibration through detailed measurements of force, pressure and velocity field on the chosen component.

Since the early 1980's, a consolidated effort has been established by the National Aeronautics and Space Administration (NASA). Headed by NASA Lewis Research Center and involving universities and industry in a multi-year program, the ultimate goal of this effort is to provide the capability to incorporate performance, stability and control analysis of iced aircraft in the overall aircraft design and performance analysis process. As Shaw[4] pointed out,

> *"Accurate predictions of aerodynamic performance degradation of an aircraft due to icing is one of the desired end products of the icing analysis methodology.... "*

In order to assess the aerodynamic performance penalties associated with a leading-edge ice accretion, the NACA 0012 airfoil section was chosen due to the availability of aerodynamic data from many earlier experiments. Since the glaze ice formation on the wing leading edge causes severe aerodynamic penalties, attention has been focused on a simulation of the glaze ice shape. The ice accretion used is a simulation of that measured on a NACA 0012 airfoil in the NASA Icing Research Tunnel, Fig. 4. The icing conditions were a free-stream velocity of 130 mph, angle of attack of 4 degrees, icing time of 5 minutes, volume median diameter droplet of 20 microns, Liquid Water Content(LWC)=2.1 g/m^3 and a temperature of 18°F.

The simulated shape, however, does not accurately model the roughness usually present on the iced surfaces. Furthermore, it has a well-defined geometry which is not an exact replica of the actual ice shape. In addition to facilitating the fabrication process, the advantage of using this simple model is that, experimentally, a real ice accretion which has a finite life time need not be handled. Computationally, it allows the modeler to focus on the code formulation while simplifying geometrical modelling of the ice shape.

The presence of glaze ice on the wing leading edge causes a significant portion of the boundary layer to separate from the wing surface. As a result, use of inviscid numerical methods are excluded. Indeed, a very recent comparison of Euler and Navier-Stokes results by Kwon and Sankar[5] has revealed major differences in the predicted flowfield using the Euler formulation versus the Navier-Stokes formulation. In addition, fully three-dimensional numerical prediction methods have been preceded by two-dimensional models. Use of two-dimensional methods has allowed the simplification of equations as well as reducing the computational cost and time while maintaining the important features attributed to the flowfield of the iced airfoil. Both viscous-inviscid models and Navier-Stokes formulations have been used to obtain flowfield predictions.

Bragg et. al.[6-9] have used the simulated ice shape shown in Fig. 4 to document the aerodynamic penalties associated with ice accretion on a NACA 0012 airfoil. These detailed measurements have been used to document the iced airfoil flowfield and verify the correctness of two-dimensional numerical prediction methods. Although much larger in size than a classic laminar separation bubble, recent detailed analysis of these data has shown that the separation bubble formed aft of the ice horns on the iced airfoil behaves in a manner similar to that of a laminar separation bubble. A sketch of the upper surface separation bubble, located aft of the ice horn, is shown in Fig. 5a.

Recent application of three-dimensional numerical methods has allowed prediction of iced-wing flowfields[10-12]. The numerical method utilizes the full three-

dimensional set of time dependent Reynolds-averaged Navier-Stokes equations to obtain velocities. The wing used for these tests has the same simulated ice shape as the earlier two-dimensional tests. Initial analysis has focused on a rectangular, untapered and untwisted planform with a NACA 0012 cross section. The wing has been tested in both the straight and swept configurations. Recent force balance and pressure measurements, as well as flow visualization, on this semispan reflection-plane wing have been used to compare the lift performance of this wing with the computational predictions[13-19].

While much data has been gathered in this area, little or no detail is available on the fluid mechanics of the airflow over three-dimensional wings with leading edge ice accretion. It is therefore the intent of the present study to further our knowledge of the flowfield of a three-dimensional wing with a simulated glaze ice accretion. This is carried out by detailed measurements using a laser Doppler velocimeter on the semispan rectangular wing, both in the clean and iced configurations. The large separation bubble aft of the ice horns, primarily responsible for the finite wing's performance degradation, will be studied in detail in the chordwise direction. Velocity surveys near the model root, centerline, and tip may provide clues to the spanwise behavior of the flow on the finite wing model. Mean velocity profile measurements in the immediate vicinity of the finite wing, in addition to unsteady data obtained by the LDV instrument will serve in improving our understanding of the flowfield details.

These non-intrusive measurements of the 3-D flowfield will complement previously obtained flow visualization results in addition to pressure and force balance measurements. Furthermore, these measurements reveal new aspects of the separated flow aft of the ice horns which may be used to guide future experimental and computational analysis.

CHAPTER II

REVIEW OF LITERATURE

The origins of research on the aerodynamics of an iced wing can be traced back to the work carried out in the late 1920's. A focused interest, however, did not develop until the late 1970's when a large increase in the use of general aviation brought new interest to this subject. This interest has covered a wide range of topics, dealing with ice accretion physics and ice protection systems in addition to iced airfoil aerodynamics. The subject of this thesis falls in the last category. Therefore, this section will provide a review of the research carried out in this area.

The research performed for this study has shown many features of the flowfield behind the simulated ice shape to be similar to those found in both classic laminar separation bubbles and rearward-facing steps. Therefore, a review of research on separation bubbles and rearward-facing steps in conjunction with laser velocimetery will follow in the subsequent sections.

2.1. Iced-Wing, Iced-Airfoil Aerodynamics - Early Research

Initial efforts at icing simulation took place in the late 1920's and early 1930's. These activities are described in References 20-24. The first wind tunnel test in the United States which involved simulated ice formation was probably that carried out by Gulick[24]. An aspect ratio 6 wing was tested in the Langley Full-Scale Wind Tunnel with roughness used to simulate ice accretion. A 25% reduction in maximum lift and 90% increase in drag were reported for the conditions tested.

The need for better ice protection for military aircraft was realized after World War II in Europe as well as in the United States. At the time, flight testing was the primary means for studying the effect of ice formation on aircraft aerodynamics and

performance. Preston and Blackman[25] conducted flight tests in a twin-engine airplane. They documented the drag rise due to natural icing conditions on the various components of the test aircraft. Flight testing in icing conditions suffered from the inherent danger associated with adverse weather conditions in addition to the lack of carefully controlled test conditions. The construction of the Icing Research Tunnel (IRT) at the Lewis Research Center in Cleveland, Ohio between 1942 and 1944 addressed this problem. With the addition of a fully operational spray system to simulate icing cloud water droplets in 1950, the tunnel was utilized to study airfoil performance in different icing conditions.

Many activities in the IRT included the development of ice formations on aerodynamic surfaces followed by evaluation of the aerodynamic performance degradation. Under carefully controlled conditions, Gray[26] conducted a series of experiments to study the effect of droplet size, liquid water content, air temperature, icing time and angle of attack. These conditions were then correlated with the resulting ice shape characteristics and airfoil drag rise.

The period between 1958 and the mid-1970's saw little activity in icing research in the United States. In Europe and Canada, however, some research did continue. The AGARD Advisory Report No. 127 provides an overview of research conducted in the early 1970's, primarily in Europe and Canada.

In the 1970's a large increase in the use of general aviation and rotorcraft vehicles brought new interest to icing research[27]. The energy crisis and rising fuel costs of that era also made the use of bleed-air systems significantly more expensive. As a result, the period following the mid-1970's saw a resurgence of international interest in icing research. The research conducted on the aerodynamic effects of ice accretion will be described in the following section.

2.2. Iced-Wing, Iced-Airfoil Aerodynamics - Recent Research

Recent research in iced-airfoil and iced-wing aerodynamics originated in the early 1980's. Initially carried out in the form of experimentation with both real and simulated ice shapes on two-dimensional airfoils , this research expanded in the

ensuing years to encompass three-dimensional flowfields. Reinmann, et al.[28] identified several reasons for the current interest in icing:

> *"(1) the more efficient high by-pass ratio engines of today and the advanced turboprop engines of tomorrow have limited bleed air for ice protection...; (2) airfoil designers do not want their modern, high-performance surfaces contaminated with ice, so they are intensifying pressure to develop ice protection systems that minimize residual ice...; (3) new military aircraft requiring severe weather capability are currently under development; (4) some existing military aircraft, being used primarily for training missions, are experiencing foreign object damage (FOD) due to icing conditions they would not normally encounter in combat; (5) designers of high performance military aircraft want to avoid burdening the aircraft with ice protection, so they want to know where and how much ice will build on the aircraft and whether the performance penalties are acceptable; (6) designers of future high performance aircraft with relaxed static stability need to know how their aircraft will perform with contaminated aerodynamic surfaces; (7) little is known about the effects of ice accretion on the operation and performance of advanced turboprops; and (8) the FAA has certified only one civilian helicopter for flight into forecasted icing, which implies a strong need for support of helicopter icing."*

The description of experimental and computational research in the 2-D flowfields will be followed by the 3-D research.

2.2.1. Experimental Research, Two-Dimensional Flowfields

Recent research on the aerodynamic penalties associated with icing have used both natural and simulated ice shapes on airfoils. Shaw et al.[29] tested a NACA 63_2-A415 airfoil section in the NASA Icing Research Tunnel (IRT) under rime and glaze icing conditions. They measured a 130 percent increase in drag coefficient for a 20 minute glaze icing encounter. The drag increased by 40 percent for a 15 minute rime icing encounter and the same aerodynamic conditions. The measured increase in the drag coefficients were found to correlate well with empirically based NACA predictions for low liquid water content, or the rime ice, cases.

Use of simulated ice accretion shapes has facilitated icing research in conventional wind tunnels. Ingleman-Sundberg et al.[30] tested a transport airfoil with slats and flaps to document the effect of five different ice shapes. These tests for the first time described the simulation technique for modeling both the ice shape and

the accompanying surface roughness.

Bragg et al.[31] tested a NACA 63_2-A415 airfoil section in the NASA Icing Research Tunnel (IRT) under simulated ice conditions in typical cruise conditions for a general aviation aircraft. Both actual and simulated ice accretion shapes were studied during this test. During the simulated icing tests, the average roughness measured on the actual ice was simulated with an abrasive. Using this technique, they reported accurate reproduction of the drag measured on the actual iced-airfoil. Their measured pressure distributions on the ice shapes showed extremely severe adverse pressure gradients in this region of the flow. For these tests the simulated ice shapes were instrumented with ten surface pressure taps. The measurements clearly indicated large regions of separated flow in the immediate vicinity of the ice shapes. A need for very dense pressure-tap placement on the simulated ice model for better resolution of the separated flowfield was also identified.

The information gathered from wind tunnel experiments of iced aircraft components has been used to construct a data base of icing variables. Correlation equations, determined from the information in this data base, have been used to relate the change in lift, drag, and pitching moment to known aerodynamic and icing variables. The first such correlations were developed by Gray[26] for various airfoils in the NACA IRT. Bragg[3] also developed correlation relations for rime icing conditions at the NASA IRT. Flemming and Lednicer[32] acquired a large data base in the Canadian NRC high-speed wind tunnel for a series of reduced-scale rotor airfoil sections.

Korkan, et al.[33,34] used this approach to analyze the helicopter rotor in hover and forward flight. The rotor configuration under analysis was the front rotor of the Boeing Chinook CH47. No experimental data existed for comparison to the predictions. However, the results compared reasonably with previously reported torque rises measured in icing for other helicopter configurations.

In the absence of more accurate methods, the procedures relying on correlation relations can provide reasonable estimates of performance degradation. However,

care must be exercised when using correlation methods. As Shaw[4] pointed out, errors in studies made with correlation methods in icing analysis can be as large as 100 to 200 percent for selected conditions. This is partly due to the limited icing data base which exists. Miller and Korkan[35] presented typical effects of using different correlation equations on the outcome of such performance analysis methods. He pointed out that in this prediction process, the empirical correlations are the weak link in the computation of lift and drag increments.

Although the use of simulated ice has allowed researchers to use conventional wind tunnels, testing under natural conditions continues to be another source of information on iced airfoil aerodynamics. Potapczuk and Berkowitz[36] measured the changes in lift, drag and pitching moment for a two-dimensional model of a Boeing 737-200 ADV wing section. The measurements were made as ice accumulated on the surface in both cruise and high-lift configurations. Their results indicated a continual increase in drag as ice accumulated on the surface. They reported no change in the pitching moment and lift until the angle of attack was varied from that at which the ice was accumulated.

With the advent of modern techniques in computational fluid dynamics and the rapid growth of computational capabilities, several researchers in the field began addressing the problem of an airfoil in icing conditions. In order to document the flowfield of an airfoil with simulated ice accretion as well as to provide a means of verifying the emerging computational results, Bragg and his co-workers have studied the flowfield of an airfoil with simulated ice shape in detail. They used a NACA 0012 airfoil section to study the effect of a simulated glaze ice accretion on the aerodynamic performance degradation due to icing. The simulated ice shape was an approximation of the ice accretion measured in the NASA IRT at the conditions stated in Fig. 4. This shape was chosen to be a simple, but representative, glaze-ice accretion shape which could also be used for computer code validation.

Bragg and Coirier[6,37] used this model to measure the surface pressure distribution at $Re = 1.5 \times 10^6$ and $M = 0.12$. The pressure distribution, in addition to integrated lift,

drag and pitching moment were reported for the conditions tested. The surface pressure distribution on the iced model clearly showed regions of separated flow aft of the ice horns. Typical C_p spikes of around -2.5 at $\alpha = 6°$ were replaced by -1.25 when the simulated glaze ice shape was used. These pressure measurements showed that regions of constant pressure, indicative of the underlying separated flow region, were followed by reattachment and recovery to free-stream values at low angles of attack. At higher angles of attack, but far lower than the baseline stall angle, the airflow failed to recover from the extremely severe adverse pressure gradient and massive flow separation occurred. The presence of the ice shape was found to grossly reduce the peak pressure values near the leading edge. In the presence of simulated ice, the maximum lift coefficient for this airfoil dropped by 55 percent (1.22 to 0.55) with little change in the lift-curve slope. The corresponding α_{stall} dropped by 57 percent (14° to 6°) when the simulated ice was tested.

The drag performance of this airfoil was also seen to deteriorate rapidly in the presence of the simulated ice shape. At $\alpha = 0°$, the baseline clean model with natural transition showed a drag coefficient of $C_{d,wake} = 0.0076$ while the drag for the iced airfoil at the same angle of attack rose by more than 240 percent to 0.0260.

The advantages of wind tunnel testing at the actual flight Reynolds number are known. However, since the number of facilities that can provide high Reynolds-number capabilities is limited and such testing can be very expensive, researchers have utilized lower Reynolds-number facilities which are operationally more cost effective. Results from such tests should be carefully analyzed before applying them to the higher, actual flight Reynolds numbers.

An aft-loaded, single-element, pressure-instrumented airfoil was used by Lynch et al.[38] to study the aerodynamic impact of very small leading-edge simulated ice (roughness) formations on lifting surfaces. With the distributed roughness applied to the airfoil leading edge to simulate the early stages of ice buildup, the tests were carried out at Reynolds numbers ranging from 2.5 to 18 million. Three roughness sizes, ranging from $k/c = 0.00007$ to 0.00053 were used for this study.

Among other forms, the results were presented in the form of percentage reduction in $C_{l,max}$ ($\Delta C_{l,max}$) for varying Reynolds number. These results, for all three roughness sizes tested, indicated a much lower reduction in $C_{l,max}$ for the $Re = 2.5x10^6$ case compared to all other test Reynolds numbers. A separation bubble, absent at the $Re \geq 5.0x10^6$ cases, was detected from the surface pressure measurements at $Re = 2.5x10^6$ on the clean airfoil. The effect of this bubble was a reduction in maximum lift of the clean airfoil. The addition of roughness eliminated the separation bubble as the maximum lift on the airfoil with rough leading edge was reported to be nearly identical for $Re = 2.5x10^6$ and $5.0x10^6$. Since the bubble on the clean model could not be successfully removed by fixing transition ahead of the bubble location, emphasis was placed on conducting all tests at the actual flight Reynolds number. It is important to note that the geometry of the airfoil used in this test lent itself to the formation of separation bubbles at low Reynolds numbers.

In separate tests conducted at the same site, Morgan et al.[39] conducted an experimental study to determine the effects of Reynolds number and Mach number on the aerodynamic performance of a two-dimensional supercritical-type airfoil. The experimental tests were conducted through a Reynolds number range from 2.8 to 20.9 million and a Mach number range from 0.10 to 0.35. The effects of glaze ice and frost formation were also studied in these tests.

The results of Morgan et al. indicated little change in $\Delta C_{l,max}$ with increasing Reynolds number. The geometry of the clean airfoil did not lend itself to formation of separation bubbles at low Reynolds numbers. The leading-edge frost was simulated by a very coarse No. 70 grit. The simulated glaze ice configuration was one with characteristic upper and lower surface horns, significantly altering the model's leading edge geometry. It is well known that in the presence of such sharp, bluff body-like protrusions, flow separates from the edges of these protrusions (see sketch of bubble flowfield, Fig. 5), independent of angle of attack or Reynolds number. Since Reynolds number effects are dependent on the type of geometry and flow conditions tested, care should be taken when interpreting the results for

different airfoils.

Pressure measurements on the clean baseline NACA 0012 airfoil used by Bragg and Coirier[6,37] with and without a transition strip at 5% chord did not indicate the presence of a separation bubble. On the iced wing, however, the simulated glaze ice shape used for the study created a large protrusion with sharp edges at the leading edge, thus causing the flow to separate at the ice horns independent of angle of attack and Reynolds number. It seems therefore that the results obtained with the iced airfoil at $Re = 1.5x10^6$ could also be applied to higher flight Reynolds numbers.

The simulated ice tested by Bragg and Coirier[6,37], also known as the smooth simulated ice shape for its lack of surface roughness, was used by Bragg and Spring[7] to study the effect of rough simulated ice on the airfoil aerodynamic performance. The addition of roughness was found to affect the airfoil performance differently at negative angles of attack compared to positive angles of attack. The cause was attributed to the difference in geometry of the upper and lower surface ice horns. The lower surface ice horn had a larger radius of curvature, thus making the flow behavior more susceptible to surface roughness than the upper surface ice horn.

Overall, however, the effect of roughness on the aerodynamics of the airfoil with simulated glaze ice was found to be negligible. As pointed out earlier, the addition of simulated glaze ice to the airfoil caused such a large loss in lift that the additional penalty due to the distributed roughness was relatively small. Note that roughness on the iced-airfoil leading edge does not have the same affect on the flowfield as roughness on the clean-airfoil leading edge. Flow separation and subsequent reattachment seem to be driven by the bluff body-like protrusions on the iced airfoil and therefore, roughness effects appear to be secondary in importance.

Using a split hot-film probe, Bragg, et al.[6-9,37] also obtained velocity profiles on the iced airfoil. Bubble lengths exceeding 35 percent chord were measured. The velocity profile measurements clearly indicated large regions of reverse flow, extending behind the ice horns on the iced airfoil. The effect of probe presence on the overall flowfield and on the separation bubble size was also examined[7]. The effect of the

probe support was seen as a reduction in static pressure in the separated region. This was attributed to the probe support's pressure field. When the probe itself penetrated the separation zone, an apparent reduction in bubble length was also observed. This by itself pointed out the benefits of a non-intrusive measurement method.

The calculated data for the momentum thickness on the iced airfoil gave information which correlated well with the reattachment location measured from the velocity profiles. These trends ceased to exist at angles near and above stall, where the unsteady nature of the bubble affected the measurements.

Bragg and Khodadoust[8] also studied the aerodynamic characteristics of a computer-generated ice shape. This new ice shape was predicted by the LEWICE computer code[40] for the same icing conditions that generated the original ice accretion in the NASA Icing Research Tunnel, used currently for simulation work.

The computer-generated ice shape was also found to severely degrade airfoil aerodynamic performance, reducing the lift and increasing the drag. The aerodynamics of the airfoil with both the computer-generated and the simulated ice shapes were found to be very similar at positive angles of attack. At negative angles of attack, however, the comparison was not in good agreement. This was primarily due to the computer code under-predicting the lower surface ice horn. These data provided an initial look at how well the ice shape must be predicted to have aerodynamic penalties similar to an actual ice accretion.

Little information on the time-dependent behavior of the ice-induced separation bubble exists today. Bragg and Khodadoust[8], however, obtained limited measurements of the frequency content for the flow over the iced airfoil. Based on the iced airfoil projected height as the reference length, the output of the power spectrum analyzer was correlated to a Strouhal number of 0.0185. The cause for this oscillation was attributed to the transitional state of the shear layer at the measurement location on the iced airfoil. This value corresponded to low-frequency, pre-stall oscillations found on clean airfoils by Zaman et al.[41]. Zaman found a

Strouhal number of approximately 0.02 for many different airfoils. Their work showed that this phenomenon occurred only for airfoils with *trailing edge stall* or *thin-airfoil stall*, but not for abrupt *leading-edge stall* involving hysteresis.

More recent work by Zaman and Potapczuk[42] has further explored this phenomenon as it applies to an airfoil with simulated glaze ice. Although their experiment was at a Reynolds number of 0.1 x 10^6, the low-frequency oscillation peaked between 6 and 7 degrees angle of attack. It is interesting that this occurred around $\alpha = 6^\circ$ where the mean flow measurements in the bubble were found to no longer follow the trends seen at lower angles. This reinforced the idea that near stall measurements may be affected by large bubble oscillations. The unsteady nature of the separation bubble near stall was also observed by Khodadoust[43] in flow visualization results.

The results from surface pressure, wake drag and velocity measurements, as well as the reduced engineering coefficients, have been thoroughly documented by Bragg[44,45]. The work carried out by Bragg and Khodadoust[8] completed the documentation of the velocity field about the airfoil with the simulated ice shape. The bulk of the acquired measurements were used for calibration and validation of computer codes used by other researchers to predict the aerodynamics of an iced airfoil.

2.2.2. Computational Research - Two-Dimensional Flowfields

Recently, sophisticated computational fluid dynamic methods have been applied to the problem of an airfoil with leading edge ice accretion. Several approaches have been used to compute the aerodynamics of an airfoil with ice accretion. One method utilized the Navier-Stokes equations in full or thin-layer form on a structured grid while another method used the unstructured grid scheme. The interactive boundary layer (IBL) approach has been used in another method to couple the solution of the inviscid flowfield using a panel method to the solution of the boundary-layer equations. Finally these performance prediction codes have been coupled to the LEWICE ice accretion code in order to study the entire ice accretion-aerodynamic

degradation cycle.

Potapczuk[46,47] used the ARC2D Navier-Stokes code which could be run in both the full or the thin-layer form. The turbulence model employed in the code was the Baldwin-Lomax model. Initially developed at NASA Ames Research Center, in conjunction with the GRAPE grid generation code, also developed at NASA Ames, the code was used by Potapczuk to analyze the aerodynamic performance of a NACA 0012 airfoil with leading-edge ice for a range of angles from zero to ten degrees.

Potapczuk compared computed velocity profiles with the experimental ones. Velocity profile comparisons were presented for transition fixed at both the leading edge and at five percent chord. The bubble size predictions from the latter results compared best with the experimental data. However, in both cases, significant differences between the computed and the experimental velocity profiles were observed. Despite this difference, the drag predictions seemed to match the experimental results rather well at low angles of attack.

The lift and drag performance results were in good agreement with experiment for angles of attack below stall. Pitching moment comparisons indicated slightly higher computed values. Below stall, computed pressure distributions were shown to compare well with the experimental distribution aft of the ice shape. Near the ice shape, particularly on top of the ice horn, Potapczuk's computations indicated large pressure spikes which were not seen in the experimental data. This was attributed to the grid spacing at this region above the highly curved surface of the model. The presence of these pressure spikes near the leading edge of the iced airfoil may explain the slightly higher computed pitching moment coefficients. In general, these anomalies did not seem to affect the computed values of lift appreciably. This may be explained in part through the fact that, although somewhat different in shape, both experimental and computational velocity profiles yielded the same boundary-layer displacement thickness, δ^*, which is the crucial parameter in determining the pressure distribution.

The use of the Baldwin-Lomax turbulence model in a flowfield with massive

separation, such as that observed on the iced airfoil near and above stall, may be considered questionable. Numerical experimentation with other turbulence models, such as the Johnson-King or the k - ϵ model, did not show major improvements over the Baldwin-Lomax model in the pre-stall regime. In the stall and post-stall regime, where regions of massively separated flows exist, the use of higher-order turbulence models have been favored[48]. Nevertheless, Potapczuk used a Modified Mixing Length (MML) turbulence model[49] and reported improved prediction in computational results. His computations performed near and above the stall regime hinted at the presence of a very unsteady separation bubble.

The Navier-Stokes formulation has also been used on an unstructured grid to study the iced airfoil. The motivation for this type of analysis has arisen from the desire to calculate ice growth as a function of time while simultaneously solving for the flowfield of the iced airfoil. Using unstructured grids, new geometries could be gridded with relative ease at each accretion time cycle.

The use of the unstructured grid in Navier-Stokes solutions for the iced airfoil flowfield was examined by Caruso[50,51]. Caruso used Euler and Navier-Stokes equations in conjunction with an unstructured mesh to solve for the flowfield over the iced airfoil. Calculation results were compared with those from structured-grid solutions for single time steps. While the unstructured grid results compared favorably with the structured grid results, the method was reported to require larger computational resources than the structured-grid technique.

Another approach for calculation of flow over iced airfoils was used by Cebeci[52,53]. He used an interactive boundary layer (IBL) method described by Cebeci et al.[54]. The same Baldwin-Lomax eddy viscosity formulation used by Potapczuk[47] was utilized in regions of transitional and turbulent flow. Cebeci used his IBL method once with the wake and once without the wake modelled. His computational results were compared against the experimental data of Bragg et al. for the iced NACA 0012 airfoil.

Without modelling the wake, the computed lift performance of the iced airfoil was

in poor agreement with experiment, even at low angles of attack. Modelling the wake improved the computed results to yield a lift-curve slope comparable with that given by experiment. Surprisingly, the computed drag values seemed to correlate better with experiment when no wake was modelled. The computed drag with the wake modelled seemed to yield lower values than experiment. Modelling the wake as a part of the iced-airfoil flowfield seems to be important, especially at high angles of attack, where the gross geometry of the simulated ice shape contributes to a premature wake growth.

Cebeci also compared the computed pressure distributions from his method with and without the wake with the experimental results. As expected, at low angles of attack, the computational procedure yielded similar results with and without modelling the wake. The pressure distributions were in good agreement with experiment downstream of the pressure plateau and transition. The rather large discrepancies upstream of transition, mainly appearing in the form of large pressure spikes not unlike those seen in the results of Potapczuk, were attributed to the strong adverse pressure gradients in the leading-edge region which also affected the transition location. At higher angles of attack, better agreement was reported for the results of the computation where the wake was modelled.

The computed velocity profiles were presented by Cebeci and compared with the experimental values. The discrepancies noted earlier also appeared in the velocity profiles. The computed velocity profiles seemed to under-represent the size of the experimentally-measured separation bubble. Outside of the separation bubble zone, better agreement was observed between computational and experimental velocity profiles.

A new version of the LEWICE ice accretion computer code was used by Potapczuk[55] to calculate ice growth on airfoils. Originally developed by MacArthur et al.[56] and later modified by Ruff and Berkowtiz[40] to predict the growth of ice on 2-D surfaces using a potential flow method, the new version of LEWICE was upgraded by Potapczuk to use the Euler equations for flowfield calculations. Results

indicated general agreement between the new and older versions of the code and reasonable reproduction of the experimental results.

Shin et al.[57] also used the LEWICE code to the calculate time-dependent aerodynamics of an iced airfoil. The IBL method due to Cebeci[54] was incorporated in LEWICE to calculate ice shapes and performance degradation of airfoils. In all the cases tested, the calculated results accounted for the drag increase due to ice accretion and, in general, showed good agreement with experimental data.

Overall, the computations carried out by Potapczuk, Caruso and Cebeci, mentioned in the preceding paragraphs, could predict the aerodynamic performance of the iced NACA 0012 airfoil with reasonable accuracy up to the stall regime. All methods, however, seemed to fail in and above the stall regime where viscous effects played a much more dominant role in the flow behavior. Since the computational techniques described here provided reasonable numbers for engineering calculations, further computational research concentrated on the more challenging problem of a three-dimensional iced wing.

2.2.3. Experimental Research - Three-Dimensional Flowfields

Recent research on the aerodynamic penalties associated with icing have used both natural and simulated ice shapes on airfoils and wings as well as flight tests using both aircraft and rotorcraft. The introductory section to the Proceedings of the International Aircraft Icing Technology Workshop[58] held at NASA Lewis Research Center in 1987 gives a concise review of progress and activities in the United States and Europe since 1978.

A procedure for estimating aircraft performance degradation due to icing, which is still widely used today, was demonstrated by Leckman[59] for light aircraft. The calculations were based on the glaze type of ice formation since the data were conservative where the drag values were concerned. The method was carried out in two phases. In the first phase the ice cross-sectional area, limits of impingement of ice accumulations in continuous maximum icing conditions, in addition to the increase in aircraft weight were calculated. In the second phase, the increase in drag

coefficient was estimated for the wing and empennage by using the drag data from icing tunnel tests using a NACA 0011 airfoil. Loschkan and Jesse[60] carried out a similar analysis for jet transport aircraft.

Using wind tunnel analysis and flight test results, Inglemann-Sundberg and Trunov[61] and Trunov and Inglemann-Sundberg[62] investigated the problem of tail stall due to icing. They identified landing with flaps deployed to be the most severe problem in ice-induced tail stall. They found that ice accretion on the tail reduced the tail maximum lift capability. The tail control surfaces therefore could not sustain the higher loads experienced by the tail during a landing with wing flaps deployed. This resulted in loss of longitudinal control on landing. A similar loss in lateral control, experienced by aircraft while taking off during icing conditions, was described by Brumby[63]. In the summary article, Brumby described several takeoff accidents where ice-induced flow separation from the wing surface caused a loss of lateral control.

By 1988, a considerably vast data base of experimental information on the aerodynamic performance of the iced NACA 0012 airfoil had been compiled by Bragg et al.[6-9,37,44,45]. This data represented the latest and best experimental measurements available for the NACA 0012 airfoil with simulated glaze ice in both the United States and Europe. Attention was then focused on the next logical step: the three-dimensional wing.

Since 1989, Bragg et al. have used a semispan, reflection-plane rectangular wing to study the effects of the simulated leading-edge ice accretion on the aerodynamic performance of a finite wing. A NACA 0012 airfoil section was chosen to compare to earlier 2-D tests. This model was used in the unswept configuration to measure the aerodynamic performance of a finite wing with simulated ice accretion[13,16,17]. The section lift and drag data compared well with the earlier 2-D data. Their measurements showed a large drag and maximum lift penalty due to the simulated glaze ice. The calculated three-dimensional span load data compared well with the inviscid computational results.

Force balance data in addition to florescent oil flow visualization were also acquired on the finite wing. Oil flow visualization showed that, at low angles of attack, the model centerline behaved in a 2-D manner. This result was in good correlation with earlier pressure measurements on the same model. The lift performance of the wing, measured by the force balance, compared favorably with calculated values from pressure measurements made earlier on the same model. Wind tunnel blockage was determined to be insignificant at low angles of attack. At high angles of attack, however, blockage corrections as high as 10 percent were used to correct the measured values.

The effects of roughness on the iced-wing aerodynamics were also examined during these tests. Two types of roughness were tested on this model: one called isotropic roughness, for its homogeneous distribution pattern, and the other called 3-D roughness, for its sparse distribution pattern. The results indicated that in the linear region of lift performance neither type of roughness had an appreciable effect on the iced-wing performance. In the non-linear region of lift, the isotropic roughness caused a small reduction in maximum lift at positive angles of attack. At negative angles of attack, an earlier stall onset was observed with a reduction in lift due to roughness. The drag polar of the wing mid-section reflected the earlier onset of flow separation due to the isotropic roughness as an early increase in drag.

The 3-D roughness was found to affect the iced-wing aerodynamic performance differently. The distinct stall angles measured previously were replaced by a change in lift-curve slope with increasing lift. This phenomenon was attributed to the vortex generator-like behavior of the 3-D roughness elements. Due to the delay in flow separation, the iced wing with 3-D roughness in the stall regime experienced a smaller drag rise compared with the iced wing with isotropic roughness.

The same wing was tested in the swept configuration[14,15]. The lift performance and span loads on the clean wing compared well with theory at low angles of attack. The vortex lift experienced by the swept wing, also observed by other researchers experimenting with swept wings, was found to cause the non-linear lift performance

of the clean wing in the stall regime.

The presence of the ice shape was found to affect the wing loading, especially in the outboard section. This effect was found to become more severe with increasing angle of attack. Roughness was found to uniformly reduce the wing loading at positive angles of attack. At negative angles of attack, however, roughness was seen to increase the wing loading with increasing angle of attack.

The integrated lift performance of the swept wing was seen to decrease appreciably in the presence of the ice shape. At positive angles of attack, a drastic reduction in the stall angle was observed with little change in the lift-curve slope. At negative angles of attack, due to the asymmetry of the glaze ice, a decrease in lift-curve slope in addition to a more gentle stall was observed. The results from surface pressure measurements, in addition to the integrated span loads, were compared with the 3-D computations. The experimental results from the swept wing were found to compare well with the computational results even without the sidewall boundary layer modelled.

Helium-bubble flow visualization, in addition to florescent oil flow visualization, was performed on the iced swept wing[15-17]. These methods revealed extensive spanwise flow in the separation bubble aft of the upper surface ice horn. This was found to compare well with the results from 3-D computations of other researchers.

Wing root-wall interaction was found to have no effect on the aerodynamics of the swept wing. This interaction, however, did affect the aerodynamics of the unswept wing, primarily due to the stall characteristics of the unswept wing. At high angles of attack, a significant sidewall boundary layer interaction was observed in the unswept wing data. When this was modelled properly in the computations, the results from span load calculations were in better agreement with measurement.

2.2.4. Computational Research - Three-Dimensional Flowfields

The experimental data obtained by Bragg et al. have been used for comparison with the results of computer codes written at Georgia Institute of Technology by Sankar and Kwon[5,10-12,64,65], under a NASA grant. The calculated chordwise pressure

distributions and the integrated sectional loads for the wing in both the straight and swept configurations were compared with experimental results.

Kwon and Sankar[10,64] computed the flow over the unswept finite wing. Conditions at 4- and 8-degree angles of attack, $M=0.12$, and $Re=1.5x10^6$ were computed on the CRAY-YMP at NASA Lewis Research Center. Results from computational modelling of the straight wing flowfield were compared with experimental results.

For this computational modelling, they used the full unsteady three-dimensional Navier-Stokes equations on an algebraic C-grid in a body-fitted coordinate system to model the flowfield about the 3-D wing. A two-layer Baldwin-Lomax eddy viscosity model patterned after the Cebeci-Smith model was used in this work.

The calculated chordwise pressure distribution and the integrated sectional loads for the clean wing at 4- and 8-degrees angle of attack compared well with experimental data except near the root where the sidewall boundary conditions differed. Sankar and Kwon[11,65] modelled the tunnel sidewall and improved the prediction near the root.

The computational results showed that the effect of the wall at the root section of the semispan reflection-plane wing was negligible on the aerodynamic loads at 4-degrees angle of attack. This effect, however, was noticed to be important at 8-degrees angle of attack were the flow was massively separated.

In the presence of the ice shape, the 4-degree pressure distribution was predicted reasonably well. The pressure spikes appearing in the leading-edge region were attributed to the sharp geometrical curvature of the ice shape, hence a need for more grid points in that region. A second reason was attributed to the use of standard second-order central differencing for all spatial derivatives. Application of a fourth-order scheme was thought to reduce the pressure spikes near the leading edge. In spite of the differences between the measured and calculated pressures near the leading edge, the rest of the pressure plateau followed by reattachment and recovery were well predicted.

In addition to the Navier-Stokes study, Kwon and Sankar[5] conducted inviscid

Euler calculations of the iced-wing flowfield. These results showed poor correlation with measured data and the viscous calculations. The predicted airloads obtained from the inviscid calculations were 10-15% higher than the viscous calculations. The importance of the inclusion of viscous effects in the numerical study of iced wings was therefore demonstrated.

Similar calculations for the swept wing have been performed by Sankar and Kwon[5,12,65]. Predicted chordwise pressure distributions, in addition to sectional integrated loads compared well with measurement. The effect of the wing-root wall interaction was found to be negligible on the predicted loads. This correlated well with experimental findings.

Cebeci et al.[66] extended their 2-D IBL technique, coupled with an extension of the LEWICE code, to provide a method for computing ice shapes along the leading edge of a wing and the subsequent calculation of the aerodynamic performance degradation for that wing. Cebeci et al. applied this code to a tapered wing with leading edge rime ice accretion to study the wing performance degradation for a range of angles of attack less than stall at a root chord Reynolds number of 4.6×10^6.

2.3. Research Related to Iced-Wing Aerodynamics

Flowfields involving different geometries, but dominated by the same characteristics, have been investigated by other researchers. Two basic geometries which exhibit the same flow characteristics as that found around the iced-wing leading edge are the laminar separation bubble and the rearward-facing step. The literature on both subjects is too large to cover completely here. A short review in each area, however, is provided in the following sections.

2.3.1. Laminar Separation Bubbles

The separation bubble phenomenon by itself has been investigated by many researchers. A sketch of a laminar separation bubble, adapted from Roberts[67], is shown in Fig. 5c. The bubble forms when a laminar boundary layer encounters an adverse pressure gradient of sufficient strength to cause separation. This is point S in Fig. 5. The separation leads to the formation of the shear layer over the bubble

and the characteristic flow reversal near the surface. At point T, the shear layer makes a transition to turbulent flow. The static pressure in the bubble is fairly constant over the bubble until transition. After transition, the magnitude of the reverse flow increases and a vortex-type flow is seen in the bubble. Before transition, the reverse flow is very slow, and this area is sometimes referred to as a dead-air region. As the turbulent shear layer entrains high-energy external flow, pressure recovery becomes possible, and the bubble reattaches at point R.

Bubbles are usually classified as short or long, not for their length, but for the effect on the flowfield as described by Tani[68]. Shorts bubbles have only a small, local influence on the airfoil pressure distribution and therefore have little effect on the airfoil performance. The short bubble bursts when it can no longer recover the required pressure. This results in the formation of a long separation bubble. A long bubble is characterized by a significant change in the airfoil pressure distribution. The suction peak on the airfoil leading edge is drastically reduced, reducing the amount of pressure recovery required by the boundary layer in the region of the separation bubble. When the long bubble can no longer provide this pressure recovery, the bubble bursts, and the resulting global change in the pressure distribution and flowfield usually leads to airfoil stall.

Jones[69] was perhaps the first to study separation bubbles. He observed the existence of separation and reattachment of the boundary layer over cambered airfoils. Gaster[70] and Horton[71] studied the structure and behavior of laminar separation bubbles on a flat plate. A small auxiliary airfoil in the inverted position over the flat plate provided an adverse pressure gradient on the flat plate through which separation and subsequent reattachment were controlled. Crimi and Reeves[72] studied leading edge laminar separation bubbles and developed a scheme for predicting the onset of transition in the laminar shear layer.

By the mid 1970's, some researchers began numerical investigations of separation bubbles. In 1974, Carter[73] investigated numerical solutions of the laminar, incompressible boundary layer equations for flows with separation and reattachment.

He used a stream function/vorticity formulation for the boundary layer equations. Solutions of the resulting finite-difference equations, were obtained by a successive column iteration scheme. In 1975, Briley and McDonald[74] utilized finite-difference solutions to the time dependent boundary layer equations for the flow in the immediate vicinity of the bubble to carry out a detailed numerical study of thin incompressible separation bubbles on a NACA 66-018 airfoil at zero incidence and chord Reynolds numbers of 2.0×10^6 and 1.7×10^6.

Mehta and Zalman[75] developed a numerical procedure to solve for the unsteady flow around any object that could be transformed into a circle with no surface singularities. They studied the effect of the separation bubble on the stalling characteristics of a 9% thick Jukowski airfoil with the maximum thickness at 28.89% chord at $Re = 1000$ and 15° incidence. The growth in size and strength of the separation bubble as a function of time on this airfoil was identified to correlate well with the increase in lift of the airfoil. The growth of a second bubble near the midchord and a subsequent third bubble near the trailing edge, in addition to the bursting of the first bubble, was cited to cause a reduction in lift. When these bubbles were cast off, the lift increased again with only one bubble remaining on the airfoil.

Roberts[67] used a semiempirical theory coupled with experimental correlation in conjunction with a modified version of Horton's method to calculate the properties of laminar separation bubbles. The comparison of these results with NACA experiments showed good agreement. Weibust et al.[76] presented computational and experimental results for flow in and around laminar separation bubbles with emphasis on the reattachment region. A 15% thick laminar airfoil was used at $Re = 1.2$ to 1.5 million with two high-frequency response pressure transducers in addition to a miniature hot wire rake to record the bubble properties. The experimental findings correlated well with computations performed based on the methods by Horton and Roberts.

In their paper, Weibust et al. cited the small physical dimensions of the bubble

in addition to its vicinity to the airfoil leading edge as the reason for lack of detailed experimental data within these short bubbles. The physical presence of a probe such as a hot wire or a pitot probe may seriously affect the entire bubble flowfield. Stack et al.[77,78] successfully used a multi-element, heat transfer sensor to simultaneously detect laminar separation, transition, and turbulent reattachment regions of a laminar separation bubble. A new phenomenon involving a 180° phase-shift in dynamic shear stress across the separation and turbulent reattachment points was discovered during these tests. The location of separation point determined from this technique was in good agreement with results from pressure measurements and stethoscope readings.

Recently some researchers have used the laser Doppler velocimeter to measure separation bubble properties. Mangalam et al.[79] used an LDV system to study the nature of laminar separation bubbles in the concave region of an airfoil. Boundary-layer parameters determined from velocity profiles were used to compare the results with existing empirical relations for describing the laminar separation bubble. Their experimental results were in good agreement with empirical correlations. Bell and Cornelius[80] used a laser velocimeter system to make two-dimensional mean velocity and Reynolds stress measurements in the separation bubble region on a natural laminar-flow airfoil at Re = 2 million. An excellent review of early experimental and theoretical work on separation bubbles can be found in Tani[68]. Further review of pertinent literature may be found in Mueller[81,82].

Detailed analysis of two-dimensional data by Bragg et al.[9] has shown that, although much larger than typical laminar separation bubbles, the separation bubble aft of the ice horn on the airfoil had several features similar to those found in laminar separation bubbles. The sketch of the bubble flowfield aft of the upper surface ice horn, Fig. 5a, is representative of the bubble geometry on this iced model. Theoretical analysis of these bubbles predicted $R_\theta = 150$ in the upper surface laminar boundary layer just ahead of separation, well below that required for transition. Therefore the ice-induced separation bubbles on the airfoil were classified as laminar separation bubbles. Additionally, the point of pressure recovery aft of the ice-

induced pressure plateau was found to correlate well with transition location in the shear layer. Furthermore, determination of flow reattachment location for these bubbles was found to correlate very well to the prediction method for laminar separation bubbles of the short type. However, since these bubbles affected the global flowfield, they were classified as separation bubbles of the long type. The separation bubble found on the iced wing will therefore be examined and compared to laminar separation bubbles.

2.3.2. Rearward-Facing Steps

The geometry of the iced wing, particularly near the leading edge where the ice horns are located, bears a striking resemblance to a rearward-facing step. This geometric resemblance becomes more pronounced with increasing angle of attack. The measured flow features of this region of the wing will be compared with those found in flows over rearward-facing steps.

Figure 5b contains a sketch of flow over a rearward-facing step. The upstream boundary layer separates at the sharp corner S. If the boundary layer is laminar, transition will take place in the ensuing free shear layer. With the dividing streamline only slightly curved, the first half of the wall-bounded shear layer appears to be much like an ordinary plane-mixing layer. A major difference between the plane-mixing and wall-bounded shear layers is the turbulence intensity on the low-speed side of the shear layer. The flow on the low-speed side of the wall-bounded shear layer is highly turbulent as opposed to the low turbulence-level stream in a typical plane-mixing layer. The turbulence intensity level is 5-10% higher than for plane mixing layers, which is believed to be due to a flapping motion of the reattaching shear layer[83].

The separated shear layer curves sharply downwards in the reattachment zone and impinges on the wall. The mean reattachment location is marked with an "R" in Fig. 5b. Part of the shear-layer fluid is deflected upstream into the recirculating flow by a strong adverse pressure gradient. The flow in this zone is very unsteady since the adverse pressure gradient and the strong interaction with the wall in the

reattachment zone affect the shear layer. Downstream of the reattachment zone the growth of a new boundary layer is initiated. The properties of this new boundary layer formation downstream of reattachment have been shown to be quite different from the properties of an ordinary boundary layer[84].

Rearward-facing steps have been studied in a variety of flow regimes by many researchers. The articles by Simpson[83] and Eaton and Johnston[85] provide an excellent review of research involving flows with shear layer reattachment. Since 1981, several researchers have published more information on the structure of a reattaching shear layer; however, the list is too long to mention in detail. Both hot-wire anemometry and laser velocimetery have been utilized to obtain measurements in the separated-flow region. Shear layer turbulence level, intermittency factor as defined by Simpson[86], and Reynolds stress magnitudes in the region behind the upper surface ice horn will be compared to similar phenomena found by other researchers in reattaching shear layers.

2.4. Present Research

So far, the bulk of 3-D research carried out on the finite wing has provided aerodynamic coefficients for the iced wing as well as the baseline wing. The details of the iced-wing flow physics have not been the primary focus of the experimental research. Such an understanding may be realized through detailed measurements and subsequent thorough analysis of that data.

In three-dimensional flowfields, detailed flowfield measurements will be best obtained through the use of a laser Doppler velocimeter (LDV). The LDV's non-intrusive nature makes it an ideal instrument for flows where three-dimensional effects are be important. The large separation bubble aft of the ice horns, primarily responsible for the finite wing's performance degradation, will be studied in detail in the chordwise direction. Velocity surveys near the model root, centerline, and tip will provide clues to the spanwise behavior of the flow on the finite wing model. Mean velocity profile measurements in the immediate vicinity of the finite wing, in addition to unsteady data obtained by the LDV instrument will serve in improving

our understanding of the flowfield details. In addition, these data may be used to further calibrate the computational methods currently available for iced-wing performance prediction.

CHAPTER III

EXPERIMENTAL SETUP

The facilities used for this experimental investigation are located in the subsonic aerodynamics laboratory of the Department of Aeronautical and Astronautical Engineering at the University of Illinois at Urbana-Champaign. A detailed description of the experimental and support facilities, wind tunnel design, and types of measurement equipment and instrumentation is provided here in order to indicate the specific scale of the flowfield and the precision and accuracy of the measurements used to obtain the velocity results.

3.1. Experimental Facilities and Ancillary Equipment

3.1.1. Wind Tunnel

The wind tunnel employed for the current study is an indraft open-circuit type tunnel (Fig. 6) which exhausts into the test room. The rectangular test section has a cross section of 2.8'x4' (0.85x1.22 m), 8' (2.44 meters) in length. With a contraction ratio of 7.5:1, and honeycomb and four anti-turbulence screens at the inlet, turbulence levels less than 0.1% (Fig. 7) have been achieved in the airspeed regime of interest.

Reynolds number of 1.5 million per foot at 160 miles per hour (4.92 million per meter at 71.5 m/s) is obtained in the test section through a 125 horsepower alternating current electric motor connected to a five-blade propeller. Variation in the tunnel speed and Reynolds number is controlled by an operator selectable variable frequency motor controller. This capability allows the operator to keep the tunnel airspeed or Reynolds number at a constant value, particularly during long-duration tunnel runs when the room temperature can rise by as much as 10°F. This

change in temperature was compensated for during this test by adjustment of tunnel speed and in this manner, the Reynolds number was kept at a constant value.

The tunnel test section has been constructed with access doors on the sides and removable top and bottom. The plexiglass side and top walls allow for ideal optical access. For laser velocimeter measurements, the plexiglass sidewall was replaced by 0.375-inch (9.5 mm) thick glass.

3.1.2. Model

The 3-D model used for this test was a semispan wing with a chord of 15 inches (0.38 meter) and a span of 37.25 inches (0.95 meter), Fig. 8. A NACA 0012 airfoil section was used on this unswept wing. This airfoil section was chosen since it was the same one used in the earlier 2-D and zero-sweep 3-D tests[6-9,13-19]. The ice accretion used was a simulation of that measured on a NACA 0012 airfoil in the NASA Icing Research Tunnel, Fig 4. The icing conditions were a free-stream velocity of 130 mph, angle of attack of 4 degrees, icing time of 5 minutes, volume median droplet diameter of 20 microns, LWC=2.1 g/m^3 and a temperature of 18°F.

The model was constructed primarily of fiberglass laid in a mold and later filled with a foam core. Aluminum was used to reinforce the joints. The model consisted of several components to allow simulated ice to be tested through interchangeable leading edges. Two leading-edge pieces were constructed for the model ahead of the 15 percent station, a NACA 0012 leading edge and the simulated glaze ice accretion. Wing sweep can be achieved by changing the root and tip components on this unswept model. The root section was steel with a fiberglass skin. A steel spar of rectangular cross section was welded to this section and extended out of the tunnel to support the assembly.

The model was equipped with surface static pressure taps. The taps were located in 5 major rows plus a row on the tip section. The centerline row of taps had 80 taps in the no-ice configuration and 83 in the iced configuration. The other 4 rows on the main element had 40 and 41 taps in the no-ice and iced configurations, respectively. Including the 21 taps on the wing tip section, the model had a total of 261 taps in the

no-ice configuration and 268 taps in the iced configuration. Pressure measurements have been made in previous experiments[13,14].

3.2. Measurement Technique

The primary measurement technique used in this investigation was laser Doppler velocimetry (LDV). Results from the LDV data will be compared to results from other measurement techniques such as static pressure measurement, fluorescent surface flow visualization and split hot-film anemometry. Detailed discussions of the latter techniques are provided in References 6-9,13-18 and will not be repeated here. The following discussion is intended to give the reader an insight into the operating principles of the LDV instrumentation used for this study. The operating principles, optical configuration, as well as data acquisition hardware and software will be discussed here.

3.2.1. Laser Doppler Velocimetry: Operating Principles

Laser Doppler velocimetry is based on the ability to measure the Doppler shift in the frequency of scattered light emitted from macroscopic particles moving with the fluid flow. If these particles move with the same velocity as the fluid, then the flow velocity will have been determined. The proper choice of particles is a very important one and will be discussed in a forthcoming section. There are several different optical configurations that will allow measurement of the Doppler shift of scattered light. The two-beam fringe-type optical setup is by far the most commonly used[87]. In this setup, the velocity of the particle is calculated from the following straightforward relationship

$$U = \frac{f\lambda}{2\sin(\theta/2)} \tag{3.1}$$

where f is the Doppler frequency, U is the component of the particle velocity which is in the plane of the two crossing beams and perpendicular to their bisector, $\theta/2$. The LDV system thus produces a method of measuring fluid velocity by detecting the frequency shift of the particles moving along with the flow and requires no

calibration of the instrument to that particular flow.

3.2.2. Transmitting and Receiving Optics

A TSI Incorporated two-color, two-component fiberoptic LDV system with an Innova Model 70 4-Watt argon-ion laser was used for these experiments. A schematic diagram of the optical components of the system is shown in Fig. 9.

The coherent, TEM_{00}, Gaussian, multi-line light beam from the 4-Watt argon-ion laser was directed through the Model 9108 beam collimator to control the beam divergence in this optical system. This control was necessary in order to assure that the beam crossing point and the waist of the focused laser beams were at the same place. Proper focusing and crossing assured that the fringes were parallel.

A Colorburst Model 9201 multicolor beam separator provided all the beamsplitting, frequency shifting, and beam alignment capabilities for the two-component system in a single compact unit. The beams that exited the Colorburst, were directly coupled into optical fibers.

When the multi-color argon-ion laser beam was directed through the Colorburst, an acousto-optic cell generated two multi-color beams - one unshifted and one shifted by 40 megahertz. Dispersion prisms separated beam colors according to green (514.5 nm), blue (488.0 nm), and violet (476.5 nm) wavelengths. The result was three beam pairs which includes one shifted and one unshifted beam of each color. In the two-component system used during this study, the green and blue beams were used and the violet beams were blocked off.

Four Model 9271 fiber couplers were used, one for each beam, to launch the outgoing beams from the Colorburst into the transmitting optical fibers. The fiber coupler contained a glass block for translating the input beam and aligning it on the fiber's optical axis. A steering lens within the module was used to place the focused laser beam onto the center of the fiber's core.

Fiberoptics carry both the transmitted and scattered light to and from the transmitting and receiving lenses, respectively. The choice of this transmitting medium was based on the desire to keep as many of the optical components as

possible in a clean control room away from the tunnel and the test section. Through this arrangement, only the transmitting probe along with the beam expander module were positioned on the traversing assembly. The optical fibers therefore improved access to the flow, eliminated the need for the complete system to be near the measuring location and made the system less susceptible to electrical noise.

The optical fiber used for transmitting the scattered light was a multimode, step-index type fiber. The optical fiber used to transmit laser beams in probes and links was a single-mode, polarization preserving fiber. The transmitting fibers delivered the input laser beam to a Model 9832 probe equipped with a 350 mm lens. The transmitting green and blue laser beams, spaced 50 mm apart, were delivered into the beam expander.

A beam expander increases the beam diameter before it arrives at the final lens. This results in a reduction of measurement volume dimensions, and more power is concentrated in a small volume. As a result both spatial resolution and signal strength are enhanced.

The Model 9190 beam expansion unit used for this study used an expansion ratio of 2.6 in order to reduce the measuring volume length and diameter by a factor of 6.7 and 2.6 respectively, and also to increase the signal-to-noise ratio by a factor of 17.

A 1200 millimeter focal length lens was used for transmission and focusing of the laser beams into the test section. This long focal distance lens was chosen so that the flowfield near the back wall of the test section, four feet away from the probe's location, could be reached. In the semi-span configuration used for this study, this would correspond to the wing root region of the model.

The passage of the two parallel laser beams through the transmitting lens caused the beams to intersect in the focal plane of the lens. The illuminating beams were simultaneously focused to spots coincident with the intersection. In the region of the focal spots, the light beams are approximately cylinders with a planar wave front. The intersection of the two planar wave fronts created a measurement volume in the

shape of an ellipsoid (Fig. 10). This measurement volume was characterized by a pattern of light and dark fringes set at a spacing determined by the wavelength of the laser light and the crossing angle of the two beams. Figure 10 summarizes the equations that define the "e^{-2}" boundaries of the ellipsoidal shape. This was the boundary where the light intensity of the Gaussian laser beam has fallen to approximately 13 percent of its peak value. The measurement volume dimensions for this optical setup are listed in Table 2.

The scattered light was collected in a coaxial backscatter mode by the 350-mm lens in the Model 9832 fiber probe. This light was transmitted back to the color separator through a multimode fiber. A receiving fiber collimator was used to collimate the scattered light from the receiving fiber of the fiberoptic probe so that it passed through the color separator. An X-Y-Z adjustment was used to center the collimated light onto the dichroic mirror. The dichroic mirror within the color separator separated the blue 488-nanometer and green 514.5-nanometer wavelengths, which were then focused onto two photodetector apertures. To eliminate crosstalk, narrow bandpass color filters were mounted directly to the color separator.

Table 2. Measurement Volume Statistics

M.V. Stats	Green	Blue
Half-Angle(deg.)	3.1	3.1
Fringe Spacing (μm)	4.756	4.512
Diameter (μm)	126.16	119.66
Length (mm)	2.329	2.209
Volume (mm^3)	0.3407	0.2907
Num. of Fringes	26	26

Two Model 9160 photomultiplier systems, one for each channel, were used for light detection. The photomultiplier system had a built-in low-noise preamplifier (25X) at the phototube which improved signal quality. Preamplification and an adjustable gain ensured good signal amplitude even at very low light levels. Its 200-MHz bandwidth was more than adequate for flow frequencies in the present study. With the apertures removed, the photodetectors were mounted directly on the output ports of the color separator.

3.2.3. Data Acquisition Hardware and Software

3.2.3.1. Frequency Shifting and Downmixing

Frequency shifting was an integral part of the transmitting optics used for this study. Two Model 9186A-4 downmixers were used for the two channel LDV system. The 40-MHz acousto-optic modulator (AOM) from one of the downmixers was used to power the Bragg cell, located inside the Colorburst module, for both the green and blue laser beams. The resulting output frequency was equal to the shift frequency when the particles remained stationary in the measurement volume. The green beam pair was aligned so that frequency shift was opposite to the mean flow direction. This resulted in the alignment of the blue beam pair in the vertical direction such that the shift direction was the same as the positive vertical flow direction. The downmix frequency of each channel was independently controlled through each of the downmixer modules.

The downmixers manipulated the output signal from the photodetectors before passing the signal to the counter processors. A 25-MHz high-pass filter, built into the downmixer, effectively removed the signal pedestal. This also meant that Doppler signals below 25 MHz could not pass through. For a beam pair aligned such that the fringe motion is opposite the positive flow direction, the *apparent shift* was imposed on the signal using the following relation:

$$(40 + f_{d,f}) - (40 - f_M) = f_{d,f} + f_M \qquad (3.2)$$

where $f_{d,f}$ is the Doppler frequency of the particle moving in the positive flow direction, and the term in the first parentheses is the frequency detected by the photodetector. f_M is the apparent shifting frequency applied through the front panel of the downmixer. For the particle moving opposite to the flow direction, the Doppler frequency is denoted by $f_{d,r}$, and the *apparent shift* is given by

$$(40 - f_{d,r}) - (40 - f_M) = f_M - f_{d,r} \tag{3.3}$$

It is evident from (3.2) that the 25-MHz high-pass filter is not a restriction for particles moving in the positive-flow direction. The incoming Doppler frequency is $40+f_{d,f}$, which passes through the 25-MHz high-pass filter. For the particles moving in the negative-flow direction, however, (3.3) indicates that 15 MHz (40-25) is the maximum Doppler frequency the particle may possess before being clipped off by the high-pass filter. For the current optical setup, this translates to a reverse-flow magnitude of 71.34 m/s for the green beams, and positive-flow magnitude of 67.66 m/s for the blue beams.

The sign in front of the frequency mixing was determined from the front panel of the downmixer box. Since the green beams were aligned such that the fringes were moving opposite to the downstream flow, the *downshift* key was used, hence the minus sign in front of f_M in (3.2) and (3.3). The blue beams were aligned such that the fringes were moving in the direction of positive vertical flow. The *upshift* key was, therefore, used on the downmixer controlling the blue-beam signal. The frequency mixing, f_M, applicable to a maximum of 10 MHz, was ultimately subtracted from the signal during digital processing of the data.

After downmixing, prior to reaching the counters, the manipulated signal went through a 25-MHz low-pass filter. This meant that the total bandwidth of the signal for this LDV system was 25 MHz. If the maximum frequency mixing of 10 MHz is applied to resolve flow reversal, the maximum detectable frequency for positive-flow detection is only 15 MHz.

In the velocity profiles within the recirculation region aft of the ice horn, the frequency limitations of the signal processing were not a problem at the majority of the survey locations. In the middle of the shear layer, where large velocity gradients existed, some data points were discarded due to this limitation. This was noted primarily as a reduction in data rate in the middle of the shear layer. In most of the velocity profiles obtained during these measurements, a gap is observed approximately in the middle of the shear layer. Two measurement locations bound this gap. The lower velocity indicates the last location where frequency mixing was applied and the higher velocity indicates the first location where frequency mixing was not applied. Since the shear layer was found to be very thin, the effect of this limitation is not severe in terms of the shape of the velocity profile. If velocity spikes larger than 71.4 m/s exist when maximum frequency mixing is applied, they would be undetectable with the current system. The turbulence properties, therefore, will be affected by this filtering process.

3.2.3.2. Signal Conditioning

A general schematic of the data acquisition, reduction and storage systems for the information obtained from LDV measurements is presented in Fig. 11. The outputs from the two photodetectors were converted into an analog signal which was representative of the Doppler shift frequency for each color. This analog signal was transferred to a pair of Model 9186A-4 downmixers for electronic downmixing of the signals into the desired range. The outputs from the downmixers were then fed into two Thermal Systems Incorporated (TSI) Model 1980B Counter-type signal processors. The operation of the signal processor was divided into two main functions: the input conditioner and the timer module.

The Model 1984B input conditioner of each counter conditioned the input signal by providing proper filtering and gain of the incoming Doppler signal. It also allowed the selection of the mode of operation and number of cycles per measurement, in addition to determining the beginning and end of a valid burst, and generation of the signal to the timer module for measurement and comparison of the

Doppler burst.

The low-pass filter removed high-frequency noise from the laser velocimeter signal. The low-pass filter was set at its maximum setting of 30 MHz since little or no high-frequency noise was present in the frequency range of interest. The high-pass filter of the input conditioner was used to remove noise just below the Doppler frequency. The high-pass filter setting was varied depending on the location of the measurement volume in the flow. Near the model surface, in the shear layer and the outer edge of the boundary-layer, where frequency shifting was applied to resolve flow direction and high turbulence intensity, high-pass filter settings as low as 100 KHz were used. Further away from the model surface, and in the free stream, a high-pass frequency of either 3 or 10-MHz was used.

The gain switch on the front panel of the input conditioner, in conjunction with the internal 34 decibel input amplifier, varied the overall gain of the system from -31 to +34 dB's in order to amplify the incoming Doppler signal into the range of the burst detector. The gain on both channels of the counter was set and varied between 0.2 and 0.4. In the absence of a strong signal, higher gain settings (up to 1) were used in order to obtain a signal. Since this would introduce noise, sometimes not distinguishable from data, this practice was avoided as much as possible.

Both counters were operated in either the total-burst mode or single-measurement-per-burst mode. In the total-burst mode, the time for the total burst was measured and stored. In the single-measurement-per-burst mode of operation, the time it took for a particle to cross a preset number of fringes was measured and stored. In all experiments in this investigation, eight Doppler cycles were required to be generated by a particle for a valid measurement from that particle. This requirement was manually set on the front panel of the counter's input conditioner. In either mode of operation, each counter measured the required time for a particle by counting the number of cycles of a four-phase, 125 MHz clock and obtaining ± 2 nanosecond accuracy through phase information.

The high-pass filter is used to remove the low-frequency component of the burst

received by the processor so that the burst is symmetric about zero volts. A double threshold comparator is used to convert the burst into a digital pulse train. The burst-envelope detector determines the beginning and end of a Doppler burst with a series of thresholds that must be crossed in a specific order. In order for the detector to detect the beginning of a burst, the signal must exceed the -50mV and +50 mV thresholds, and then cross 0 volts. The end of the burst is determined when the signal fails to cross either the -50 or +50 mV threshold, but still crosses the +20 mV zero-crossing threshold[88]. At the end of the first valid cycle that meets the burst-detector criteria, a signal is generated that switches on the N-cycle gate and the comparison-cycle gate. The N-cycle gate and comparison cycle gate counters start counting the zero crossing digital signal, which is generated by the burst-envelope detector Schmitt trigger. When the number of Doppler-cycle crossings selected by the Cycles/Burst switch have been counted, the N-cycle gate and the comparison-cycle gate are switched off. At the end of the N-cycle gate, if the burst-envelope detector still indicates a valid burst, and both the saturation detector and the amplitude limit detector have not been set off, the amplitude validation logic will consider the measurement to be a valid burst. The saturation detector and amplitude limit detector are both manually set from the front panel of the input conditioner.

The amplitude limit detector eliminates data from larger particles that may lag the flow. This is done by limiting the amplitude of acceptable signals to some selectable level prior to high-pass filtering. The larger, flow lagging, particles in the flow have a larger amplitude signal than the smaller particles. The size of the amplitude is also dependent on the particle path through the measurement volume. The particles which pass through the center of the measurement volume give a signal with a larger amplitude compared to particles passing through other parts of the measurement volume. Therefore, there is potential for the amplitude limit detector to introduce complications to the directional sensitivity of the LDV[89]. In addition, for this experimental investigation, in order to affect the LDV results, the amplitude

limit detector had to be set such that the data rate decreased drastically. As a result, the amplitude limit detector was not used.

3.2.3.3. Computation of Particle Transit Time

The Model 1985B timer module began computation of the signal time duration after the amplitude validation logic decided that a valid measurement had been made on a Doppler cycle. The timer module accurately timed the N-cycle gate and the comparison-cycle gate signals generated by the 125-MHz, four-phase clock that yielded ±2 nanosecond resolution through phase information. The timer modules provided both manual or auto exponent selection for the 24-bit time measurement. Auto exponent mode and N=8 were used for the measurement of the N-cycle gate and the comparison-cycle gate on the timer module of both counters for this investigation.

The resolution of the measurement is affected by the ±2 nanosecond uncertainty in the clock resolution. The effect of the clock uncertainty can be minimized by increasing the measured time for the Doppler cycle. Lowering the Doppler frequency (by downmixing), and/or increasing the number of fringe crossings for a valid measurement, increases the time measured by the signal processor. Without downmixing, the minimum frequency which can be resolved in the current system, with 8 fringes selected (and assuming 38 MHz incoming frequency), is 357 kHz or 1.7 m/s. If downmixing is employed to lower the incoming frequency to say, 15 MHz, the minimum frequency which could be resolved is 56 kHz or 0.26 m/s.

Note that the resolution could also be increased by increasing the number of fringes from 8 to 16, or 32, for signal validation. This, however, limits the detection probability of the particles in the measurement volume by introducing a directional bias in the velocity measurements. The advantage of using the downmixer in the current LDV system, therefore, is an increase in the resolution of the particle velocity measurement by the counter processor without compromising the directional sensitivity of the instrument.

The comparison time, set to 1 percent on the front panel of the timer module for

this investigation, was used to eliminate or minimize random background noise or phase-noise contributions. The comparison was performed by adding the constant two(2) to the 8-cycle time, multiplying the sum by 5/8, and comparing that sum to the time for the comparison-cycle gate. Additionally, the constant two(2) was added to the comparison-cycle gate time and compared that sum to the N-cycle gate and multiplying it by 5/8. Therefore, the measurement passed comparison if

$$T_N * \frac{5}{8} - 2 \leq T_{N_c} \leq T_N * \frac{5}{8} + 2 \tag{3.4}$$

where T_N was the time for N-cycle measurement and T_{N_c} was the comparison-cycle time measurement, both in nanoseconds. If the measurement passed comparison, the time data from the N-cycle counter was latched into the output buffer registers. At this point a master reset signal was generated to clear both the timer module and the input conditioner for accepting new data points.

The signal from the photodetector collecting the scattered green light was input to the first counter signal processor while the similar signal from the photodetector collecting the scattered blue light was input to the second signal processor. The two signal processors were linked together through a Model 1988M master interface and a Model 1988S slave interface. The master and slave interfaces collected the incoming valid Doppler burst from the timer module and passed this information to the storage medium. At certain locations in the flow, especially near the model surface, where the signal-to-noise ratio for the blue beam fell beyond measurable levels, the counter signal processors were operated in random mode. In this mode of operation, the incoming data from either the green or the blue measurement volume counted as one valid measurement. At all other locations in the flow, the counters were operated in non-priority coincidence mode. In this mode, both counters had to receive a valid measurement from a Doppler burst within a preset time window. This coincidence window was set at 10 micro-seconds on the master interface during this investigation. This setting of the coincidence window time interval provided a high level of confidence that the green and blue measurements

were coming from the same particle.

3.2.3.4. Data Reduction, Analysis and Storage

Once the master interface collected the time measurements from the timer modules, along with the measurement of time between valid data, the information was sent to an AT&T WGS-386 micro computer via direct memory access (DMA). Using DMA transfer mode between the micro computer and the signal processors, high data rates were achieved. Depending on the measurement volume location and data rate, anywhere between 1024 and 4096 instantaneous velocity realizations were collected. All data acquisition and preliminary reduction were performed through TSI's Flow Information and Display (FIND) version 2.5 LDV data acquisition and analysis software package.

A schematic diagram of the FIND data acquisition and analysis software is shown in Fig. 12. The program contains several different features which give the user complete control over the data acquisition and reduction process. The data acquisition program collects data from the signal processors and controls movement of the traverse table. It can also be used to produce realtime histograms. The realtime histogram, in combination with an oscilloscope, was used at several locations in the flowfield prior to data collection in order to ensure that the hardware was operating properly. It also proved to be useful in establishing the Doppler frequency of the flow.

After the data points were acquired within a preset DMA timeout period, the information was stored on the micro computer hard disk. Each raw data file consisted of an ASCII header, which contained information about the optical setup of the laser velocimeter, various electronic settings on the signal processor, and information on the measurement location. The ASCII header of the raw data file was followed by the velocity information stored in binary format. Velocity information for each sample was stored in a three-word data format. The first 16-bit word, word A, contained the number of cycles from the signal processor, address of the processor, and processor mode: random or coincidence. The second 16-bit word,

word B, contains the time information for N cycles, passed on to the micro computer as a 12-bit mantissa plus a 4-bit exponent. The third 16-bit word, word C, contained the information on time between data (TBD) as a 12-bit mantissa and a 4-bit exponent. The velocity for each sample was calculated according to

$$V = d_f \times \left(\frac{N}{T_n} \times 1000 - f_s\right) \tag{3.5}$$

where d_f was the fringe spacing in microns, T_n was the time for N cycles in nanoseconds, and f_s was the frequency shift in MHz.

Once the raw data were stored on the micro computer hard disk, the FIND program could be used to reduce and analyze the data. Further reduction and analysis of data were carried out on an EXCEL 486-33 micro computer. Equipped with 8 MB of RAM, and 210 MB 16 millisecond access hard disk, the micro computer provided more than adequate computational power for off line data reduction and analysis. The velocities measured at each location in the flow were stored in a velocity data file. The velocity data were used to calculate various flow statistics such as the flow mean, standard deviation and turbulence intensity. If the measurements were taken in coincidence mode, then cross-flow information such as Reynolds stress, total velocity magnitude and direction were also provided.

The velocity data were also used to generate velocity histograms. These histograms provided the capability to edit the velocity distribution on screen and then to regenerate the refined statistical analysis. This capability was used at those measurement locations where several empty velocity bins existed between full velocity bins and the main histogram. Such a situation would arise from setting the signal processor gain at a more-than-adequate value, thereby introducing noise in the data[90].

The histogram editor also provided the option to discard the velocity data beyond a preset value of standard deviation. This option of the program was not exercised in the course of data reduction for two reasons. First, the majority of data acquired

above the model surface, outside of the boundary layer and the shear layer, showed clean velocity histograms. A small fraction of these measurement locations resulted in histograms with slight scatter of velocity points about the main histogram; these measurement locations were manually edited. Second, the data acquired in the boundary layer, recirculation zone, and shear layer above the model surface showed a large spread in the histogram data. Since the flow was expected to have very high turbulence intensities in those regions, a large spread in the histogram data was expected. Therefore, these histograms were treated without refinement. During the data acquisition process, the low-pass filter was set at 30-MHz and the high-pass filter was set at 100-KHz. As pointed out earlier, due to limitations imposed by the built-in filters in the downmixer, instantaneous velocities above 71.34 m/s in the shear layer, where 10-MHz frequency-shift was employed, were probably discarded.

In order to minimize contamination of data with noise, the gain setting on the signal processor was set just high enough so that a Doppler signal could be observed on the oscilloscope screen. While this gain would not be the optimum gain setting for maximum data rate, it would ensure that a minimum amount of noise was introduced into the system. This method of data acquisition was adopted since a priori knowledge of velocity fluctuations in the shear layer was not available.

The statistical data along with a file header similar to the one in the raw data file were stored as a direct access file. The equations used to calculate the various flow statistics are presented in Appendix 1. Further off-line reduction of the data was carried out using separate computer programs written in FORTRAN. During each run, the tunnel velocity measured from pre-calibrated facility transducers as well as temperature and ambient pressure were recorded. The offline reducer used the velocity information from the statistical files, along with ambient and tunnel conditions to produce non-dimensional velocity profiles.

3.3. Seeding

One of the key elements affecting the performance of an LDV system is the source of the Doppler signal: the particles in the flow. The seeding particles in LDV

must be small enough to move with the flow, yet large enough to scatter sufficient light for good signal quality from the photodetector.

Three factors were considered in choosing proper seed material: first, the unventilated operating environment of the UIUC tunnel excluded the use of chemicals not suitable for human intake; second, seed particles had to be large enough to provide adequate signal-to-noise (SNR) ratio; and third, the seed particles had to follow the flow fluctuations with high fidelity.

A set of experiments was conducted in order to assess the suitability of the different seeding materials available at the laboratory. These were sugar solution in water, polyethylene glycol (PEG 400), propylene glycol, and polystyrene latex spheres (PSL). Although PSL particles provided a high degree of monodispersion, using them as the seeding material was ruled out due to their infinite lifetime and the tunnel exhausting inside the test room. Polyethylene glycol also was cited as harmful[92]. Sugar in water caused frequent atomizer breakdown and clogging. Propylene glycol, primarily for its very low toxicity[92], was chosen as the seed material.

A TSI Model 9306 general-purpose atomizer was used to generate atomized particles of seed material. The atomizer was operated with all six jets in the open position and the input pressure, supplied by the laboratory compressor, set at 30 psig. Experimentation with the location of atomizer showed that the best position for the seeder was just upstream of the honeycomb at the wind tunnel inlet. The honeycomb and settling screens produced a smooth stream tube of seeds entering the tunnel, while eliminating most flow fluctuations due to the presence of the seeder and support equipment.

Propylene glycol produces harmless polydisperse particles with a median diameter of approximately 0.9 μm[93]. This size particle produces adequate SNR and will follow the flow fluctuations up to 7.0 kHz with better than 99% fidelity[94].

3.4. Alignment and Traverse Equipment

Accurate velocity measurements strongly depend on the accuracy and alignment of the LDV fiber probe with the model in the wind tunnel test section. This warrants

some discussion of the LDV setup procedures. The primary items of concern are alignment of the LDV traverse gear to the wind tunnel test section, and the accurate placement of the measurement volume at the flowfield "origin" in the wind tunnel test section.

In the following sections, the model location and it's orientation in the tunnel test section will be described. The reference coordinate system that was used for the LDV measurements will be presented. The traverse mechanism along with the supporting equipment will be described in detail. The alignment of the LDV measurement volume with respect to the model and the wind tunnel test section will also be discussed.

3.4.1. Model and Tunnel Coordinate System

The position of the wind tunnel in the laboratory allowed significant optical access only from one direction. In order to obtain this optical access, the finite wing model had to be mounted upside down in the tunnel test section, Fig. 13. This placed the model in a right-handed coordinate system, where coordinates have been rotated 180° about the x-axis. As shown in Fig. 13, the positive x-direction was in the streamwise flow direction, positive y-direction was into the tunnel wall where the model root was supported, and positive z-direction was into the tunnel floor. Therefore, the positive u-velocity is in the streamwise direction, while the the positive w-velocity is perpendicular to the streamwise direction, into the tunnel floor.

3.4.2. Traverse Mechanism

The two-component laser Doppler velocimeter used for this investigation used fiberoptic cables for transmitting the illuminating and scattered light to and from the fiber probe. Using the fiber probe meant that a bulky traverse table, capable of moving the laser head and the entire receiving and transmitting optics, could be avoided.

The laser head and power generator, as well as the majority of the transmitting and receiving optics, were mounted on a Newport Research Corporation (NRC) optical bread board having threaded holes in 25.4 mm square grids. The optical

bread board itself was mounted on a rigid counter top in the data acquisition room. The fiber probe, the beam expansion unit, and the transmitting and collecting lens were the only optical components mounted on the traverse system. Figure 14 shows a photograph of the LDV electronics and optics in the data acquisition room. Figure 15 shows a photograph of the LDV transmitting probe mounted on the traverse gear, and aligned next to the test section.

A VELMEX traverse system provided the movement of the measurement volume within a 60 cm cube. The VELMEX traverse system combined a DC stepper motor with a high-precision threaded rod assembly to provide accurate placement of the measurement volume to within 0.001 inch (0.025 mm) of the desired location. Three sets of traverse assemblies provided movement in three orthogonal axes. This package was controlled by a Model 8300 controller box. The controller box could be used to either manually position the measurement volume or to communicate with the micro computer, through a serial communication link, in order to automatically scan up to 99 different locations in the flowfield. The FIND data acquisition software was used to command the traverse gear through a predetermined path of measurement locations.

In keeping with convention, the measured velocity profiles were developed by traversing the LDV measurement volume in a direction normal to the wing contour. For this purpose, a mapping routine was written in FORTRAN to transfer the LDV measurement locations from the model coordinate system to the wind tunnel orthogonal coordinate system. The routine allowed the operator to choose any scan length and increment combination normal to the airfoil surface, normal to the chord, or normal to the free stream. It used this information to generate (x,z) pairs of coordinates in the measurement plane on the model surface. The generated coordinates were placed in a direct-access file and linked to the LDV three-axis traverse driver program. All boundary-layer sweeps, unless otherwise noted, were made normal to the airfoil upper surface. Figure 13 shows the model coordinate system in relation to the test section coordinate system.

3.4.3. Alignment Procedure

For all the velocity scans during this study, the green beams were aligned to measure the x-component of the velocity. In order to make velocity measurements near the model surface, the measurement volume had to be placed adjacent to the model surface. The geometry of the illuminating beams and the model contour would force the illuminating beams to be clipped by the model contour (see Fig. 16a) before the measurement volume could be positioned very close to the surface. In order to achieve close distances to the model surface, the transmitting probe was tilted so that the shifted illuminating blue beam was parallel with the model surface (see Fig. 16b).

Tilting the probe did not affect the measurements in the streamwise direction (green beams). It did, however, contaminate the measurements from the vertical component (blue beam) with a contribution from the spanwise flow. Analysis of the optical setup used in these measurements indicated that, this contamination was very small for tilt angles below 5°. This was found to be true even when a spanwise-flow magnitude up to 30 percent of the vertical-flow magnitude was considered.

A method was developed that allowed for accurate placement of the measuring volume at the desired location. In order to achieve this alignment, two precision-crafted alignment blocks were used. The blocks, supplied with the LDV optical package were each drilled with five alignment holes, one at 4.25 inches (10.8 cm) above the base, and four on a circle of radius 50 mm.

Alignment of the model with the laser velocimeter involved two steps. In the first step, the illuminating laser beams were aligned with the model so as to ensure that the traverse path of the measurement volume always remained in the measurement plane perpendicular to the leading edge of the model, at the desired y/b location. In the second step, the traverse gear coordinate system was matched to the coordinate system of the semispan wing in the wind tunnel test section.

The semispan wing was set to zero degrees angle of attack. The alignment blocks were placed on the model surface: one block aligned with tap row 1 at y/b=0.168

and the other block aligned with tap row 5 at y/b=0.852. The first and the fifth tap rows were used as spanwise reference (see Fig. 17a) and the 15 percent chord location was use as the chordwise reference (see Fig. 17b). With the traverse table roughly aligned with the semispan wing, the fiber probe was rotated about the x-axis until the frequency shifted blue beam passed through the center hole of the alignment blocks. Fine adjustments were made by traversing the probe in the x-, y-, and z-directions, rotating the traverse table or the fiber probe as necessary. In this manner, the measurement volume was aligned with the model.

For the second step of alignment, an alignment tool was designed and built. This tool was used to place the measurement volume in the measurement plane at the origin of the wing coordinate system. With the model oriented at zero degrees angle of attack, the alignment tool was placed on the model surface near the leading edge at the desired y/b location, Fig. 18. The lengths "b" and "c" were known quantities. Once the alignment block was properly positioned on top of the alignment tool, the length "a" was measured with a digital readout vernier. Adding the lengths "a" and "b" to 4.25 inches, and the length "c" gave the z- and the x-locations of the measurement volume. Once the (x,z) location of the measurement volume was determined, the traverse table controller was used to manually move the measurement volume to (0,0) in order to place the measurement volume at the origin in the model frame of reference at that y/b station.

3.4.4. Measurement Locations

In order to eliminate flow-induced vibration at high angles of attack, the model was held rigid by two tension wires extending from the wing tip to the test section ceiling. The model used for this investigation was tested in two different configurations - iced and uniced. The clean, or uniced, model was used to establish baseline data which were used to compare with computational as well as other experimental results. For this case, measurements were made in the xz-plane at y/b=0.470 on the model upper surface at α =0, 4, and 8 degrees. In order to fix transition, a trip strip was installed at x/c = 0.05 on the upper and lower surfaces of

the model.

In the iced configuration, the model was tested at $\alpha = 0$, 4, and 8 degrees. Velocity measurements were made in the xz-plane at y/b = 0.175, 0.470, and 0.819 on the model upper surface. Results from previous split hot-film measurements on a similar model[6-9,37] were used to determine the measurement locations. In order to capture the recirculation zone due to the separation bubble, velocity profiles were measured in x/c=0.02 increments from the wing leading edge. Once the recirculation zone was captured, velocity profiles were measured in larger x/c increments until just before the trailing edge, x/c=0.99, was reached.

A typical scan of the velocity profiles consisted of measurements at 20 to 30 locations along a path normal to the airfoil contour. The measurement volume would be positioned 0.050 inches (1.27 mm) above the model surface and then traversed a predetermined distance in predetermined increments. With the present optical arrangement, it was not possible to place the measurement volume closer than 0.050 inch (1.27 mm) to the model surface. Distances smaller than this amount would result in rapid decrease of signal visibility. This was readily observed by monitoring the rise of the signal pedestal on the oscilloscope screen. Another source of background noise was the reflection of the illuminating beams from the back sidewall of the wind tunnel. Although that sidewall, where the model strut exited the test section into the support structure outside of the wind tunnel, was painted flat black in order to minimize reflections and flare, a significant amount of background noise was observed in the photodetector signal when measurements where made near the root section of the model. This problem was significant enough to cause very low data rates for the measurements near the root of the model. Here, the outgoing beams had not diverged significantly. Therefore each beam hit the back wall, having diffused only a small portion of their energy in the radial direction. One additional source of noise was the reflection of the illuminating beams from the glass side wall of the wind tunnel. These reflections impacted the fiber probe directly and as a result, their paths into the fiber probe were blocked off with small patches of

electrical tape.

Of the several methods that were tried to reduce the background noise, fluorescent paint provided the best solution on the back wall. It causes the outgoing beams to reflect at a frequency other than the original laser beam frequency and therefore made the measurements near the back wall feasible. On the model surface, fluorescent masking tape was applied. The addition of the tape strip to the model surface, however, was deemed to affect the flowfield under study. Therefore it was decided to settle for the 0.050 inch (1.27 mm) minimum approach distance and leave the model surface uncontaminated with layers of paint or tape.

Figure 19 shows typical measurement locations on the model upper surface at $\alpha = 4^\circ$ and $y/b = 0.470$. Note that near the leading edge of the iced model, due to extreme curvature of the contour, it was decided to conduct velocity profile measurements normal to the chord instead of normal to the model surface. This procedure was adopted up to $x/c = 0.10$ in the chordwise direction. From $x/c = 0.10$ and beyond, the velocity scans were conducted normal to the contour.

3.5. Error Analysis

In this section, sources of error associated with the use of laser Doppler velocimetry are addressed. These include errors due to the instrumentation and optical configuration limitations, fringe and velocity bias, gradient bias, as well as statistical bias.

3.5.1. Systematic Uncertainty

The relation $f = U/d_f$ is used to obtain velocity measurements in the LDV instrument. Put in another form, this relation can be expressed as

$$U = \frac{\lambda f}{2 \sin\frac{\theta}{2}} \tag{3.6}$$

where λ is the laser wavelength, f is the Doppler frequency, and $\theta/2$ is the bisector angle between the illuminating beams at the cross-over location. Young et al.[95] used the above relation to investigate the sources of error in their LDV optical setup and

instrumentation. This type of uncertainty analysis is covered in general detail in Ref. 96. Differentiation of the above relation sheds light on the variables that cause an error in the velocity measurements:

$$dU = \frac{\lambda}{2}\left(\frac{df}{\sin\frac{\theta}{2}} - \frac{f d\theta}{2\sin\frac{\theta}{2}\tan\frac{\theta}{2}}\right) \tag{3.7}$$

Since the laser wavelength is considered to be stable, it is not considered a source of error[95]. Therefore,

$$\frac{dU}{U} = \frac{df}{f} - \frac{d\theta}{2\tan\frac{\theta}{2}} \tag{3.8}$$

The optical arrangement used for the current study gave $\theta \sim 3°$, therefore $\tan(\theta) \sim \theta$ which, upon substitution into above equation, gives

$$\frac{dU}{U} = \frac{df}{f} - \frac{d\theta}{\theta} \tag{3.9}$$

As Young et al. state, the error in frequency df/f is affected by the bisector angle θ, the parallelism of the fringes, and the position of the measurement volume. The electronic system in the signal conditioner also contributes to the frequency error. Young et al. have categorized these errors as the limiter threshold error, reference clock synchronization error, and quantizing error.

The bisector angle error $d\theta/\theta$ is affected by the accuracy of the transmitting optics. These include the focal distance of the transmitting lens and the spacing between the illuminating beams prior to entry into the beam expansion module. The uncertainty in the measurement of the bisector angle yields a fixed bias error in the velocity measurement. Based on the accuracy in beam spacing of the optical fibers prior to entry into the beam expansion module, in addition to accuracy of the transmitting lens focal length, both supplied by the probe manufacturer, the uncertainty in the bisector angle is estimated to be $\pm 0.65\%$.

Non-parallelism in the fringe spacing occurs when the two illuminating beams do not cross to form a measurement volume at their focal points and, as a result, a measurement inaccuracy occurs[97]. This lack of coincidence is caused by the small divergence in the laser beam due to the concave reflectors inside the laser and divergence from thermal blooming in the optics. This problem can be circumvented by passing the laser beam through a beam collimator on the transmitting optics train. The beam collimator in the optical setup used for the current study, consisting of a positive and negative lens, placed the beam crossing point and the focused-beam waist in the same location, thus assuring that the fringes were parallel. Due to the optical configuration of the LDV instrument, it was impossible to observe the fringe pattern and therefore the usual method of visual verification of this fact was not possible. If total compensation is not made, a random error and a bias error will occur. The random error is given by Young et al.[95] as

$$\frac{df}{f} = \frac{l_{mv}}{\Delta y \left[1 + \left(\frac{\pi d_{mv}^{\,2}}{\lambda \Delta y} \right)^2 \right]} \tag{3.10}$$

where l_{mv} is the measurement volume length, Δy is the distance between the beam focus and the measurement volume and d_{mv} is the measurement volume diameter.

The bias error caused by the change in fringe spacing is also given by Young et al.[95] as

$$e_{bias} = \frac{d_{mv} - d_{bw}}{d_{mv}} \tag{3.11}$$

where the beam waist diameter, d_{bw} is given by

$$d_{bw} = d_{mv} \left[1 + \left(\frac{\lambda \Delta y}{\pi d_{mv}} \right)^2 \right]^{\frac{1}{2}} \tag{3.12}$$

Since the measurement volume diameter is always larger than the beam waist diameter, the relation given in equation 3.11 is biased towards lower velocities.

Despite the presence of the collimator, there is a chance that the collimator did not collimate the laser beam perfectly so as to assure beam crossing at the focal point. Since the proper magnifying instrumentation was not available to visually measure the discrepancy between the location of the measurement volume and the beams' focus, an exaggerated value of 5 mm is used to calculate the "worst case" scenario. The value of $\Delta y = 5$ mm is chosen since it can be visually detected without the need for magnifying instrumentation. This yields $df/f = \pm 0.12\%$, and $e_{bias} = -0.13\%$ for the green beam.

The electronic limitations inherent to the signal processing system also provide a source of uncertainty in the measurements. Time jitter, described above, is due to threshold crossings occurring at a different part of the signal cycle in the beginning of the signal burst than at the end. This error is eliminated if the counter incorporates a true zero-crossing detector and the signal pedestal frequency has been completely removed[98]. Clock synchronization error is discussed in the next section.

3.5.2. Clock Resolution

The TSI 1980B counter has a 125-MHz, four phase clock which yields a ± 2 nanosecond accuracy through phase information. When eight Doppler cycles are selected for burst validation, the time measured by the clock is

$$\tau_n = \frac{8\ cycles}{20\ MHz} \tag{3.13}$$

which is equal to 0.4 microseconds or 200 clock counts on a 2-nanosecond clock. The value of 20 MHz in the denominator is the highest expected Doppler frequency in the flowfield under investigation (u_x = 100 m/s).

When the number of Doppler cycles in a valid burst is counted, the generated digital pulse train is always off by at most ± 1 clock counts[99]. The clock count ambiguity translates to ± 0.5 percent for the counter system used in this study. Put another way, the clock uncertainty can be expressed as

$$clock\ uncertainty = \frac{f_D \times 2 \times 10^{-9}}{N_f} \tag{3.14}$$

where f_D is the Doppler frequency, and N_f is the number of required cycles for a valid measurement. The factor $2x10^{-9}$ accounts for the 2 nanosecond limit imposed by the speed of the clock.

As a part of signal validation, the timer module of the signal processor performed a comparison between 5/8 multiplied by the time it took for eight Doppler cycles, and five Doppler cycles within the same burst. The maximum clock uncertainty in measuring the time based on eight Doppler cycles was 0.5%. The maximum uncertainty in time measurements based on five Doppler cycles was 0.8%. Since these two time measurements were compared, the overall uncertainty could reach as high as 0.5 + 0.8 = 1.3 percent. This 1.3% uncertainty in counter clock resolution was more than the 1% comparison level set on the front of the counters. It should be noted that the maximum expected Doppler frequency of 20 MHz was reached at only a small fraction of measurement locations. As a result, at those locations, some good data points may have been discarded due to this stringent comparison setting. At the majority of measurement locations, the signal frequency was considerably less than 20 MHz.

The clock resolution also limits the minimum level of turbulence that can be resolved by the LDV instrumentation. In order to produce a valid measurement, a particle must produce N preselected number of Doppler cycles. The signal processor measures an average of n clock counts (equation 3.14) for the N Doppler cycles. Due to the ± 1 clock count ambiguity, it is equally probable that the number of clock counts is either n-1, or n, or n+1. The standard deviation of the number of clock counts then is:

$$\sigma_n = \left\{\frac{[(n-1)-n]^2 + (n-n)^2 + [(n+1)-n]^2}{3-1}\right\}^{\frac{1}{2}} = 1 \tag{3.15}$$

As a result, 0.5% turbulence intensity is the minimum value that the counter can

resolve due to the clock resolution alone. Again, it should be noted that this presents the "worst case" turbulence intensity resolution. At the majority of the flow locations, where the Doppler frequency is lower than 20 MHz, the clock resolution, and therefore the turbulence intensity resolution due to the clock alone, is higher. Also note that, as discussed earlier, the minimum resolution can be improved by increasing the number of required Doppler cycles.

The individual systematic errors, in addition to the total error due to the optics and electronics, are tabulated in Table 3.

Table 3. Systematic Errors

Item	Bias(%)	Random(%)
Cross-Beam Angle	±0.65	–
Clock Synchronization	+0.25	±0.25
Diverging Fringes	-0.13	±0.12
Total System Error	+0.77, -0.53	±0.37
Total Effective Error	0.65% to 0.85%	

3.5.3. Fringe Bias

In order to produce a valid burst, a particle must cross a predetermined number of fringes in the measurement volume. If the particle is moving in a direction parallel to the fringes in the measurement volume, then no measurements can be made on that particle. Highest preference is given to particles that travel through the measurement volume normal to the plane of the fringes and at the center of the measurement volume, and the least preference is given to particles that travel parallel to the fringes. Therefore, the probability of making a measurement on a particle becomes correlated with the vector direction of that particle. This problem is known as fringe or directional bias.

In a highly turbulent flowfield, a particle's direction can be oriented from 0 to 360 degrees in relation to the fringes. In addition to the direction of the velocity vector, the probability of a particle crossing N_F fringes, depends on the total number of fringes, N_T. Buchhave[100] considered particles passing through an ellipsoidal measurement volume and estimated the probability of the particle detection for an LDV system. He equated this probability to the ratio of the effective measurement volume area to the total measurement volume area:

$$P = \frac{A_E}{A_M} = 1 - Q^2(1 + \tan^2\phi) \tag{3.16}$$

where ϕ is the angle between the velocity vector and the normal to the fringes, also known as the acceptance angle, and $Q = N_F/N_T$. In order to maximize the detection probability, the second term on the right hand side must be minimized, either by increasing N_T or by decreasing N_F or both. If $Q > 1$, no data would be sampled because there wouldn't be enough fringes in the measurement volume. Similarly, if $Q = 1$, then data would be taken only from particles passing through the center of the measurement volume with a velocity vector normal to the plane of the fringes. $Q < 1$ allows velocity vectors to penetrate the measurement volume away from the center and at shallow angles to the fringes.

In order to reduce Q, N_T is maximized by imposing a frequency shift on one of the illuminating beams. The result is an effective movement of the fringes, in the direction of the higher-to-lower frequency beam. This fringe velocity can be calculated by multiplying the fringe spacing by the shift frequency. In the present optical configuration, the beams were frequency-shifted by 40 MHz, which translated to a fringe velocity, V_F, of 190 meters per second.

In the case of frequency shifting, the modified form of the above equation is given as[89]

$$P = \left(\frac{A_E}{A_M}\right)_{shifted} = 1 - \frac{Q^2(1 + \tan^2\phi)}{\left(1 - \frac{V_F}{|U|\cos\phi}\right)^2} \tag{3.17}$$

where V_F is the fringe velocity, and $|U|$ is the magnitude of the velocity vector.

Whiffen[101] and Whiffen et al.[102] examined the fringe bias problem by assuming a cylindrical measurement volume. Whiffen's result for the probability is

$$P = [1 - \frac{Q}{\cos\alpha + \frac{V_F}{U_P}}]^{\frac{1}{2}} \tag{3.18}$$

where α is 180° minus the angle of the particle's velocity vector to the fringe plane normal to the direction of the fringes. For Q=0.5, Whiffen shows that if $|V_F/U_P| \geq 2$ then the probability of particle detection is at least 90 percent and valid for nearly the entire 360 degree range of possible incident angles. In the present investigation, N_F=8 and N_T=26 which yielded Q=0.31 for all of the flowfield data.

For a two-component simultaneous measurement, the overall probability is given by

$$P_{01} = P_0 \times P_1 \tag{3.19}$$

where P_0 and P_1 are the probabilities of particle detection in channels 0 and 1 respectively. If P_{01} is zero for any range of velocity direction, then the LDV will not "see" the particles coming from that direction[103].

Petrie[89] used equation 3.17 to examine fringe bias effects in excellent detail. Here ϕ_1 was the angle between the instantaneous velocity vector magnitude $|U|$ and the positive channel 1 flow direction. Results from a similar analysis, based on $Q_0=Q_1=8/26$ and $|V_{F0}| = |V_{F1}|$, shown in Fig. 20, indicated that for $|V_F/U_P| \geq 2$, a nearly uniform effective measurement volume area is obtained. The result for $|V_F/U_P| = 1.5$ is highly non-uniform however. Figure 21 shows similar results for Q=4/26. Here, since only four Doppler cycles were required for measurement validation, higher peak probability values were observed for all frequency shift values. The opposite was seen to be true when 16 Doppler cycles were required for measurement validation. The case for Q=16/26 is shown in Fig. 22. Here, even at $|V_F/U| = 2.0$, the probability of detection is highly asymmetric.

From these results, it was evident that maximum detection probability, when both channels were used in coincident mode, occurred when the fringes were at $\pm 45^{\circ}$ to the mean velocity direction. While this may pose little problem in investigating free shear layers, it imposed a limitation on the minimum approach distance when investigating wall-bounded shear flows such as the flowfield under study. Near the model surface, where data was acquired in random mode and mainly from the green beam (parallel to the free stream) the detection probability was a function of fringe velocity in one channel only. Figure 23 shows these probability values for a single channel. Once again, with the application of frequency shift equal in magnitude to at least twice the maximum flow frequency, the directional ambiguity was essentially removed. In the optical configuration used for the current study, the green beams were frequency shifted by 40 MHz at separation in the Colorburst. The resulting 190 m/s fringe velocity was more than twice the maximum velocities encountered in any of the measurement locations.

Petrie[89] extended his analysis further by assuming an isotropic turbulence field and using a directional sensitivity analysis similar to above. Samimy[103] carried out a similar analysis for an elliptic turbulence field. Their results indicated that for specified values of V_F/U_{mean}, σ_U/U_{mean} and the mean velocity angle α, values of $V_F/|U|$ and P_{01} can be determined versus ϕ_1 so that the LDV is not blind to the maximum anticipated velocities in the flowfield. While this type of study was not carried out for the flowfield under investigation here, in hindsight, it would have provided a better scientific estimate of measurement volume orientation with respect to the flowfield.

3.5.4. Velocity Bias

The LDV instrument makes measurements on the particles that produce a valid Doppler burst as they pass through the measurement volume. If the flow entering the measurement volume is uniformly seeded in a spatial sense, more particles will produce valid Doppler bursts at higher velocities than at lower velocities. As a result, the arithmetic averaging of the velocity samples will be biased towards the

higher velocities[99]. This problem, known as velocity bias, has been addressed by many investigators. If certain criteria and conditions are met, then the measured velocities can be corrected for this bias.

Unlike frequency trackers and hot wire anemometers, which sample the flow at equal-time intervals, the frequency counters, such as the ones employed in this investigation, sample the flow every time a valid Doppler burst is detected in the measurement volume. In other words, the sampling process is *flow-controlled*. If the data density of the flowfield, defined as the rate that the burst processor measures particles times the Taylor time microscale of the flow[104], is high enough so that a particle passes through the measurement volume at all times, then the factor governing the data acquisition rate is the speed at which the processor can collect, transfer and store data and prepare for the next valid signal. In these conditions, the LDV data is acquired by a *controlled processor*[105,106]. In this situation, as Dimotakis suggested[107], the data are weighted by the particle interarrival time, which is constant at high data rates. As Amatucci reports[108], the experimental investigations of Stevenson et al.[109,110] and Johnson et al.[111] indicate that this condition exists when the sampling rate of the processor is about 50 times less than the validated particle data rate.

On the other hand, if the data rate is low enough so that the processor can measure, process , store and prepare for the next sample without missing any possible particles in the measurement volume, then the processor is called *free running*[112]. There is no way to correct for data acquired in conditions between free-running processors and processor-controlled flows and must therefore be avoided[103].

The processor sampling rate for the TSI counter processor used for this investigation was 250,000 words per second. Each velocity sample required three words for complete information on that velocity sample. Therefore, the maximum sample rate of the processor under the conditions used in this study was approximately 83,000 samples per second. This was, at worst, a factor of 50 times, and more often a factor of 150 times, faster than the data rate encountered with the

data density of the flowfield under study. Therefore, the signal processor and the data rate conditions in the flowfield of current investigation represent the free running processor case.

In 1987, the results of a panel discussion[104] on particle bias in laser velocimetry were published. The panel chaired by Edwards, hereafter referred to as the panel, reviewed the various methods of bias correction and gave its recommendation on the suitability of each method. The first correction scheme, proposed by McLaughlin and Tiederman[113], who also were the first to note the velocity bias effect, uses the one-dimensional velocity data to statistically weight the samples. The basic assumptions for this method are spatially uniform seeding, spherical measurement volume, and 4π stradians acceptance angle. This method, correct only for unidirectional flows, has been extended to use the full velocity vector for statistical weighting of 2- and 3-dimensional LDV measurements. This method was not recommended by the panel, since at times, it would increase the error over that obtained in applying no correction.

The second method reviewed by the panel, uses the burst time as the weighting factor. First proposed by George[114], and later by Hosel and Rodi[115]. This method was given a qualified recommendation by the panel. The idea here is that the burst time is inversely proportional to the magnitude of the three-dimensional velocity vector. The experimenter would have to ensure that particle seeding density was spatially uniform, that filter bias effects were not present, and that the processor could give an accurate estimate of the residence time. Briefly stated, filter bias may exist due to the frequency response of the photodetection system and the filter settings on the burst processor. The panel had no specific recommendations for dealing with filter bias. The photodetectors used in this study, which have a 200 MHz frequency response range, were assumed to have a flat response in the low frequency range of this study.

The measurement on the burst time can be provided by the counter, if it is operated in the Total-Burst mode. In this mode, the total number of Doppler cycles,

plus the time of the entire burst that a particle produces is measured and used to calculate the velocity. There are three reasons why this mode may not be the ideal mode to operate the counter.

First, the signal processor does not offer cycle comparison in this mode. The 5/8 cycle comparison used in Single Measurement per Burst mode rejects spurious signals and much of the background noise as described in section 3.2.3.2. The lack of such a comparison, particularly in regions of flow with high fluctuations, would contribute to the mean velocity gradient inside of the measurement volume. This in turn, would drive up the false turbulence. Petrie[89] and Stevenson et al.[109,110] used a counter similar in features to the counter used in the current investigation. They reported poor performance of the signal processor when operating in the total burst mode.

Second, the flow signal could reach such high frequencies that the counter resolution would become an important concern. While this may have been the cause of poor performance in Petrie's supersonic flow, Stevenson's 26 m/s flow was not susceptible to high velocity resolution problems. This effect becomes more pronounced, particularly if frequency shifting is used, such that the shift direction is opposite of the mean flow direction. Gould et al.[116] reported the difficulty of the counter processor in residence time measurement when frequency shifting was used.

Third, in addition to being inversely proportional to the velocity, the particle transit time is also dependent on the particle size and the location at which the particle passes through the measurement volume[111] and these dependencies add an uncertainty interval to the correction[89]. Petrie has argued that for two-component LDV systems which make measurements in a plane, the third component of the velocity will dominate the transit time in flows where the velocity vector is predominantly in the third, unmeasured, component. The situation becomes more pronounced when the measurement volume has a large length to diameter ratio, whereby the particle spends a significant amount of time traversing in that direction. Therefore the transit time method will overweight these data. Previous measurements on the semi-span wing model[13] have shown that the wing centerline

behaves in a predominantly two-dimensional fashion. Near the wing tip and the wing-wind tunnel wall regions, however, strong local three-dimensional effects may exist, in addition to the spanwise flow induced by the wing downwash.

Edwards and Jensen[117] noted the effect of frequency shifting on the particle statistics. They state that, when frequency shifting is used, the processor output occurs in clusters with a well defined spacing between events in the cluster, determined by the counter reset time and the particle velocity. In other words, the slower particles have a longer burst time. If the counter reset time is fast enough, the burst may still be present by the time it has been processed as a valid measurement. As a result, chances of making more than one measurement on a single particle are increased. The effect of frequency shifting is, therefore, to bias the mean velocity toward the lower velocity samples since slower particles will produce more Doppler bursts than faster moving particles. Meyers and Clemmons[118] incorporated the effect of frequency shifting in their weighting function and arrived at

$$V_{\text{corrected}} = \frac{\Sigma A_i V_i}{\Sigma A_i} \tag{3.20}$$

where

$$A_i = \frac{10 L_{fr} + T_r (V_f + V_i)}{D_{mv} (V_f + V_i)} \tag{3.21}$$

Here L_{fr} is the fringe spacing, D_{mv} is the measurement volume diameter, T_r is the counter reset time, V_f is the fringe velocity, and V_i is the individual velocity measurement made by the counter.

Hoad et al.[119] conducted an LDV survey in the Langley V/STOL tunnel, and used the velocity correction scheme described above. They used an aspect ratio eight wing, similar in planform and cross section to the model under study in this investigation, under free-stream conditions similar to those in this study. They noted that the arithmetic mean and the corrected mean for velocity and frequency shift bias

yielded similar results. They concluded that when frequency shifting is used, if the shift frequency is large compared to the signal frequency, then bias errors were negligible.

The third method reviewed by the panel uses the measurement rate corresponding to each velocity vector, either computed or measured, as the weighting function. This method was also given a qualified recommendation by the panel. Along this idea, Meyers et al.[120] suggested that a correlation parameter be used to correct for velocity bias. This correlation parameter, they contended, relates the data rate to velocity and when zero, it implies no bias corrections are necessary. This method assumes moderate to high data density, so that particle interarrival times are on the order of the integral time scale of the flow. They used two flowfields: a jet from a turbulent pipe flow, and the flow about a backward facing step. The data were analyzed using classical statistical methods with and without velocity bias corrections. Their results indicated that the general assumption of uniform spatial seeding is not generally valid and even when it is, the sampling may still not require correction. This method, although promising, is still in the development stages[121]. Conditional bias correction of data is used by other researchers as well. Dutton[90], for example, uses the turbulence intensity as a measure of when bias correction may be needed.

In order to determine where corrections may be necessary in the flowfield under study, an analysis was conducted on a small subset of the acquired data. The velocity scan on the iced model upper surface at $x/c=0.10$, $\alpha=4°$, and two spanwise locations $y/b=0.470$ and $y/b=0.819$, was chosen. At $\alpha=4°$, the separation bubble aft of the ice horn controls the recirculation zone and presents some of the largest turbulence intensities in the flowfield. Based on the analysis of a similar but two-dimensional model flowfield[9], the $x/c=0.10$ chordwise location, coincides with the strongest recirculating portion of the bubble at $\alpha=4°$. In addition, at $y/b=0.819$, the proximity of this measurement location to the wing tip, hence the tip-induced spanwise flow, ensures that the third component of the velocity is non-negligible. A total of 1024 velocity samples were collected at the first six locations and 2048 samples were

collected at the remaining 14 survey locations in random mode in both traverses. The data were reduced using both simple arithmetic averaging, and also weighted using the Langley weight function (equation 3.21). This weight function was chosen since it accounts for the effect of frequency shifting of the laser beams.

The velocity profiles, made non-dimensional by the free-stream value, are plotted versus non-dimensional height for the centerline location in Fig. 24 and for the wing tip location in Fig. 25. Note the small difference between the corrected and uncorrected data near the wing centerline and near the wing tip. In both cases, the largest corrections seem to be in the middle of the shear layer, where the turbulence intensities are also the highest. Near the wing centerline, this corresponds to 31% turbulence intensity, while near the wing tip 34% turbulence intensity coincided with the location of maximum correction. From both figures, it is evident that hardly any correction is needed in the outer edge of the shear layer on outward into the free stream.

The corrected and uncorrected non-dimensional velocity profiles at $\alpha = 8^{\circ}$, $y/b = 0.470$, and $x/c = 0.02$ for the same free-stream conditions as above are shown in Fig. 26. These measurements were acquired in the Total Burst Mode of the counter, therefore the total burst time was available as a correction tool. Previous measurements using surface pressure taps[13] have shown that the wing flowfield is highly unsteady at this angle of attack. Figure 26 shows a thick boundary layer with a reverse flow region at $x/c = 0.02$. Once again, the corrections are largest in the middle of the shear layer, were the recorded turbulence intensity was at its largest value of 32 percent. The data were also reduced using the Langley weight function (equation 3.21), and the results are displayed on the same plot. The velocity profiles before and after correction show very little difference. Close examination reveals that in the shear layer the Langley weight function applies a smaller correction, whereas in the reverse-flow region, it applies a larger correction factor than the residence time.

Overall, examination of the corrected and uncorrected velocity profiles in Figs.

24 - 26 shows that, velocity bias, albeit small, seems to be present in the shear layer inward towards the wall. Both correction schemes shown here *correct* the data in the right direction, although at different magnitudes. The difference between the corrected and uncorrected profiles, however, seemed to be minute when either the burst time weight function or the Langley weight function were used. The largest corrections coincide with the recirculating region aft of the ice horn and the shear layer above it. At these locations, one of the underlying assumptions of the corrections schemes (spatially uniform seeding) is violated since it is not possible to uniformly seed a recirculation region[122]. It is therefore not clear what the extent of the corrections are, and whether these corrections yield the *correct* numbers or just different numbers from the raw, uncorrected data. In light of these findings, and considering the general uncertainties regarding the correction methods that are echoed in the literature, it was decided to present the data in this dissertation without correction for velocity bias.

3.5.5. Spatial Resolution or Gradient Bias

The velocity measured by the LDV is assumed to correspond to the velocity at the center of the measurement volume. However, due to the finite size of the sample volume, errors may be introduced into the measurements, particularly in spatial locations where the velocity or turbulence intensity gradients are quite large. In order to determine the effects of the finite size of the measurement volume, a reasonable estimate of the spatial resolution error is required.

Kried[123], Karpuk and Tiederman[124], and Mayo[125] have examined this problem analytically. Due to the effect of the velocity gradients, the measured mean velocity does not necessarily equal the mean velocity at the center of the measurement volume. Because of the finite size of the measurement volume, in the presence of velocity gradients, a particle which travels along the center of the measurement volume produces a velocity value different (in the mean) from a particle that generates its signal by crossing fringes closer to the edge of the ellipsoidal measurement volume. This dependence of the measured instantaneous velocity on

the location of the particle passage through the measurement volume is directly related to the severity of the local mean velocity gradient, independent of the actual local velocity fluctuations. It contributes a false fluctuation, or false turbulence to the turbulence intensity measurement with the LDV system.

The measured value of velocity must correspond to the mean velocity at some point located within the measurement volume. Therefore, the error in the mean velocity can not be larger than the maximum value of velocity gradient times the measurement volume diameter. The effect of the velocity gradients on the turbulence intensity consists of that due to velocity fluctuations at the center of the measurement volume, pseudo fluctuations due to variation of the mean velocity across the measurement volume, and the gradient of the turbulence intensity across the measurement volume. Karpuk and Tiederman[124], assumed a linear variation of U and u' across the measurement volume by letting

$$U = U_o + S(y - y_o) \tag{3.22}$$

and

$$u' = KU = K[U_o + S(y - y_o)] \tag{3.23}$$

Assuming a rectangular cross section, they suggested that the biased mean velocity differed from the true velocity at the center of the measurement volume according to

$$U_m = U_o + \frac{S^2 w^2}{12 U_o} \tag{3.24}$$

and the corresponding relation for turbulence intensity is

$$u_m'^2 = u_o'^2 + \frac{S^2 w^2}{12} + \frac{S^2 w^2 K^2}{12} \tag{3.25}$$

where the subscript "m" refers to the measured values and the subscript "o" denotes the values at the center of the measurement volume. S and K are the slopes of the mean velocity and the turbulence intensity, and w is the width of the measurement

volume. The first term on the right hand side of the turbulence intensity relation is due to the actual turbulent fluctuations at the center of the measurement volume, the second term is due to the mean velocity gradients, also known as false turbulence. The last term is due to the gradient of the turbulence intensity. The rectangular cross section assumption provides a "worst case" estimate since the rectangular shape will have more area further from the center of the measurement volume than the ellipsoidal measurement volume.

Spatial resolution can be increased by decreasing the dimensions of the measurement volume. For the most part, the flowfield of the rectangular wing under study, is two-dimensional. Therefore, the length of the measurement volume, which runs along the wing span of the model, is not as critical as the diameter of the measurement volume. This increase in spatial resolution, however, should be weighted against the need to have a large enough measurement volume so that an adequate number of fringes with reasonable spacing can be established. Failure to do so could result in having to use particles that are smaller than necessary, thus giving up valuable signal-to-noise ratio. Decreased fringe spacing also drives up the Doppler frequency, which in some instances, may place the flow frequency in the unreliable range of the signal processor.

An estimate of the error in mean velocity and turbulence intensity measurements can be obtained by rewriting equations 3.24 and 3.25 as follows:

$$12U_o^2 - 12U_oU_m + S^2w^2 = 0 \tag{3.26}$$

and

$$u_o'^2 = \frac{u_m'^2 - \frac{S^2w^2}{12}}{1 + \frac{S^2w^2}{12U_o^2}} \tag{3.27}$$

Therefore, knowing the measured mean velocity, and the mean velocity gradient, equation 3.26 can be evaluated for the measurement volume centerline mean

velocity, U_o. Once U_o is known, it can be used in equation 3.27, and knowing the measured mean turbulence intensity, the mean turbulence intensity at the center of the measurement volume, u_o', can be evaluated.

In the semispan wing flowfield under study, the maximum velocity gradients in the mean velocity occur in the middle of the shear layer near the model surface. Gradients as steep as 36 m/s per millimeter existed in the 28 m/s shear layer. For the green beam, which has a measurement volume diameter w = 126 microns, this yields 0.25% error for the mean velocity and 0.22% for the turbulence intensity due to spatial resolution. These values represent the "worst cases" in the flowfield under study. Less than 5% of the measurement locations have such high mean velocity gradients, therefore, the spatial resolution error was negligible in almost all locations in the flowfield.

3.5.6. Statistical Uncertainty

The high-speed counter used for velocity measurements during this study operates on individual bursts that are produced by particles passing through the measurement volume. These random individual realizations are collected into an ensemble from which the flow mean velocity and higher statistical moments are calculated. Since a finite number of samples is used to calculate these quantities, statistical procedures can be used to estimate the number of samples which would be required to determine mean velocity and turbulence intensity within an acceptable error level for a given confidence interval and an assumed population distribution[126].

Figure 27 shows the uncertainty in the measured mean value versus sample size for five turbulence intensity levels and a 95% confidence interval from a normal or Gaussian distribution. The result of a similar analysis for the uncertainty in standard deviation is shown in Fig. 28. Here, for a normally distributed parent population, the uncertainty in standard deviation is only the function of the confidence level and the sample size.

Based on the curves generated shown in Figs. 27 and 28, at a 95% confidence limit, the statistical uncertainty in the mean velocity was less than 1 percent at a

turbulence level of 20 percent when 2048 samples were taken. The uncertainty was 3 percent at a 50 percent turbulence level and 6 percent at a 100 percent turbulence level when 1024 samples were acquired. At the 95 percent confidence limit, the statistical uncertainty in standard deviation was 4.3 percent for a sample size of 1024 and 3.1 percent for a sample size of 2048. The number of samples collected in the flowfield of the current investigation depended on the data rate and the turbulence intensity. Near the wing surface, in the shear layer, or in the recirculation zone aft of the ice horn, the data rate decreased substantially. Only 1024, and whenever possible, 2048 data samples were taken at these locations. An attempt was made to collect more data points at these locations, but the amount of time required to obtain this ensemble proved to be unrealistic (on the order of 30 minutes per measurement location) in a boundary-layer survey consisting of at least six such locations. In the free stream, the data rate was very high, but the recorded turbulence intensities were no more than 2 percent, therefore only 1024 data samples would have sufficed in order to achieve a high degree of accuracy. When the data rate was not too low, 4096 data samples were collected. This included the region near the stagnation point on both the clean and the iced wing leading edges.

CHAPTER IV

RESULTS AND DISCUSSION

The results from the LDV measurements on the finite wing are presented in this section. Measurements taken on the baseline geometry, or the clean wing, will be presented first. These data will be compared to results from inviscid computational methods, and whenever possible, to other experimental results.

The data from the iced wing will be discussed next. These data will be compared to the measurements on the baseline geometry. Furthermore, the iced-wing measurements will be compared to previous measurements taken on a similar but 2-D geometry in addition to data taken using other measurement techniques on the same wing. The iced-wing results will also be compared to Navier-Stokes computations performed on the same geometry.

The quality of the test-section flow is very important. High turbulence intensity in the tunnel may promote premature transition of the boundary layer on the finite wing from laminar to turbulent. Additionally, the effects of free-stream turbulence on the outer part of the boundary layer ($y/\delta > 0.7$) lead to a slightly fuller mean velocity profile and an increase in the level of $\overline{u'^2}$ and $\overline{u'w'}$. The increase has been reported to be as high as 150 percent for a turbulence intensity level of five percent[127]. Prior to the analysis of results from the finite wing, the flow quality in the tunnel test section will be discussed.

4.1. Empty Test Section (Model Not Mounted in Tunnel)

The free-stream flow in the tunnel test section ideally should have no turbulence intensity and flow angularity. However, due to the condition of the flow arriving at the inlet and subsequently passing through the honeycomb and screens, small

turbulence intensities in addition to flow variation may exist. Being aware of these conditions, if present, will help the interpretation of data from the test section.

Before proceeding with the LDV measurements on the finite wing, the tunnel test section flow quality was examined. A single hot-wire probe was used at the test section center to measure the turbulence intensity over a range of tunnel speeds. Figure 7 shows the measured turbulence intensity. At Re=1.5 million, the test Reynolds number for the finite wing experiments, the average measured turbulence intensity was no more than 0.07%.

Data presented in Reference 128 suggest that turbulence intensity higher than 0.2 percent is needed to promote transition to turbulent flow in a boundary layer. Therefore, the very low level of turbulence intensity in the test section should not affect the state of the boundary layer on the finite wing.

In order to check the flow variation, the tunnel test section was mapped with the LDV instrument at the entrance of the test section (end of the contraction zone). Figure 29 shows the measured free-stream velocities at a measurement plane perpendicular to the free stream, and four inches into the test section. The measurements covered a 2-foot by 2-foot plane at the center of the test section. The plotted results in Fig. 29 show a measured mean velocity of 46.3 m/s (103.5 MPH). Note the nearly constant tunnel speed, with minute velocity variations amounting to approximately one percent. The tunnel speed, measured by the facility transducer, was at 46.2 m/s (103.3 MPH) during the LDV scans of the test section.

4.2. LDV Measurements - Clean Wing

Measurements were taken on the centerline of the clean wing in order to establish a baseline for future comparison with the iced-wing results. In addition, comparison of these results with inviscid computational methods verified the LDV measurements. Earlier pressure measurements on this wing have shown that the centerline of this wing behaved in a 2-D manner.

4.2.1. Pressure Distribution on the Wing Centerline

The pressure distribution obtained on the centerline of this 3-D wing is shown in

Fig. 30. In the same figure, a plot of the pressure distribution from the airfoil code of Smetana et al.[129] with the same NACA 0012 geometry is displayed. The measured pressures were at a wing angle of attack of 8 degrees and the theory was at a matched lift coefficient[13]. The comparison was very good, as expected.

Figure 31 shows the sectional drag polar of this wing compared to the drag results from Eppler's airfoil code for the 2-D NACA 0012 airfoil[13]. The sectional drag measurements on this model were in good agreement with Eppler's result for the natural transition case. With the transition fixed at 5% chord on the upper and lower surfaces, the measurements on the 3-D wing also compared very well with predictions made by the EPPLER code[130].

4.2.2. Comparison with Computation

The measurement plane on the clean wing was one inch offset from the centerline tap row, Fig 32. This placed the LDV measurement locations near the wing centerline, yet away from the static pressure taps on the model centerline in order to avoid any possible interference due to the presence of the taps. The scan locations in this measurement plane are shown in Figs. 33-35 for $\alpha = 0$, 4, and 8 degrees respectively.

Profiles taken with the laser Doppler velocimeter (LDV) on the clean wing are compared to inviscid flowfield computations. The measurements were taken at y/b = 0.470 on the model. All LDV surveys on the clean model, starting at 0.050 inches (1.27 mm) from the model surface, were taken normal to the wing surface.

Figure 36 shows the results from LDV measurements on the clean wing centerline at $\alpha = 0^{\circ}$ at x/c = 0.02, 0.30, 0.50, and 0.99. Here measurements have been compared to an inviscid method based on Theodorsen's conformal mapping technique[3]. Note that this computational method does not account for the presence of wind tunnel walls. Another inviscid computational approach, based on a panel method, was also used for comparison with measurements. This code, originally developed to study the effect of wind tunnel walls on impinging droplet trajectories[131], was modified to yield the flowfield velocities at the corresponding LDV measurement locations.

Away from the model surface, measurements were in excellent agreement with both computational methods. Near the surface, however, measurement results did not match the inviscid predictions. This was an expected result since the inviscid methods do not account for the viscous effects near the model surface. This trend was also observed in the measurement results at higher angles.

At x/c=0.02, the model surface had a positive slope at $\alpha = 0^{\circ}$. The (w)-component measurement indicated an initial positive value near the model surface. This was to be expected for the flow to remain attached to the model surface. Moving away from the surface in a direction normal to the surface, the (w)-component gradually reduced to it's free-stream non-dimensional value of 0.0. The streamwise component, initially retarded by the presence of the model, was measured to have an initial value smaller than 1.0 near the surface, increasing to it's free-stream non-dimensional value of 1.0 away from the model surface.

As the flow moved downstream along the model surface, the primary component became the (u)-component with the (w)-component offering a small contribution as a function of the model surface slope. At x/c=0.30, where the model surface slope was 0.002, the measured (w)-component was very small. The (u)-component was measured to have an initial value larger than 1.0 near the model surface, gradually recovering to 1.0 out in the free stream.

At x/c=0.50 and 0.99, where the model surface had a negative slope (Fig. 33), the (w)-component was seen to have a negative value near the model surface, converging to 0.0 in the free stream. Near the model trailing edge, at x/c=0.99, the LDV measurements for the (u)-component indicated a fully developed, turbulent boundary layer velocity profile.

At all x/c locations shown, comparison between measurement and computation was quite good. As the trailing edge was approached, however, an increasing difference between the two prediction techniques was observed. In comparison with results from Theodorsen's conformal mapping technique, the results from the panel technique (where the tunnel walls were modelled) were in better agreement with

measurement. Therefore, measurements at $\alpha = 4^\circ$ and 8° will be compared only to the results from the panel technique with the tunnel walls modelled.

Measurements at $\alpha = 4^\circ$ are shown in Fig. 37 for x/c=0.02, 0.30, 0.50, and 0.99. Away from the model surface, very good agreement was observed between measurement and computation. Near the surface, as expected, little agreement is observed between measurement and computation. Figure 34 shows measurement locations at $\alpha = 4^\circ$ on the model upper and lower surfaces. Referring to these measurement locations will aid in understanding the flow behavior at each scan location.

At x/c=0.02, the LDV measurements indicated a large value for the (u)-component near the model surface. Moving away from the model in the normal direction to the surface, the measured velocities were seen to decrease to non-dimensional values of 1.0 and 0.0 for (u) and (w) respectively. Outside the attached boundary layer, in the inviscid stream, the dynamic pressure of the flow was at its largest near the model surface. This was readily observed in the (u)-component measurements at x/c=0.02. The (w)-component measurements indicated a large positive value near the model surface, followed by recovery to the free-stream value.

Measurements at locations further downstream, shown for x/c=0.30, 0.50, and 0.99, indicated that the (w)-component had its largest magnitude near the model surface, converging to the free-stream value of 0.0 in the free stream. In order for the flow to remain attached to the model surface, as shown by pressure measurements made previously on the model centerline[13] (Fig. 38), the (w)-component must be negative near the model surface. Indeed the LDV-measured (w) velocities showed that the velocities near the surface were negative.

At 8 degrees angle of attack, previous pressure measurements on this model[13] (Fig. 39) showed that the flow on the wing centerline had not separated yet. However, the LDV measurements indicated that the boundary-layer growth on the upper surface was noticeable. At x/c=0.10, pressure measurements indicated a steep gradient on the upper surface of the clean model. This may be seen through the

decreasing trend in the (u)-component of velocity as the LDV measurement volume was moved downstream on the model surface, Fig. 40. For example, at $x/c=0.10$, $(u/U_\infty)_{max}=1.60$; at $x/c=0.30$, $(u/U_\infty)_{max}=1.40$; at $x/c=0.50$, $(u/U_\infty)_{max}=1.25$; and at $x/c=0.99$, $(u/U_\infty)_{max}=1.13$ near the model surface. The reduction of velocity near the surface, in the streamwise direction, indicates the reduction of C_p on the model surface in the streamwise direction. The (w)-velocity, was seen to have a small positive value near the surface. At $\alpha=8°$, the surface slope was 0.03654 at $x/c=0.10$ which, in the presence of an attached boundary layer, suggested a small positive value for the (w)-component.

Further downstream, at $x/c=0.30$, recovery of the streamwise component to the free-stream value was not as severe. The (w)-velocity, owing to the fact that the boundary layer had remained attached to the surface (which had a negative slope of -0.13850 at $\alpha=8°$ and $x/c=0.30$), started with a negative value near the surface, gradually recovering to the free-stream value of zero.

At $x/c=0.99$, a marked increase in the boundary layer thickness was observed through the measured (u)- and (w)-component velocity profiles. Near the trailing edge, the (u)-component does not appreciably deviate from 1.0 outside of the boundary layer. Both (u) and (w) velocity profiles represented fully developed turbulent boundary layer velocity profiles.

At all locations shown, comparison showed very good agreement away from the surface between prediction and measurement. Near the surface, due to viscous effects not modelled in the inviscid predictions, the comparison was not in good agreement. Additionally, the difference between measured and predicted values increased as the trailing edge was approached. This was also to be expected. The growth of the boundary layer on the model surface led to a different *inviscid* geometry which was not the same as that used in the computations.

Although present, the tunnel blockage effect was calculated to have an insignificant contribution to the magnitude of velocity. Based on the method devised in Ref. 132, the increase in velocity was 0.8% at $\alpha=4°$. At $\alpha=8°$, the highest angle

where measurements were made, this contribution increased to 3.0%.

The comparison between measurement and the computational method where the tunnel walls were modelled showed nearly the same result near the leading edge as the comparison between measurement and computational method where the walls were not modelled. However, as the trailing edge was approached, the first computational method clearly was in better agreement with measurement. The measured (u)-component velocity profiles at $x/c=0.99$ were higher than prediction by a small amount. This seems to be true for all angles at which the wing was tested.

The presence of tunnel walls was observed through an increase in velocity. The boundary-layer thickness increased as the trailing edge was approached and therefore the tunnel blockage effect became more significant. This increase in velocity was observed through the velocity profiles at $x/c=0.99$.

Minor differences, observed away from the model surface, between measurement and prediction are attributed to the procedure used to obtain non-dimensional velocities. The tunnel mean velocity, measured through a facility transducer, was used to make LDV measurements non-dimensional. A slight variation in the tunnel velocity from point to point would cause the non-dimensional value to shift slightly. Additionally, despite the proper filter settings on the signal acquisition equipment, separation of noise and good signal at times became an art rather than science.

Figures 33 through 35 show the measurement locations at $\alpha = 0$, 4, and 8 degrees. The detailed discussion above represented only a fraction of measurements carried out on the clean finite wing. The complete set of the measured mean velocity profiles on the clean wing, along with computational comparison are given in Figs. 2.1-2.7 in Appendix 2.

4.2.3. Evolution of (u)- and (w)-Velocities Normal to the Finite Wing's Surface

The clean rectangular wing did not exhibit any major inconsistencies. No large regions of separated, or reverse flow, were observed. Near the trailing edge at $\alpha = 4^\circ$ and 8°, inflections in the mean (u)-velocity profiles, indicative of instability in the boundary layer, were observed. Otherwise, the velocity measurements made with the

LDV instrument resulted in smooth profiles. Due to the small thickness of the boundary layer at most measurement locations, except near the trailing edge at $\alpha = 4^\circ$ and 8°, only the outer edge of the boundary layer was captured during most measurements.

Near the wing leading edge, double-peak histograms were observed at some locations during the LDV scans. While conducting similar experiments on a NACA 0012 rectangular wing in the Langley 7'x10' tunnel, Hoad et al.[119] obtained double-peaked histograms at $\alpha = 4.75^\circ$. They indicated that the double-peaked histograms in their experiments were the result of flow unsteadiness with oscillating velocity fields. It was postulated that the double peaks were due to the presence of an oscillating shear layer, and possibly a separation bubble, on the wing surface.

In the present investigation, double peaks were observed at $\alpha = 0^\circ$ and 4° cases near the leading edge, at x/c=0.02. The histograms resulting from measurements at $\alpha = 0^\circ$, x/c=0.02 on the wing's upper surface are shown in Fig. 41. At z/c=0.0033, 0.050 inches (1.27 mm) away from the surface, the (u)-component histogram showed a single spike. At z/c=0.0066, 0.10 inches (2.54 mm) away from the wing surface, a double-peaked histogram developed for the (u)-component. The left peak was larger than the right peak, indicating more occurrences of the lower velocity than the higher velocity. If a shear layer were present, this would correspond to the low-velocity side of the shear layer. At the next position, z/c=0.0099, the histogram indicated that the flow experienced the lower velocity and the higher velocity with equal frequency. Three positions later, at z/c=0.0198, the flow experienced the higher velocity more than the lower velocity. Again, if a shear layer were present, this point would be on the opposite side of that shear layer. Further away from the model surface at z/c=0.0297, the histogram returned to a single-peak distribution.

In similar measurements reported by Hoad et al.[119], near the leading edge (x/c=0.047), double-peaked histograms were reported as far as z/c=0.057 (z=0.68 inches) away from the surface on their 12-inch chord model. Examination of the boundary-layer thickness on a 12-inch chord NACA 0012 using a 4th-order Polhausen

velocity profile[133] shows that the boundary-layer thickness at 5 percent chord is less than 0.01 inches. The presence of double-peaked histograms in the data of Hoad et al. at a much higher location than theory predicts may have been due to a high level of turbulence intensity, unfortunately not reported.

The double-peaked histograms were observed at both $\alpha = 0°$ and 4° runs near the leading edge at $x/c = 0.02$. Hoad et al.[119] obtained similar velocity histograms only at $\alpha = 4.75°$. Their results at $\alpha = 0.6°$ indicated smooth flow over the wing-section's leading edge. Additionally, analysis by Eppler's airfoil code[130] failed to reveal a separation bubble on the NACA 0012 airfoil at all of the angles of attack mentioned above. Furthermore, pressure measurements on the finite wing's centerline did not show the presence of a separation bubble at either $\alpha = 0°$ or 4°.

These results, therefore, seem to disagree with those of Hoad et al.'s. The mean velocity profiles resulting from the present study's measurements, however, compared favorably with inviscid computational results (shown in Figs. 36,37,40, 2.1-2.7 in Appendix 2). Therefore, although the presence of a separation bubble on the clean wing's leading edge could not be verified, the double-peaked histograms at $\alpha = 0°$ and 4° hinted at the possibility of the presence of a shear layer on the leading edge of the clean wing.

Other reasons may exist for the appearance of the double-peaks in the velocity distributions. The double-peaked histograms may be due to the seed particles impinging on the leading edge. The larger particles in the polydisperse seed solution would lag the flow, which in turn would cause the appearance of the double-peaks in the velocity histograms.

The presence of the double-peaked histograms near the model leading edge may also be attributed to the presence of seed particles in the LDV measurement volume from more than one source. A similar phenomenon has also been encountered in droplet trajectory analysis of particles impacting axisymmetric bodies of revolution[134]. During such analysis, collection efficiencies two to three times higher than anticipated had occurred. Particles arriving at these locations from more than one source were

found responsible for the higher collection efficiencies. In a similar analogy, particles from more than one source maybe arriving at the measurement volume, thus causing the double-peaked distributions.

Small irregularities observed in the mean velocity profiles stemmed from the presence of some amount of noise in the data. The portions of data which were obviously attributable to noise, were edited. At times, however, noise was not distinguishable from data at some measurement locations. In order to provide an insight to the flow details, the velocity profile at a typical chord location will be analyzed.

The mean velocity profile at $\alpha = 0^{\circ}$, $x/c = 0.50$, is shown in Fig. 42 for the (u)- and (w)-components. At this location, the LDV instrument registered a (u)-velocity of 99.50 MPH (44.5 m/s) and a (w)-velocity of -1.08 MPH (-0.486 m/s) at a distance of 0.050 inches (1.27 mm) normal to the wing upper surface. A maximum velocity, or edge velocity, of 52.68 m/s (117.79 MPH) for the (u)-component and -3.19 m/s (-7.13 MPH) for the (w)-component was not realized until 0.250 inches (6.35 mm) away from the model surface. Beyond this point, a gradual recovery to the free-stream value was initiated.

The velocity histograms, which comprise the mean results just described, provide a wealth of information on the distribution of the measured instantaneous velocities. In addition, various flow statistics can be extracted from these distributions. The equations used for the calculation of various flow statistics are listed in Appendix 1. The histograms for the measurements made at $\alpha = 0^{\circ}$, $x/c = 0.50$, are shown in Fig. 43. A total of 2048 samples was taken in coincidence mode for each measurement location. In each display, the (u)-component is always on the right while the (w)-component is the distribution on the left.

At 0.050 inches (1.27 mm) away from the model surface ($z/c = 0.0033$), the (w)-component possessed a symmetric and narrow histogram with a sharp peak, while the (u)-component displayed a broad histogram which was more representative of a shear layer-type distribution. Such combinations have been encountered by others while

measuring similar flow situations. Hoad et al.[119] have shown histograms with similar distributions for their measurements on a NACA 0012 wing at $\alpha = 0.6°$ and $x/c = 0.58$, in similar flow conditions.

Further away, at 0.150 inches (3.81 mm) normal to the surface ($z/c = 0.0099$), the velocity histograms for both (u) and (w) velocities show well-defined, tall and narrow distributions with distinguished peaks. This trend continued until the last measurement location, approximately five inches away from the model surface.

Various flow moments were deduced from these measurements. The turbulence intensity, or the square root of the second moment, is shown in Fig. 44 for the (u)- and the (w)-components. These results indicate the degree of fluctuation of the measured values about the mean velocity for that component. The displayed values were made non-dimensional using the fluid's local velocity. The highest value for both components was measured at the first measurement location, 0.050 inches (1.27 mm) normal to the model surface. The turbulence intensity for the (w)-component, made non-dimensional with respect to the fluid's local (w) mean velocity, appeared much higher than the (u)-component.

Both (u) and (w)-components, however, reduced sharply 0.250 inches (6.35 mm) away from the model surface, with the (u)-component dropping to 1.5 percent and the (w)-component dropping off to 11.9 percent.

The third moment, or skewness, of a histogram gives information on the degree of symmetry of the distribution. A completely symmetric distribution would have zero third moment or skewness. A positive value of skewness would indicate the occurrence of velocity spikes which are higher than the mean.

The third moment for the (u) and (w) velocity distributions is shown in Fig. 45. For both velocity components, a large positive initial value was recorded at 0.050 inches (1.27 mm) away from the model surface. This would indicate that velocities larger than the mean were occurring in the flow. Further away, the third moment for the (w)-component reduced rapidly to near-zero. The (u)-component, however, first crossed zero, took on a negative value, and then recovered rapidly to near-zero

values, indicating that velocity spikes lower than the mean were occurring frequently. This can also be verified through visual inspection of the histogram for $z/c=0.0099$ in Fig. 43.

The fourth moment of the distribution, also called kurtosis or excess, is shown for the (u)- and (w)-components in Fig. 46. The value of kurtosis is large if the histogram has frequent values far away from the median. In a fluid flow situation, this would be indicative of large velocity spikes away from the mean. In both the (u)- and (w)-components, the largest value of kurtosis was calculated at the first measurement location, 0.050 inches (1.27 mm) away from the model surface. The kurtosis then fell off to near-zero for both velocity components at $z/c=0.0132$, indicating very little variation of velocity about the mean from this point outward.

The coefficients of skewness and kurtosis, made non-dimensional by the third and fourth powers of standard deviation, are shown in Fig. 47 and Fig. 48, respectively, for the (u)- and (w)-component of the velocity. These results are in general agreement with those of Hoad et al.[119]

The Reynolds shear-stress provides information on the degree of flow fluctuations as a function of both components' velocities. In other words, when both flow components display large and correlated fluctuations, the Reynolds shear-stress becomes significant. The calculated Reynolds shear-stress for $x/c=0.50$ at $\alpha = 0^{\circ}$ is shown in Fig. 49. Here the stresses were large up to $z/c=0.0099$, then dropping off rapidly to zero at the measurement locations further away from the surface.

The mean magnitude of the total measured velocity vector, in addition to the mean angle are shown in Fig. 50. The profile of the total velocity magnitude tended to follow the profile of the (u)-component of velocity since the (u)-component carried a substantial portion of the total velocity. The mean angle for the velocity profile indicated that initially the direction of the mean velocity vector was negative, following the model surface slope. At $\alpha = 0^{\circ}$, $x/c=0.50$, the surface slope of the wing was -0.05967. If the flow is to remain attached to the surface at this location, the flow angle must be negative. Therefore, the measured velocities suggest that flow

separation had not yet occurred at this location on the model's upper surface. This result was in agreement with previous pressure measurements on the finite wing.

4.3. LDV Measurements - Iced Wing

Results from the LDV measurements on the iced wing will be presented in this section. These measurements will be compared to the split hot-film measurements carried out on a similar 2-D airfoil. Navier-Stokes computations, performed on the finite wing geometry, will also be compared to the LDV measurements. Furthermore, the results of these measurements will be compared to those from the clean wing.

The wing was tested with the simulated ice shape at three angles of attack: $\alpha = 0°$, 4°, and 8°. Measurements were carried out in three xz-planes at each angle of attack; the inboard scan was carried out at $y/b = 0.175$, the centerline scan at $y/b = 0.470$, and the outboard scan was carried out at $y/b = 0.819$, Fig. 51.

The measurements were carried out normal to the model surface, except from the leading edge of the iced model, $x/c = -0.02$, to $x/c = 0.10$. Due to the ice shape's extreme curvature, the measurements were carried out normal to the model chord in this chord range. The measurement locations on the iced model are shown in Figs. 52-54.

4.3.1. Comparison with Earlier Measurements

A comparison of the pressure measurements made on the 3-D wing[13] and the 2-D airfoil[6-8] is shown in Fig. 55. Two pressure distributions were selected which had similar lift coefficients. The 2-D data had a lift coefficient of 0.375 at an angle of attack of 4 degrees and the data from the 3-D wing came from the centerline tap row with a lift coefficient of 0.395 at a wing angle of attack of 5 degrees. The good comparison here further reinforces that the 3-D wing is behaving at the midsection, at low angles of attack, much the same as the 2-D data would predict.

Flow visualization results are also in agreement with this finding. The result from florescent oil flow visualization on the finite wing[17] at $\alpha = 4°$, $Re = 1.2$ million is shown in Fig. 56. The surface shear stress pattern on the finite wing is essentially two-

dimensional at $\alpha = 4°$.

Comparison of the boundary layer profiles on the 3-D model centerline with those made on the similar but 2-D model also shows the two-dimensional behavior of the iced 3-D wing centerline at low angles of attack. No LDV measurements on the 2-D model have been made. Split hot-film measurements, however, were obtained on the 2-D model in the Ohio State University tunnel[6-9]. In order to compare the split hot-film-measured profiles from the OSU tunnel with the LDV-measured profiles in the UIUC tunnel, the proper 3-D wing angle of attack had to be determined. Doing so would ensure that the flowfield at the wing centerline would behave in the same manner as the flowfield on the 2-D model in the OSU tunnel.

The split hot-film measurements at OSU were taken at $\alpha = 4°$ in a tunnel similar to the one in use at UIUC. The measured pressure distribution for this 2-D model was compared to the measured pressure distribution at $y/b = 0.497$ for the 3-D model, also tested in the OSU tunnel[13]. The information obtained from this comparison was used to determine a suitable angle of attack for the 3-D model in the UIUC tunnel, which has a different test-section dimension.

Assuming that the spanload distribution of the model in the UIUC tunnel was the same as that in the OSU tunnel, it was determined that at $\alpha = 4.7°$, the 3-D model centerline would have the same pressure distribution as the 2-D model at $\alpha = 4°$, where the split hot-film profiles were obtained in the OSU tunnel.

In Fig. 57, a subset of the LDV measurements obtained at $y/b = 0.470$ on the iced 3-D wing are compared with split hot-film measurements made on the similar 2-D model in the OSU wind tunnel. The hot-film profiles were obtained by traversing a split hot-film probe normal to the free stream. For these comparisons, the LDV profiles were also obtained by traversing the measurement volume normal to the free stream.

Results for $x/c = 0.02$ show very good agreement in the reverse-flow region and through the shear layer near the wing surface. The LDV-measured edge velocity differs from the split hot-film-measured edge velocity by as much as ten percent.

Both measurements, however, seem to approach the same non-dimensional free-stream velocity.

The trends described above are also seen at further downstream stations displayed in Fig. 57, at x/c=0.04 and 0.10, and those not shown here. Comparison shows very good agreement near the model surface through the shear layer. Further away from the surface, near the edge of the boundary layer, a larger edge velocity is observed from the LDV measurements. At the last station shown, x/c=0.30, both split film and LDV measurements show that the flow has reattached downstream of the separation bubble.

While the edge velocities were measured to be different on the 2-D and the 3-D models at all stations shown, the boundary layer thickness derived from both measurements seem to match closely. At x/c=0.02, $(\delta/c)_{LDV}=0.03649$ and $(\delta/c)_{split\ film}=0.03654$ while at x/c=0.04, $(\delta/c)_{LDV}=0.03574$ and $(\delta/c)_{split\ film}=0.03591$.

The higher edge velocity measured by the LDV instrument also translated into a larger displacement and momentum thickness, compared to those calculated from the split film measurements. Again at x/c=0.02, $(\delta^*/c)_{LDV}=0.03193$ and $(\delta^*/c)_{split\ film}=0.03037$ while at x/c=0.04, $(\delta^*/c)_{LDV}=0.03100$ and $(\delta^*/c)_{split\ film}=0.02846$. The complete set of velocity profiles obtained from the LDV measurements, and the split film comparisons, are shown in Appendix 3.

In some of the profiles shown in Appendix 3, in approximately the middle of the shear layer, a large gap exists in which no velocity was measured by the LDV instrument. As discussed in Chapter III, this is an instrument-related event and does not affect the shape of the profiles.

For these comparisons, $\alpha=4.7^\circ$ was chosen based on an estimate of how closely the pressure distribution on the centerline of the 3-D wing and that on the 2-D model in the OSU tunnel would match. Earlier pressure measurements on this model indicated that at $\alpha=4^\circ$, the separation bubble extended well beyond ten percent chord in the streamwise direction. The edge velocity was $u/U_\infty=1.463\pm3\%$ for the hot-film-measured profiles shown in Fig. 57. The edge velocity measured by

the LDV instrument was $u/U_\infty = 1.614 \pm 1\%$ for the LDV-measured profiles shown in Fig. 57. This means that, based on the edge velocity, both sensors indicated a constant-pressure region with a 27 percent difference in the level of pressure plateaus. The presence of the split hot-film probe inside the separation bubble is known to reduce the length of the bubble[9].

Several possibilities exist for the difference in the edge velocities from the two different measurements. The lift coefficients were matched for the wing centerline and the 2-D airfoil. Although direct measurements of pressures normal to the surface were not made, the mismatch of the pressure coefficients based on the edge velocity further reinforces the concept that constant pressure in the transverse direction in a boundary layer is not a valid assumption in complex boundary layer flows involving large regions of flow separation and reversal.

Close examination of Fig. 55 reveals that, although $C_{l,2D}$ is lower than $C_{l,3D}$, the pressure plateaus in the 2-D measurements are at a higher level than those in the 3-D pressure measurements. A better approach, perhaps, would have been to match the pressure plateaus between the 2-D and the 3-D measurements. In this manner, the effect of the separation bubble in the 2-D measurements would have been better reproduced in the 3-D measurements.

Additional sources of mismatch range from the 3-D effects present on the finite wing, which may have not been accounted for by simply matching the pressure distributions, to mis-alignment of the model prior to the flowfield measurements. The difference in instrumentation between the two tests could be regarded as another source of discrepancy. A better approach would be to test the same 2-D model used in the split-film measurements in the present tunnel with the LDV instrument.

No attempts have been made to further investigate this discrepancy; results from both instruments are in good agreement with each other in the reverse-flow region and the shear layer. Overall, the flowfield and aerodynamic performance of the 2-D airfoil compared very well to the centerline of the 3-D model.

4.3.2. Comparison with Navier-Stokes Calculations

As pointed out earlier in Chapter II, the experimental data obtained as a part of the ongoing iced-airfoil/iced-wing performance degradation analysis program has been used for comparison to computational results. Kwon and Sankar[10,64] computed the flow over the unswept finite wing. Conditions at 4- and 8-degrees angles of attack, M=0.12, and Re=1.5x10^6 were computed on the CRAY-YMP at NASA Lewis Research Center. The calculated chordwise pressure distributions and the integrated sectional loads for the wing have been compared with experimental results.

For this computational modelling, they used the full unsteady three-dimensional Navier-Stokes equations on an algebraic C-grid in a body-fitted coordinate system to model the flowfield about the 3-D wing. A two-layer Baldwin-Lomax eddy viscosity model patterned after the Cebeci-Smith model was used in this work. Details of the computational procedure are available in References 5,10,12,64.

The computational grid consisted of 141 streamwise points (95 on the wing surface), 19 spanwise points (14 on the wing), and 44 points in the normal direction. The code was also run with a larger number of spanwise and streamwise grid points in order to improve the flow prediction near the wing root-end wall juncture. The computational wing along with the grid are shown in Fig. 58 and Fig. 59[135].

4.3.2.1. Comparison at y/b=0.470

Comparison between the LDV-measured velocity profiles and the Navier-Stokes-predicted velocity profiles[136] are shown in Fig. 60. Here the profiles for α = 4°, y/b = 0.470 on the upper surface of the iced wing are shown at x/c =-0.02, 0.04, 0.08, and 0.60. At x/c = -0.02, on top of the ice horn, both LDV-measured and CFD-predicted profiles indicate attached flow. Near the outer edge of the velocity profile, the LDV results differ from the CFD results by as much as 10 percent. The CFD-predicted edge velocities are lower, possibly because of the very large values of the F-function in the turbulence model[135]. This would in turn drive up the eddy viscosity, hence slowing the fluid more than anticipated.

At x/c = 0.04 and 0.08, both the LDV instrument and the Navier-Stokes computation show a region of reverse flow near the model surface. The experimental profile resembles a hyperbolic tangent profile which is typical of wall-bounded shear layers with flow reversal. The shear layer in the measured profiles appears to be fuller than that in the predicted profiles. If the viscosity is low, it would create inadequate mixing. Inadequate mixing in the shear layer would cause the computational shear layer not to be as flat as the LDV-measured profile. In addition, the slight overshoot at the boundary-layer edge, observed in the measured profiles, is absent in the predicted profiles. Further downstream, at x/c = 0.60, the measured velocity profile appears fuller than the predicted profile. The trends described above also appear at other x/c stations not shown here. The complete set of measurements on the iced wing root, centerline, and tip, in addition to the Navier-Stokes comparison, are given in Figs. 61-66.

In some of the profiles shown in Figs. 61-66, in approximately the middle of the shear layer, a large gap exists in which no velocity was measured by the LDV instrument. This was determined to be due to the frequency limitations imposed by the downmixing hardware and did not affect the shape of the profiles.

The differences in the measured and predicted profiles are attributed to the grid resolution and the turbulence model utilized in the computation. A total of 44 grid points were used in the direction normal to the wing surface. Approximately 10 grid points were packed within the first half-inch (12.7 mm) normal to the surface. Based on the LDV measurements, this is the average height of the shear layer on the iced model at $\alpha = 8°$. The rest of the grid points are distributed up to seven chord-lengths normal to the model, decreasing exponentially in concentration away from the surface.

In addition, in order to keep the computer resources within a reasonable range, the grid points in the spanwise direction were sparsely distributed. As pointed out earlier, 14 spanwise grid points were used on the wing. This means that, as shown in Fig. 58, a grid point was placed every 7.7 percent span on the wing. The predicted

profiles shown in Fig. 60, were constructed by interpolating the computed velocities at eight computational grid points surrounding the desired location.

In the middle of the shear layer, where the velocity profile appears fuller in comparison with computation, a denser grid spacing would improve the predicted profiles. Further away from the model surface, at the boundary-layer edge, this would also aid in a better definition of the velocity profile. Currently, only 3 to 4 grid points normal to the surface occupy the space where the edge of the shear layer appears in the measured profiles.

A two-layer Baldwin-Lomax eddy viscosity model was used in this computational work. Use of such a simple model in massively separated flows may be considered questionable. Potapczuk[49] used a modified mixing length turbulence model in a similar but 2-D flowfield and found an improved prediction of the velocity profile in the shear layer. Kwon and Sankar[10], however, reported that earlier studies with higher order turbulence models in two-dimensional stalled flows showed little overall improvement in the final result. Consequently, in order to keep the computer resources small, the algebraic eddy viscosity model was used in all the Navier-Stokes computations of the iced-wing/iced-rotor aerodynamics[11].

4.3.2.2. Comparison at y/b=0.175 and y/b=0.819

The predicted velocity profiles at the inboard and outboard scan planes follow the same pattern as the predicted profiles on the centerline plane. These profiles are shown, along with the measured profiles, in Figs. 61-63 for $\alpha = 4°$. The main feature here is that in the outboard measurement plane, both measurement and prediction show a shortened separation bubble. This is a direct consequence of the tip-induced vortex flow. The velocity gap seen in some of the profiles is due to the limitation of the downmixing hardware, as discussed in Chapter III.

Previous calculations by Sankar et al. had shown that the wing root-wall interaction had little influence on the aerodynamic coefficients at $\alpha = 4°$. At y/b=0.175 and 0.470, both measurement and prediction show the bubble reattaching between x/c=0.12 and 0.14. At y/b=0.819, however, the flow was measured (and

predicted) to reattach between x/c=0.10 and 0.12 (see Fig. 63).

The initial purpose of such computations has been to predict the global aerodynamic parameters such as the lift, drag, and pressure coefficients. In order to calculate the pressure coefficient and subsequently the lift coefficient, the boundary-layer displacement thickness must be predicted reasonably well. The three-dimensional algorithm, along with its earlier 2-D counterparts, have predicted the global parameters reasonably well[5,11,46,47,65].

Drag prediction, on the other hand, is a function of how well the velocity profiles can be predicted. Accurate prediction of drag would therefore depend on the accuracy of the prediction of the momentum deficit, which is a function of the accuracy of prediction of the velocity profiles.

The first step of a more detailed comparison with computation would require improved grid resolution, at least within the height of the iced-wing boundary layer, without altering the present turbulence model. Due to its flexibility in adaptation to complex geometry and ease of re-packing where needed[50,51], the unstructured grid may be the alternative to pursue. Further calculations with higher order turbulence models would be the next step in a more detailed comparison between computational and measurement results[137].

4.3.3. Mean Measurement Results

The ensemble averaged results for the LDV measurements reveal features of the flow development both in the downstream direction and normal to the wing surface. Results from the spanwise measurements will aid in revealing spanwise aspects of the flow development that can not be deduced otherwise.

The gross geometry of the leading edge ice accretion on the finite wing appears as a formidable obstacle in the way of fluid particles as they attempt to negotiate the pressure field created by the presence of the iced wing in the free stream. For example, in the clean wing case at $\alpha = 4°$, the leading edge C_p spike has been measured to be as high as -1.5[13]. The accelerating fluid particles near the leading edge of the model surface have sufficient momentum to form an attached boundary

layer on the model.

On the iced wing upper surface at $\alpha = 4°$, however, the situation is different. Analysis of the pressure field using Eppler's code[130] reveals C_p predictions of -10.5 for the NACA 0012 iced airfoil at the same angle of attack. The boundary layer on the model leading edge can not maintain the very high adverse pressure gradient imposed by the outer potential flow. The measured value on the iced 2-D model was -1.45[13]. Additionally, the geometry of the iced-wing leading edge is very similar to a rearward facing step. As the boundary layer passes over the upper surface ice horn, it separates and changes into a shear layer.

4.3.3.1. Evolution of Flow Normal to the Wing Surface

The pattern of flow development described above can be observed in the measured velocity profiles, Figs. 61-69. Based on their shapes, the profiles constructed from the LDV measurements on the rectangular wing may be placed into three categories. Each type will be discussed individually.

4.3.3.1.1. Profiles Upstream of the Separation Bubble

These profiles indicate a fully attached flow on the model surface. Researchers experimenting with rearward facing steps have called this the approach boundary layer. Laminar, transitional, and turbulent approach boundary layers have been used in the experiments described in the literature. Based on the momentum thickness calculations for these profiles, $Re_\theta = 101$, 148, and 114 for $\alpha = 0°$, 4°, and 8°. The Eppler analysis code[130] was used here since, similar to the clean model, the boundary-layer profiles were too small to capture with the LDV instrument. Since this is below the transitional value of $Re_\theta \sim 200$, the flow here is considered to be laminar.

At the first measurement location, $x/c = -0.02$ on top of the ice horn, measurement indicated the flow was attached to the surface at all angles of attack tested (Figs. 61-69). The velocity profile is that of an attached flow, with the velocity initially smaller than the free-stream value near the wall, gradually recovering to the non-dimensional value of 1.0 away from the surface. This recovery is more pronounced at $\alpha = 0°$. At

the higher test angles, $\alpha = 4^{\circ}$ and 8°, the effect of flow blockage shows itself as a delay in velocity recovery to free-stream values. Ruderich and Fernholz[138] made similar observations during their measurements in the reverse flow region on a bluff-plate/splitter-plate configuration.

4.3.3.1.2. Profiles Inside of the Separation Bubble

The separation bubble is characterized by a region of recirculating fluid. The LDV-measured (u)-component velocity profiles in this region indicated flow reversal near the model surface. The reverse flow was measured with magnitudes reaching as high as 30 percent of the free-stream value (Figs. 61-69). Chandrsuda and Bradshaw[139] documented similar results while obtaining measurements in the reverse flow region downstream of a rearward facing step. In a review article, Simpson[83] pointed out that such large magnitudes of reverse flow velocity are not uncommon in large separation bubbles.

Moving away from the model surface, the reverse flow region is next followed by a shear layer. The shear layer is characterized as a thin layer of rapid velocity increase. This increase is capped by a maximum which is, by convention, denoted the edge of the boundary layer for a given velocity profile. From this location, a gradual recovery to the free-stream value is initiated.

Note that over the separation bubble, the velocity profiles indicated a velocity overshoot at the edge of the boundary layer. This overshoot is indicative of the inviscid velocity at the outer edge of the boundary layer. Such velocity overshoots have also been observed by other researchers experimenting with similar geometries. While investigating the presence of large-scale vortices using multi-sensor hot-wire, Troutt et al.[140] made velocity measurements downstream of a rearward facing step at several locations. Their results in the reverse flow region indicated velocity overshoots similar to those observed in the present study. Similar to the results of the present study, the overshooting velocity profiles had a sharp recovery to the free-stream. Further downstream, near the reattachment location, the velocity profiles indicated a more gentle recovery back to the free-stream value.

Chandrsuda and Bradshaw[139] also presented results from velocity measurements in the separated region downstream of their rearward facing step. Using a cross hot-wire and a pressure probe in the reverse flow region they indicated an overshoot in the mean-velocity profile with a sharp recovery to the free stream near separation and a more gentle recovery to the free stream near reattachment.

Castro and Haque[141] performed measurements with a pulsed-wire anemometer in a turbulent shear layer bounding a separation region. The mean velocity profiles generated from these measurements inside of the recirculating-fluid region indicated the same type of behavior observed from the LDV measurements of the current investigation.

Ruderich and Fernholz[138], carrying out measurements by a hot-wire and pulsed-wire anemometer on a bluff-plate/splitter-plate configuration, measured velocities in the shear flow and reverse flow and the reattachment regions downstream of the plate. Here also they reported velocity overshoots in the separation bubble with sharp recovery near separation and more gentle recovery near reattachment. In their experiments, Ruderich and Fernholz indicate that the maximum velocity remained everywhere higher than the upstream velocity U_∞. This was attributed to the blockage effect of the separation bubble on the flow.

A similar effect was also observed in the present LDV measurements. The effect was particularly pronounced at $\alpha = 8°$, where previous measurements with surface pressure taps had shown the largest size for the separation bubble and therefore the largest blockage effect due to the separation bubble.

4.3.3.1.3. Profiles Downstream of the Separation Bubble

At low angles of attack, the separated flow past the ice horn, reattaches to the surface. This phenomenon has been measured by Bragg et al. on a similar 2-D geometry using the split hot-film method[6-9]. On the 3-D wing of this study, the same phenomenon has been measured through surface pressures and observed through flow visualization results. Similar to a laminar separation bubble, or flow over a rearward-facing step, the flow downstream of reattachment is seen to grow as a wall-

bounded shear layer.

The most notable characteristic observed in the streamwise mean-velocity profiles here was the lack of rapid adjustment to a fully developed turbulent boundary layer. Chandrsuda and Bradshaw[139] also noticed the very slow adjustment of reattached flow to a self-preserving boundary-layer mean-velocity profiles. Bradshaw and Wong[84], reflecting on the results of their own experiments on a rearward-facing step, in addition to those from other experiments on similar obstacles, pointed out that a key flow feature at reattachment is the splitting of the shear layer. In flows involving large separation bubbles, they indicated that the bifurcating shear layer must provide support for the mass balance inside the bubble. Bradshaw and Wong[84] point out that at reattachment, part of the eddies in the shear layer are fed back into the separation bubble in order to sustain it, while the remaining eddies are convected downstream to supply the growing boundary layer. As a result of this *split* at the reattachment location, the profiles will not grow at the same rate as a boundary-layer profile in flows without separation.

As a result of the splitting of the shear layer, the flow downstream of reattachment does not develop at the same rate as a boundary layer without massive separation. This can be readily observed from the velocity profiles downstream of reattachment on the iced-wing's upper surface for $\alpha = 0°$ and 4° (Figs. 61-63,67-69). Further downstream, at $x/c = 0.60$ for $\alpha = 0°$ and 4°, the profiles resemble the fully-developed turbulent shapes on the model at $y/b = 0.470$.

As discussed by Bradshaw and Wong[84], the strength of the perturbation caused by the incoming boundary layer over the rearward-facing step, can be classified by the value of H/δ^*, where H is the step height of the rearward-facing step and δ^* is the thickness of the approach boundary layer. $H/\delta^* \gg 1$ corresponds to an overwhelming perturbation, which is one in which the shear layer changes to one of a different species. Based on a representative ice height on the 15-inch-chord model, Fig. 70, $H/\delta^* \gg 1$ for all three angles. Based on this height, the last measurement station ($x/c = 0.99$) was located approximately 120 and 150 step heights downstream

of separation at $\alpha = 4°$ and $0°$ respectively. At these distances downstream of separation, the profiles had adjusted to the fully developed shapes. In the Bradshaw and Wong experiment, at the last measurement station, 52 step-heights downstream of separation, the profile was very different from that in a normal boundary layer, possibly requiring many more step-heights before returning to the normal state.

4.3.3.2. Evolution of Flow in the Streamwise Direction

The non-streamlined geometry of the ice shape on the leading edge of the iced wing produces a large separation bubble, which varies in size with angle of attack. The size and behavior of this bubble may be evaluated through the separation streamlines, the boundary-layer thicknesses, and transition and reattachment lengths.

4.3.3.2.1. Stagnation and Separation Streamlines

Figures 71 and 72 show the bubble size and shape on the iced-wing upper surface as indicated by the separation and stagnation streamlines at $\alpha = 0°$, 4°, and 8° at $y/b = 0.470$. The stagnation streamline height is merely the height above the surface where the (u) velocity is zero, separating the reverse flow from the flow in the streamwise direction. The separation streamline y_{sep} is the height above the surface such that all of the fluid below is recirculated in the bubble in a two-dimensional steady model. This is found by integrating up from the surface until the mass of the fluid flowing in a reverse sense is equal to that flowing downstream. That is, for a constant-density flow,

$$\int_0^{z_{sep}/c} \frac{u}{U_e}\, d\left(\frac{z}{c}\right) = 0 \qquad (4.1)$$

At $\alpha = 0°$, the bubble is quite large. As the angle increases to $\alpha = 4°$, the bubble size also increases in both the streamwise and vertical directions. The pressure distributions and lift data of Bragg and Khodadoust[13] on this geometry show that the bubble begins to grow rapidly between 6° and 8°. Maximum lift at this wing section was obtained at $\alpha = 9°$ where the upper surface bubble was clearly burst. The

unsteady nature of the bubble near stall has clearly changed the character of these time-averaged calculations at $\alpha = 8°$.

4.3.3.2.2. Boundary Layer Thicknesses

The integrated values of boundary-layer displacement and momentum thickness for y/b = 0.470 on the wing upper surface are given in Fig. 73 and Fig. 74 respectively. The displacement thickness was calculated in the usual way:

$$\delta^*/c = \int_0^{\delta/c} (1-\frac{u}{U_e})\, d(\frac{z}{c}) \tag{4.2}$$

For profiles that may have reverse flow, the momentum thickness is given by

$$\theta/c = \int_0^{\delta/c} |\frac{u}{U_e}| (1-\frac{u}{U_e})\, d(\frac{z}{c}) \tag{4.3}$$

The displacement thickness is seen to grow linearly from x/c=-0.02 to 0.02. The slope increases as the angle of attack increases. For $\alpha = 0°$ and 4°, a maximum value is reached at x/c=0.02. From the 2-D numerical calculations of Crimi and Reeves[72] and Briley and McDonald[74], δ^* reaches its maximum value at the transition point. This is the same location where the constant pressure in the bubble ends and pressure recovery begins. The location of δ^*_{max} seen here does not agree with the transition location. In the analysis of a similar 2-D geometry by Bragg et al.[9], this difference was attributed to the ice shape geometry, Fig. 4. Note that δ^* reaches a maximum value at x/c=0.02 where the ice shape meets the airfoil contour and the height of the surface above the chord line is a local minimum. The δ^* appears to reflect this special geometry and not the usual trends seen in bubbles on smooth airfoils. There is, however, a clear difference between the δ^* development at $\alpha = 4°$ and 8°. As pointed out earlier, the unsteady flowfield on the model upper surface at $\alpha = 8°$ tends to change the character of these time-averaged measurements.

The momentum thickness distribution for y/b=0.470 is shown in Fig. 74. Unlike

the growth pattern in δ^*, here a decrease in θ is observed initially. Compared to δ and δ^*, θ is very small. The velocity development near the surface, therefore, will play an important role in the value of θ. Lack of information in this region will not allow proper calculation of the momentum deficit in the boundary layer at that location. Examination of the velocity profiles indicates that the measurements at $\alpha = 0°$, 4°, and 8° for $x/c = -0.02$ are not close to the surface. Further downstream, a local minimum is reached at $x/c = 0.0$ which is then followed by an increase in θ up to $x/c = 0.02$ at $\alpha = 0°$ and 0.06 at 4°.

Disallowing for the first measurement point, the initial growth in θ is almost linear. For $\alpha = 0°$ and 4°, a local maxima is reached which increases and moves downstream with increasing angle of attack. No clear local maximum is observed in the $\alpha = 8°$ data. In the analysis of similar 2-D data, Bragg. et al.[9] found that the location of the local maximum corresponds to the shear layer transition location as indicated by the measured surface pressures.

4.3.3.2.3. Transition and Reattachment

Briley and McDonald[74] show calculated θ/c values in a laminar separation bubble on a NACA 66_3-018 airfoil. Their data do not show the initial rapid rise in θ/c due to their very different geometry. A slight reduction in θ/c, however, is seen in their results after transition with a rapid rise occurring just before reattachment. The trend in these data near transition is qualitatively similar to the data of Briley and McDonald, and the x/c locations compare well with the 2-D pressure and θ/c data.

After transition, θ/c decreases with x/c, then increases again up to a second local maximum. While the second local maximum is not present in the 2-D data[9] at $\alpha = 4°$, it is present in the 3-D data shown in Fig. 74. Note that the quasi-2D angle of attack for this wing section is 3.4°. Therefore, the effective section angle of attack of the wing centerline is lower than that in the 2-D measurements.

As pointed out earlier, the transition locations deduced from the first maximum in the momentum thickness distribution matched well with those deduced from pressure measurements on the similar 2-D geometry. The local maximum of the data

from the 3-D iced wing are shown in Fig. 75, plotted against the 2-D results of Bragg et al.[9] These compare very well at $\alpha = 0°$ and 4° but not at $\alpha = 8°$ where the character of the bubble has changed. Note that in Fig. 75, the quasi-2D angle of incidence at $y/b = 0.470$ for the finite wing is used ($\alpha = 3.4°$) for comparison against the 2-D data.

An indication of the size of the separation bubble can be found in the reattachment length of the separation bubble. This may be deduced by examination of the measured velocity profiles near the wing surface. At $\alpha = 0°$, $y/b = 0.470$, the LDV measurements indicate flow reattachment occurs between $x/c = 0.06$ and 0.08. The reattachment length is between $x/c = 0.12$ and 0.14 at $\alpha = 4°$.

The second local maximum observed in the momentum thickness distribution at $y/b = 0.470$, in addition to the data from the velocity profiles, has been used to compare the estimated reattachment location to the 2-D results of Bragg et al.[9] These data are shown in Fig. 76. The comparison is very good at $\alpha = 0°$ but the data at $\alpha = 4°$ show that the estimated reattachment points are upstream of their 2-D counterparts. This is the correct trend, since the effective section angle of incidence is lower ($\alpha = 3.4°$) than the geometric incidence of the airfoil used for the 2-D tests. Consequently, shorter separation bubbles and shorter reattachment lengths would be expected. Also note that the estimated reattachments from θ/c are slightly upstream of those estimated from the velocity profiles from the 3-D data alone. Had the velocity profiles been obtained in closer intervals than two-percent chord, a closer match between the reattachment length estimates from LDV measurements and momentum thickness calculations would have been obtained. A similar discrepancy was encountered when analyzing the 2-D data, also shown in the same figure.

At $\alpha = 8°$, the flowfield was observed to be highly unsteady on the model upper surface. Previous pressure measurements on this model[13] had shown that the flow was nearly separated on the model upper surface at $\alpha = 8°$. Flow visualization using surface tufts and surface oil flow yielded similar results qualitatively[17]. The LDV measurements indicated that the mean reattachment length was located beyond 60 percent chord at $y/b = 0.470$.

4.3.3.3. Evolution of Flow in the Spanwise Direction

The finite wing under study was sidewall-mounted from the wind tunnel wall. Due to the presence of the tip on one end, and the wing-root wall juncture on the other, in addition to the induced downwash across the span, three-dimensional effects exist in the flow. The downwash effects have been shown to be negligible except near the wing tip where their effect is the strongest. Indeed comparison of pressure distributions from the model centerline to those on a similar 2-D geometry have shown excellent agreement at matched lift coefficient. The three-dimensional effects have been documented through previous surface oil and surface tuft flow visualization. Pressure measurements obtained from five spanwise tap rows on the same model have also shown the three-dimensional effects near both ends of the model[13,16,17].

Figures 56 and 77 show the florescent surface oil flow at $\alpha = 4°$ and 8° on the iced-wing upper surface, respectively. The presence of the tip-induced vortex flow and the root-induced vortex flow may be observed primarily as a reduction in the separation bubble size in those regions. Figure 78 shows the separation streamlines for $y/b = 0.175$, 0.470 and 0.819 at $\alpha = 0°$. Little effect is observed at $\alpha = 0°$ with the smallest size of the separation bubble calculated near the root. The effect of the wing tip is not evident in the results from the outboard section as the separation streamline from that section and from the wing centerline match closely. At $\alpha = 4°$, Fig. 79, a stronger effect is observed both near the root and the tip. The separation bubble is largest at the midsection measurement location, while the outboard and inboard measurement locations show little difference in the first half of the bubble. Near the reattachment location, however, they appear to be different. The location of bubble reattachment near the wing root has been found to be very sensitive to the effect of the wall boundary-layer interaction with the model[142]. Removing different amounts of mass from the wall boundary layer by a variable suction system resulted in drastic changes in the reattachment location of the separation bubble near the root, as seen through florescent oil flow visualization. The difference between the

reattachment lengths near the root and the tip, however, is too small to be detected through oil flow visualization.

A very strong 3-D effect was observed at $\alpha = 8°$ where separation bubble size was shortened drastically near the wing tip, Fig. 80. The bubble is seen to reattach well ahead of x/c=0.30 at this outboard measurement location. The highly unsteady bubble at the model midsection, however, changed the character of the time-averaged calculations. A similar effect was observed in the pressure measurements of Bragg and Khodadoust[13]. While the wing midsection (y/b=0.497) was found to stall at $\alpha = 9°$, the outboard pressure tap row (y/b=0.852) never did stall. The pressure distribution at $\alpha = 8°$ is shown in Fig. 81. The variation in the extent of the separation bubble at different spanwise locations is evident through the downstream extent of the pressure plateaus. The pressure distribution on the centerline (y/b=0.497) indicates a large separation bubble, while the distribution on the wing outboard (y/b=0.852) indicates a bubble roughly half the size of that on the centerline.

Due to instrument error, LDV measurements obtained near the root at this angle were meaningless near the model surface, and therefore are not presented here. Nevertheless, wall effects at this angle are considered to be important. Computation[5] has shown that the presence of the wall has a significant effect on the lift performance of the finite wing. The effect of the sidewall boundary layer was studied[142] and was shown to drastically alter the flowfield near the model root.

The calculated displacement and momentum thickness for the wing root and wing tip measurement locations are shown in Figs. 82-85. Trends follow those from the centerline results discussed earlier. An interesting feature here is the displacement thickness distribution at $\alpha = 8°$ at the outboard section (y/b=0.819). The calculated separation streamline discussed earlier, indicated a much smaller bubble here compared to the model midsection. The displacement thickness profile follows the same pattern as those for the two lower angles tested. The same pattern is observed in the momentum thickness distribution.

4.3.3.4. Reynolds Number Effects

Measurements on clean airfoils and wings have shown that the performance of some geometries, particularly those which lend themselves to the formation of a leading-edge separation bubble, is dependent on the Reynolds number[38,39]. In order to examine the effect of Reynolds number on the measured velocity profiles on the iced wing, measurements were carried out at $x/c=0.10$ on the model $y/b=0.470$, at $\alpha=4^\circ$ and $\alpha=8^\circ$ over a range of Reynolds numbers.

The effect of Reynolds number on the boundary-layer profile development on the iced wing is shown in Fig. 86 for $\alpha=4^\circ$ and Fig. 87 for $\alpha=8^\circ$. Tunnel speed was adjusted through a variable-frequency drive in order to obtain the desired Reynolds number based on the model chord length. At $\alpha=4^\circ$, Fig. 86, the velocity at the first measurement location near the wall is positive at Re=0.2 million. Therefore, the bubble growth in the chordwise direction has not exceeded $x/c=0.10$ at this Reynolds number. At Re=0.5 million, the chordwise extent of the bubble has clearly exceeded the $x/c=0.10$ station on the model surface. At this Reynolds number and those higher, the most negative flow velocity was recorded at the first measurement location, 0.050 inches (1.27 mm) above the wing surface.

Increasing the Reynolds number causes an increase in the reverse-flow magnitude up to Re=1.5 million, where the magnitude of reverse flow at the first measurement location decreases in comparison with those measured at lower Reynolds numbers. This behavior is consistent with the physical model of the separation bubble. A region of slower moving fluid near the beginning of the bubble is followed by a region of faster moving fluid near the end of the bubble, where reattachment occurs. As the Reynolds number increases, the reattachment location approaches $x/c=0.10$ and passes it. Consequently, a rise in the reverse-flow magnitude, followed by a subsequent drop, may be expected.

Increasing the Reynolds number caused little appreciable change in the boundary-layer thickness and the slope of the shear layer. The displacement thickness, however, was calculated to nearly double in value from 0.0124 at Re=0.2 million to

0.0208 at 1.5 million. The bubble height z_{sep}/c almost triples in magnitude, from 0.0067 at Re=0.5 million to 0.0183 at 1.5 million. An additional noteworthy feature occurs at the edge of the boundary layer. Here, at Re=0.2, 0.5 and 1.0 million, the edge velocity approaches the free-stream velocity very rapidly. At Re=1.2 and 1.5 million, the edge velocity first overshoots the free-stream value and then gradually recovers to the free-stream. This is typical of wall-bounded flows involving large acceleration near the surface.

At $\alpha = 8°$, Fig. 87, the reverse-flow magnitude does not change appreciably with change in the Reynolds number. The boundary-layer thickness remains approximately constant to within ±5 percent. The displacement thickness grows by 10 percent and the bubble height grows by 15 percent at this station when the Reynolds number is increased from 0.2 million to 1.5 million. Also noted in the $\alpha = 8°$ data is a change in the shear-layer slope with increasing Reynolds number, indicating a decrease in the thickness of the shear layer at this station.

Note that at $\alpha = 8°$, x/c=0.10 corresponds to a region of slow-moving fluid well upstream of the reattachment in the bubble. At $\alpha = 4°$, however, x/c=0.10 is near reattachment. According to the physical model of the bubble, high velocities and turbulence intensities associated with the reattachment process exist in this region. Consequently, due to the location in each bubble where the measurements were taken, variation in the free-stream Reynolds number may not affect the $\alpha = 8°$ measurement as profoundly as the measurement at $\alpha = 4°$.

4.3.3.5. Time-Dependent Measurement Results

The time-dependent features of the flow over the iced finite wing are reported and discussed here. Since the LDV measurements comprise an ensemble of velocities due to individual particles, it is possible to extract information such as the shedding frequency through the time-record of the data in the shear layer, and turbulence quantities through the various moments of the flow. Due to the quantity of the available data, only data at $\alpha = 4°$ on the wing centerline in the vicinity of the separation bubble are discussed and presented here.

4.3.3.5.1. Histogram Distributions

The probability distribution of the ensemble-averaged LDV measurements can be examined through a histogram for the data at each location where measurements were made. Examination of the velocity distributions reveals information about the character of the flow at each location.

The velocity histograms for the centerline (u)-component at x/c=0.08 on the iced wing upper surface at $\alpha = 4^{\circ}$ are shown in Fig. 88. At the first two measurement locations shown, z/c=0.00332 and 0.00666, the histograms indicate the fluid is predominantly moving in the upstream direction. Intermittency factor for these two locations are 0.0306 and 0.0635, indicating that the fluid moves in the upstream direction 97 percent and 94 percent of the time, respectively. This shear layer is characterized by a region of rapid changes in velocity and a high level of turbulence. This is observed through the histogram distributions as the LDV measurement volume traverses away from the model surface. As the measurement volume traverses through the separation bubble, the histogram spreads out, covering a wide range of velocities. At z/c=0.0133, the recorded average velocity is -4.62 m/s. The turbulence intensity, however, is at the highest value throughout this profile. The measured turbulence intensity, based on the free-stream velocity is 30.6 percent. The intermittency factor is at 0.34, indicating the flow is in the upstream direction 66 percent of the time.

The broad double-peaks observed in the velocity histograms at z/c=0.0133 and z/c=0.01994 are indications of the flapping of the shear layer. At the outer edge of the shear layer, z/c=0.02991, the histogram indicates uniform flow which, with further traverse away from the surface, moves towards the free-stream value. Turbulence intensity also decreases from its highest value of 30.6 percent in the middle of the shear layer to 5.7 percent at the last measurement location.

The histograms described above were obtained for each velocity profile. A more detailed look at the evolution of the turbulence quantities derived from these histograms, particularly near reattachment of the separation bubble may produce

some insight into the character of the shear layer bounding the recirculation region. The intermittency values for several velocity profiles are shown in Fig. 89. The profiles range from x/c=0.02 to 0.14 in 0.02 intervals. γ_p=0 corresponds to fluid moving upstream 100 percent of the time, while γ_p=1 indicates fluid motion in the downstream direction 100 percent of the time. At the first location shown, x/c=0.02, γ_p has values near zero the furthest away from the model surface. The location x/c=0.02 is just downstream of the ice shape, Fig. 4, and the large occurrence of reverse-flow up to z/c=0.0199 is an indication of the size of the separation bubble at this location. At the downstream measurement locations, γ_p retains its near-zero value, indicating large occurrences of reverse flow.

Near reattachment, the separation streamline at α=4°, y/b=0.470, is curved toward the model surface, Fig. 71. This is an indication of the shear layer colliding with the model surface. As a result, fluid moving in the streamwise direction is brought closer to the surface. A decrease in the occurrence of reverse-flow, combined with the presence of streamwise flow, closer to the wing surface is observed in the γ_p distributions of Fig. 89 as the reattachment location is approached. Note that velocity magnitude may not be inferred from γ_p; only the velocity direction can be determined.

The mean results from the LDV measurements indicate that reattachment occurs between x/c=0.12 and 0.14. The profiles constructed from γ_p values for these x/c locations are shown in Fig. 89. While γ_p has increased markedly compared to upstream values, these profiles indicate that even at x/c=0.14 there is still some reverse-flow present. The presence of reverse flow where the mean results have shown reattachment, is an indication of *flapping* in the shear layer reattachment location. Due to this flapping motion, reattachment moves upstream and downstream of the mean location. Similar phenomena have been reported by other researches[143-145] while analyzing the time-dependent behavior of the shear layer over similar geometries. The frequency of the flapping motion can not be deduced from the present measurements. More detailed velocity surveys near the model surface

in the vicinity of the mean reattachment location can give useful information regarding this unsteady behavior. Surface-mounted sensitive pressure probes[144] and thermal tufts[145] have also been used to deduce this information. A recent technique, which takes advantage of a phase reversal phenomena[77,78] in detecting turbulent reattachment in laminar separation bubbles may be used here to infer the dynamic behavior of the bubble near reattachment.

4.3.3.5.2. Turbulence Intensities

The turbulence intensities in the shear layer are at their maximum values in the middle of the layer, where the largest velocity gradients exist. These values, made non-dimensional with respect to the free-stream velocity, are shown in Fig. 90 for the iced wing at $\alpha = 4°$, $y/b = 0.470$. At all x/c stations shown, maximum turbulence intensity occurs away from the model surface. At $x/c = 0.02$, this location is the farthest up from the model surface compared with all other x/c locations downstream. This once again indicates the height of the separated shear layer, which at $x/c = 0.02$, has just passed over the ice horn.

The height of the maximum intensity location gradually decreases toward the model surface with increasing downstream distance. The slopes of the mean velocity profiles in the reverse-flow region aft of the ice horn show that the shear layer bounding the recirculating fluid has a very small thickness. The reduction of the height where the maximum turbulence intensity (middle of the shear layer) occurs with increasing x/c, therefore, is clearly an indication of the shear layer colliding with the model surface.

Note that prior to reattachment, $x/c = 0.14$, the maximum value of turbulence intensity made non-dimensional with respect to the free-stream velocity, is between 30 and 35 percent. In a review of separated flow phenomenon, Simpson[83] points out that this is a common value for flows over rearward-facing steps. This is 10-15 percent higher than typical values for plane mixing layers. The high turbulence level, similar to that found behind a backward facing step, is believed to be largely due to a low frequency vertical or flapping motion of the reattaching shear layer[83,146].

Contours of the streamwise turbulence intensity, made non-dimensional with respect to the free-stream velocity, in the vicinity of the separation bubble at $\alpha = 4^{\circ}$ are plotted in Fig. 91. The stagnation and separation streamlines, calculated from the mean velocity profiles at this angle of attack are also shown in the same figure. In the analysis of data from other's, Eaton and Johnston[85] point out that the turbulence intensity reaches a peak value very near the reattachment location, then decays rapidly.

A similar trend is observed in the data plotted in Fig. 91. Two peaks for the maximum intensity are evident in this figure; one near the middle of the separation bubble where the separation streamline experiences a change in slope, and one near reattachment. Just ahead of reattachment, the turbulence intensity decays rapidly. The locus of points where the turbulence intensity is a maximum dips toward the wall in the reattachment zone. This result is consistent with that from other researchers' findings[85,146]. Interestingly, the location of the first peak in maximum turbulence intensity (x/c=0.06) coincides with the transition location deduced from the momentum thickness distribution.

4.3.3.5.3. Reynolds Normal Stresses

According to Kiya and Sasaki[147] the locus of $\overline{u'^2_{max}}$ is interpreted as the center of the shear layer. Contours for the Reynolds normal stress $\overline{u'^2}$ in the vicinity of the ice-induced separation bubble are shown in Fig. 92. The stagnation and separation streamlines, which were derived from the mean velocity profiles discussed earlier, are also shown in this plot. The separation streamline, which defines the upper bound of the separation bubble, passes through the locations where the Reynolds normal stresses are at their maximum. Note that this trend is also evident in the streamwise turbulence intensity contours, shown in Fig. 91. This is to be expected since the Reynolds normal stress $\overline{u'^2}$ is simply the square of the streamwise turbulence intensity.

Kiya and Sasaki[147] reported similar behavior in a separation bubble formed along the sides of a blunt flat plate. Ruderich and Fernholz[138] have also obtained similar

conclusions from analysis of their data over a bluff plate attached to a splitter plate in its plane of symmetry. In both analyses, however, the similarity in location of $\overline{u'^2_{max}}$ and the separation streamline ends beyond the middle of the separation bubble. A similar pattern is observed in the present data. The separation streamline, however, continues to coincide with the locus of $\overline{u'^2_{max}}$ well past the middle of the separation bubble. It begins to deviate from the locus of $\overline{u'^2_{max}}$ near reattachment. Note that as the reattachment location is approached, $\overline{u'^2}/U_\infty^2$ approaches zero. A rapid decay of Reynolds normal stresses within the reattachment zone has been observed by other researchers studying flow over similar geometries[83,139,148].

As evidenced from the present LDV measurements, the following physical description may help in understanding the details of the turbulent transport in the vicinity of the separation bubble. The rapid decay of turbulence quantities near the reattachment zone in flows over similar geometrical obstacles has been attributed to the destruction of large eddies in this region. Bradshaw and Wong[84] were the first to conclude that the strong streamwise pressure gradients, in addition to the imposition of the normal velocity constraint near the wall (w=0), cause the large eddies to be torn in two in the reattachment zone. The reduction in length scale would therefore be responsible for the decrease in the level of turbulence quantities.

CHAPTER V

SUMMARY, CONCLUSIONS AND RECOMMENDATIONS

The flowfield on the upper surface of a semispan rectangular wing with a simulated glaze ice accretion was mapped with a laser Doppler velocimeter. Detailed measurements of the flow velocities, particularly in the vicinity of the ice-induced separation bubble, were performed in three spanwise locations on the finite wing. The results from this work provide information about the iced-wing flowfield which was not available prior to this research.

The massive separation bubble aft of the upper surface ice horn was found to behave in a manner similar to laminar separation bubbles and separation bubbles aft of rearward-facing steps. The bubble size was found to have little variation with spanwise location at low angles of attack. Close to the surface, and in the shear layer region, the LDV-measured velocity profiles were found to be in very good agreement with 2-D split film-measured profiles. Reasonable agreement was obtained from the comparison of the LDV-measured profiles with predictions from Navier-Stokes computations. These major results, in addition to other results, are given below in further detail.

5.1. Summary and Conclusions

Velocity measurements were carried out on a semispan, reflection-plane, rectangular wing at Re = 1.5 million and M = 0.12 in order to study the effects of an in-flight ice accretion on the flowfield. The wing was tested in two configurations: clean and iced. In the clean configuration, the wing had a NACA 0012 cross-section with a constant chord from root to tip. The iced wing had a similar configuration, except at the leading edge where a simulation of a glaze ice accretion was mounted

in order to study the effects of the ice shape on the flowfield.

A laser Doppler velocimeter (LDV) was used as the primary measurement instrument. The non-intrusive nature of the LDV allowed the study of the complex flowfield aft of the ice horns on the iced wing. The LDV was also used to map the flowfield inside of the tunnel prior to model installation. The velocity survey, carried out at a plane near the beginning of the test section, revealed a nearly constant velocity in that plane. Hot-wire measurements at the center of the tunnel indicated average free-stream turbulence value of 0.07 percent at the test Reynolds number.

5.1.1. Clean Wing

Velocity surveys were performed on the midsection of the clean wing upper and lower surfaces at $\alpha = 0°$, 4°, and 8°. A trip strip was used on both surfaces at the 5 percent chord location along the span of the wing. Comparison of measurement with inviscid computation showed excellent agreement away from the model surface. Near the model surface, differences exist due to the inviscid code's inability to predict viscous effects.

Velocity histograms were presented for representative locations on the wing. Near the leading edge, double-peaked distributions were observed in the histograms. The trend in these data matched those from a similar experiment[119]. The complete set of mean velocity profiles from LDV measurements, along with comparison with computation, are given in Appendix 2.

5.1.2. Iced Wing

The streamwise component of velocity from the LDV measurements was presented for the iced-wing upper surface. The surveys were carried out at the wing midsection, as well as one outboard section and one inboard section. The wing was tested at $\alpha = 0°$, 4°, and 8°.

5.1.2.1. Comparison with Other Measurements and Theory

Comparison with split-film measurements on a similar 2-D model showed excellent agreement near the model surface, through the shear layer up to the location of maximum velocity in the boundary layer. A discrepancy existed at this

location between the LDV-measured profiles and those from the split-film measurements. The differences were attributed to several plausible factors. No attempts were made, however, to further investigate this discrepancy, primarily because measurement results from both instruments were in good agreement in the reverse-flow region and the shear layer.

The mean velocity profiles from the LDV measurements were compared to the Navier-Stokes computations performed on a coarse grid[137]. The computation predicted reverse flow where the LDV measurements also indicated that reverse flow was present on the finite wing. The profile shapes, however, disagreed with those from LDV measurements. The mismatch between measurement and computation was attributed to the lack of fine grid resolution in the vicinity of the boundary layer, in addition to inadequate turbulence modeling . The code, however, has been able to predict lift and moment distributions reasonably well, with only mild success in prediction of drag near stall. Near the root and wing tip, where strong three-dimensional effects existed, both measurement and computation showed a shortened separation bubble.

5.1.2.2. Mean Measurement Results

The mean velocity profiles on the finite wing were categorized in three classes:

1. Profiles upstream of the separation bubble: These profiles indicated attached flow on the upper surface, and behaved similar to the approach boundary layer in experiments with flows over similar obstacles. Momentum thickness calculations indicated that these profiles were laminar.
2. Profiles inside the separation bubble: These profiles generally had an inverse hyperbolic tangent shape, typical of velocity profiles with reverse flow. The shear layer was characterized by a very thin region of rapid velocity change. All profiles in this region indicated an overshoot when the maximum velocity was attained. The overshoot was attributed to the blockage effect of the separation bubble. Near the beginning of the bubble, the overshoots were followed by a sharp recovery to the free stream while towards the end of the bubble, a more gentle

recovery to the free stream was observed.

3. Profiles downstream of the separation bubble: These profiles indicated attached flow at $\alpha = 0°$ and 4°. The profiles, however, did not reach the shape of fully-developed turbulent profiles until well downstream of reattachment. This, as explained by Bradshaw and Wong[84], is believed to be due to the destruction of large eddies in the shear layer near reattachment.

Bubble size and extent were found to be a function of angle of attack. At $\alpha = 8°$, where previous pressure measurements had indicated the wing was near stall, the unsteady flowfield changed the character of the time-averaged results. This was evidenced by the momentum and displacement thickness distributions, and the separation and stagnation streamlines. The calculation of the stagnation and separation streamlines showed the bubble size and extent to grow with increasing angle of attack.

Transition, as detected from momentum thickness calculations, matched well with results from 2-D data at matched angle of attack. The agreement at $\alpha = 0°$ was better than at $\alpha = 4°$, where transition from 3-D data occurred slightly upstream of the 2-D value. This was thought to be due to the effective section incidence of the finite wing being lower ($\alpha = 3.4°$) than the incidence angle at which the 2-D data were taken.

The bubble reattachment location was found to be a function of angle of attack and spanwise location. The reattachment distance for the upper surface bubble increased with increasing angle of attack at all spanwise stations. At $\alpha = 8°$, the mean results indicated reattachment beyond 60 percent chord.

Spanwise effects were negligible at $\alpha = 0°$, where little change in the bubble size was noticed at the three spanwise measurement locations. At $\alpha = 4°$, a shorter separation bubble was observed near the wing tip and root compared to the wing midsection. This result was in agreement with surface pressure measurements and fluorescent oil flow visualization[13,17]. At $\alpha = 8°$, the outboard separation bubble reduced sharply in size, primarily due to the tip-induced vortex flow.

The effect of Reynolds number was examined on the boundary-layer profiles at $x/c=0.10$ for $\alpha=4^\circ$ and 8° at $y/b=0.470$ on the semispan wing. A strong dependence of the reattachment length on the Reynolds number was deduced for the $\alpha=4^\circ$ case. The mean results at $\alpha=8^\circ$ did not indicate this strong dependence. However, a thickening of the shear layer was observed with decreasing Reynolds number.

The difference was attributed to the location of measurement inside the separation bubble. At $\alpha=4^\circ$, $x/c=0.10$ was near the mean reattachment location, where a high turbulence intensity existed. The measurement location $x/c=0.10$ at $\alpha=8^\circ$, however, was well upstream of the flow reattachment, where flow fluctuations were not as strong as those near reattachment.

5.1.2.3. Turbulence Quantities

The streamwise turbulence intensity and Reynolds normal stress, in addition to the intermittency factor γ_p, were studied at $\alpha=4^\circ$ on the wing midsection in the vicinity of the bubble. The γ_p distribution clearly indicated the extent of the reverse flow in the separation bubble. Also, γ_p revealed the presence of reverse flow at the location of mean reattachment. This gave an indication of the unsteady reattachment process. The flapping of the shear layer at reattachment has been reported by others investigating similar flows.

Analysis of turbulence intensities on the wing midsection at $\alpha=4^\circ$ showed values as large as 35 percent occurring in the shear layer. Peak values of turbulence intensity were measured near the middle of the bubble and also near the bubble reattachment followed by a rapid decay. The locus of maximum turbulence intensity dipped toward the wall in the reattachment zone. These results were in agreement with those from studies over rearward-facing steps. The location of the first peak coincided with the transition location, as determined from the momentum thickness distribution.

The Reynolds normal stress results indicated that the center of the shear layer, where $\overline{u'^2}$ was a maximum, matched well with the separation streamline defining the outer bound of the separation bubble. A rapid decay of the Reynolds normal

stress was observed near the reattachment zone, again in agreement with results from flows over similar obstacles.

The streamwise turbulence intensity and the Reynolds normal stress represent the same type of information, since the latter is just the square of the former. Both forms, however, were presented in order to provide a one-to-one comparison with the information available in the literature.

These results clearly indicate that the separation bubble aft of the ice horn behaved similar to those found downstream of many generic obstacles such as rearward-facing steps or bluff flat plates in the free stream. The transition characteristics, as determined from momentum thickness distributions, indicated that the massive separation bubble also had features that are peculiar to laminar separation bubbles. The data provided here may be used to verify computational methods currently in development for prediction of performance degradation of iced surfaces.

5.2. Recommendations

The following recommendations are given as possible avenues in which the flowfield about the iced wing can be further explored:

1. Flow over rearward-facing steps and laminar separation bubbles were found to be very similar to the flow under study here. Studying directions and trends from these basic geometries may lead to improvements in the modelling of the flowfield about wings with glaze ice accretion.

   The separation and dividing streamline in the separation bubbles over basic geometries have been suggested as important regions of the flow for further study[138]. More measurements along these two streamlines have been recommended for flows over similar but basic geometries. Doing the same could prove useful here.

2. The present experiment has been able to successfully document the (u)-velocity on the iced wing. The data obtained for the (w)-velocity, however, due to very low data rate, was sparsely distributed in the flowfield, and therefore

proved inadequate for the determination of the full velocity vector in the majority of the flow measurement locations. Information from this component, in addition to the (v)-velocity, will be particularly useful for further exploration of the iced-wing aerodynamics using computational tools.

3. Furthermore, comparison with the currently available computational results indicated that a finer grid resolution is required to capture the flowfield details. Unstructured grids may provide an alternate solution for locally improving the grid resolution. An improved turbulence model may increase the accuracy of the numerical predictions.

4. Accurate description of the near-wake region of a lifting body with turbulent separation is very important to the overall drag prediction. The flow structure in the vicinity of the wing trailing edge can be resolved with the LDV instrument. This will aid in verifying the drag prediction capabilities of the computational models.

5. Reynolds number was noted to affect the velocity profile. Measurements carried out at one location indicated reattachment was affected by a variation in Reynolds number. Complete survey of the separation bubble could help clarify this dependency.

6. The present study has provided velocity measurements downstream of a smooth simulated ice shape. The effect of surface roughness, however, is a subject of great interest and needs to be examined in detail. Previous measurements using surface pressures and a force balance[13,18] have indicated that roughness affects the aerodynamic performance of the finite wing with simulated glaze ice. The effects of roughness on the flowfield, however, are largely unknown.

Additionally, the effect of the presence of roughness needs to be distinguished from the presence of ice. Earlier measurements have indicated that the effect of roughness on the clean wing is different from the effect of an ice shape[18]. Since roughness greatly affects the state of the boundary layer, mapping the flowfield

in the vicinity of the wing with roughness should provide a wealth of information on the effect of roughness on the wing flowfield.

7. The present work has been a part of an extensive effort which has been sponsored by both government and industry. A wealth of data in terms of lift and drag penalties due to ice has already been complied and published. The results from the present work augment this data with velocities and information previously not available. Analysis of the performance degradation due to other ice shape geometries, however, demands equal attention. These new shapes may be due to different accretion conditions or different geometries, including the effect of wing sweep.

8. The measurements carried out on the baseline geometry revealed bimodal distributions of velocity near the wing leading edge. This hinted at the presence of an oscillating shear layer near the wing leading edge. While the results appear to be in agreement with those from a similar study[119], there are also indications that what is perceived as unsteadiness in the flow may be due to other elements. The leading edge of the NACA 0012 wing could be further studied in order to determine whether the unsteady phenomena alluded to here is a fluid dynamic event, or one which is merely related to the particle dynamics peculiar to the LDV.

REFERENCES

1. Cole, J., and Sand, W., " Statistical Study of Aircraft Icing Accidents," AIAA-91-0558, paper presented at the 29th Aerospace Sciences Meeting, January 7-10, 1991, Reno, Nevada.

2. Mason, B. J., *The Physics of Clouds*, 2nd edition, Clarendon Press, Oxford, CT, 1971.

3. Bragg, M. B., "Rime Ice Accretion and Its Effect on Airfoil Performance," Ph.D. Dissertation, The Ohio State University, Columbus, Ohio, 1981.

4. Shaw, R. J., "NASA's Aircraft Icing Analysis Program," NASA TM-88791, Sept. 1986.

5. Kwon, O. J., and Sankar, L. N., "Numerical Investigation of Performance Degradation of Wings and Rotors Due to Icing," AIAA-92-0412, paper presented at the 30th Aerospace Sciences Meeting, Reno, Nevada, January 6-9, 1992.

6. Bragg, M. B., and Coirier, W. J., "Aerodynamic Measurements of an Airfoil with Simulated Glaze Ice," AIAA-86-0484, paper presented at the 24th Aerospace Sciences Meeting, Reno, Nevada, Jan. 6-9, 1986.

7. Bragg, M. B., and Spring, S. A.,"An Experimental Study of the Flow Field About an Airfoil with Glaze Ice," AIAA-87-0100, paper presented at the 25th Aerospace Sciences Meeting, Reno, Nevada, January 12-15, 1987.

8. Bragg, M. B., and Khodadoust, A., "Experimental Measurements in a Large Separation Bubble Due to a Simulated Glaze Ice Accretion," AIAA-88-0116, paper presented at the 26th Aerospace Sciences Meeting, Reno, Nevada, January 11-14, 1988.

9. Bragg, M. B. ,Khodadoust, A., and Spring, S. A., "Experimental Measurements in a Large Leading-Edge Separation Bubble Due to a Simulated Airfoil Ice Accretion," *AIAA Journal*, Vol. 30, No. 6 June 1992, pp. 1462-1467

10. Sankar, L. N., Wu, J. C., and Kwon, O. J., "Development of Two- and Three-Dimensional Navier-Stokes Solvers for Aircraft Icing Studies," presented at the Annual Airfoil Performance-in-Icing Workshop, NASA Lewis Research Center, Cleveland, Ohio, July 25, 1988.

11. Kwon, O., and Sankar, L., "Numerical Study of the Effects of Icing on Finite Wing Aerodynamics," AIAA-90-0757, paper presented at the 28th Aerospace Sciences Meeting, Reno, Nevada, January 8-11, 1990.

12. Sankar, L., and Kwon, L., "Numerical Studies of the Effects of Icing on Fixed and Rotary Wing Aircraft Aerodynamics," presented at the Airfoil-in-Icing Workshop, Nasa Lewis Research Center, Sept. 1990.

13. Bragg, M. B., and Khodadoust, A., "Effect of Simulated Glaze Ice On a Rectangular Wing," AIAA-89-0750, paper presented at the 27th Aerospace Sciences Meeting, Reno, Nevada, January 9-12, 1989.

14. Khodadoust, A., and Bragg, M. B., "Measured Aerodynamic Performance of a Swept Wing With a Simulated Glaze Ice Accretion," AIAA Paper 90-0490, 1990.

15. Bragg, M., Khodadoust, A., Soltani, R., Wells, S., and Kerho, M., "Effect of Simulated Ice Accretion on the Aerodynamics of a Swept Wing," AIAA-91-0442, paper presented at the 29th Aerospace Sciences Meeting, Reno, Nevada, Jan. 7-10, 1991.

16. Bragg, M., Khodadoust, A., Soltani, R., Wells, S., and Kerho, M., "Aerodynamic Measurements on a Finite Wing With Simulated Ice", AIAA-91-3217, paper presented at the 9th Applied Aerodynamics Meeting, Baltimore, Maryland, Sep. 23-25, 1991.

17. Bragg, M. B., Khodadoust, A., Kerho, M., "Aerodynamics of a Finite Wing With Simulated Ice," paper presented at the 5th Symposium on Computational and Physical Aspects of Aerodynamic Flows, Cebeci, T., ed., Long Beach, California, January 1992.

18. Khodadoust, A., Bragg, M., Kerho, M., Wells, S., and Soltani, M., "Finite Wing Aerodynamics with Simulated Glaze Ice," AIAA-92-0414, paper presented at the 30th Aerospace Sciences Meeting, Reno, Nevada, Jan. 6-9, 1992.

19. Khodadoust, A., Bragg, M., and Kerho, M., "LDV Measurements on a Rectangular Wing with a Simulated Glaze Ice Accretion," AIAA-92-2690, paper presented at the 10th Applied Aerodynamics Meeting, Palo Alto, California, June 22-24, 1992.

20. Carroll, T. C. and McAvoy, W. H., "Formation of Ice on Airplanes," *Airway Age*, Sept. 1928, pp. 58-59.

21. Bleeker, W., "Einige Bemerkungen uber Eisanatz an Flugzeugen," *Meteorologishe Zeitschrift*, Sept. 1932, pp. 349-354 (also available as NACA TM no. 1027).

22. Jacobs, E. N., "Airfoil Section Characteristics as Affected by Protuberances," NACA Report No. 446, 1932.

23. Jones, R., and Williams, D. H., "The Effect of Surface Roughness on the Characteristics of the Aerofoils NACA 0012 and RAF 34," British ARC, R&M No. 1708, 1936.

24. Gulick, B. G., "Effects of Simulated Ice Formation on the Aerodynamic Characteristics of an Airfoil," NACA WR L-292, 1938.

25. Preston, G. M., and Blackman, C. C., "Effect of Ice Formations on Airplane Performance in Level Cruising Flight," NACA TN-1598, 1948.

26. Gray, V. H., "Prediction of Aerodynamic Penalties Caused by Ice Formation on Various Airfoils," NASA TN D-2166, February 1964.

27. Bragg, M. B., and Shaw, R. J., "The Effect of Ice Accretion on Aircraft Aerodynamics," unpublished manuscript, Aug. 1990.

28. Reinmann, J. J., Shaw, R. J., and Ranaudo, R. J., "NASA's Program on Icing Research and Technology," NASA TM-101989, May 1989.

29. Shaw, R. J., Sotos, R. G., and Solano F. R., "An Experimental Study of Airfoil Icing Characteristics," NASA TM 82790, 1982.

30. Ingleman-Sundberg, M., Trunov, O. K., and Ivaniko, A., "Methods for Prediction of the Influence of Ice on Aircraft Flying Characteristics," Report JR-1, a joint report from the Swedish-Soviet Working Group on Flight Safety, 6th Meeting, 1977.

31. Bragg, M. B., Gregorek, G. M., and Shaw, R. J., "Wind Tunnel Investigation of Airfoil Performance Degradation Due to Icing," AIAA-82-0582, 1982.

32. Flemming, R. J., and Lednicer, D. A., "High Speed Ice Accretion on Rotorcraft Airfoils," NASA CR-175092, 1985.

33. Korkan, K. D., Dadone, L., and Shaw, R. J., "Performance Degradation of Propeller/Rotor Systems Due to Rime Ice Accretions," AIAA paper 82-0286, Jan. 1982.

34. Korkan, K. D., Dadone, L., and Shaw, R. J., "Performance Degradation of Helicopter Rotor Systems in Forward Flight Due to Rime Ice Accretion," *Journal of Aircraft*, Vol. 22, No. 8, Aug. 1985, pp. 713-718.

35. Miller, T. L., and Korkan, K. D., "Analytical Determination of Propeller Performance Degradation Due to Ice Accretion," AIAA-85-0339, Jan. 1985.

36. Potapczuk, M. G. and Berkowitz, B. M., "An Experimental Investigation of Multi-Element Airfoil Ice accretion and Resulting Performance Degradation," NASA TM-101441, Jan. 1989.

37. Bragg, M. B., and Coirier, W. J., "Detailed Measurements of the Flow Field in the Vicinity of an Airfoil with Glaze Ice", AIAA-85-0409.

38. Lynch, F. T., Valarezo, W. O., and McGhee, R. J., "The Adverse Aerodynamic Impact of Very Small Leading-Edge Ice (Roughness) Buildups on Wings and Tails," AGARD-CP-496, 1991, pp. 12.1-12.8.

39. Morgan, H. L., Ferris, J. C., and McGhee, R. J., "A Study of High-Lift Airfoils at High Reynolds Numbers in the Langley Low-Turbulence Pressure Tunnel," NASA TM-89125, July 1987.

40. Ruff, G. A., and Berkowitz, B. M., "User's Manual for the NASA Lewis Ice Accretion Prediction Code (LEWICE)," NASA CR-185129, May 1990.

41. Zaman, K. B. M. Q., McKinzie, D. J. and Rumsey, C. L., "A Natural Low Frequency Oscillation of the Flow Over an Airfoil Near Stalling Conditions," *Journal of Fluid Mechanics*, Vol. 202, 1989, pp. 403-442.

42. Zaman, K. B. M. Q. and Potapczuk, M. G., "The Low Frequency Oscillation in the Flow Over a NACA 0012 Airfoil with an Iced Leading Edge," *Proceedings of the Symposium on Low Reynolds Number Aerodynamics*, Springer-Verlag, 1989, pp. 271-282.

43. Khodadoust, A., "A Flow Visualization Study of the Leading Edge Separation Bubble on a NACA 0012 Airfoil with Simulated Glaze Ice," M.S. Thesis, Ohio State University, June 1987, also NASA CR-180846.

44. Bragg, M. B., "An Experimental Study of the Aerodynamics of a NACA 0012 Airfoil with a Simulated Glaze Ice Accretion, Vol. I," The Ohio State University, AARL TR-8602, November 1986, also NASA CR-179571.

45. Bragg, M. B., "An Experimental Study of the Aerodynamics of a NACA 0012 Airfoil with a Simulated Glaze Ice Accretion, Vol. II," University of Illinois at Urbana-Champaign, Department of Aeronautical and Astronautical Engineering Report, June 1990, also to be published as NASA CR.

46. Potapczuk, M. G. and Gerhart, P. M., "Progress in the Development of a Navier-Stokes Solver for Evaluation of Iced Airfoil Performance," AIAA-85-0410, Jan. 1985.

47. Potapczuk, M. G., "Numerical Analysis of a NACA 0012 Airfoil with Leading Edge Ice Accretions," AIAA-87-0101, Jan. 1987.

48. Wu, Jiunn-Chi, "Numerical Studies of Turbulent Separated Flows," paper presented at the Aircraft Performance-in-Icing Workshop at NASA Lewis Research Center, Cleveland, Ohio, August 1987.

49. Potapczuk, M. G., " Navier-Stokes Analysis of Airfoils With Leading Edge Ice Accretions," Ph.D. Dissertation, The University of Akron, Akron, OH, 1989.

50. Caruso, S. C., "Development of na Unstructured Mesh/Navier-Stokes Methods for Aerodynamics of Aircraft with Ice Accretion," AIAA-90-0758, Jan. 1990.

51. Caruso, S. C. and Farshchi, M., "Automatic Grid Generation for Iced Airfoil Flowfield Predictions," AIAA-92-0415, Jan. 1991.

52. Cebeci, T., "Interactive Boundary-Layer Analysis of Iced Airfoils," paper presented at the Airfoil Performance-in-Icing Workshop, NASA Lewis Research Center, July 17-18, 1986.

53. Cebeci, T., "The Calculation of Flow Over Iced Airfoils," AIAA-88-0112, Jan. 1988.

54. Cebeci, T., Clark, R. W., Chang, K. C., Halsey, N. D. and Lee, K., "Airfoils with Separation and the Resulting Wakes," *Journal of Fluid Mechanics*, Vol. 163, 1986, p. 323.

55. Potapczuk, M. G., "LEWICE/E: An Euler Based Iced Accretion Code," AIAA-92-0037, also NASA TM-105389, Jan. 1992.

56. MacArthur, C. D., Keller, J. L. and Leurs, J. K., "Mathematical Modeling of Ice Accretion on Airfoils," AIAA-82-0284, Jan. 1982.

57. Shin, J., Berkowitz, B., Chen, H. and Cebeci, T., "Prediction of Ice Shapes and Their Effect on Airfoil Performance," AIAA-91-0264, also NASA TM 103701, Jan. 1991.

58. *Proceedings of the International Aircraft Icing Technology Workshop*, NASA Lewis Research Center, Cleveland, Ohio, Nov. 4-6, 1987.

59. Leckman, P. R., "Qualification of Light Aircraft for Flight in Icing Conditions," Society of Automotive Engineers, Paper No. 710394, 1971.

60. Loschkan, B. and Jesse, R. E., "Ice Accretion and Its Effects on Aerodynamics of Unprotected Aircraft Components," AGARD AR-127, 1977, pp.4.1-4.22.

61. Ingleman-Sundberg, M. and Trunov, O. K., "Wind Tunnel Investigation of Hazardous Tail Stall Due to Icing," Report JR-2, a joint report from the Swedish-Soviet Working Group on Flight Safety, 1977.

62. Trunov, O. K., and Ingleman-Sundberg, M., "On the Problem of Horizontal Tail Stall Due to Icing," Report JR-3, a joint report from the Swedish-Soviet Working Group on Flight Safety, 1985.

63. Brumby, R. E., " The Effect of Wing Ice Contamination on Essential Flight Characteristics," Douglas Paper 8501, also AGARD-CP-496, 1991, pp. 2.1-2.4,presented at the 68th AGARD Fluid Dynamics Panel Specialists Meeting on Effects of Adverse Weather on Aerodynamics, April 1991, Toulouse, France.

64. Sankar, L., and Kwon, L., "Effects of Icing on Finite Wing Aerodynamics," paper presented at the Airfoil-in-Icing Workshop, Nasa Lewis Research Center, Sept. 1989.

65. Kwon, O. J., and Sankar, L. N., "Numerical Study of the Effects of Icing on Fixed and Rotary Wing Performance," AIAA -91-0662, Jan. 1991.

66. Cebeci, T., Chen, H. H., Kaups, K., Schimke, S., and Shin, J., "Analysis of Iced Wings," AIAA-92-0416, Jan. 1992.

67. Roberts, W. B., "Calculation of Laminar Separation Bubbles and Their Effect on Airfoil Performance," *AIAA Journal*, Vol. 18, No. 1, 1980, pp. 25-31.

68. Tani, I., "Low-Speed Flows Involving Bubble Separation," *Progress in Aerospace Sciences*, Vol. 5, 1974, pp.70-103.

69. Jones, B. M., "An Experimental Study of the Stalling of Wings," NACA Reports and Memoranda No. 1588, Dec. 1933.

70. Gaster, M., "The Structure and Behavior of Laminar Separation Bubbles", *Separated Flows II, AGARD Conference Proceedings No. 4, Part 2*, presented at AGARD Fluid Dynamics Panel Meeting on Separated Flows, pp. 813 - 854, Rhode-Saint-Genese, Belgium, May 10-13, 1966.

71. Horton, H. P., "A Semi-Empirical Theory for the Growth and Bursting of Laminar Separation Bubbles", Aeronautical Research Council Current Paper No. 1073, June 1967.

72. Crimi, Peter and Reeves, Barry L., "Analysis of Leading Edge Separation Bubbles on Airfoils", *AIAA Journal*, Vol. 14, No. 11, December 1976.

73. Carter, James E., "Solutions for Laminar Boundary Layers with Separation and Reattachment", AIAA-74-583, presented at the 7th Fluid and Plasma Dynamics Conference, Palo Alto, California, June 17-19, 1974.

74. Briley, Roger W. and McDonald, Henry, "Numerical Prediction of Incompressible Separation Bubbles", *Journal of Fluid Mechanics*, Vol. 69, Part 4, 1975, pp. 631-656.

75. Mehta U. B. and Zalman, L., "Starting Vortex, Separation Bubbles and Stall: A Numerical Study of Laminar Unsteady Flow Around an Airfoil," *Journal of Fluid Mechanics*, Vol. 67, Part 2, pp. 227-256.

76. Weibust, E., Bertelrud, A. and Ridder, S. O., "Experimental Investigation of Laminar Separation Bubbles and Comparison with Theory," *Journal of Aircraft*, Vol. 24, No. 5, 1987, pp. 291-297.

77. Stack, J. P., Mangalam, S. M. and Berry, S. A., "A Unique Measurement Technique to Study Laminar Separation Bubble Characteristics on an Airfoil," AIAA-87-1271, June 1987.

78. Stack, J. P., Mangalam, S. M. and Kalburgi, V. "The Phase Reversal Phenomenon at Flow Separation and Reattachment," AIAA-88-0408, Jan. 1988.

79. Mangalam, S. M., Meyers, J. F., Dagenhart, J. R. and Harvey, W. D., "A Study of Laminar Separation Bubble in the Concave Region of an Airfoil Using Laser Velocimetery," *Proceedings of the Int'l Symposium on Laser Anemometry*, Nov. 17-22, 1985, Miami Beach, Florida, pp. 265-272.

80. Bell, W. A. and Cornelius, K. C., "An Experimental Investigation of a Laminar Separation Bubble on a Natural Laminar Flow Airfoil," AIAA-87-0458, Jan. 1987.

81. Mueller, T. J., "Low Reynolds Number Vehicles," AGARDograph AG-288, 1984.

82. Mueller, T. J. (ed.), *Low Reynolds Number Aerodynamics*, Lecture Notes in Engineering, Vol. 54, Springer-Verlag, June 1989.

83. Simpson, R. L., "REVIEW-A Review of Some Phenomena in Turbulent Flow Separation," *Transactions of ASME: Journal of Fluids Engineering*, Vol. 103, 1981, pp. 520-533.

84. Bradshaw, P., Wong, F. Y. F., "The Reattachment and Relaxation of a Turbulent Shear Layer," *Journal of Fluid Mechanics*, Vol. 52, 1972, pp. 113-135.

85. Eaton, J. K., and Johnston, J. P., "A Review of Research on Subsonic Turbulent Flow Reattachment," *AIAA Journal*, Vol. 19, No. 9, 1981, pp. 1093-1100.

86. Simpson, R. L., "Interpreting Laser and Hot-Film Anemometer Signals in a Separating Boundary Layer," *AIAA Journal*, Vol. 14, No. 1, 1976, pp. 124-126.

87. Adrian, R. J., "Laser Velocimetery," *Fluid Mechanics Measurements*, Hemisphere Publishing, 1983, pp. 155-244.

88. TSI Inc, *TSI 1980B Counter-Type Signal Processor Instruction Manual*, St. Paul, MN, Feb. 1987.

89. Petrie, H. L., " A Study of Compressible Turbulent Free Shear Layers Using Laser Doppler Velocimetry," Ph.D. Thesis, Department of Mechanical and Industrial Engineering, University of Illinois at Urbana-Champaign, 1984.

90. Dutton, J. C., Private Communication, February 1992.

91. TSI, Inc., *TSI Flow and Information Display (FIND) Software Instruction Manual*, Ver. 2.5, St. Paul, MN, March 1991.

92. Registry of Toxic Effects of Chemical Substances, 1985-86, p.3691.

93. TSI, Inc., *TSI Model 9306 6-Jet Atomizer Manual*, St. Paul, MN, June 1987.

94. TSI, Inc, "Laser Velocimetry, Theory, Application and Techniques," *TSI Short Course Notes*, St. Paul, MN, Aug. 8-11, 1988.

95. Young, Warren H., Meyers, James F., Hepner, Timothy E.," Laser Velocimeter Systems Analysis Applied to a Flow Survey Above a Stalled Wing," NASA TN D-8408, 1977.

96. Coleman, H. W., and Steele, W. G., *Experimentation and Uncertainty Analysis for Engineers*, John Wiley & Sons, New York, 1989.

97. Hanson, S., "Broadening of the Measured Frequency Spectrum in a Differential Laser Anemometer Due to Interference Plane Gradients," *Journal of Physics, D: Appl. Phys.* Vol. 6, No. 2, Jan. 1973, pp.164-171.

98. Meyers, J. F., "Application of Laser Velocimetery to Large Scale and Specialized Aerodynamic Tests," *TSI Quarterly*, Vol. 5, Issue 4, 1979.

99. Durst, F., Melling, A., Whitelaw, J. H., *Principles and Practice of Laser-Doppler Anemometry*, Academic Press, New York, 1981.

100. Buchhave, P., "Biasing Errors in Individual Particle Measurements with the LDA-Counter Signal Processor," *Proceedings of LDV Symposium*, Copenhagen, Denmark, 1975, pp.258-278.

101. Whiffen, M. C., "Polar Response of an LV Measurement Volume," *Proceedings of the Minnesota Symposium on Laser Anemometry*, Bloomington, Minnesota, October 1975, pp. 589-590.

102. Whiffen, M. C., Lan, J. C., and Smith, D. M., "Design of LV Experiments for Turbulence Measurements," *Laser Velocimetry & Particle Sizing*, Thompson, H. D. and Stevenson, W. H. (eds.), Hemisphere Publishing Corp., Washington, 1979, pp.197-207.

103. Samimy, M., " An Experimental Study of Compressible Turbulent Reattaching Free Shear Layers," Ph.D. Thesis, Department of Mechanical and Industrial Engineering, University of Illinois at Urbana-Champaign, 1984.

104. Edwards, R. V., "Report on the Special Panel on Statistical Bias Problems in Laser Anemometry," *Transactions of ASME: Journal of Fluids Engineering*, Vol. 109, June 1987, pp. 89-93.

105. Erdmann, J. C., and Tropea, C., "Turbulence Induced Statistical Bias in Laser Anemometry," *Proceedings of the Seventh Symposium on Turbulence*, University of Missouri-Rolla, September 1981.

106. Edwards, R. V., "A New Look at Particle Statistics in Laser Anemometer Measurements," *Journal of Fluid Mechanics*, Vol. 105, 1981, pp. 317-325.

107. Dimotakis, P. E., "Single Scattering Particle Laser Doppler Measurements of Turbulence, pp. 10.1-10.14, *Applications of Non-Intrusive Instrumentation in Flow Research*, H. J. Pfeifer and Haertig, J., eds., AGARD CP-193, 1976.

108. Amatucci, V. A., "An Experimental Investigation of the Two-Stream, Supersonic, Near-Wake Flowfield Behind a Finite-Thickness Base," Ph.D. Thesis, Department of Mechanical and Industrial Engineering, University of Illinois at Urbana-Champaign, 1990.

109. Stevenson, W. H., Thompson, H. D., and Roesler, T. C., "Direct Measurement of Laser Velocimeter Bias Errors in a Turbulent Flow," *AIAA Journal*, Vol. 20, No. 12, December 1982, pp 1720-1723

110. Stevenson, W. H., Thompson, H. D., and Craig, R. R., "Laser Velocimeter Measurements is Highly Turbulent Recirculating Flows," *Transactions of ASME: Journal of Fluids Engineering*, Vol. 106, Series I, No. 2, June 1984, pp. 173-180.

111. Johnson, D. A., Modarress, D., and Owen, F. K., "An Experimental Verification of Laser Velocimeter Sampling Bias and Its Correction," *Transactions of ASME: Journal of Fluids Engineering*, Vol. 106, Series I, No. 1, March 1984, pp.5-12.

112. Erdmann, J. C., and Tropea, C., " Statistical Bias of the Velocity Distribution Function in Laser Anemometry," *Proceedings of the International Symposium on Applications of Laser Doppler Anemometry to Fluid Mechanics*, Lisbon, Portugal, July 1982, paper 16.2.

113. McLaughlin, D. K., and Tiederman, W. G., "Biasing Correction for Individual Realization of Laser Anemometer Measurements in Turbulent Flows," *The Physics of Fluids*, Vol. 16, No. 12, December 1973, pp. 2082-2088.

114. George, W. K., "Limitations to Measuring Accuracy Inherent in the Laser Doppler Signal," The Accuracy of Flow Measurements by laser Doppler Methods," *Proceedings of the LDA Symposium*, Buchave, P., Delhaye, J. M., Durst, F., George, W. K., Refslund, K., and Whitelaw, J. H., (eds.) 1974, Hemisphere, Washington D. C., 1977, pp.20-63.

115. Hosel, W., and Rodi W., "New Biasing Elimination Method for Laser-Doppler Velocimeter Counter Processing," *Review of Scientific Instruments*, Vol. 48, 1977, pp. 910-919.

116. Gould, R. D., Stevenson, W. H., and Thompson, H. D., "Parametric Study of Statistical Bias in Laser Doppler Velocimetery," *AIAA Journal*, Vol. 27, No. 8, August 1989, pp. 1140-1142.

117. Edwards, R. V., and Jensen, A. S., "Particle-Sampling Statistics in Laser Anemometers: Sample-and-Hold Systems and Saturable Systems," *Journal of Fluid Mechanics*, Vol. 133, 1983, pp.397-411.

118. Meyers, J. F., and Clemmons J. I., Jr, "Processing Laser Velocimeter High-Speed Burst Counter Data," *Laser Velocimetry & Particle Sizing*, Thompson, H. D. and Stevenson, W. H. (eds.), Hemisphere Publishing Corp., Washington, 1979, pp.300-313.

119. Hoad, D. R., Meyers, J. F., Young, W. H., Hepner, T. E., "Laser Velocimeter Survey About a NACA 0012 Wing at Low Angles of Attack, NASA TM-74040, 1978.

120. Meyers, J. F., Kjelgaard, S. O., and Hepner, T. E., "Investigation of Particle Sampling Bias in the Shear Flow Field Downstream of a Backward Facing Step," *Proceedings of the Fifth International Symposium on Applications of Laser Techniques to Fluid Mechanics*, Lisbon, Portugal, July 9-12, 1990.

121. Kjelgaard, S. O., Private Communication, March 1992.

122. Adrian, R. J., Private Communication, Feb. 1992.

123. Kried, D. K., "Error Estimates for Laser Doppler Velocimeter Measurements in Non-Uniform Flow", *Proceedings of the Second International Workshop on Laser Velocimetry*, Vol. I, Perdue University, West Lafayette, Indiana, March 1974, pp. 398-425.

124. Karpuk, M. E., and Tiederman, W. G. Jr., "Effect of Finie-Size Probe Volume Upon Laser Doppler Anemometer Measurements," *AIAA Journal*, Vol. 14, No. 8, August 1976, pp. 1099-1105.

125. Mayo W. T. Jr., "A Discussion of Limitations and Extensions of Power Spectrum Estimation with Burst-Counter LDV Systems," *Proceedings of the Second International Workshop on Laser Velocimetry*, Vol. I, Perdue University, West Lafayette, Indiana, March 1974, pp. 90-101

126. Miller, I. and Freund, J. E., *Probability and Statistics for Engineers*, 3rd Edition, Prentice-Hall, Englewood Cliffs, New Jersey, 1985.

127. Bradshaw, P. (ed.), *Turbulence*, Springer Verlag, New York, 1978, p.65.

128. Hinze, J. O., *Turbulence*, McGraw-Hill publishing, New York, 1987, p. 660.

129. Smetana, F. O., Summey, D. C., Smith, N. S., and Carden, R. K., "Light Aircraft Lift, Drag, and Moment Prediction - A Review and Analysis," NASA CR-2523, May 1975.

130. Eppler, R., and Somers, D. M., "A Computer Program for the Design and Analysis of Low-Speed Airfoils," NASA TM-80210, Aug. 1980.

131. Wells, S. L. and Bragg, M. B., "A Computational Method for Calculating Droplet Trajectories Including the Effects of Wind Tunnel Walls," AIAA-92-0642, paper presented at the 30th Aerospace Sciences Meeting, Reno, Nevada, January 6-9, 1992.

132. Rae, W. H. and Pope, A., *Low-Speed Wind Tunnel Testing* 2nd ed., Wiley-Interscience, New York, 1984.

133. Schlichting, H., *Boundary Layer Theory*, 7th ed., McGraw-Hill Publishing, New York, 1979, pp. 206-211.

134. Bragg, M. B., Private Communication, October 1992.

135. Potapzuck, M. G., Private Communication, April 1992.

136. Kwon, O. J., Private Communication, April 1992.

137. Sankar, L. N., Private Communication, April 1992.

138. Ruderich, R. and Fernholz, H. H., " An Experimental Investigation of a Turbulent Shear Flow with Separation, Reverse Flow, and Reattachment," *Journal of Fluid Mechanics*, Vol 163, 1986, pp. 283-322.

139. Chandrsuda C. and Bradshaw, P., "Turbulence Structure of a Reattaching Mixing Layer," *Journal of Fluid Mechanics*, Vol. 110, 1981, pp. 171-194.

140. Troutt, T. R., Scheelke, B., and Norman, T. R., "Organized Structures in a Reattaching Separated Flow Field," *Journal of Fluid Mechanics*, Vol. 143, 1984, pp.413-427.

141. Castro, I. P. and Haque, A., "The Structure of a Turbulent Shear Layer Bounding a Separation Region," *Journal Fluid Mechanics*, Vol. 179, 1987, pp. 439-468.

142. Wells, S. L., "The Effect of Sidewall Suction on the Aerodynamics of a Semispan Wing with Simulated Ice," M.S. Thesis, University of Illinois at Urbana-Champaign, Urbana, Illinois, 1992.

143. Driver, D. M., Seegmiller, H. L., and Marvin, J., "Unsteady Behavior of a Reattaching Shear Layer," AIAA-83-1712, July 1983.

144. Driver, D. M., Seegmiller, H. L., and Marvin, J., "Time-Dependent Behavior of a Reattaching Shear Layer," *AIAA Journal*, Vol. 25, No. 7, 1987, pp. 914-919.

145. Cherry, N. J., Hillier, R., and Latour, M. E. M. P., "Unsteady Measurements in a Separated and Reattaching Flow," *Journal of Fluid Mechanics*, Vol. 144, 1984, pp. 13-46.

146. Etheridge, D. W. and Kemp, P. H., "Measurements of Turbulent Flow Downstream of a Rearward-Facing Step," *Journal of Fluid Mechanics*, Vol. 86, 1978, pp. 545-566.

147. Kiya, M. and Sasaki, K., "Structure of a Turbulent Separation Bubble," *Journal of Fluid Mechanics*, Vol 137, 1983, pp. 83-113.

148. Durst, F. and Tropea C., "Turbulent, Backward-Facing Step Flows in Two-Dimensional Ducts and Channels," *Proceedings of the Turbulent Shear Flows Conference III*, Davis, CA, Sept. 1982, pp. 18.1-18.6.

FIGURES

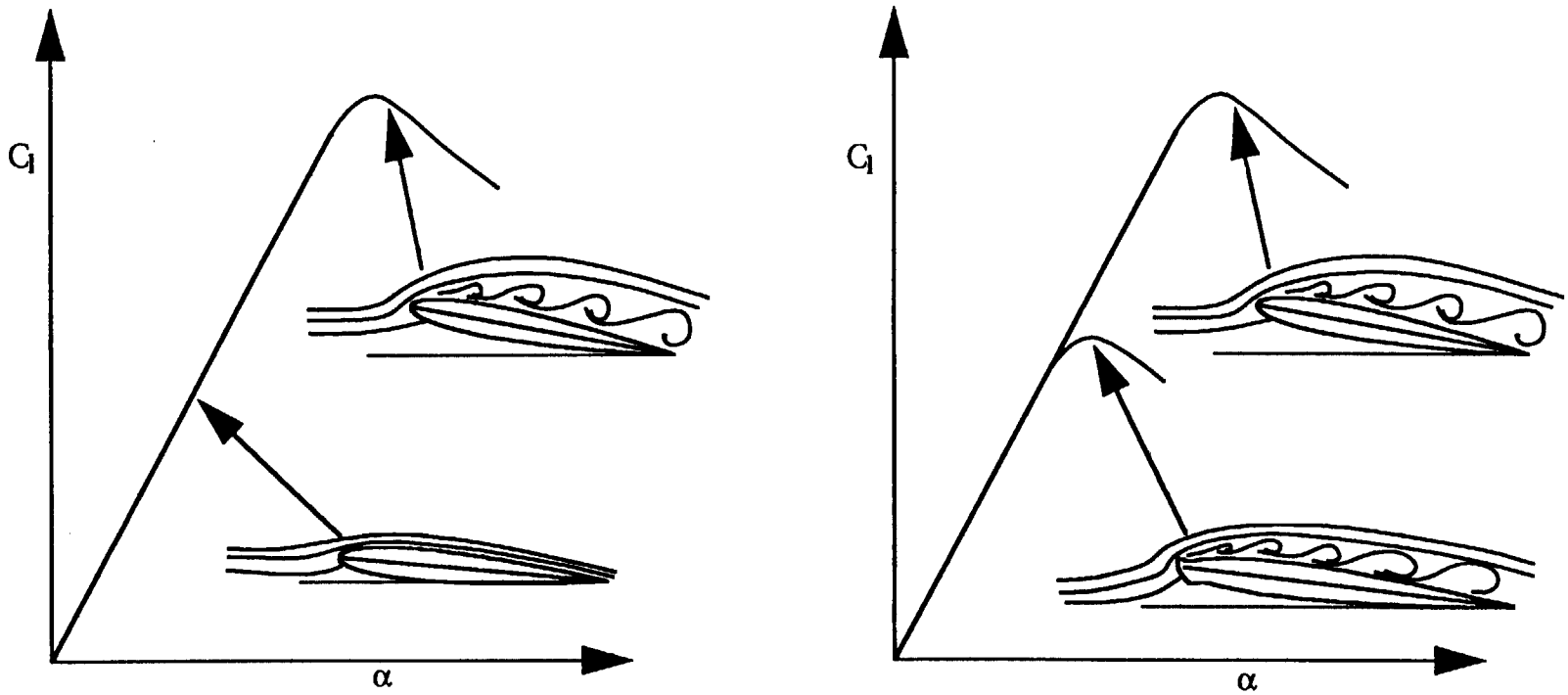

At low angles of attack, the airflow follows the clean airfoil contour and the lift is linearly proportional to the angle of attack. As angle of attack is increased, the airflow begins to separate from the airfoil surface (stall onset) and the lift begins to vary non-linearly with angle of attack.
The presence of ice shape forces the airflow to separate from the airfoil surface at a lower angle of attack . This results in a reduction in maximum lift and an increase in drag.

Figure 1. Effect of Leading Edge Ice Accretion on the Lift Perfromance of an Airfoil

RIME ICE

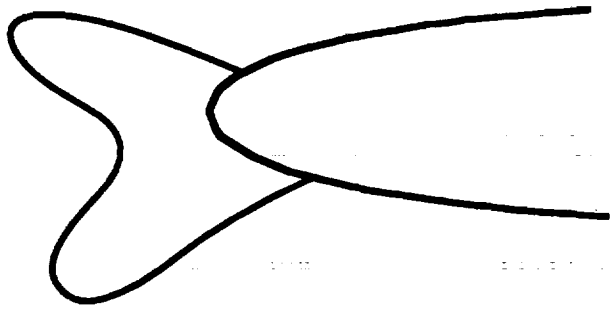

GLAZE ICE

Figure 2. Typical Rime and Glaze Ice Accretions.

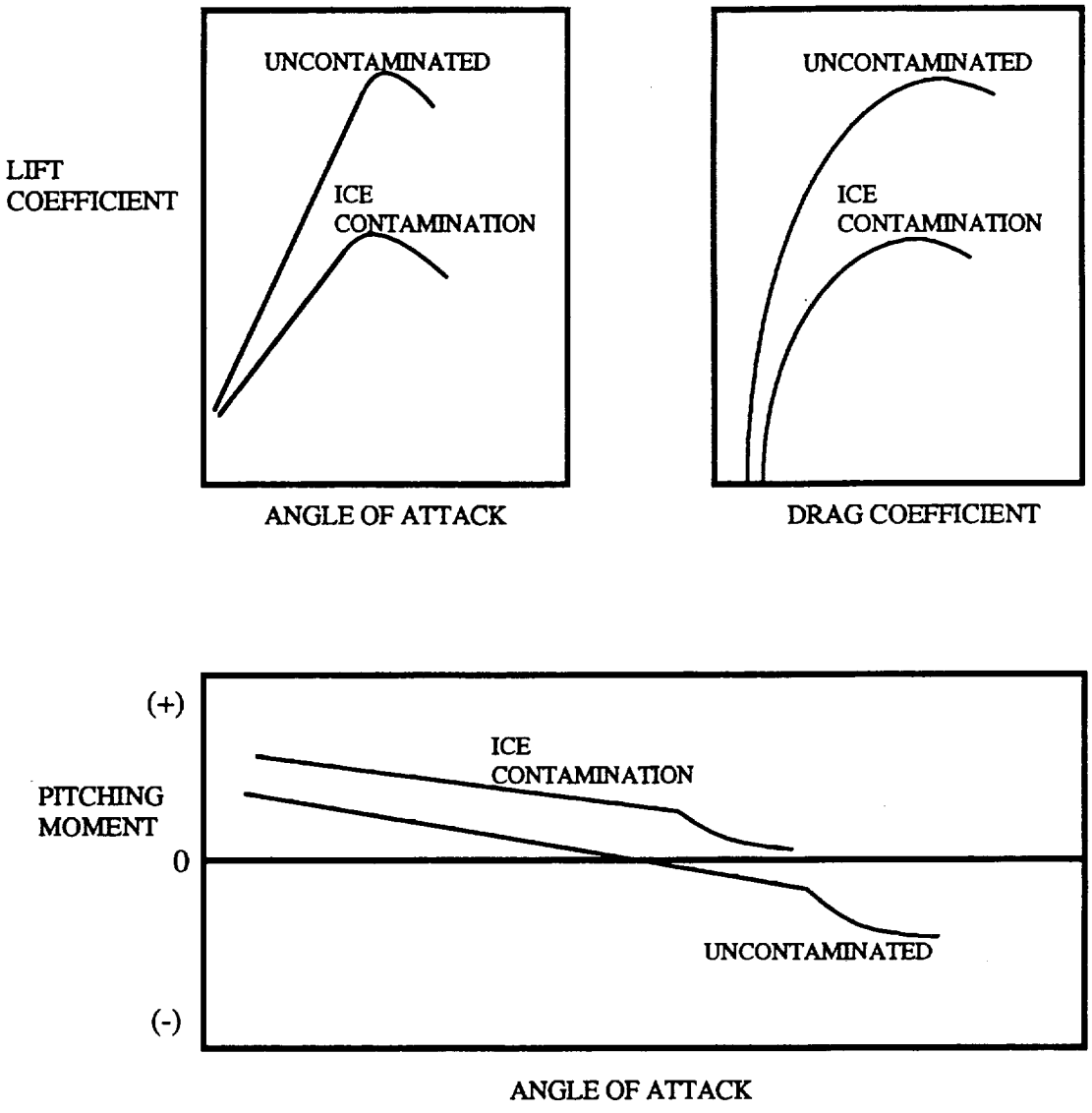

Figure 3. Effect of Wing Ice Contamination on Lift, Drag, and Pitching Moment

NACA 0012 Icing Conditions

$\alpha = 4°$ $U_\infty = 130$ mph

$\bar{d} = 20$mm LWC = 2.1 g/m3

T = 18°F

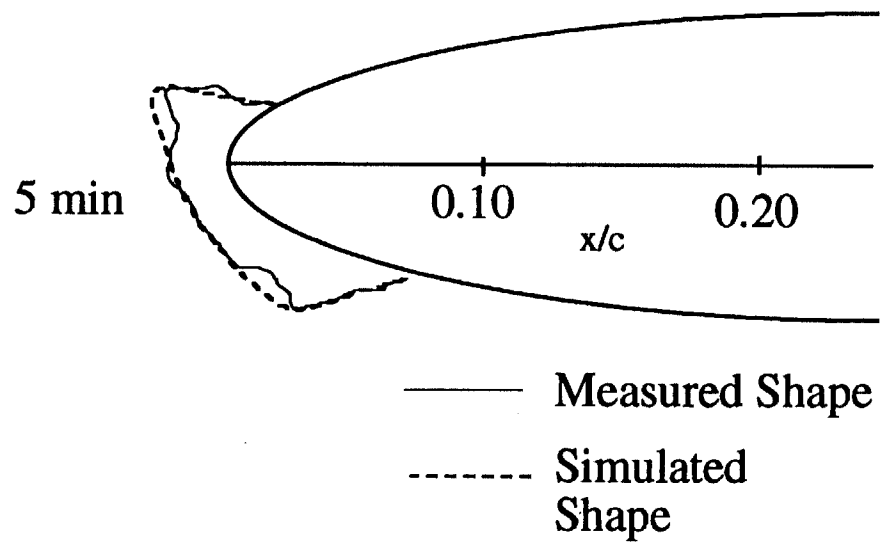

Figure 4. Real and Simulated Glaze Ice Shapes

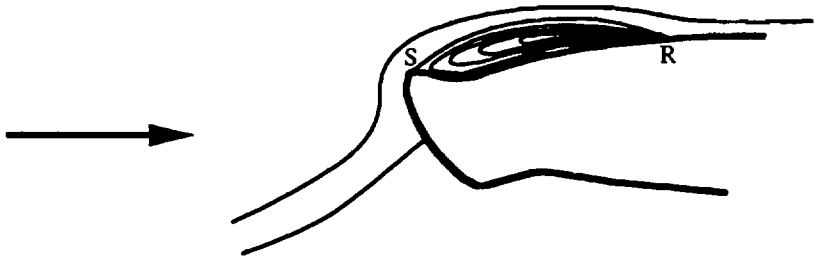

a) Bubble Flowfield on the NACA 0012 with Simulated Glaze Ice

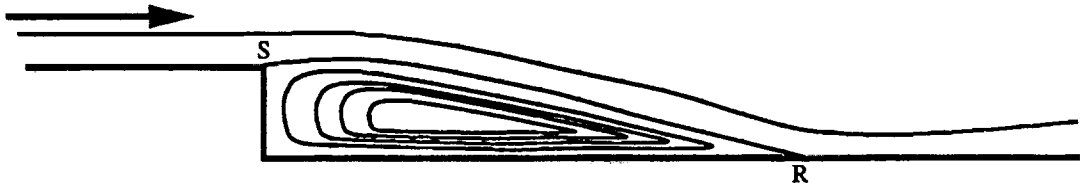

b) Bubble Flowfield behind a Rearward-Facing Step

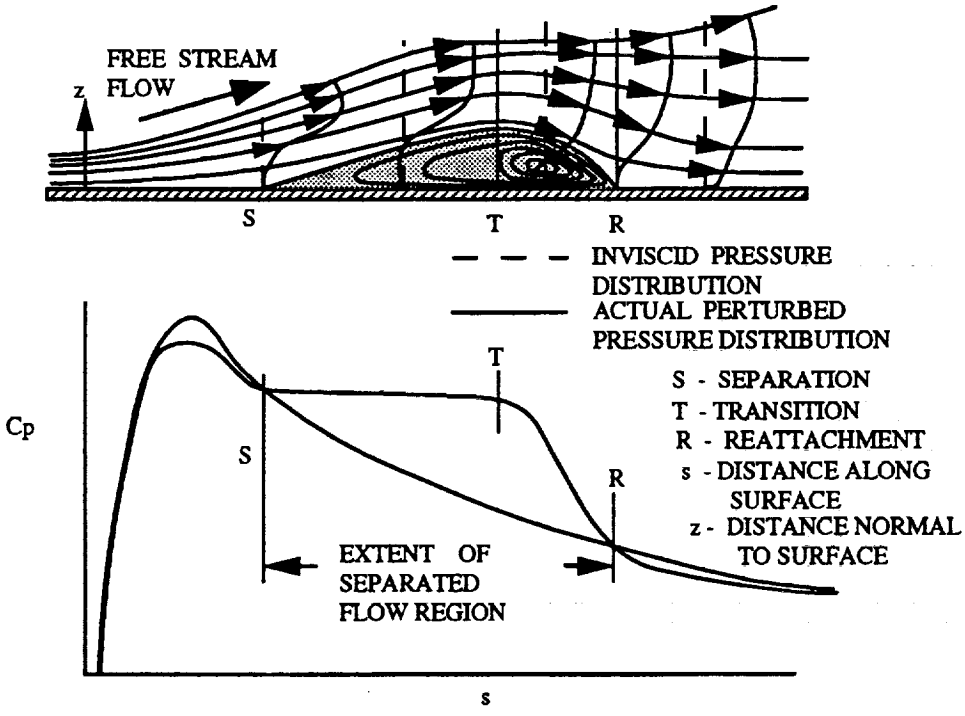

c) Laminar Separation Bubble Flowfield

Figure 5. Model of the Separation Bubble Flowfield

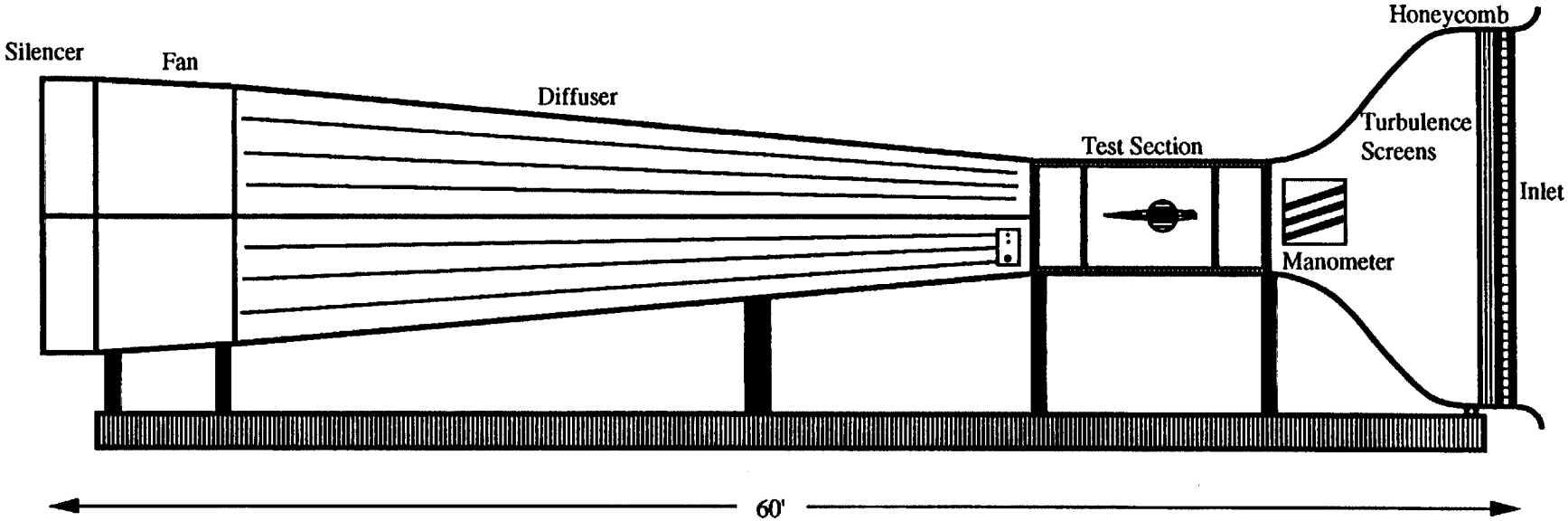

Diagram Not to Scale
Test Section Dimensions: 2.8' x 4' x 8'
Power Source: 125 HP Variable Frequency AC Drive
Max. Speed: 165 MPH

Figure 6. Schematic of the UIUC - AAE Open-Circuit Subsonic Tunnel

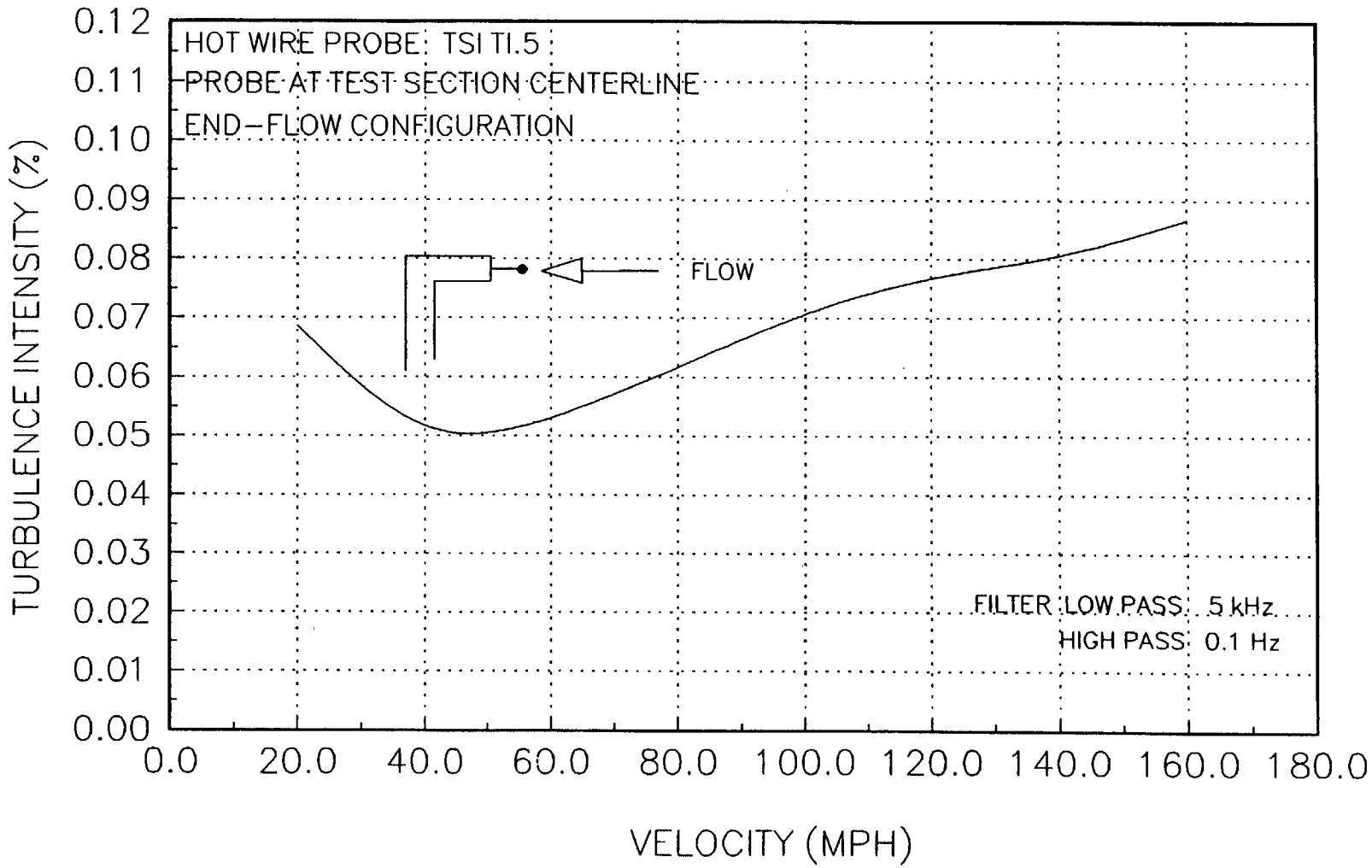

Figure 7. Variation of Turbulence Intensity with Tunnel Speed

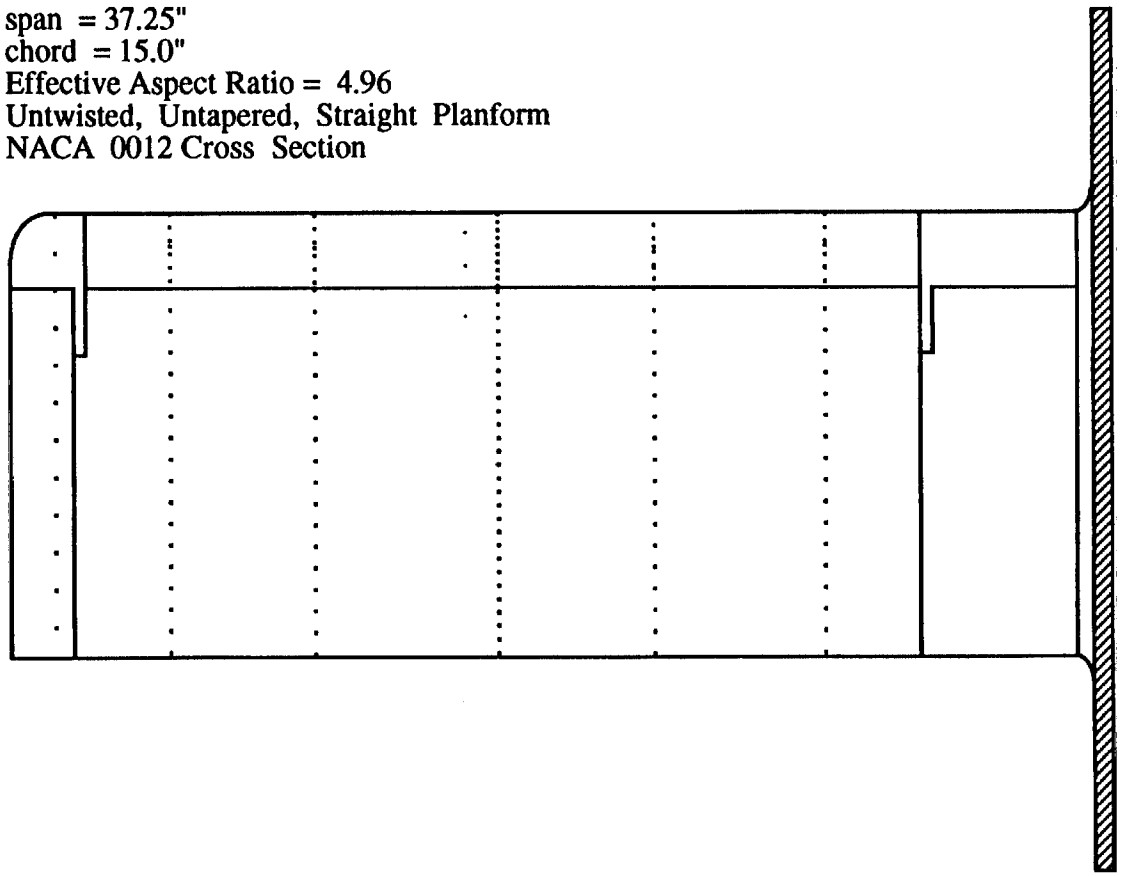

Figure 8. Semispan Wing Model

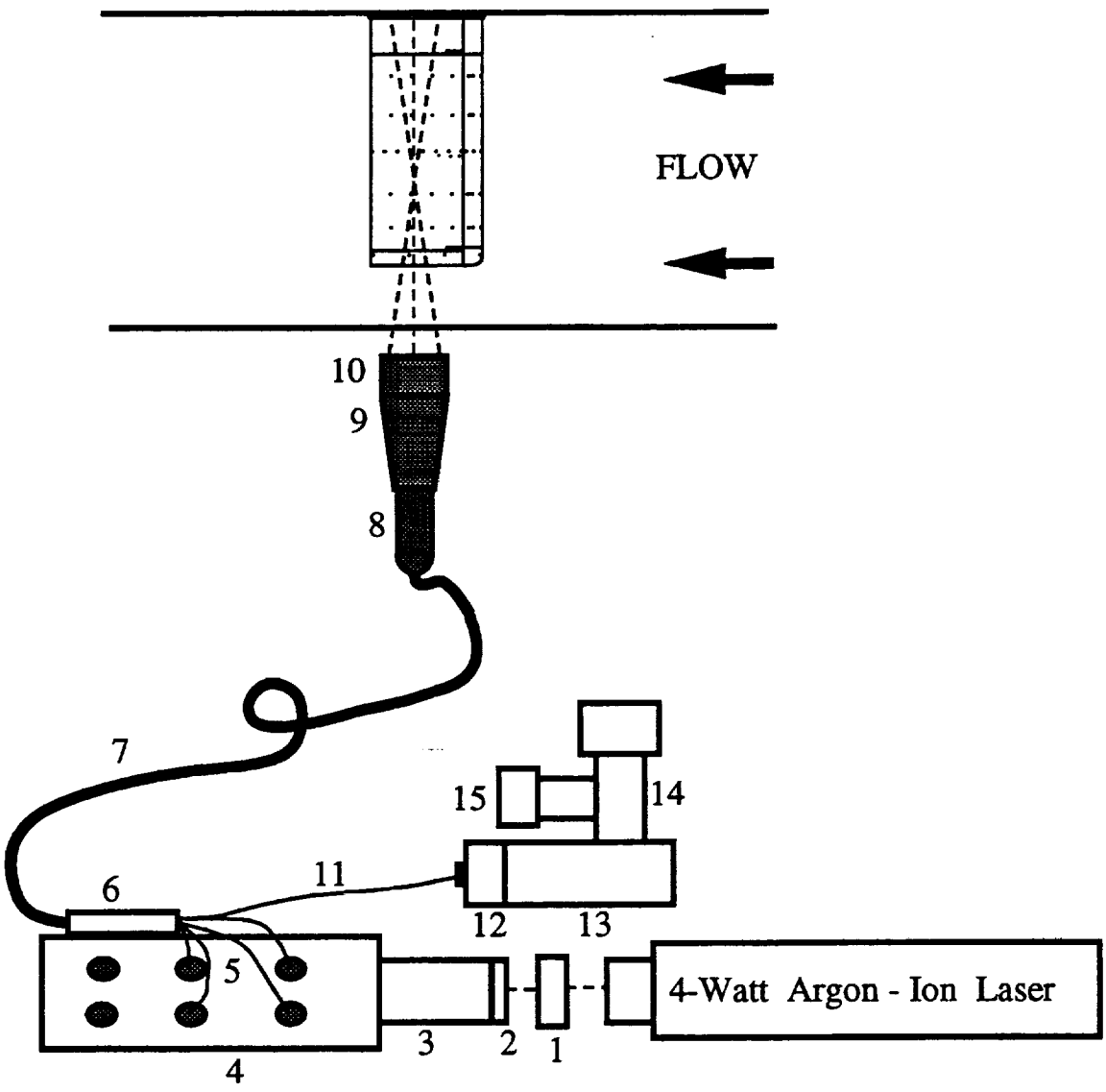

1. Collimator
2. Optical Filter
3. Beam Guide
4. Color Burst
5. Transmitting Fiber Optic Cables
6. Fiber Coupler
7. Fiber Optic Bundle
8. 50 mm Fiber Probe
9. Beam Expander
10. Transmitting Lens
11. Receiving Fiber Optic
12. Receiving Collimator
13. Dichroic Mirror
14. Photomultiplier (green)
15. Photomultiplier (blue)

Figure 9. Schematic of the Optical Arrangement of the Transmitting and Receiving Optics of the Laser Doppler Velocimeter System

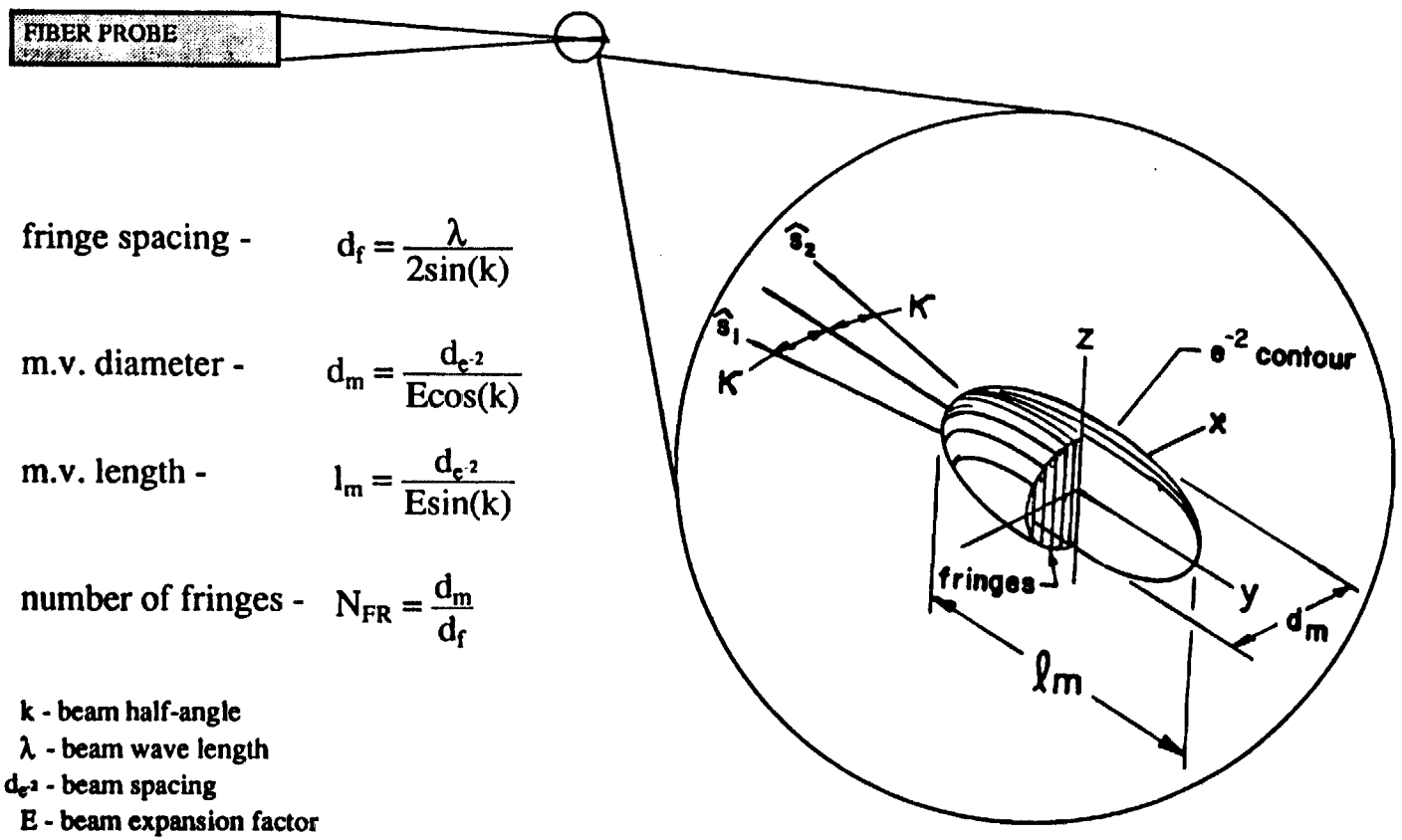

Figure 10. Measurement Volume Characteristics.

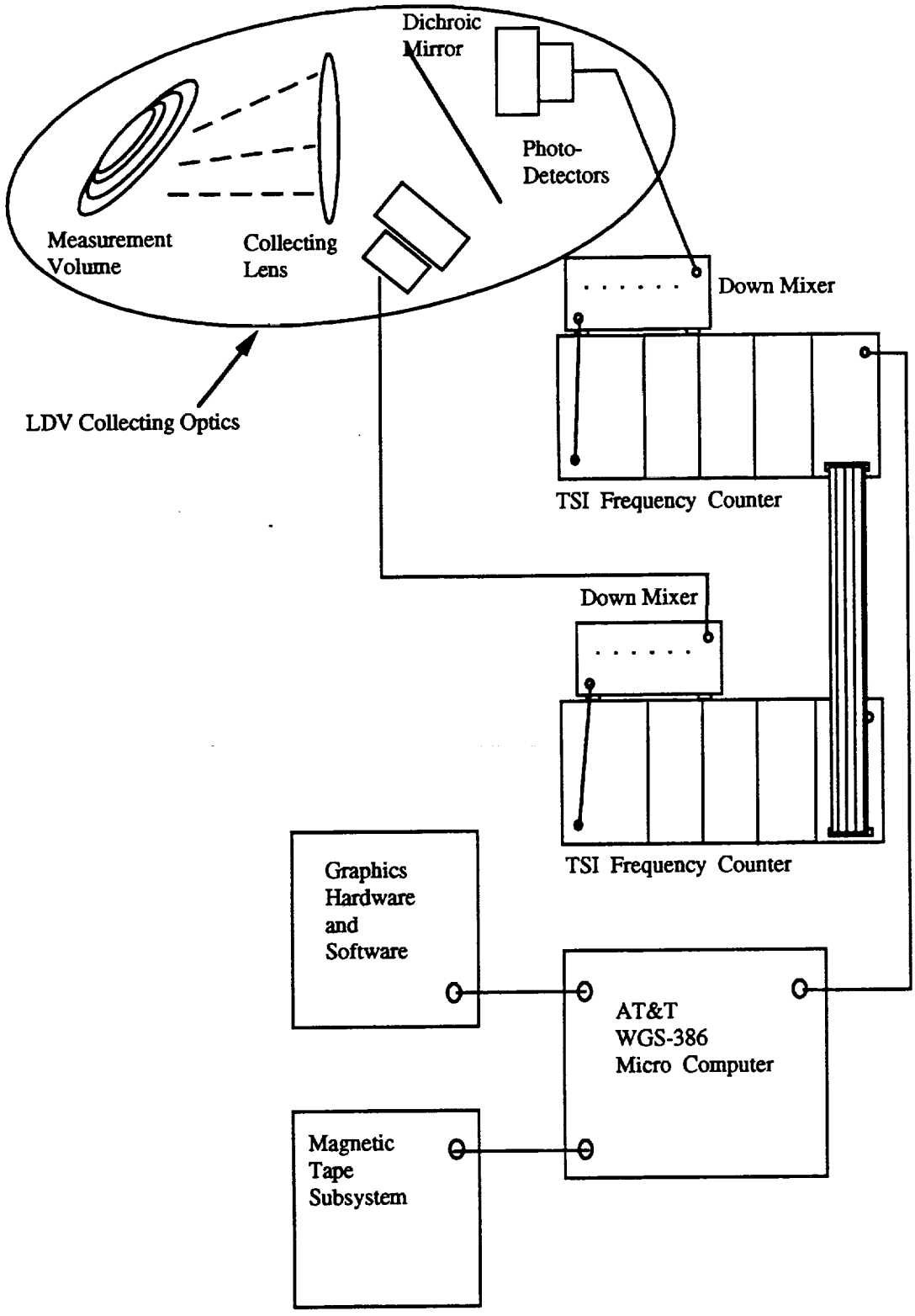

Figure 11. Illustration of the Data Acquisition, Reduction, and Storage Systems

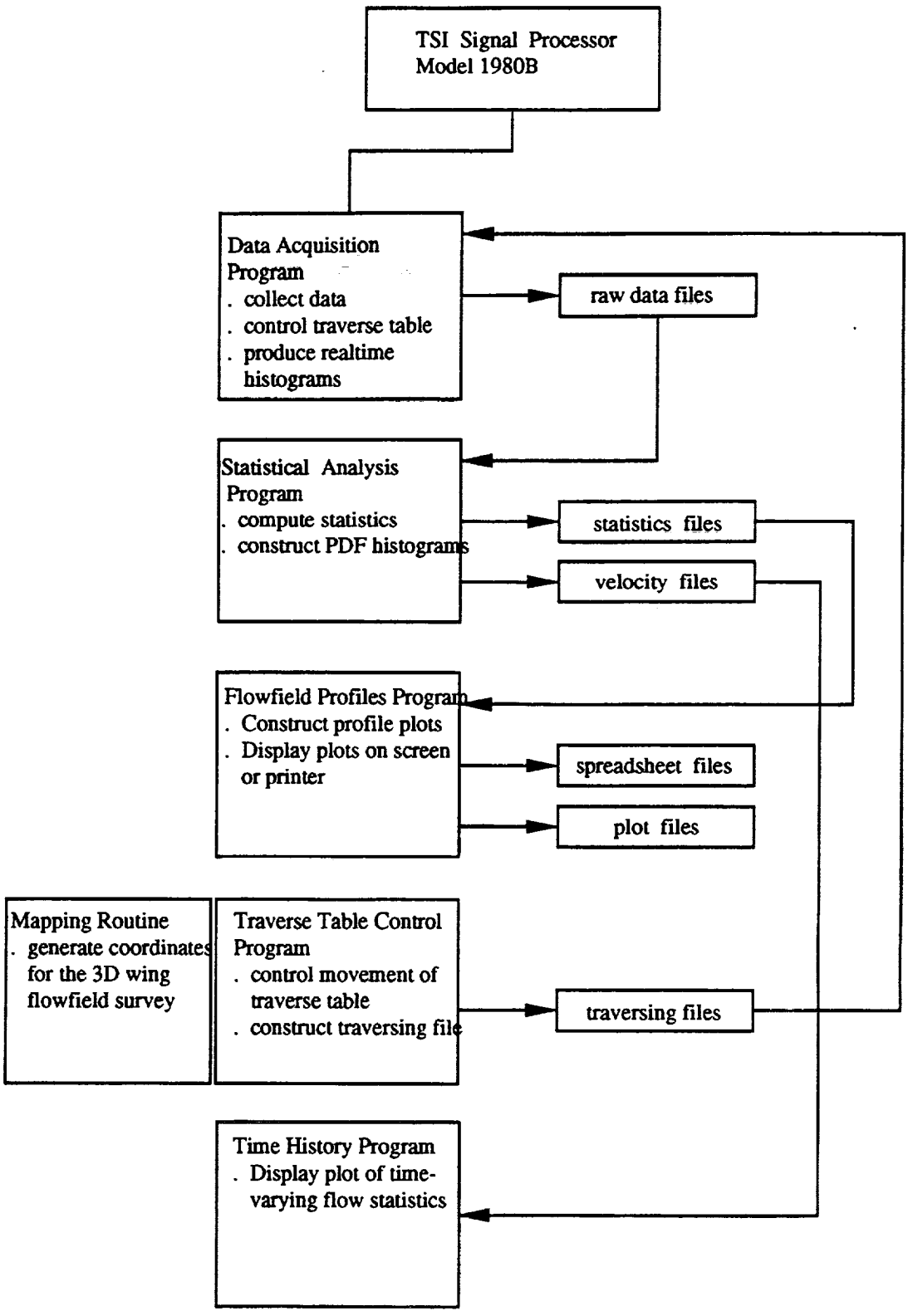

Figure 12. Schematic Diagram of the FIND Data Acquisition and Analysis Software.

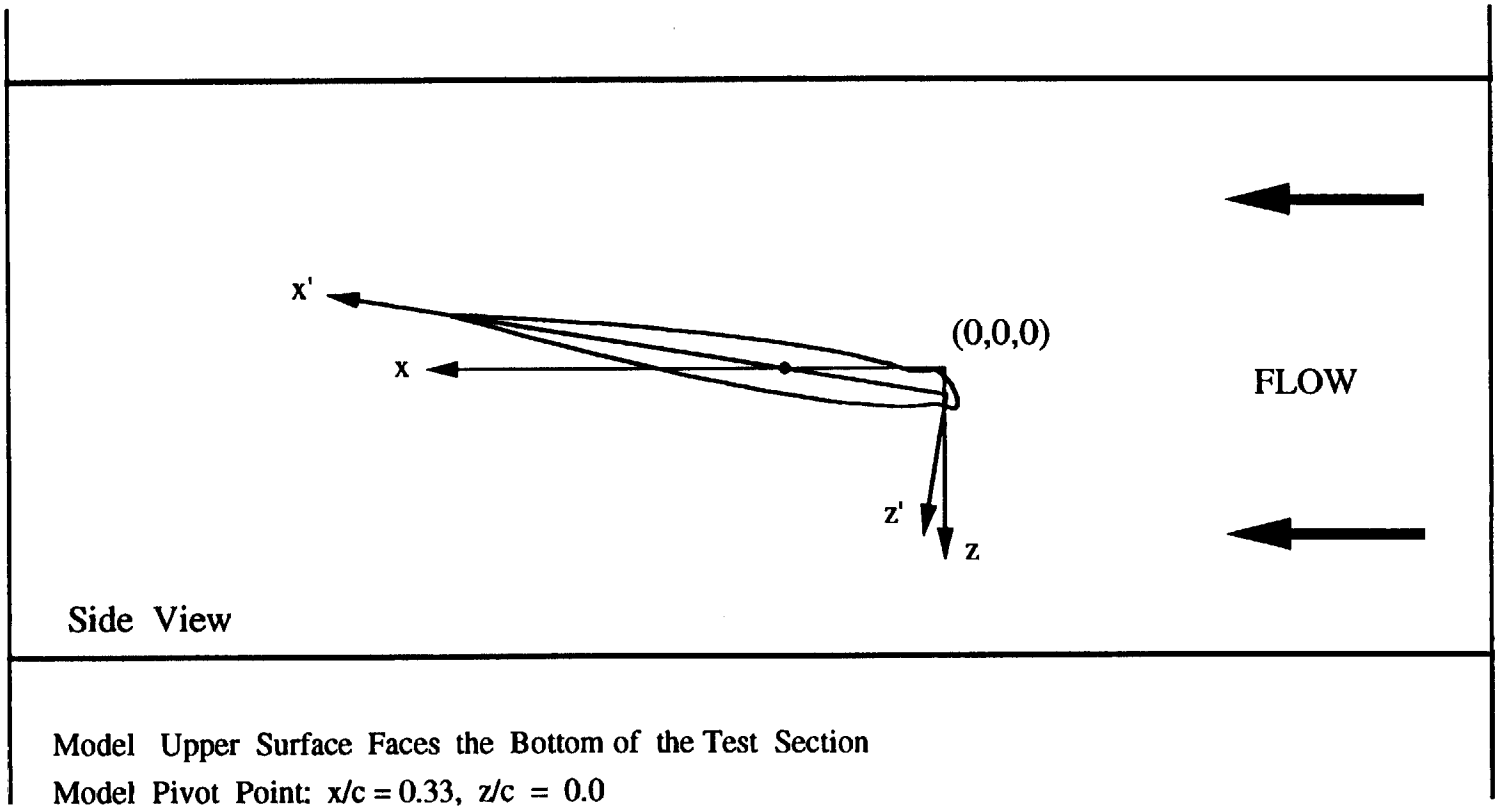

Figure 13. Model Coordinate System with Respect to the Tunnel Coordinate System

Figure 14. Acquisition Room with Laser, Optics and Electronics.

ORIGINAL PAGE
COLOR PHOTOGRAPH

Figure 15. Tunnel Test Section with Three-Component LDV Traverse System.

ORIGINAL PAGE
COLOR PHOTOGRAPH

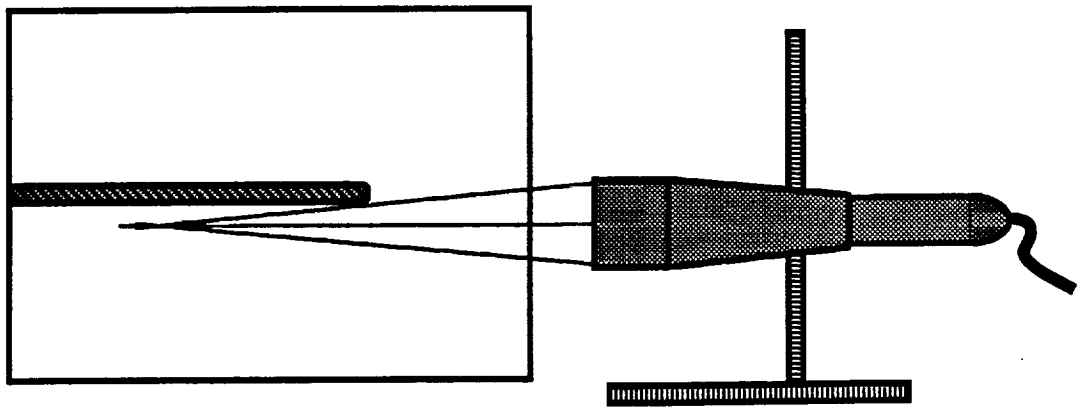

a. Fiber Probe Aligned With the Semispan Wing Inside the Wind Tunnel Test Section, Shifted Blue Beam From the Untilted Probe is Clipped by the Model .

Subsonic Tunnel 3 x 4 Foot Test Section With the Semispan WIng Installed. Flow Direction is Out of the Page.

2-Component Fiber Probe Mounted on the X-Y-Z Traverse System

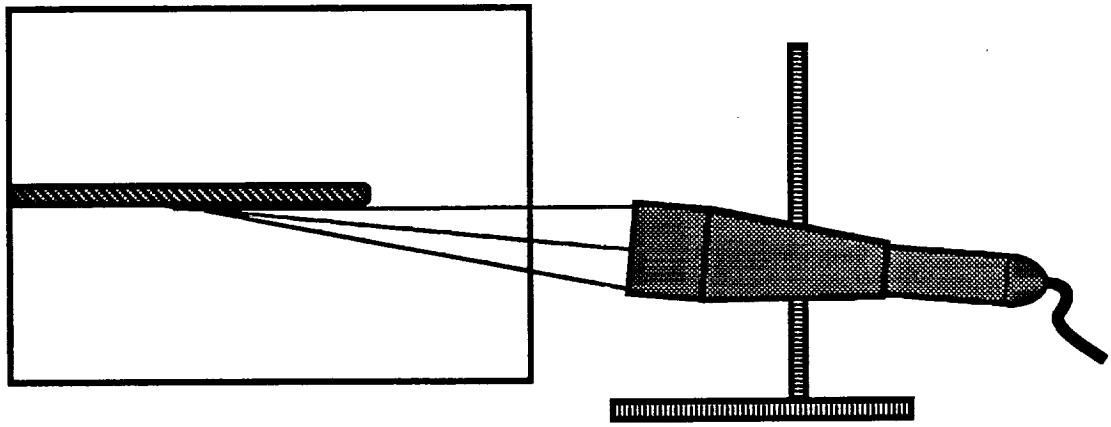

b. Fiber Probe Aligned With the Semispan Wing Inside the Wind Tunnel Test Section, Shifted Blue Beam From the Tilted Probe Can Approach Very Close to the Wing Surface .

Figure 16. Effect of Probe Tilting on the Alignment of Transmitting Optics with the Model

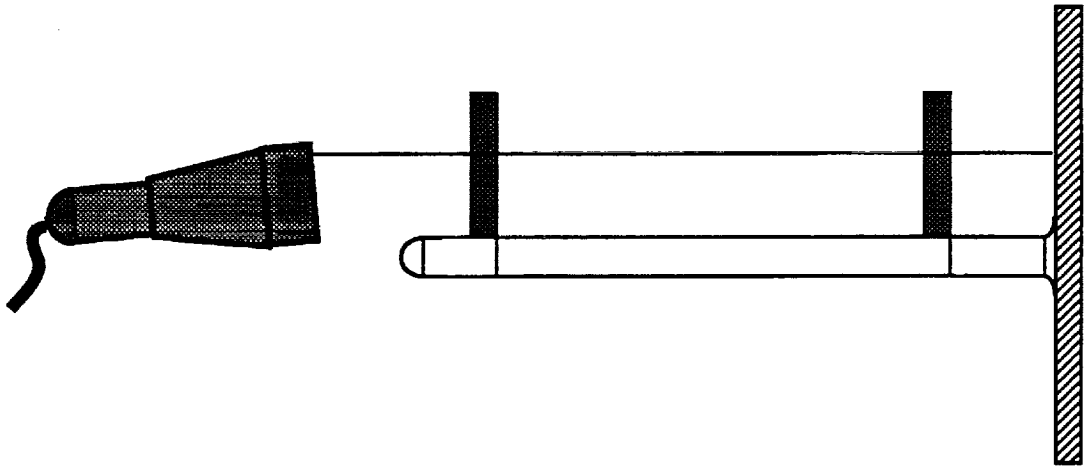

a. Front View -- Alignment Blocks Lined Up with First and Fifth Tap Rows Probe is Tilted so that the Shifted Blue Beam Passes Through the Center Hole of the Alingment Blocks.

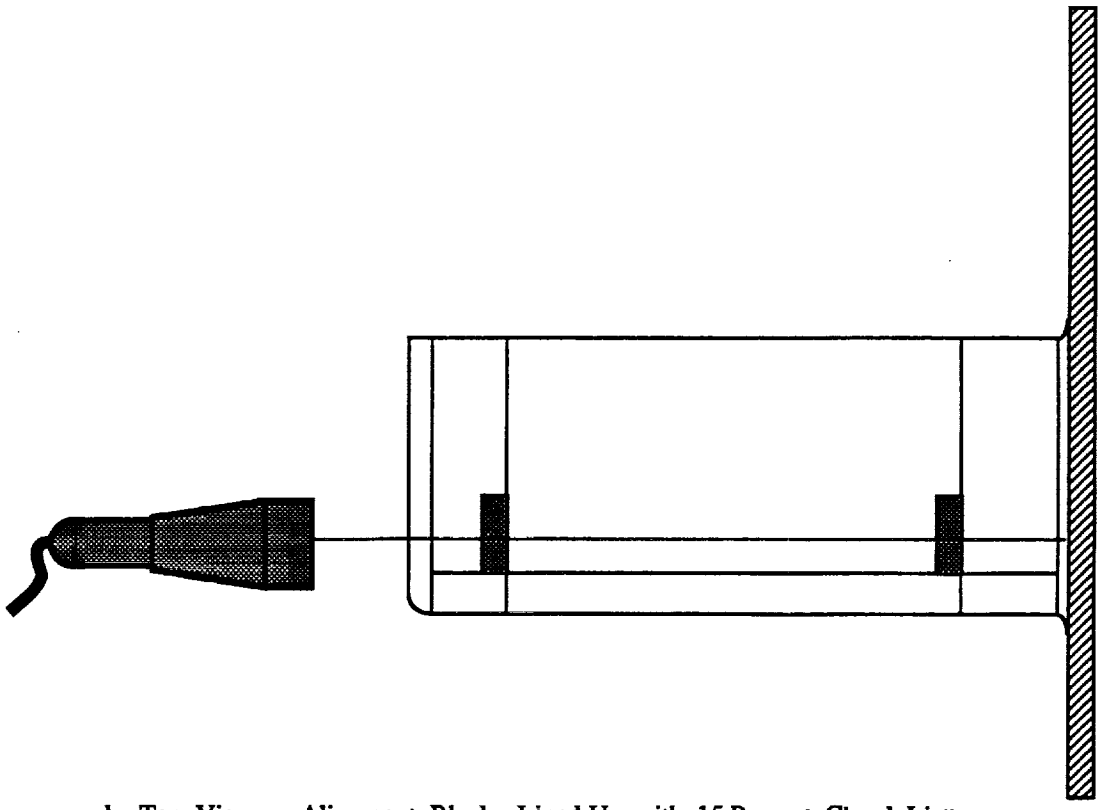

b. Top View -- Alignment Blocks Lined Up with 15 Percent Chord Line Shifted Blue Beam Passes Through the Center Hole of the Alignment Blocks.

Figure 17. Alignment of the Transmitting Beams with the Model

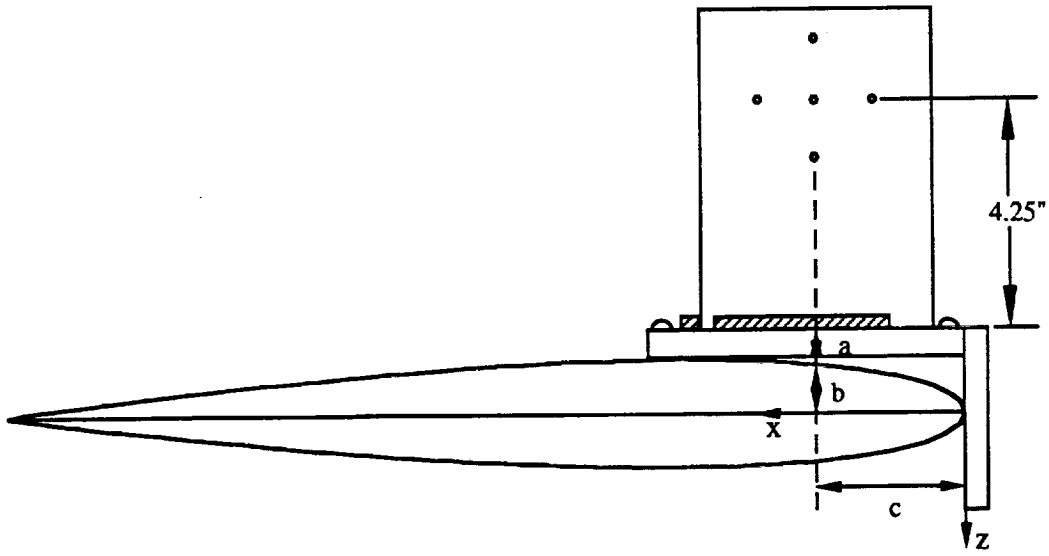

a. Clean Wing Airfoil Cross Section (Model Upper Surface is on the Lower Side)

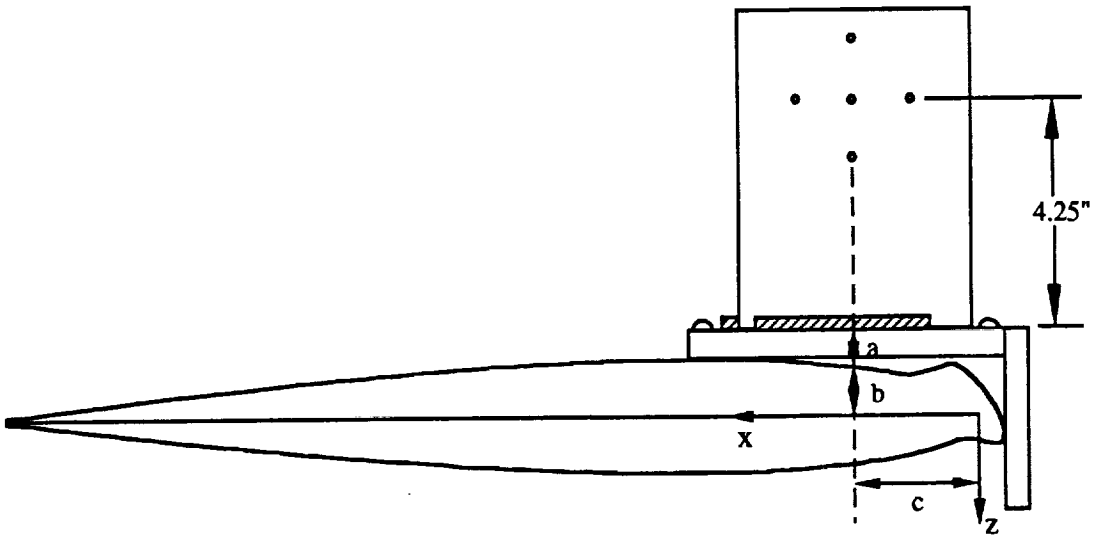

b. Iced Wing Airfoil Cross Section (Model Upper Surface is on the Lower Side)

Figure 18. Alignment Tool Used for Positioning the Probe Measurement Volume at the Origin in the Wind Tunnel Coordinate System.

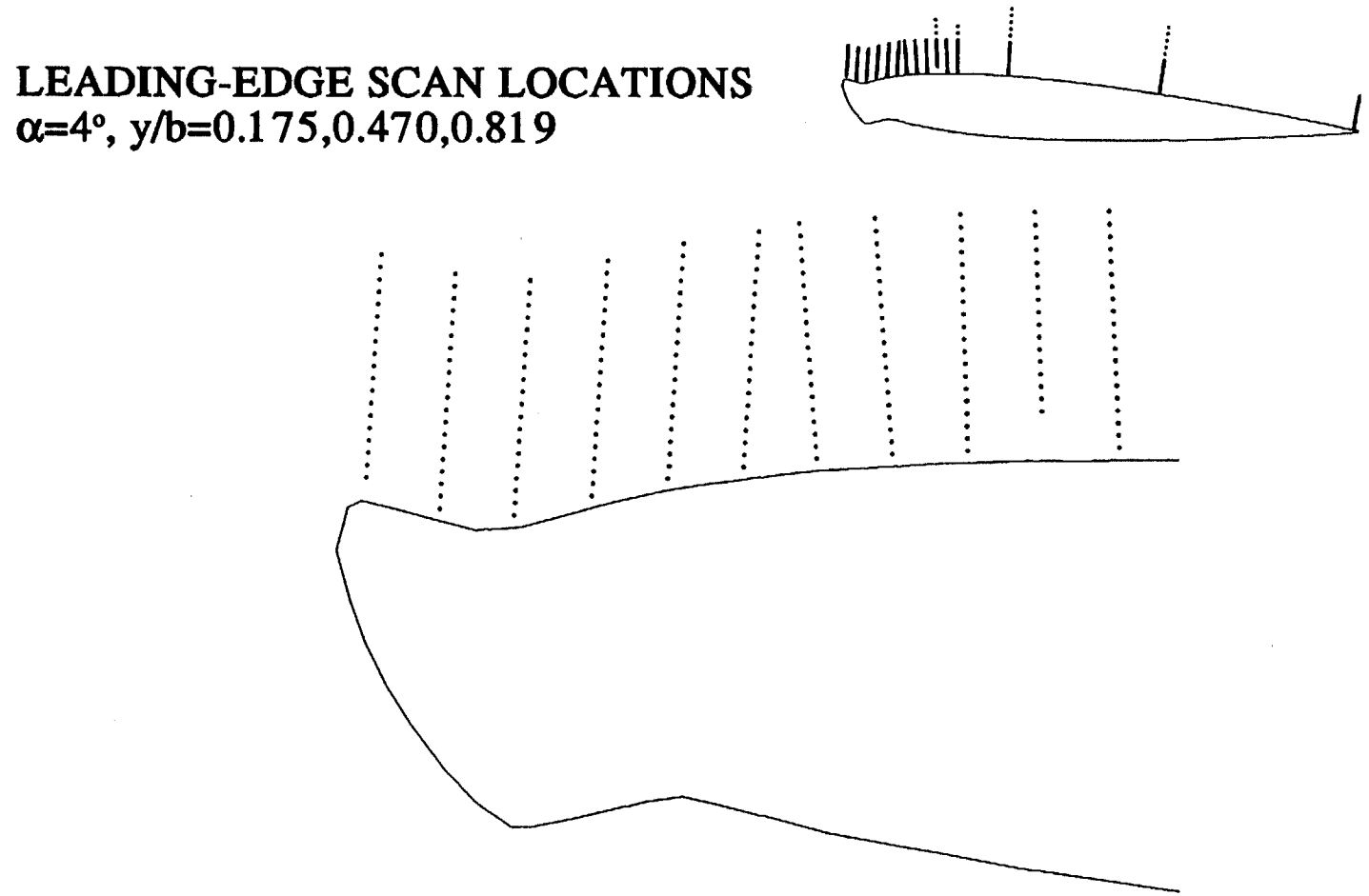

Figure 19. Typical Measurement Locations Near the Ice Horn on the Model Upper Surface.

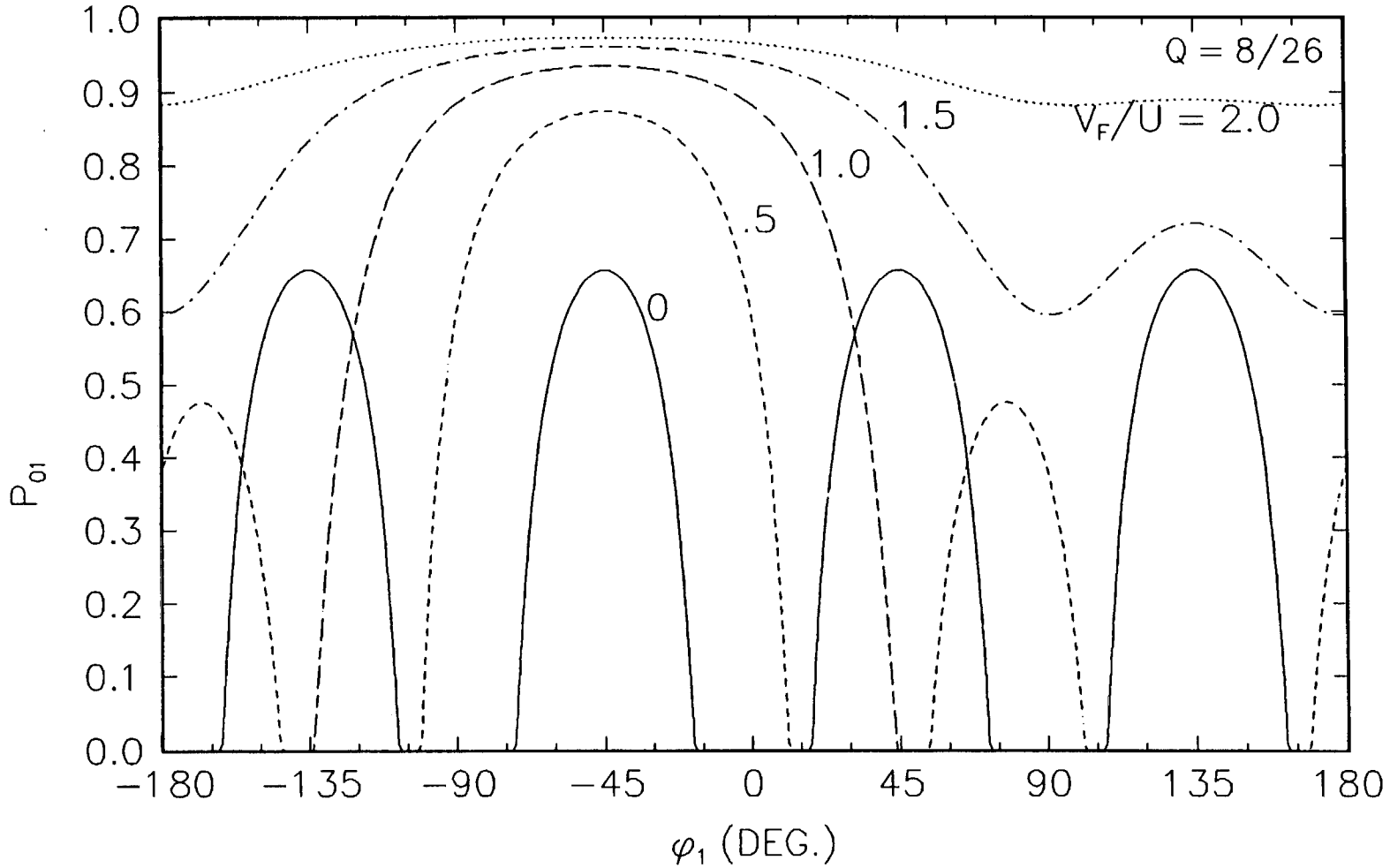

Figure 20. Probability of Particle Detection in Coincidence Mode for Q=8/26.

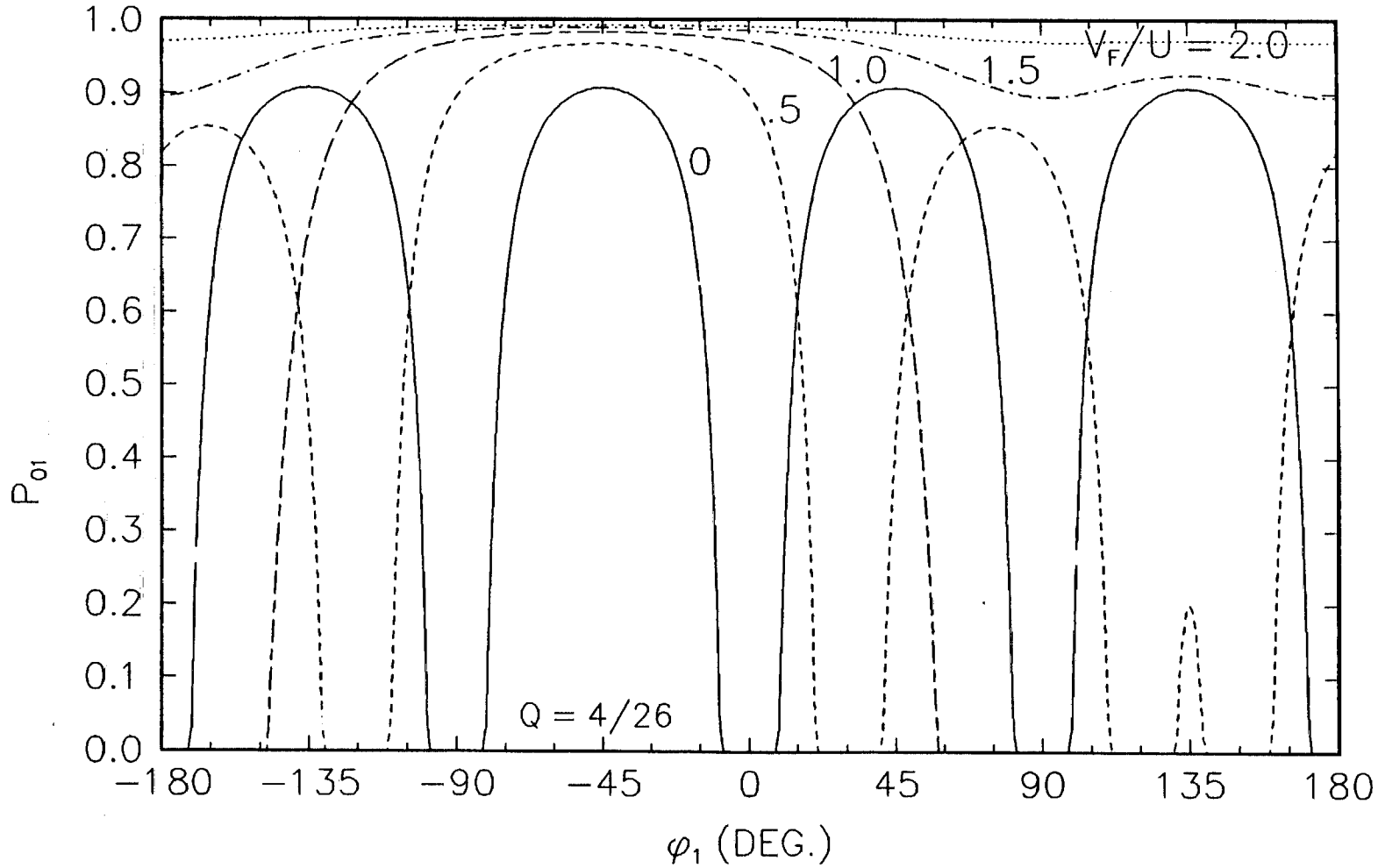

Figure 21. Probability of Particle Detection in Coincidence Mode for Q=4/26.

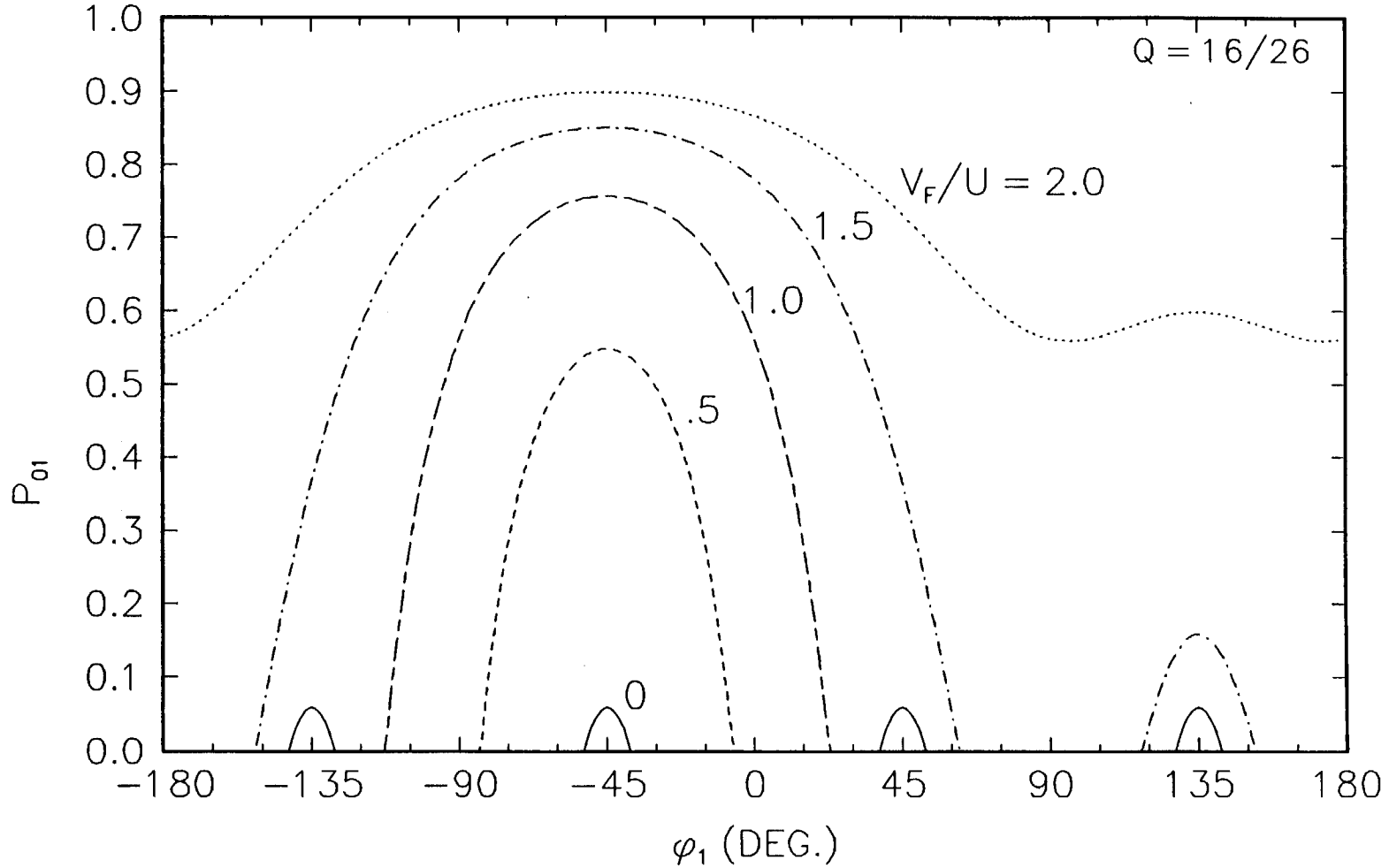

Figure 22. Probability of Particle Detection in Coincidence Mode for Q=16/26.

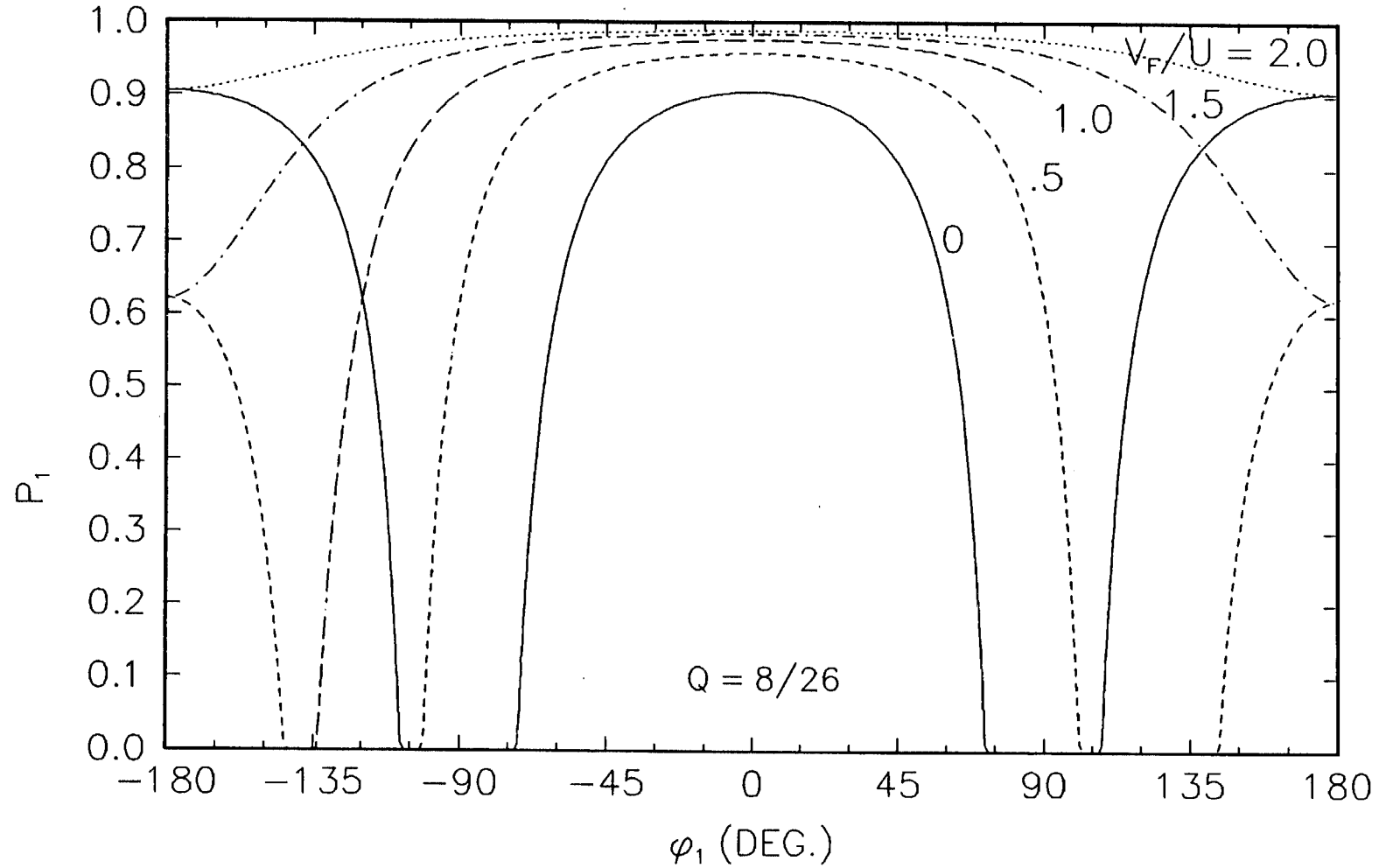

Figure 23. Probability of Particle Detection in Random Mode for Q=8/26.

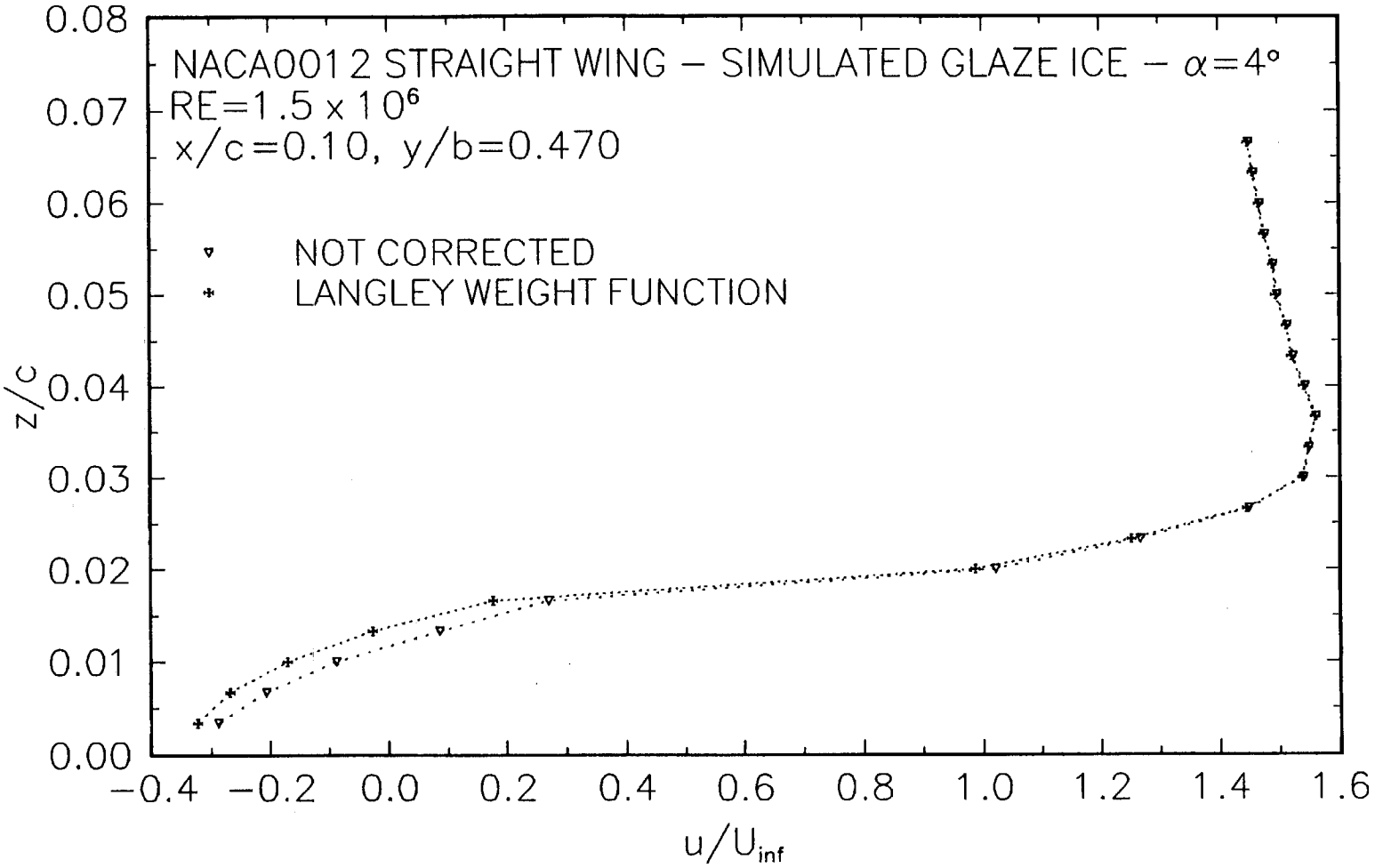

Figure 24. (u)-component Velocity Profile on the Upper Surface of the Iced Wing, y/b=0.470.

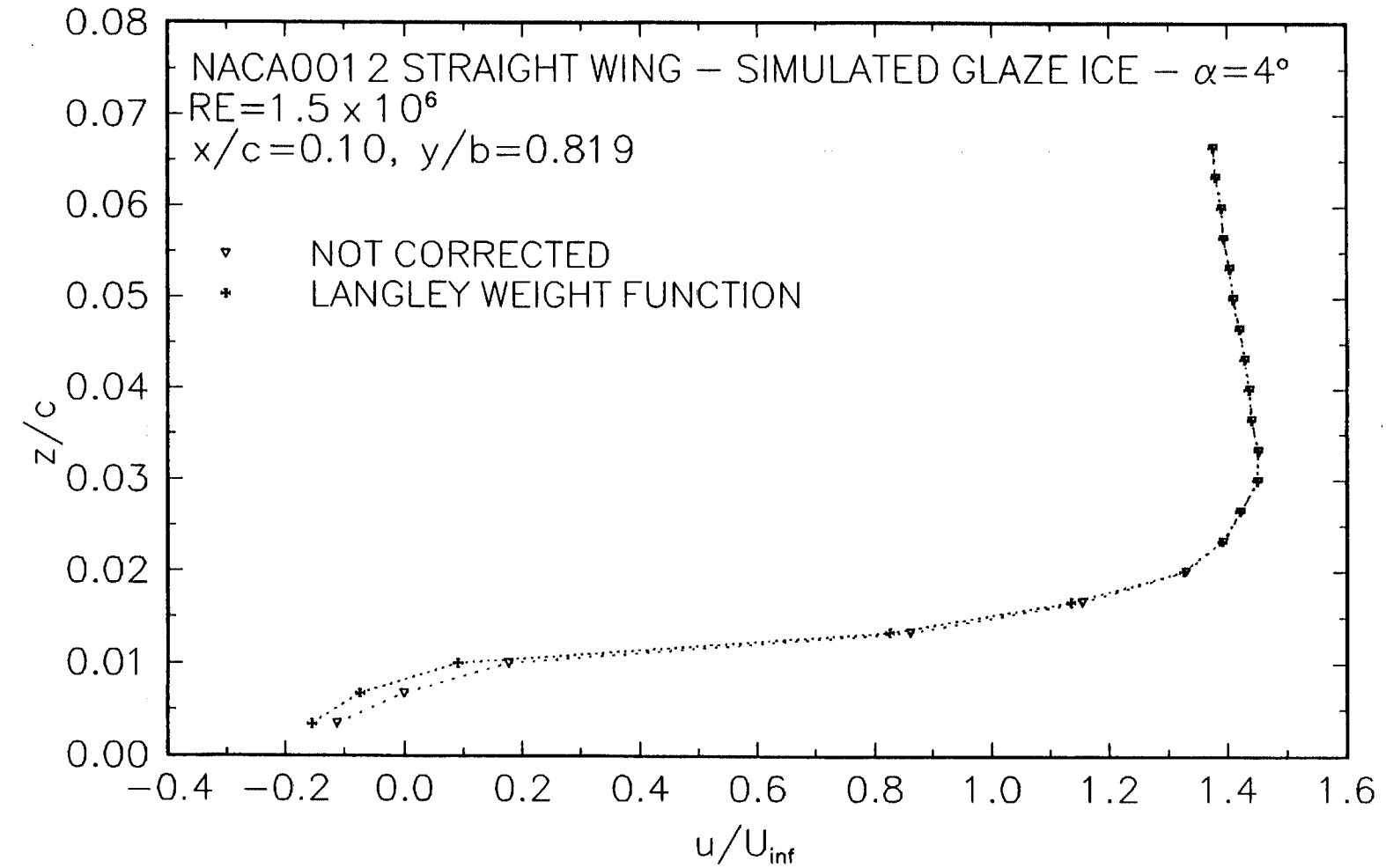

Figure 25. (u)-component Velocity Profile on the Upper Surface of the Iced Wing, y/b=0.819.

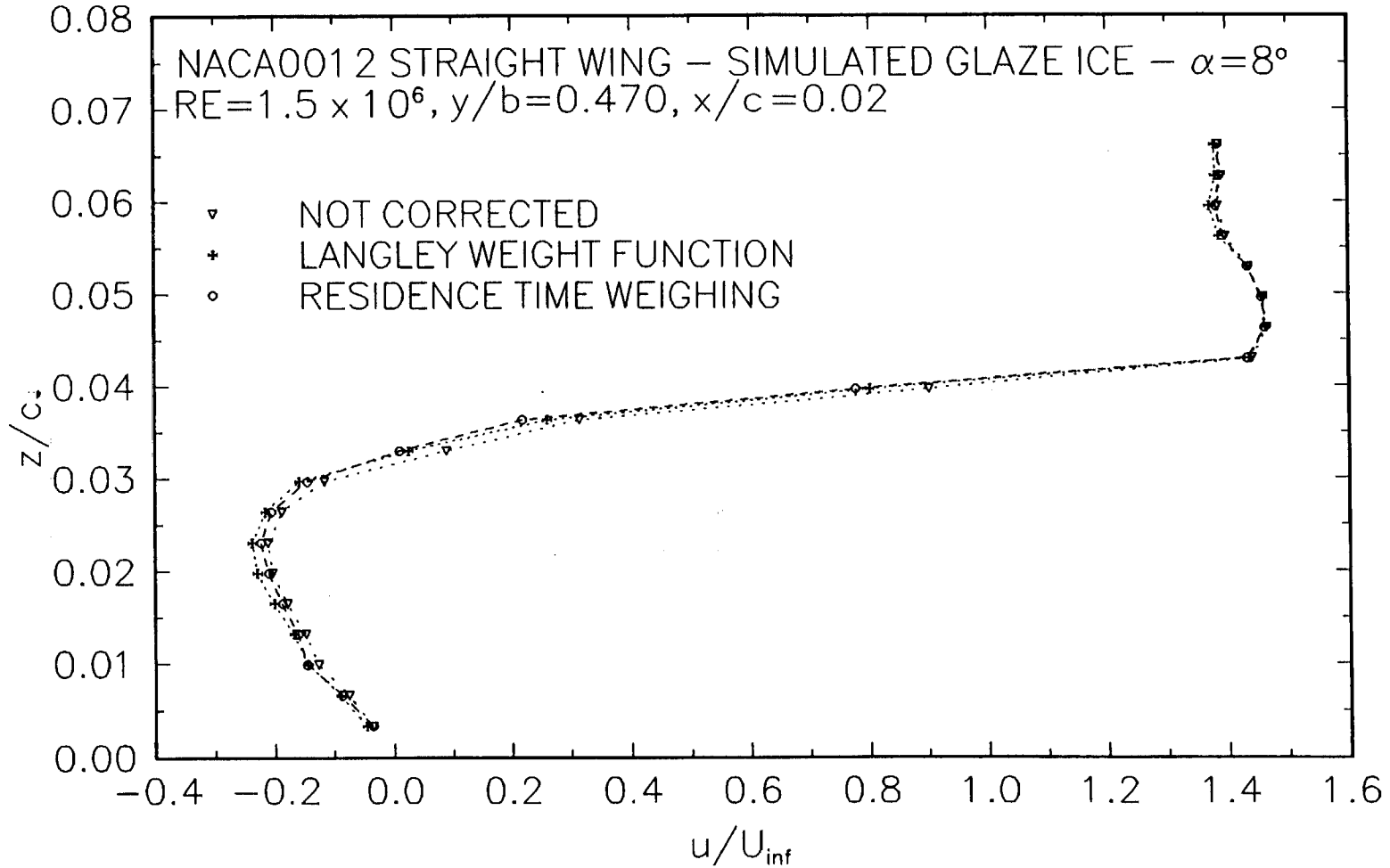

Figure 26. (u)-component Velocity Profile on the Upper Surface of the Iced Wing, y/b=0.470.

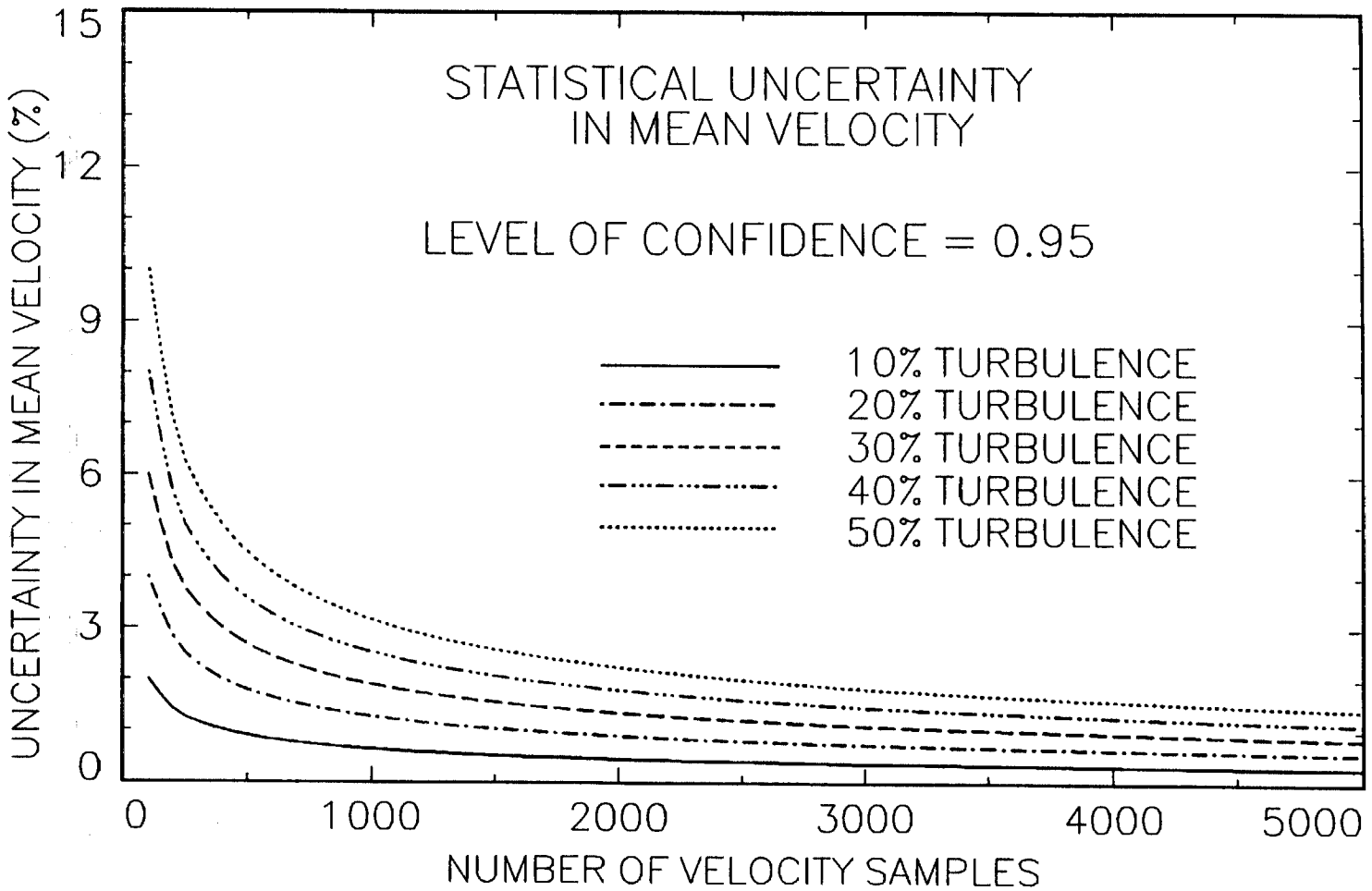

Figure 27. Statistical Uncertainty in the Mean Velocity.

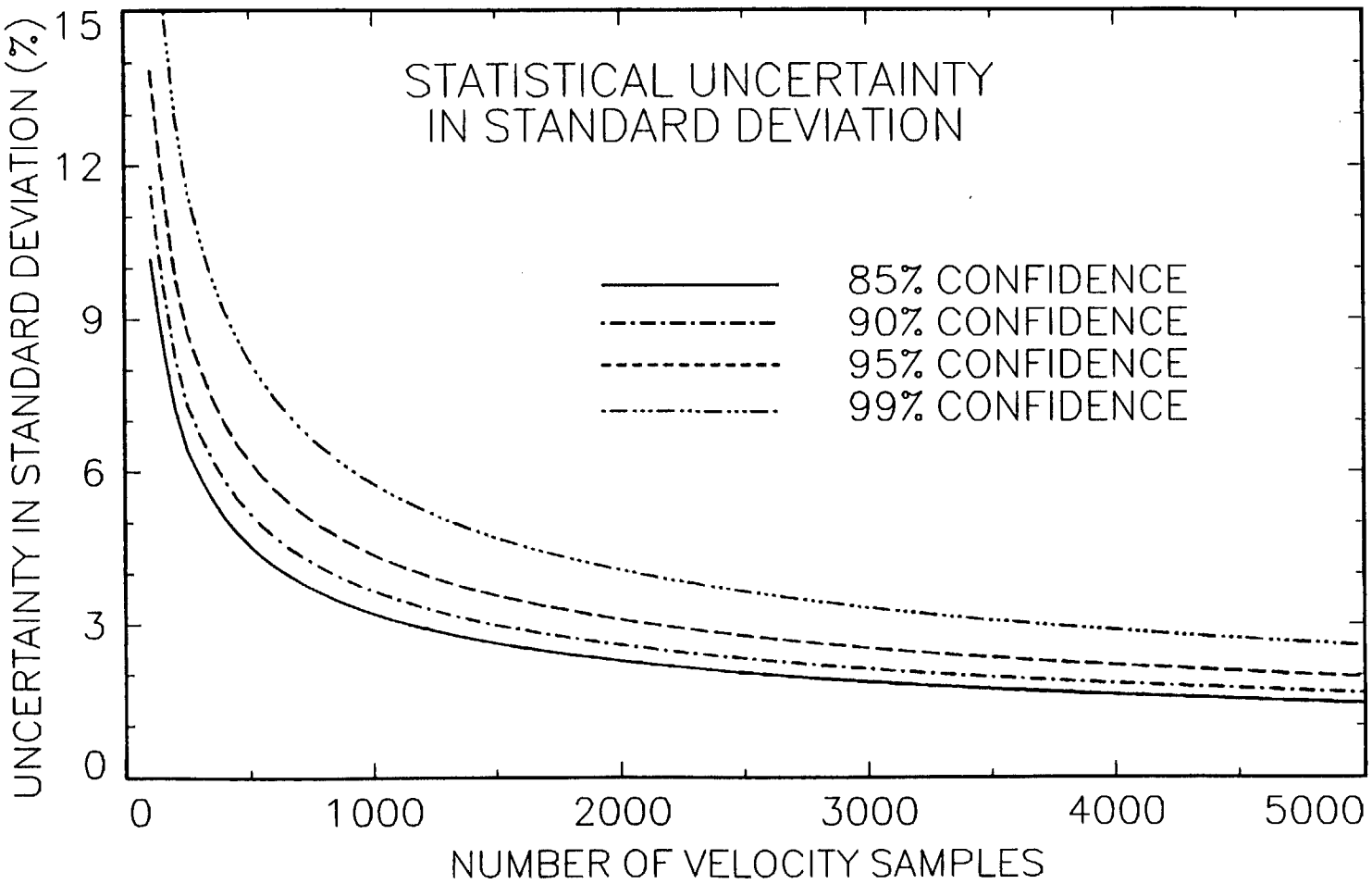

Figure 28. Statistical Uncertainty in the Standard Deviation.

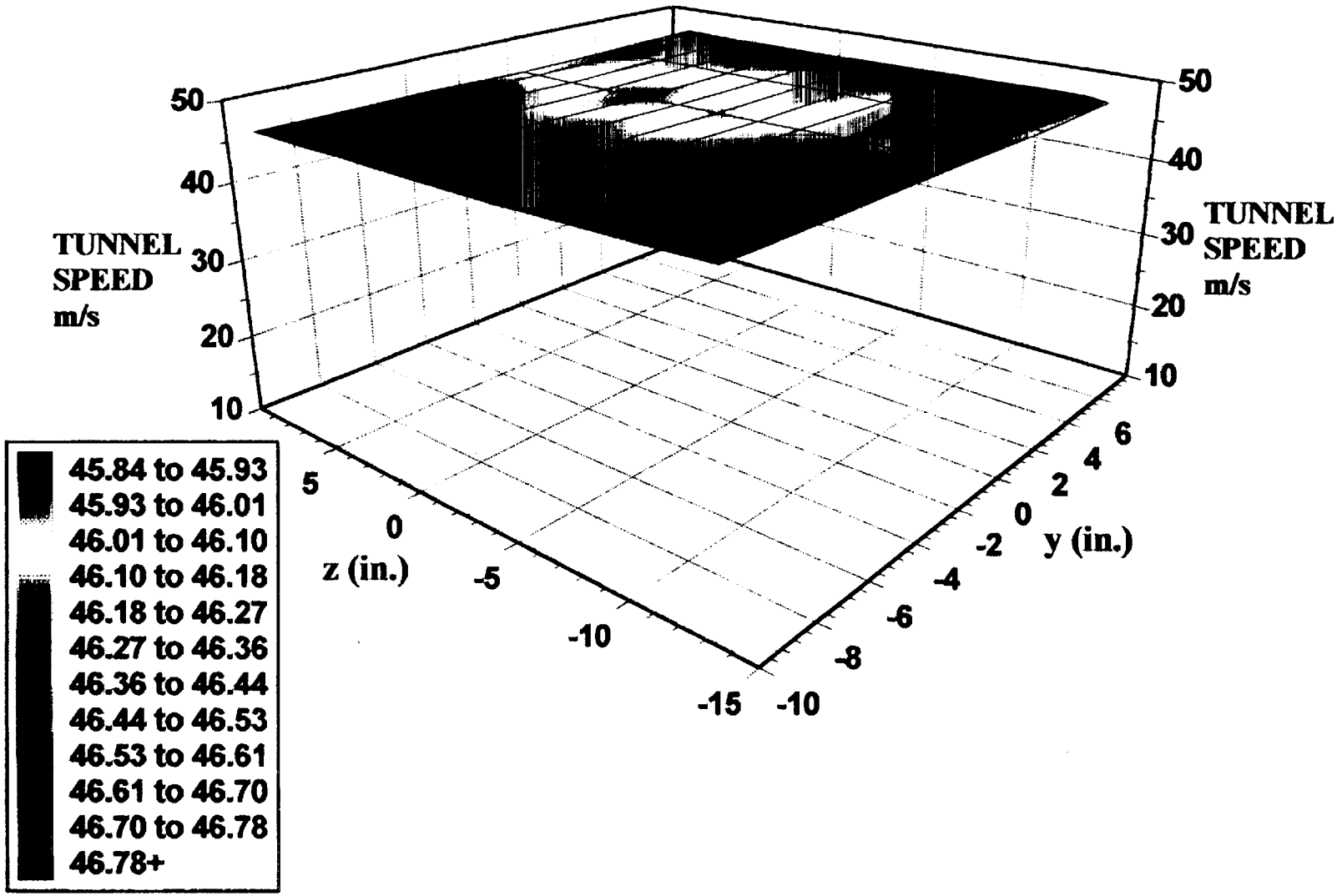

Figure 29. Tunnel Speed Profile; Measurement Location: 4" (10.16 cm) Into The Test Section.

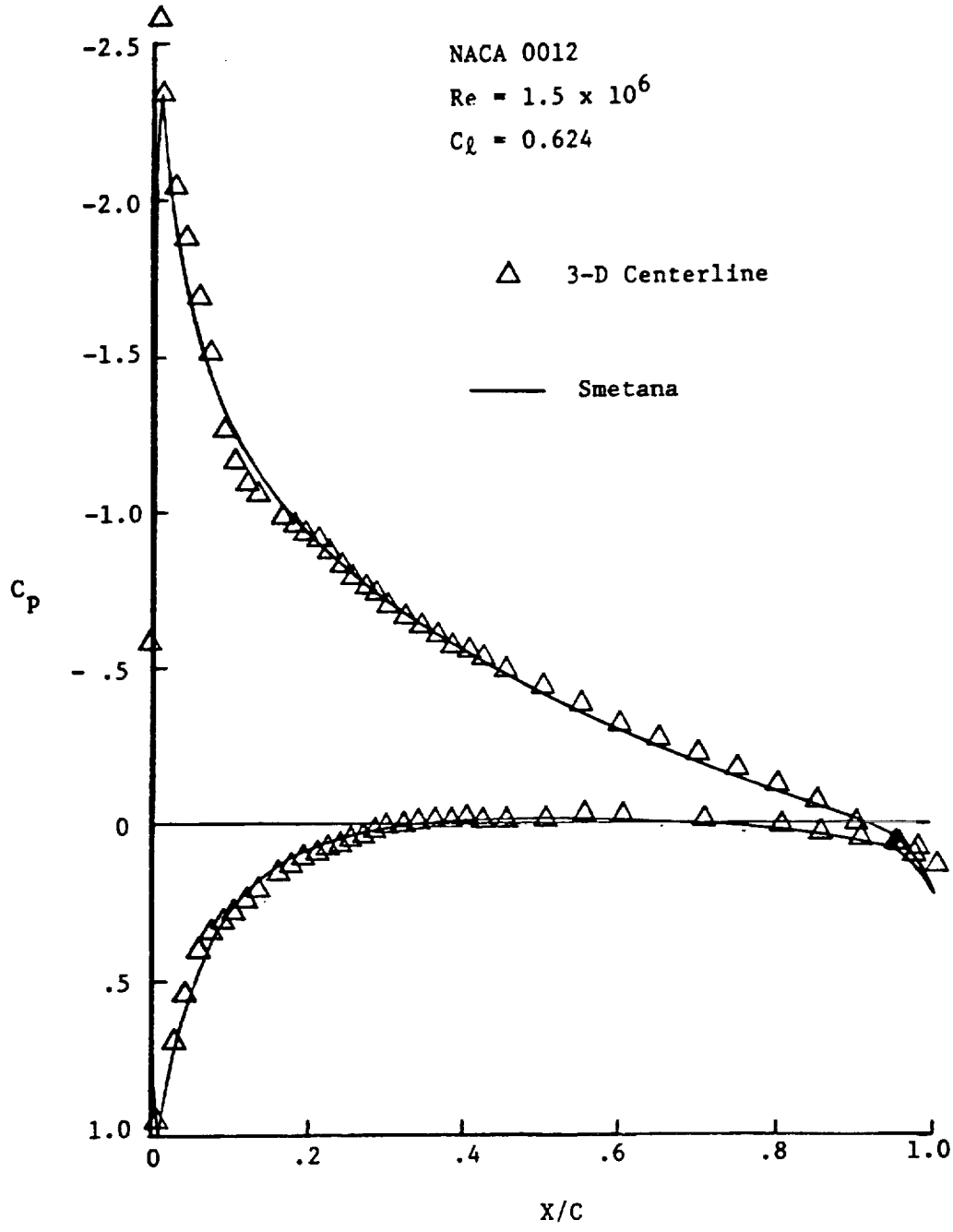

Figure 30. Surface Pressure Distribution from Wing Midspan Compared to Theory

PAGE 162 INTENTIONALLY BLANK

PRECEDING PAGE BLANK NOT FILMED

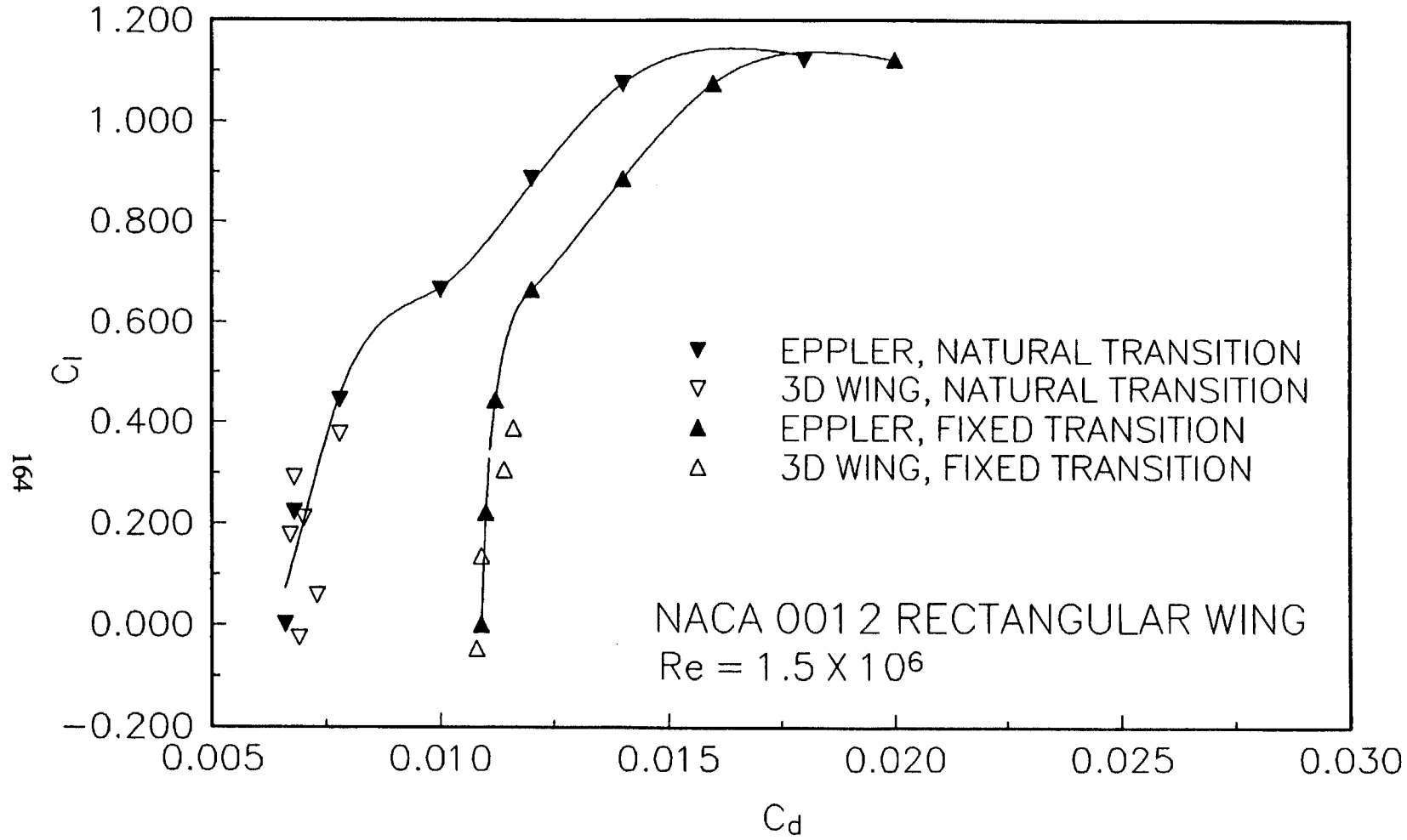

Figure 31. Drag Polar of the Wing Midspan Compared to Theory.

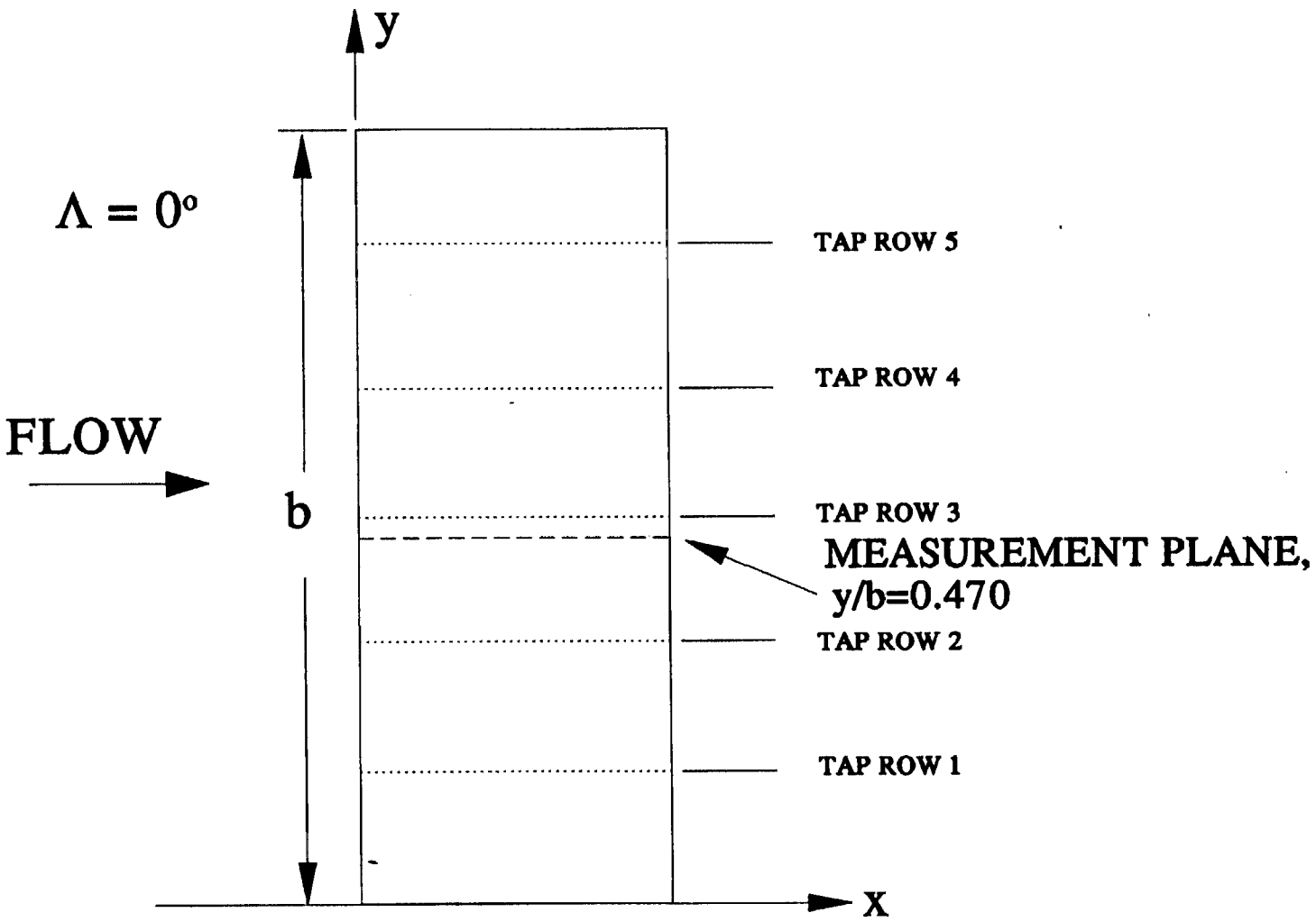

Figure 32. Measurement Plane on the Upper Surface of the Clean Wing.

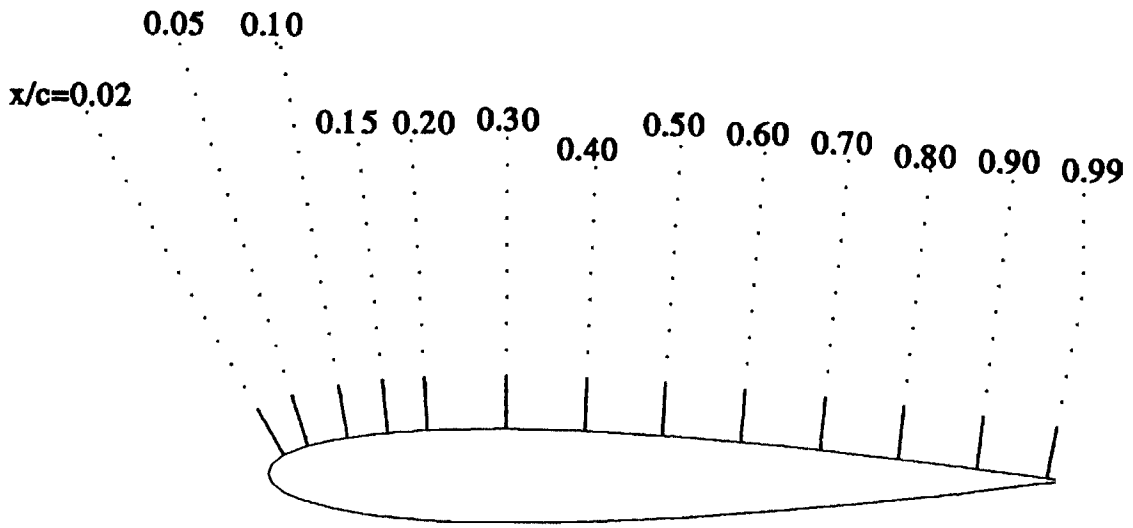

Figure 33. Measurement Locations on the Clean Wing at y/b=0.470, α=0.

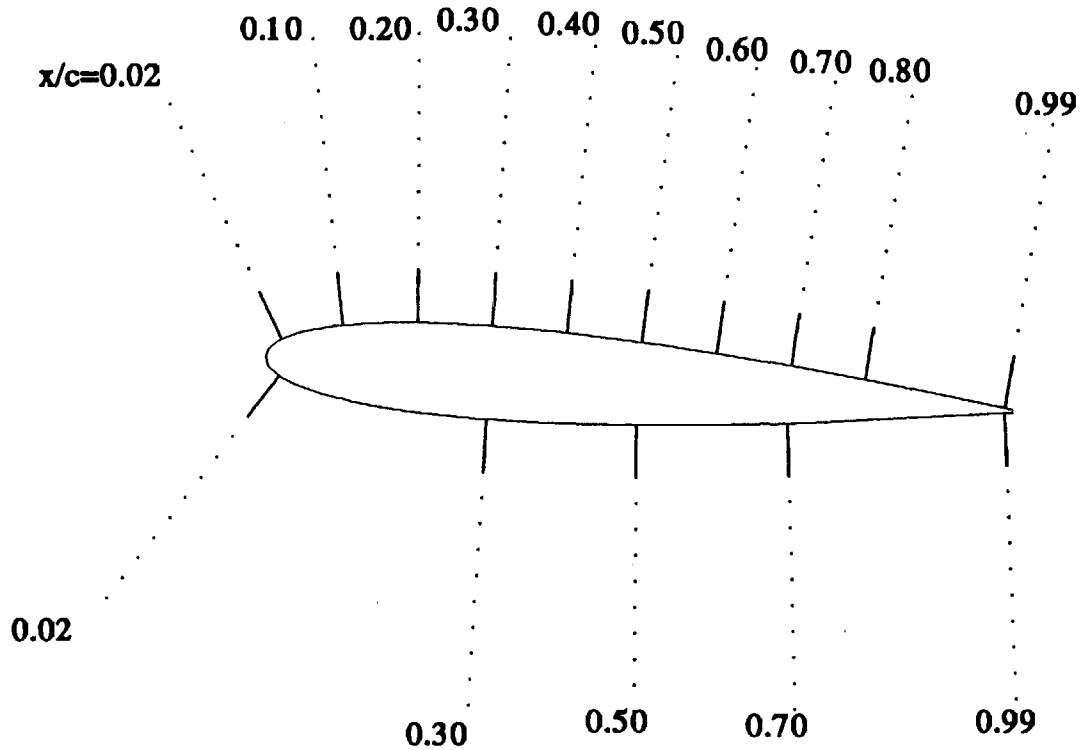

Figure 34. Measurement Locations on the Clean Wing at y/b=0.470, α=4.

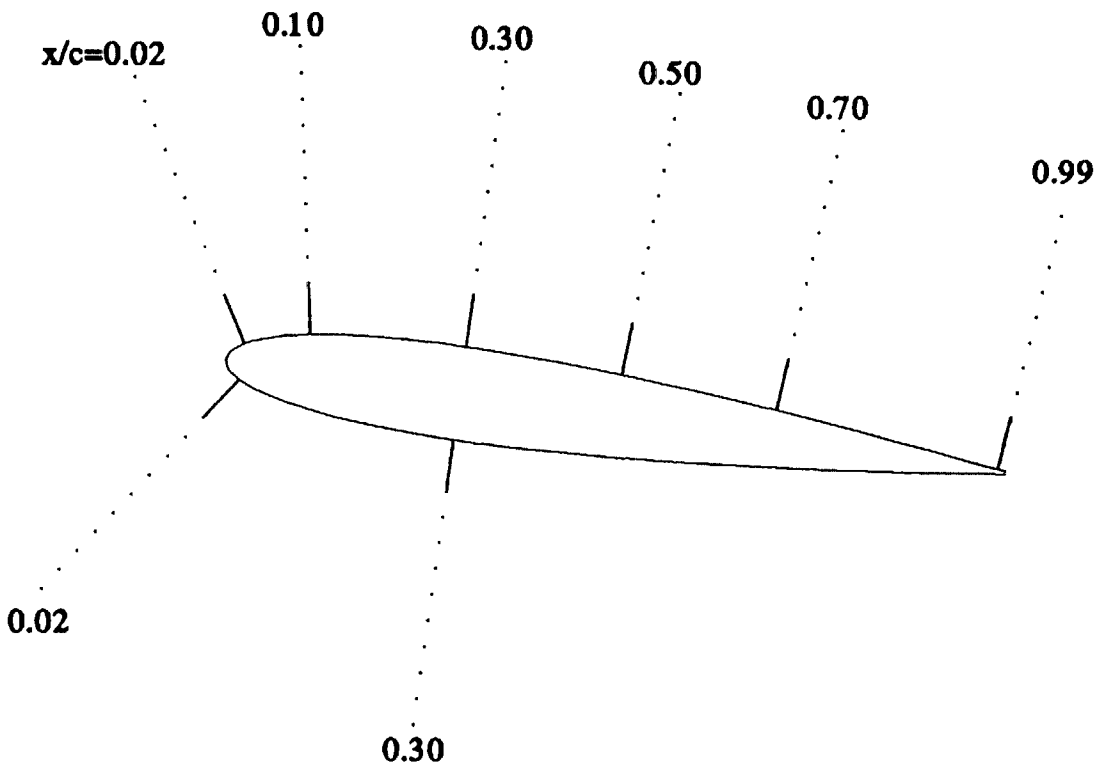

Figure 35. Measurement Locations on the Clean Wing at y/b=0.470, α=8.

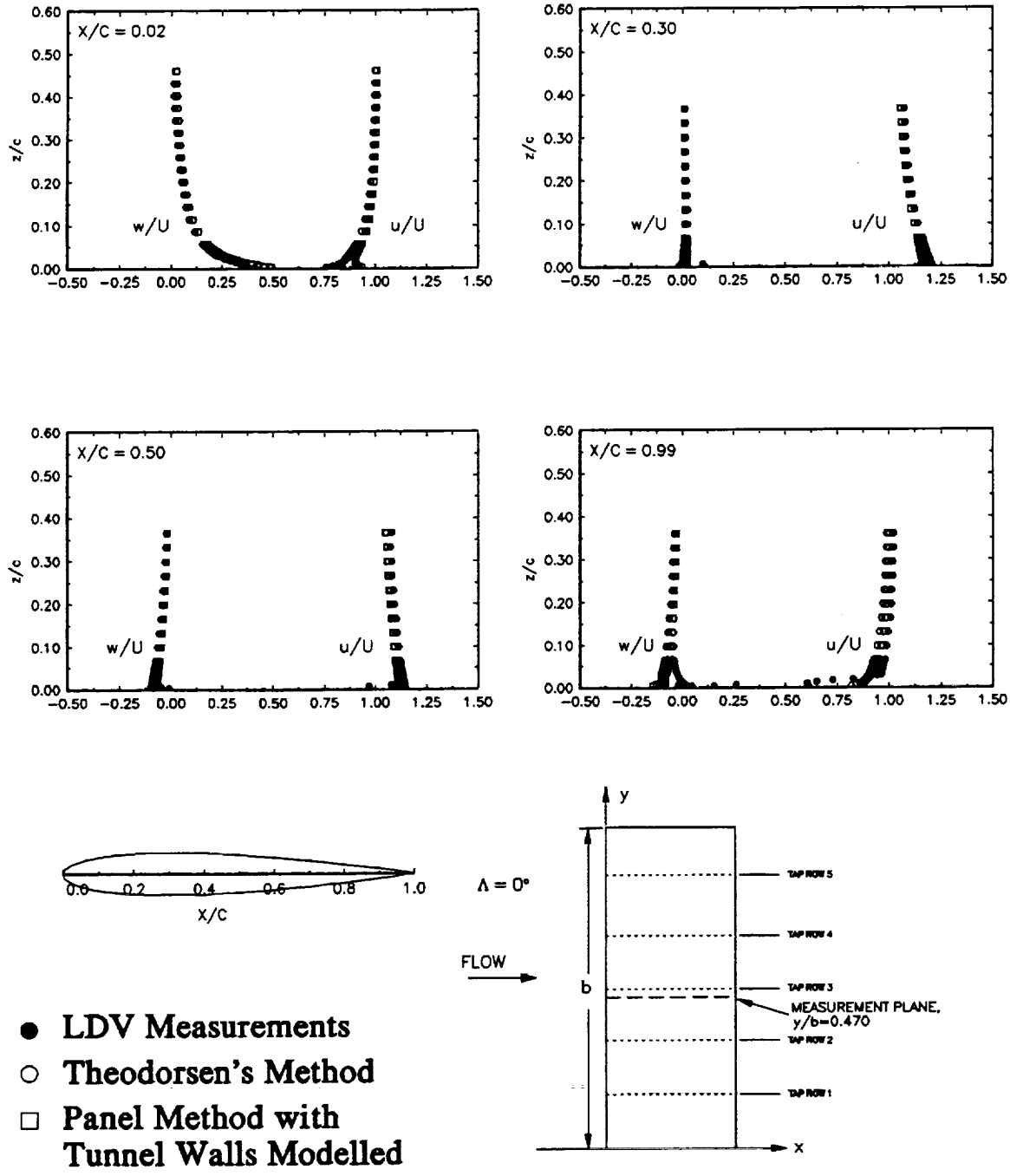

Figure 36. Velocity Profiles on the Clean Rectangular Wing at $\alpha = 0$, Re = 1.5 Million, from LDV Measurements and Computation.

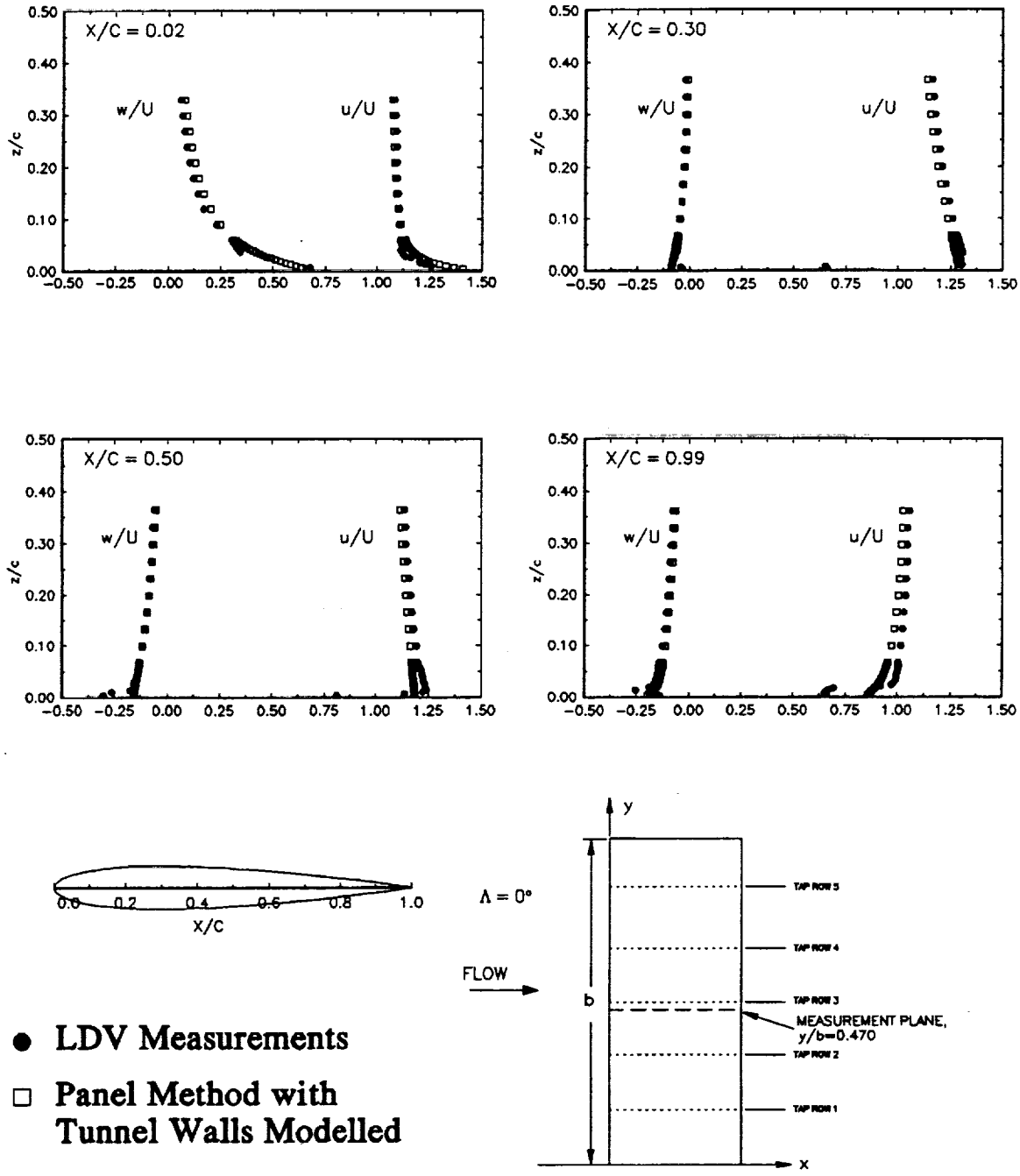

Figure 37. Velocity Profiles on the Clean Rectangular Wing at $\alpha = 4$, Re = 1.5 Million, from LDV Measurements and Computation.

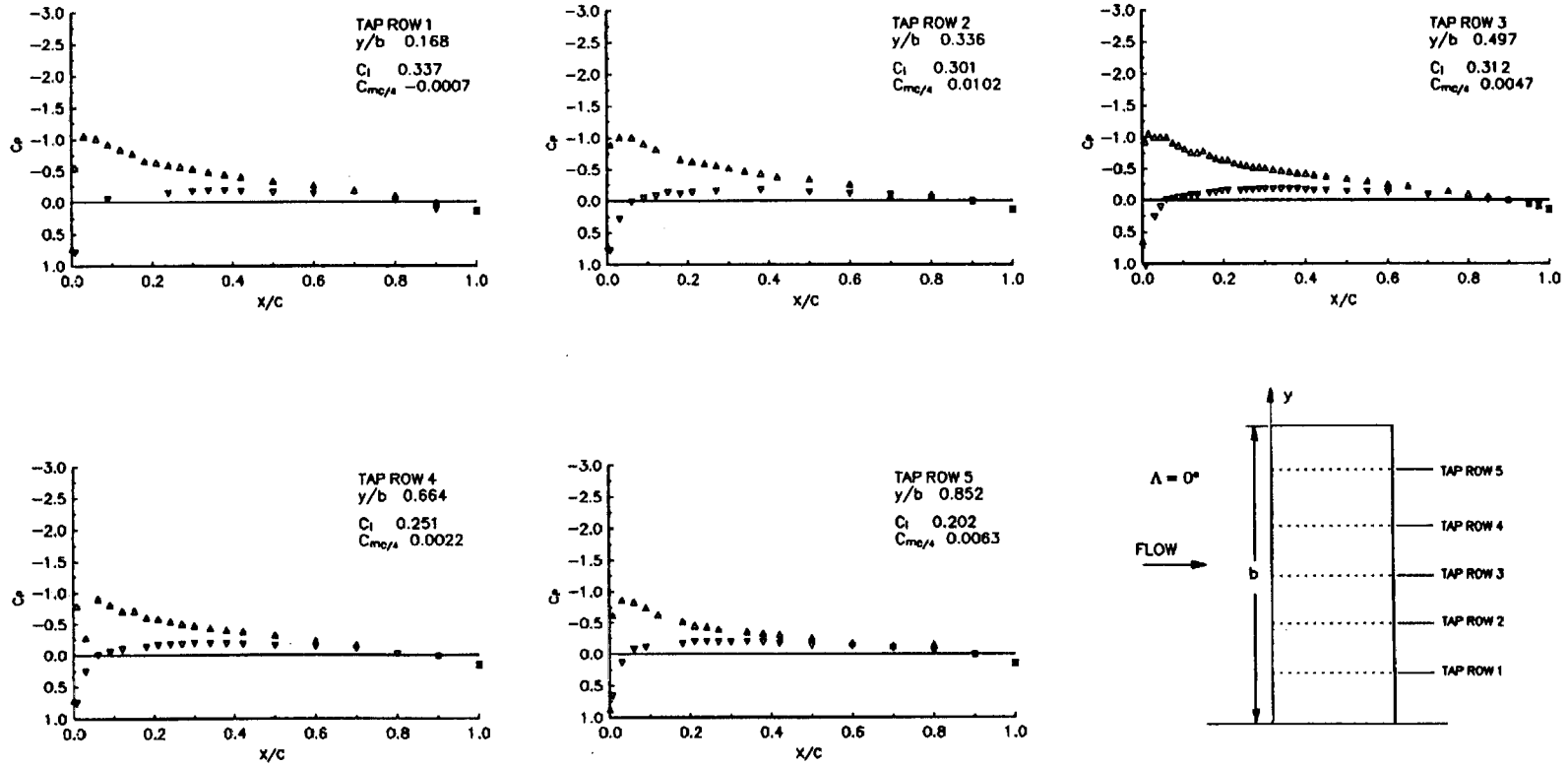

NACA 0012 RECTANGULAR WING $\alpha_{GEOMETRIC}$ **4°**
CLEAN LEADING EDGE **MACH** **0.13**
NO TRIP USED **RE** **1.45 X 10⁶**

Figure 38. Pressure Distribution on the Clean Wing at α=4.

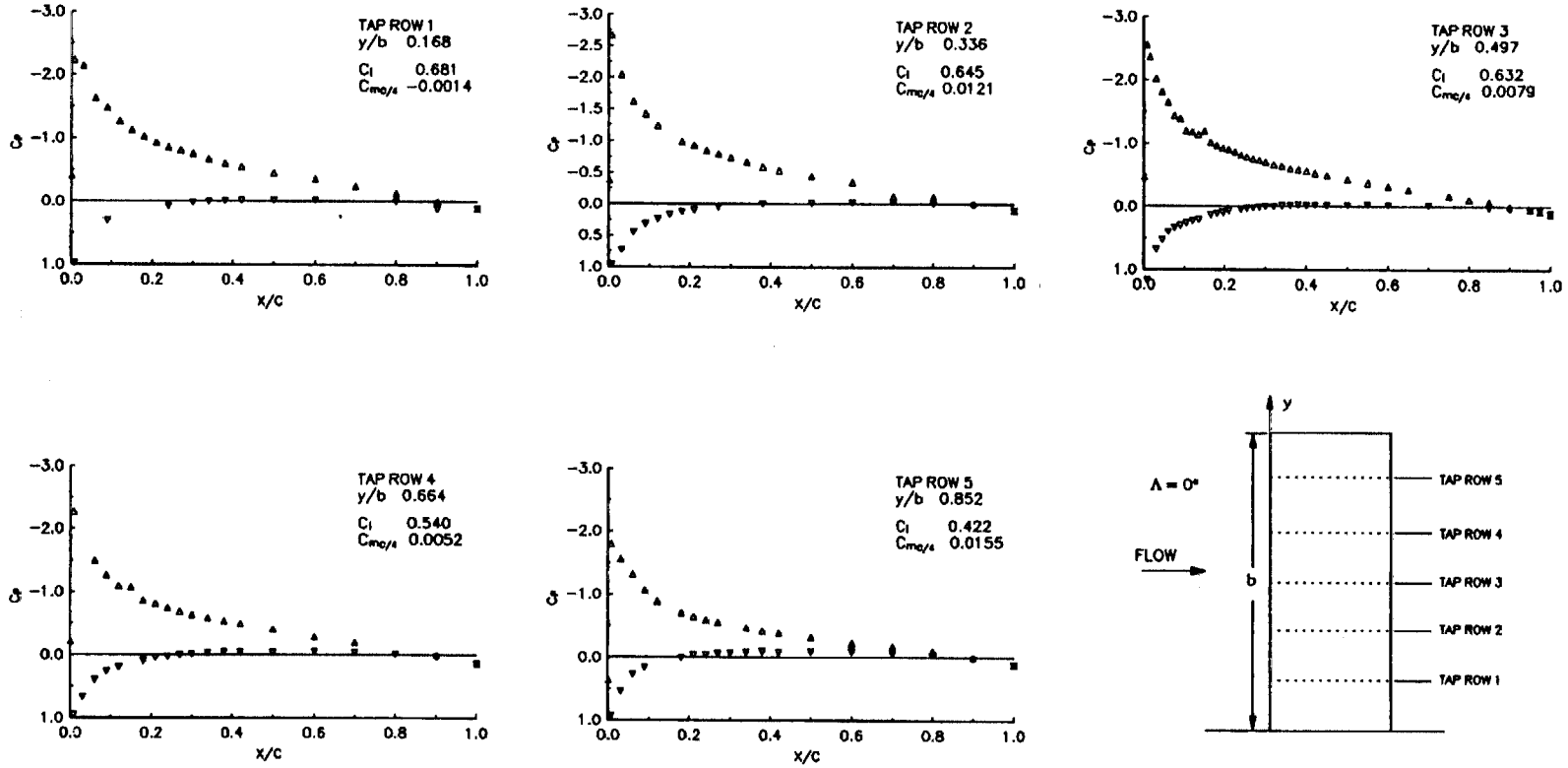

NACA 0012 RECTANGULAR WING $\alpha_{GEOMETRIC}$ **8°**
CLEAN LEADING EDGE **MACH** **0.13**
TRIP AT X/C=0.05 **RE** **1.45 X 10⁶**

Figure 39. Pressure Distribution on the Clean Wing at α=8.

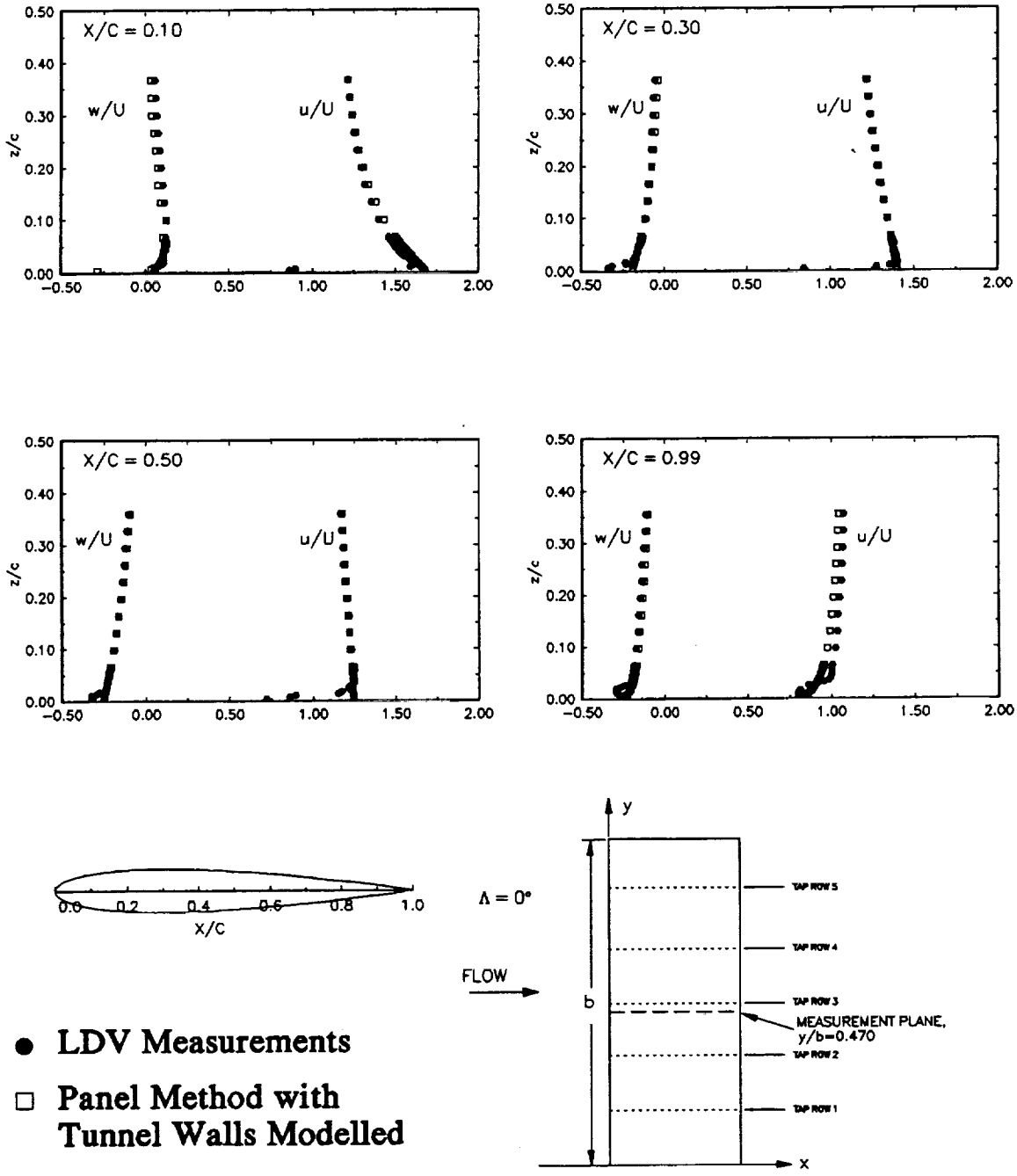

Figure 40. Velocity Profiles on the Clean Rectangular Wing at $\alpha = 8$, Re = 1.5 Million, from LDV Measurements and Computation.

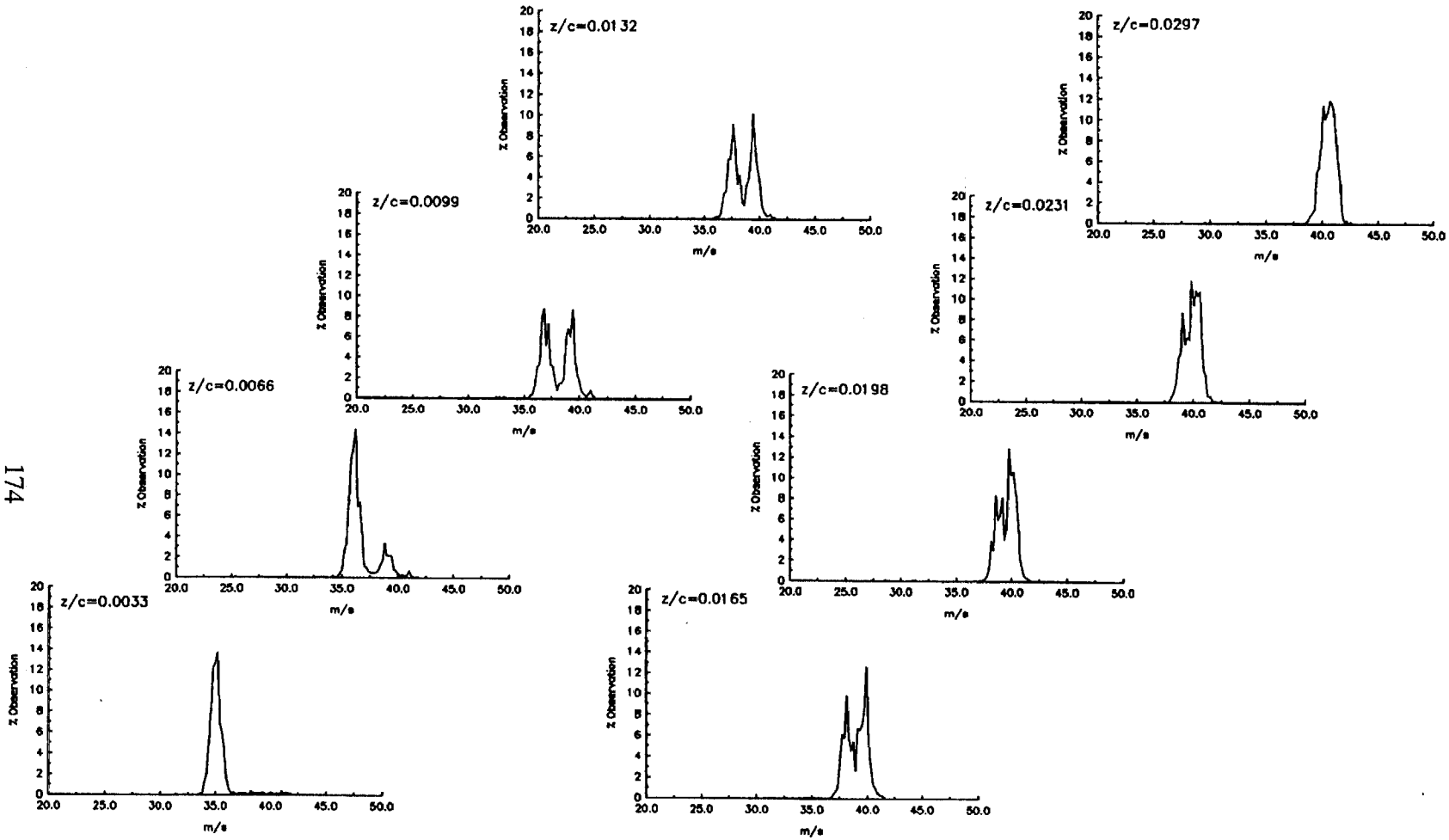

Figure 41. Velocity Histograms for the (u)-component on the Clean Wing at α=0, x/c=0.02, y/b=0.470, Re=1.5 Million.

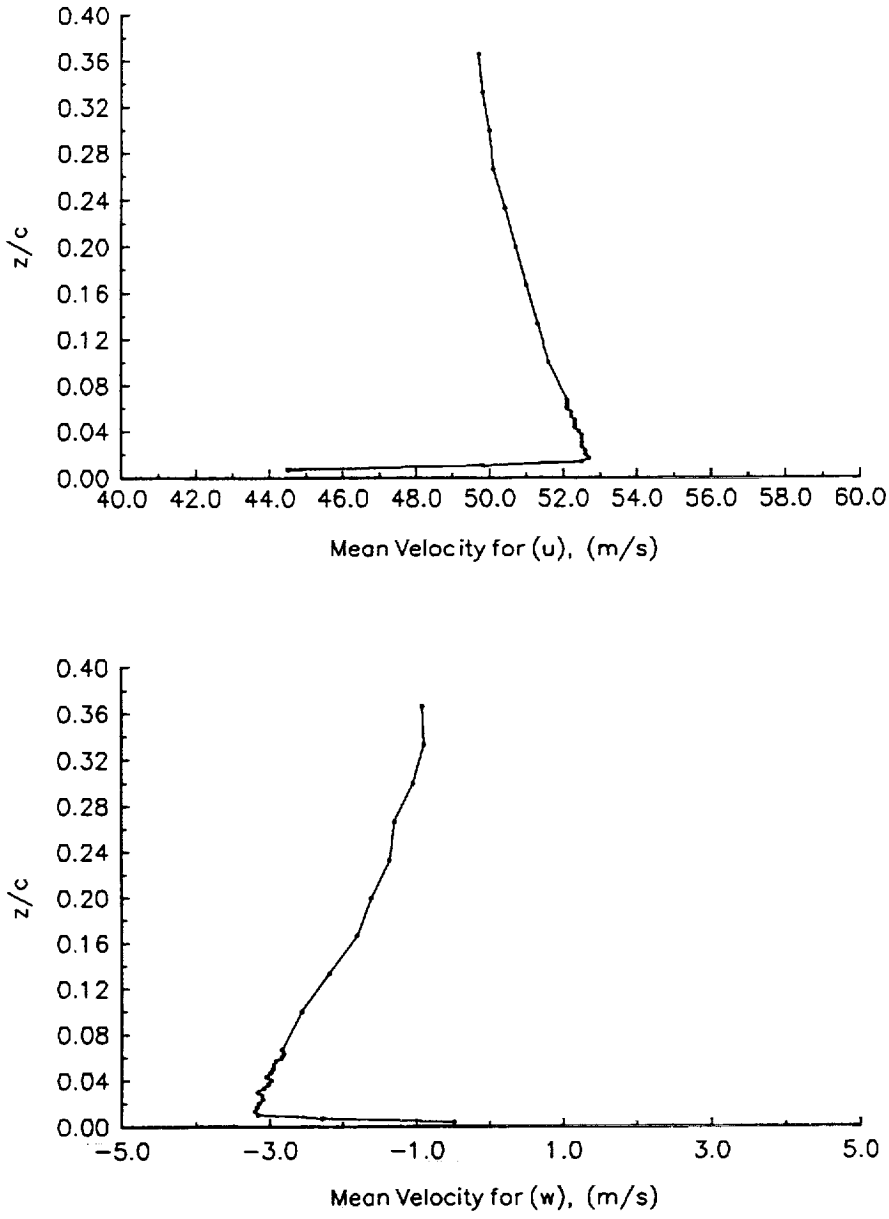

Figure 42. Mean (u) and (w) Velocity Profiles on the Clean Wing at $\alpha = 0$, Re = 1.5 Million, x/c = 0.50, y/b = 0.470.

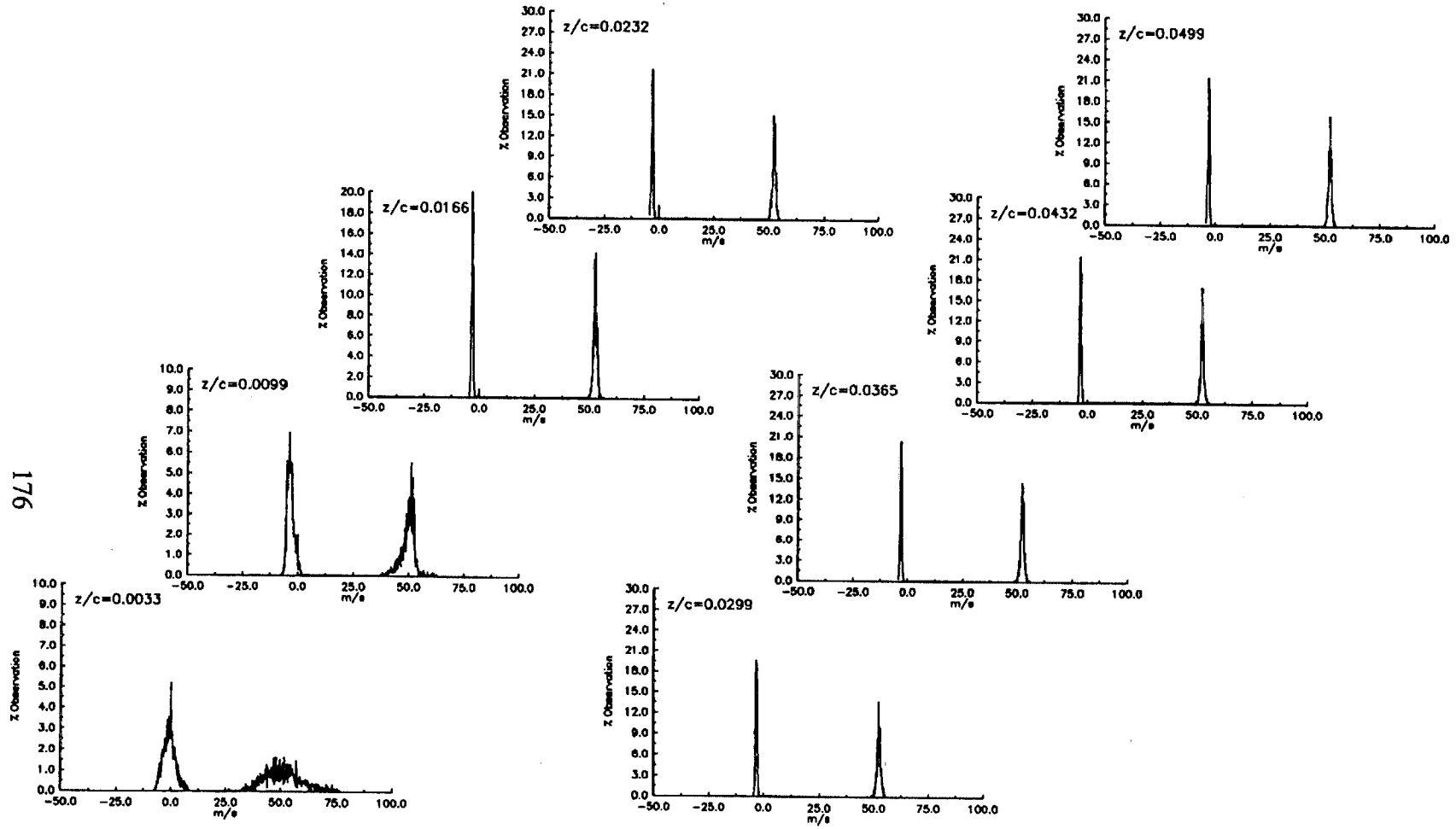

Figure 43. Velocity Histograms for the (u)- and (w)-components on the Clean Wing at α=0, x/c=0.50, y/b=0.470, Re=1.5 Million.

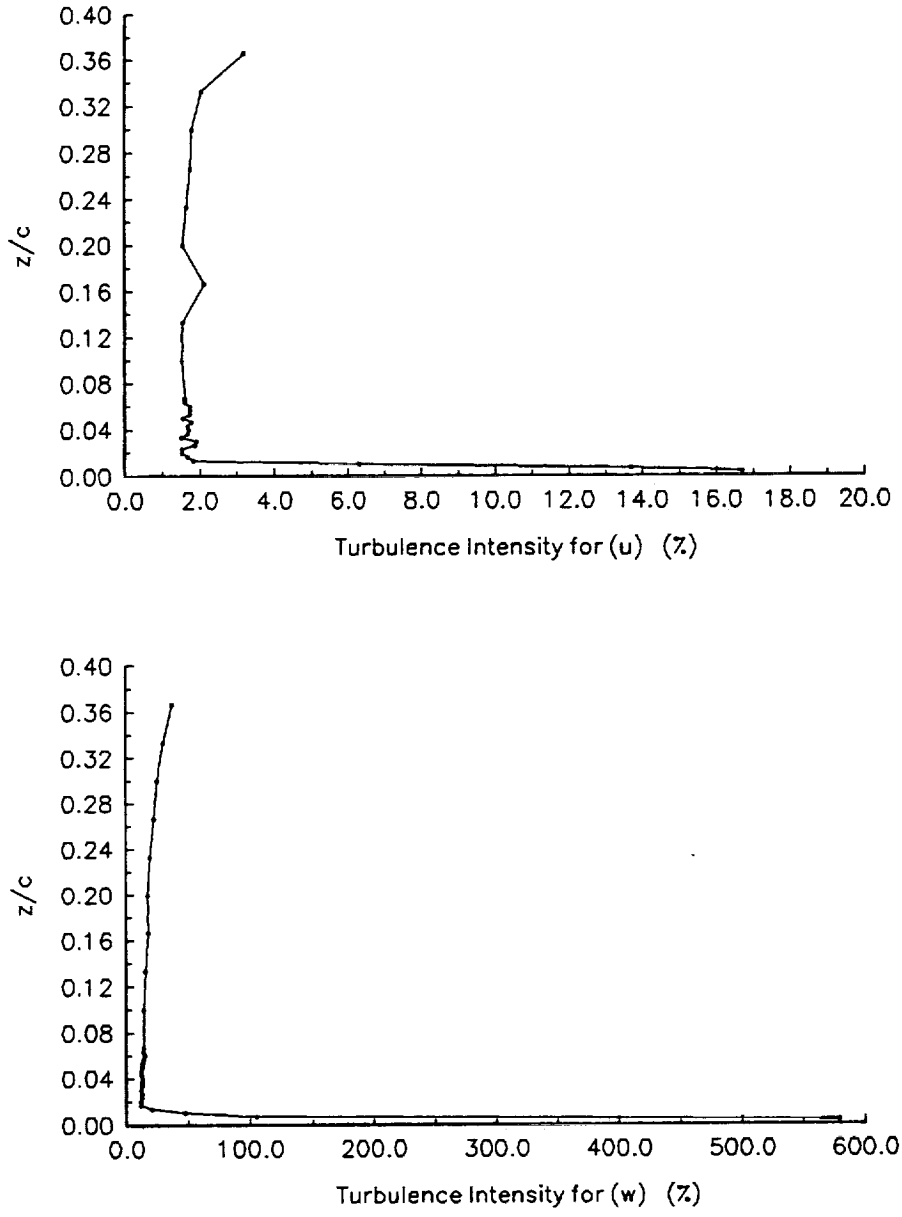

Figure 44. (u) and (w) Turbulence Intensity Profiles on the Clean Wing at $\alpha = 0$, Re = 1.5 Million, x/c = 0.50, y/b = 0.470.

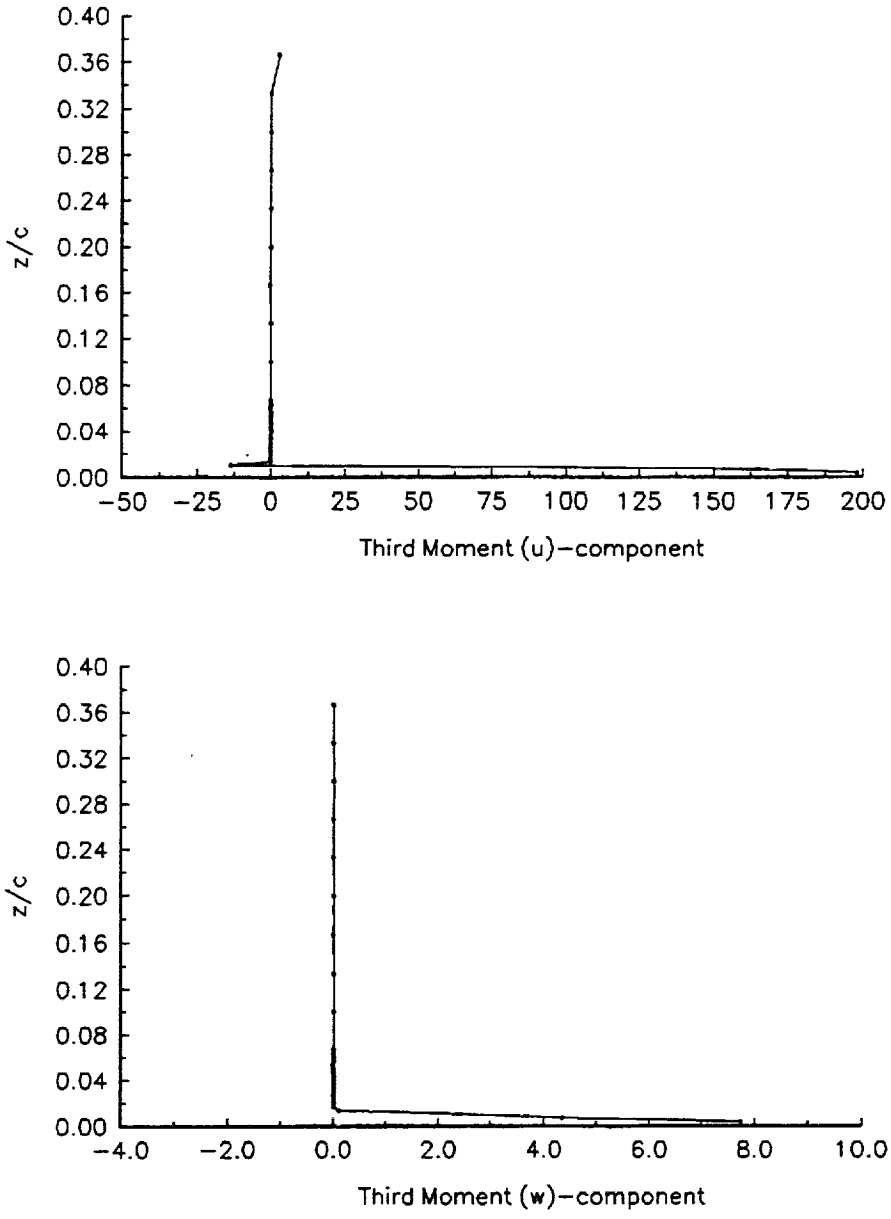

Figure 45. (u) and (w) Third Moment Profiles on the Clean Wing at $\alpha = 0$, Re = 1.5 Million, x/c = 0.50, y/b = 0.470.

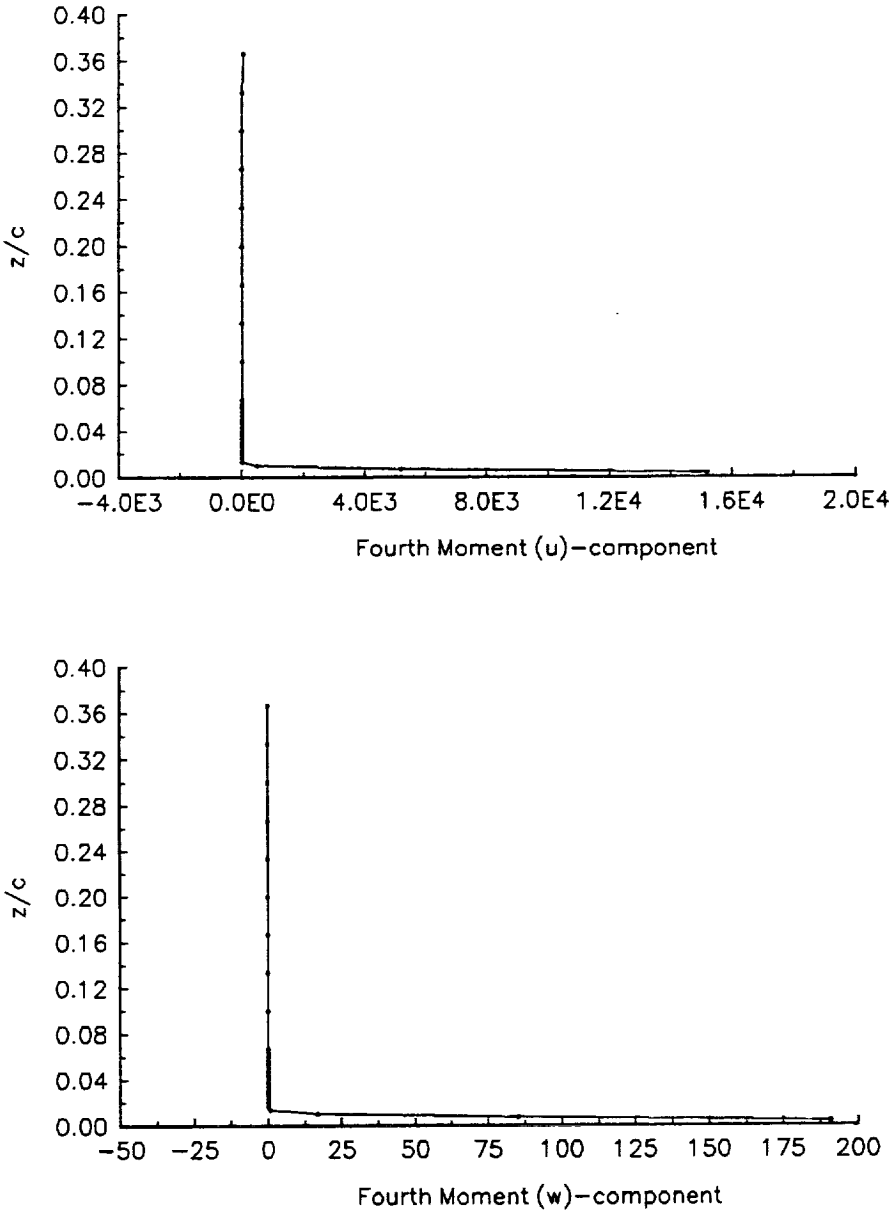

Figure 46. (u) and (w) Fourth Moment Profiles on the Clean Wing at $\alpha = 0$, Re = 1.5 Million, x/c = 0.50, y/b = 0.470.

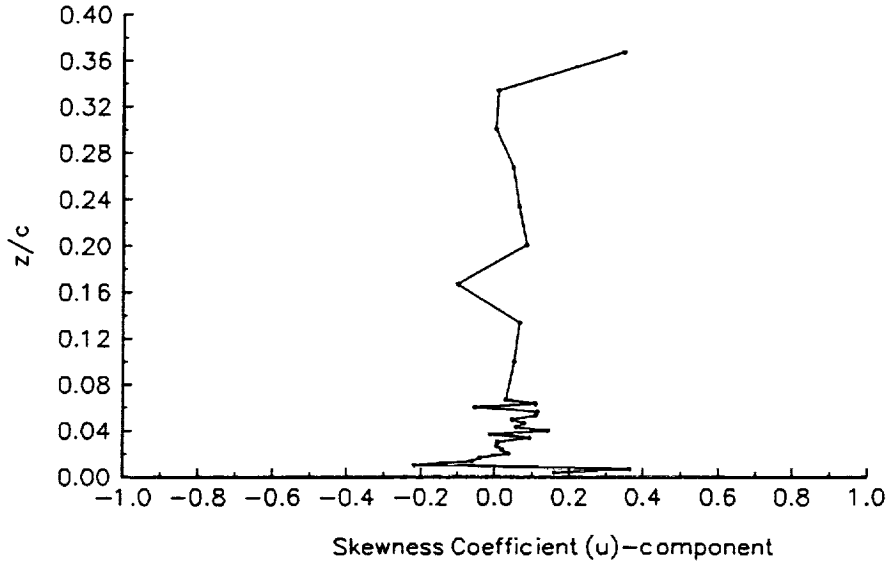

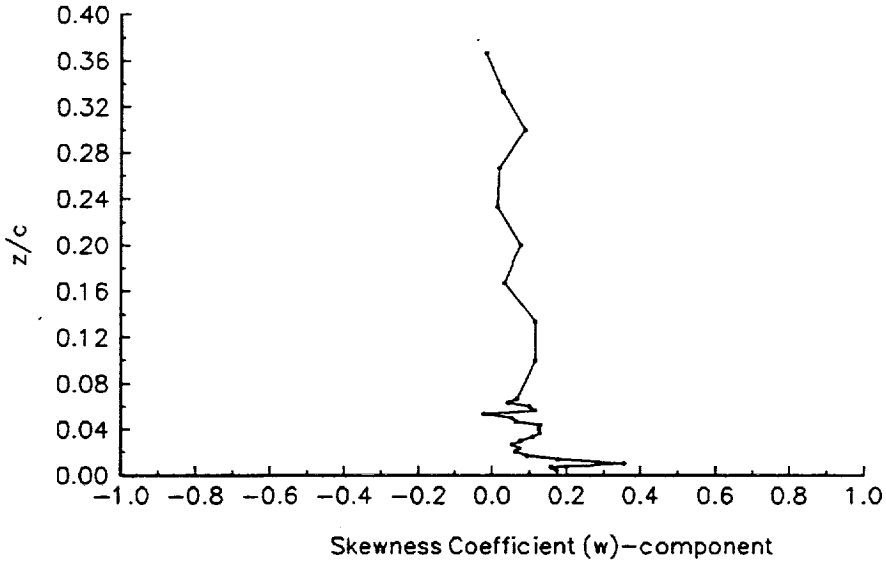

Figure 47. (u) and (w) Skewness Coefficient Profiles on the Clean Wing at $\alpha = 0$, Re = 1.5 Million, x/c = 0.50, y/b = 0.470.

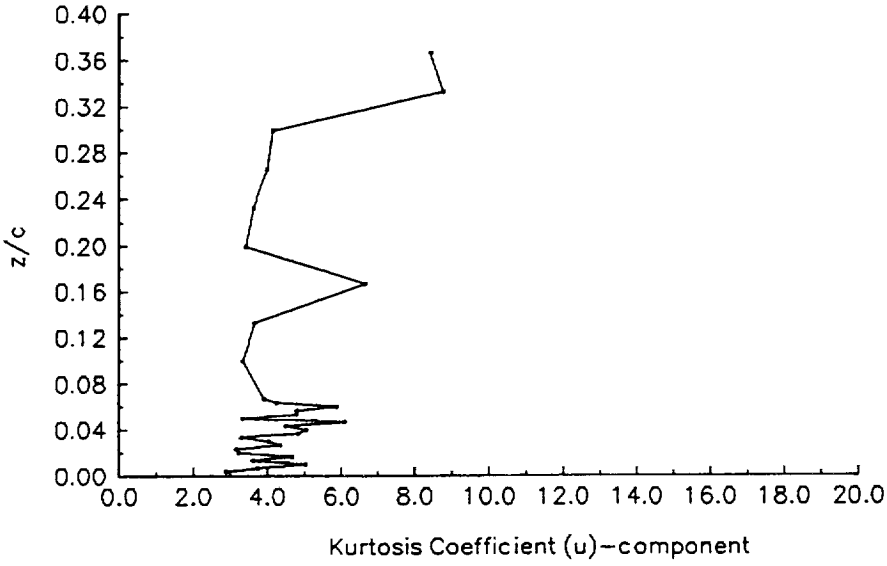

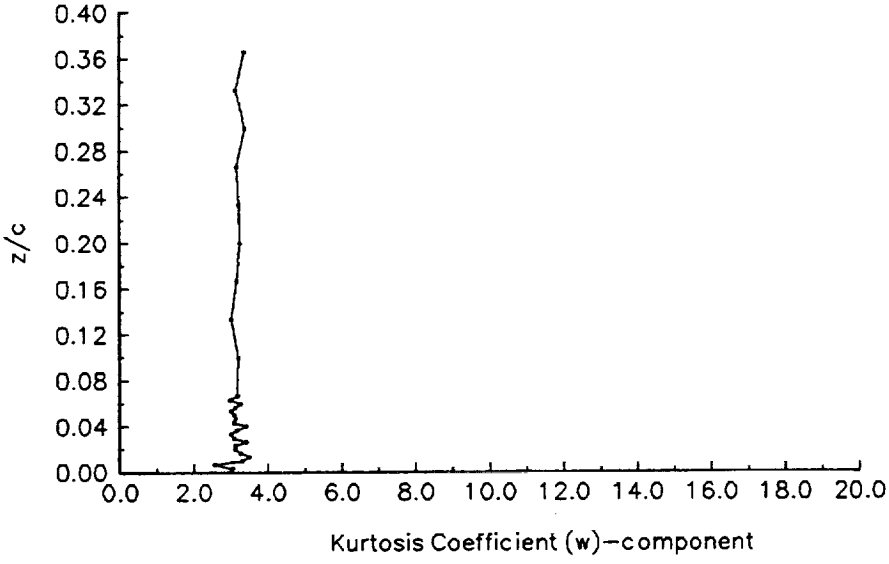

Figure 48. (u) and (w) Kurtosis Coefficient Profiles on the Clean Wing at $\alpha = 0$, Re = 1.5 Million, x/c = 0.50, y/b = 0.470.

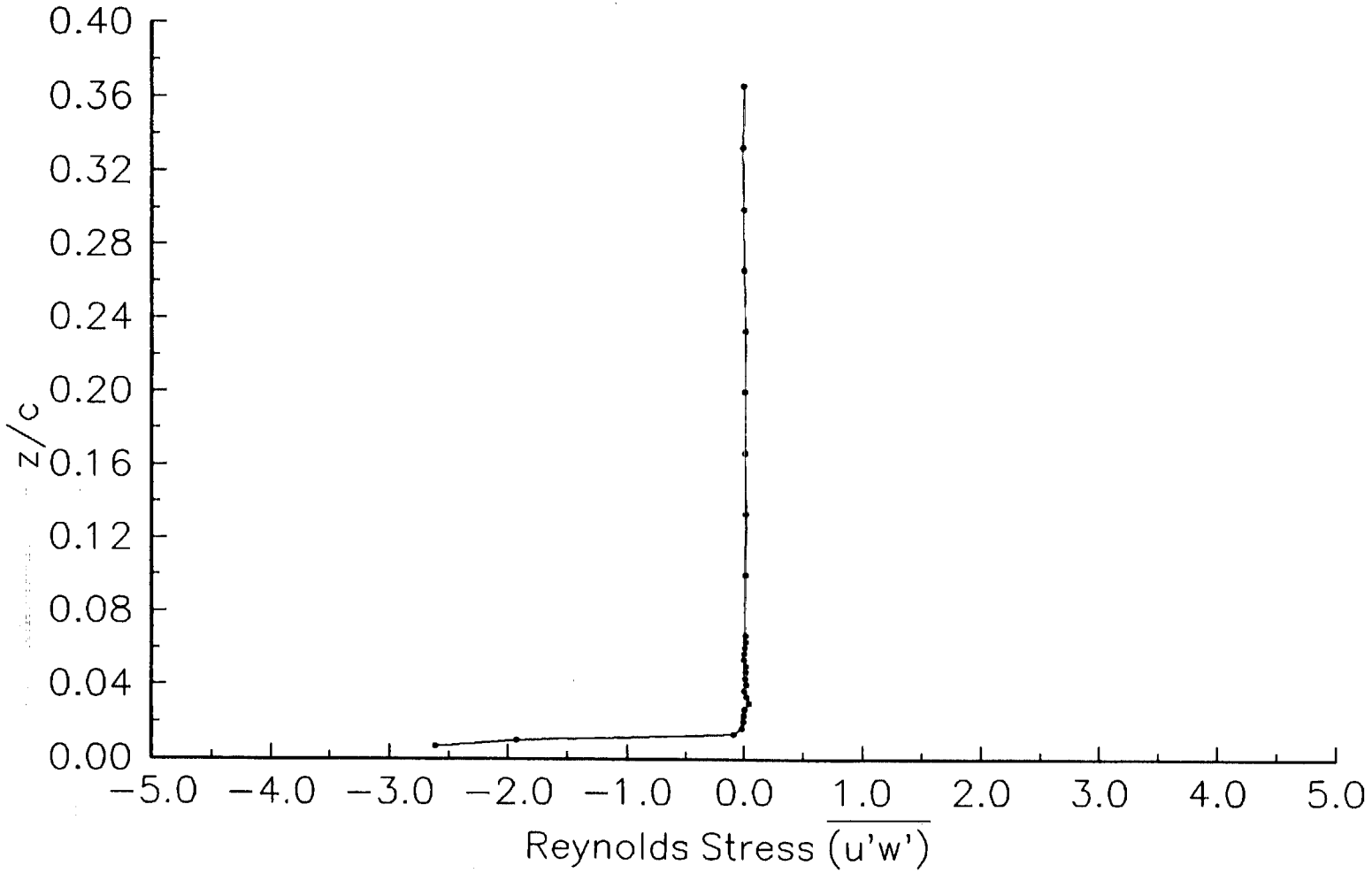

Figure 49. Reynolds Shear Stress Profile on the Clean Wing at x/c=0.50, y/b=0.470, α=0, Re=1.5 Million.

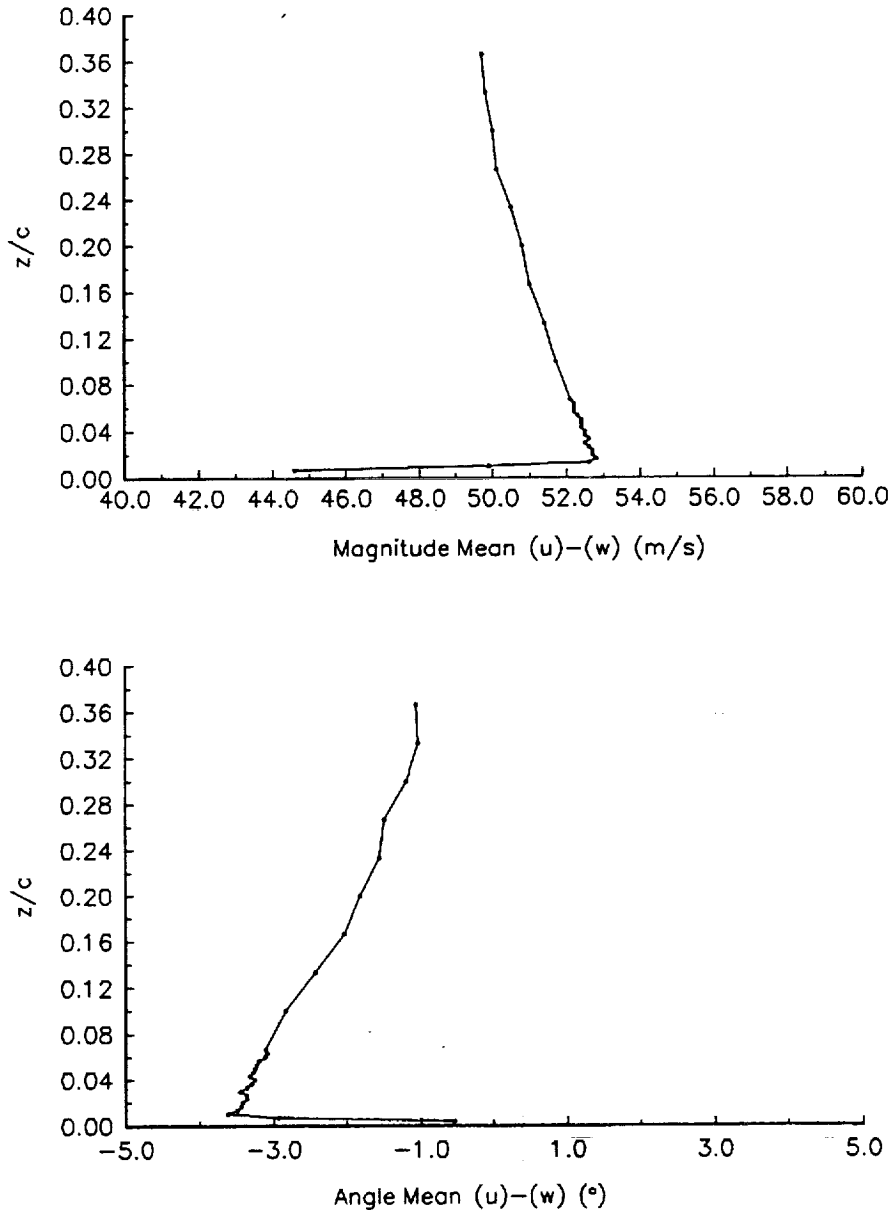

Figure 50. Magnitude and Angle of the Mean Velocity Vector on the Clean Wing at $\alpha = 0$, Re = 1.5 Million, x/c = 0.50, y/b = 0.470.

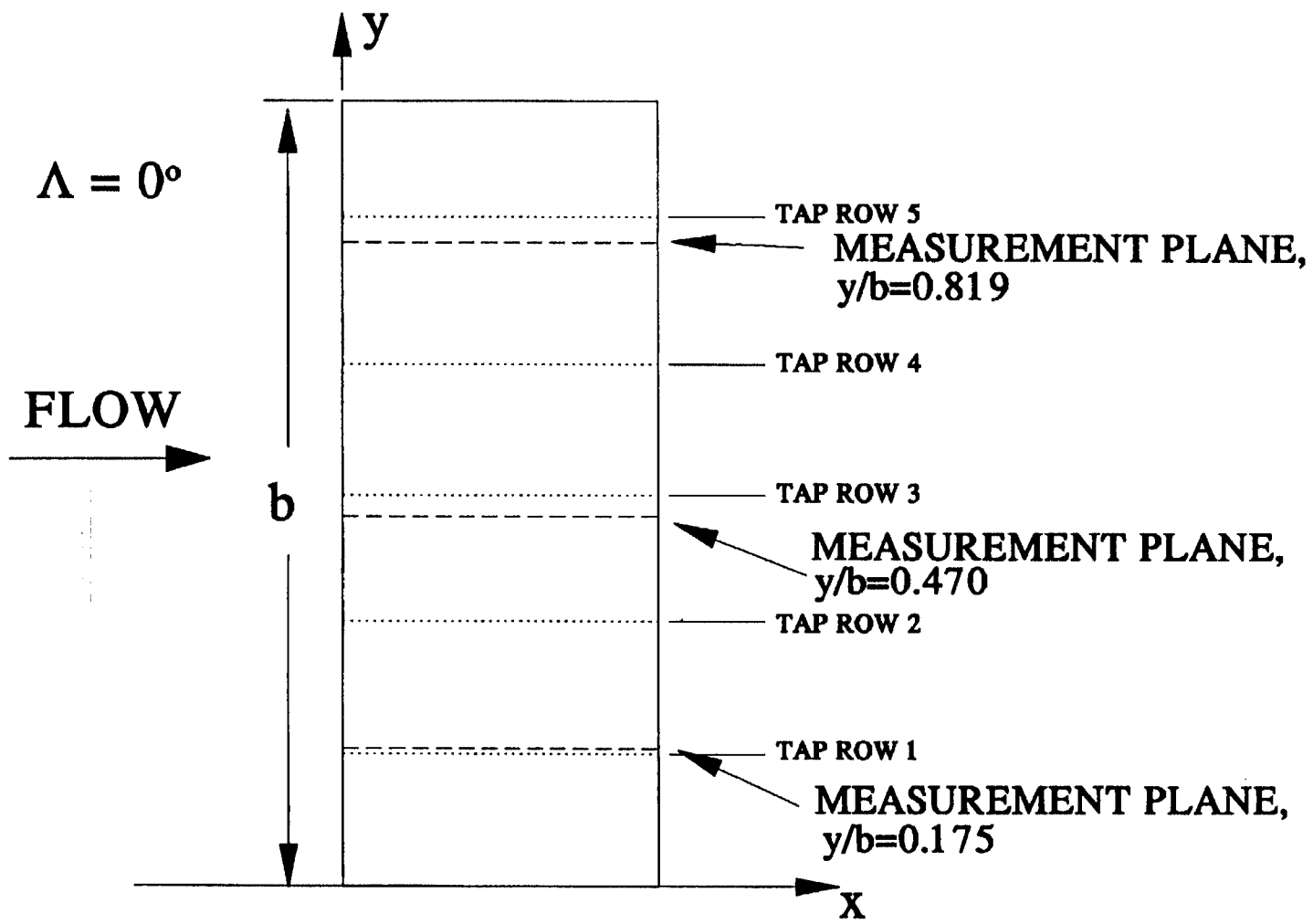

Figure 51. Measurement Planes on the Iced Wing Upper Surface.

x/c
-0.02
0.00
0.02
0.04
0.06
0.08
0.10
0.12
0.30
0.60
0.99

NACA 0012 RECTANGULAR WING
ICED LEADING EDGE
MEASUREMENT LOCATIONS AT y/b=0.175, 0.470, 0.819
$\alpha=0^{\circ}$

Figure 52. Measurement Locations on the Iced Wing at y/b=0.175, 0.470, 0.819, $\alpha=0$.

x/c
-0.02
0.00
0.02
0.04
0.06
0.08
0.10
0.12
0.14
0.16
0.18
0.20
0.30
0.60
0.99

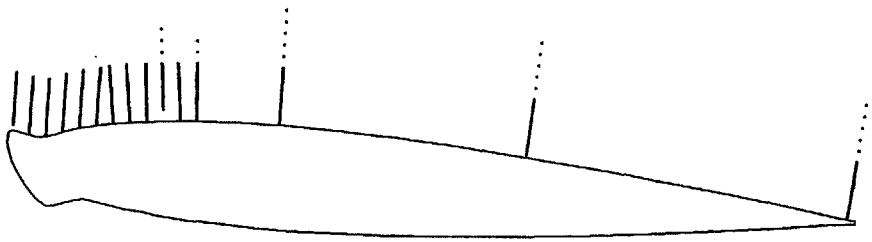

NACA 0012 RECTANGULAR WING
ICED LEADING EDGE
MEASUREMENT LOCATIONS AT y/b=0.175, 0.470, 0.819
α=4°

Figure 53. Measurement Locations on the Iced Wing at y/b=0.175, 0.470, 0.819, α=4.

C-3.

x/c
-0.02
0.00
0.02
0.04
0.06
0.08
0.10
0.12
0.14
0.16
0.18
0.20
0.22

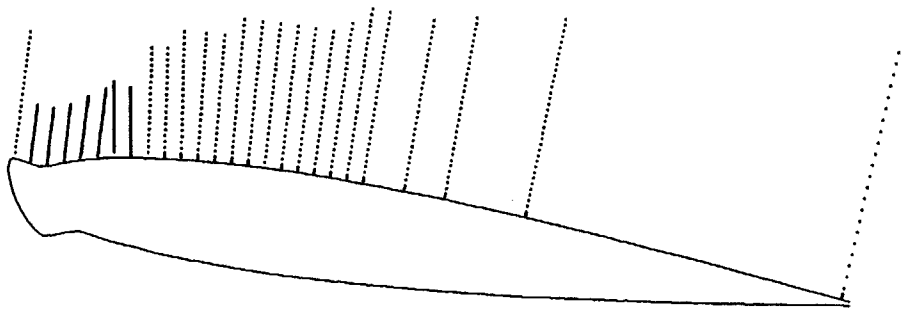

x/c (cont'd)
0.24
0.26
0.28
0.30
0.32
0.34
0.36
0.38
0.40
0.45
0.50
0.60
0.99

NACA 0012 RECTANGULAR WING
ICED LEADING EDGE
MEASUREMENT LOCATIONS AT y/b=0.175, 0.470, 0.819
α=8°

Figure 54. Measurement Locations on the Iced Wing at y/b=0.175, 0.470, 0.819, α=8.

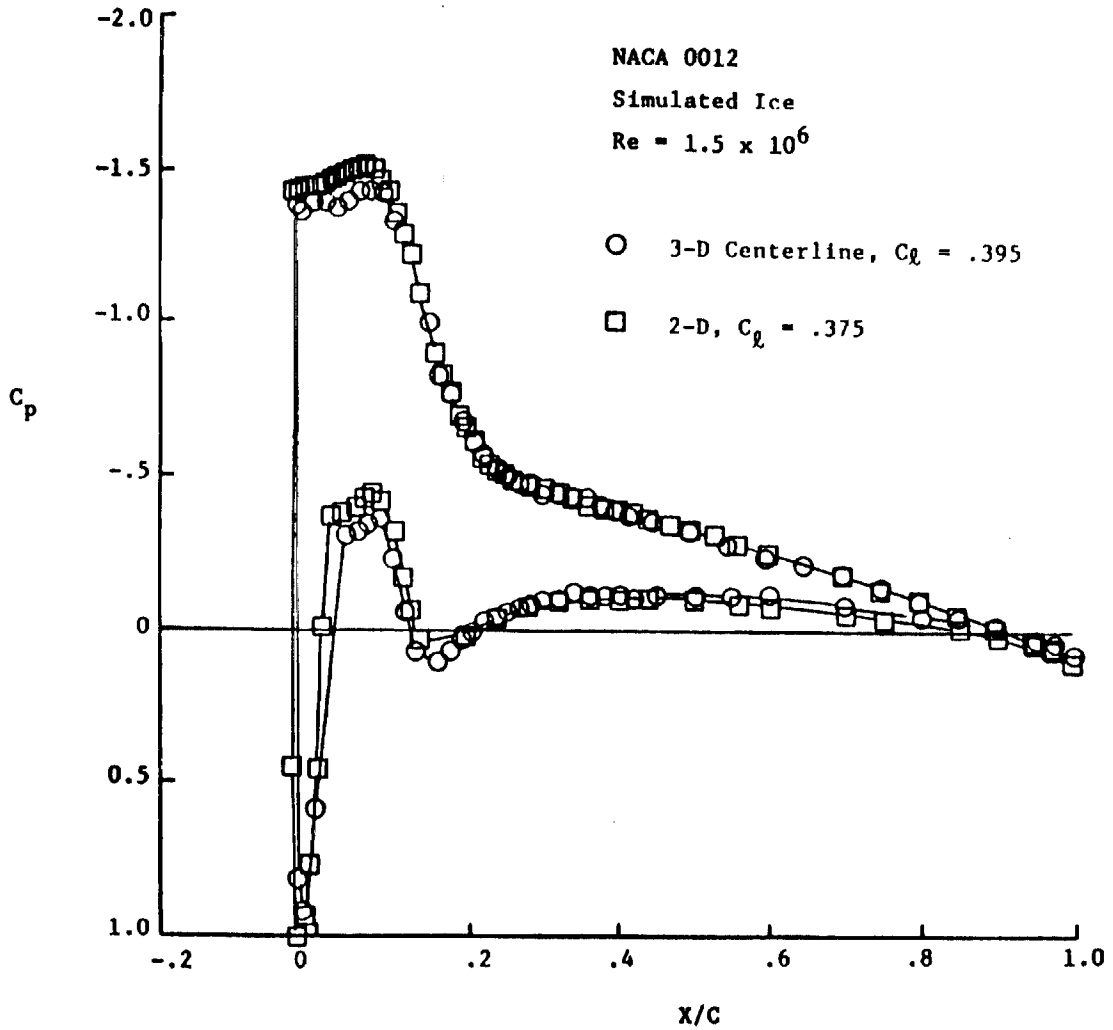

Figure 55. Surface Pressure Distribution from the Wing Midspan Compared to 2-D Data.

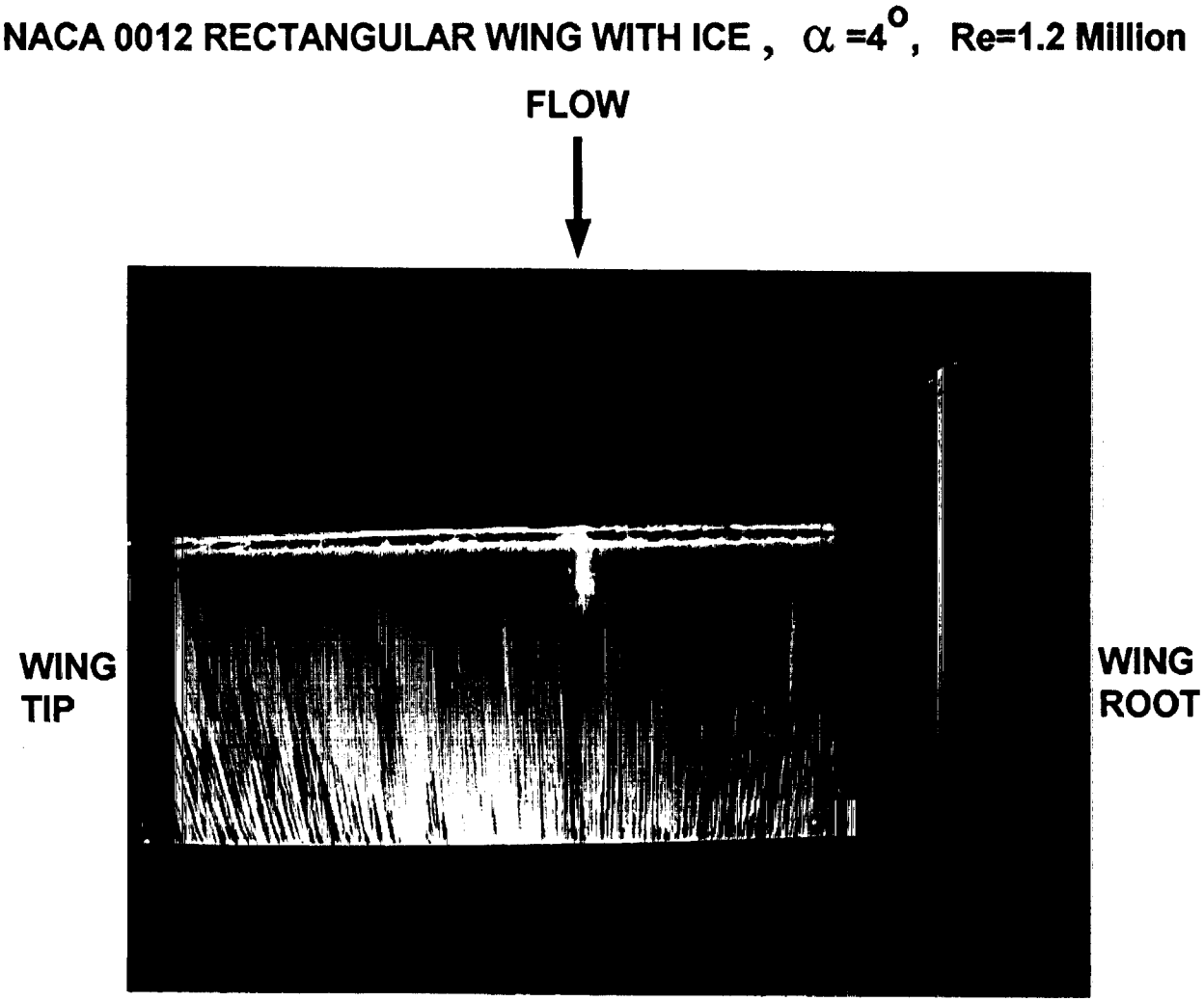

Figure 56. Flourescent Oil Flow Visualization on the Upper Surface of the Iced Wing, Re=1.2 Million, $\alpha = 4$.

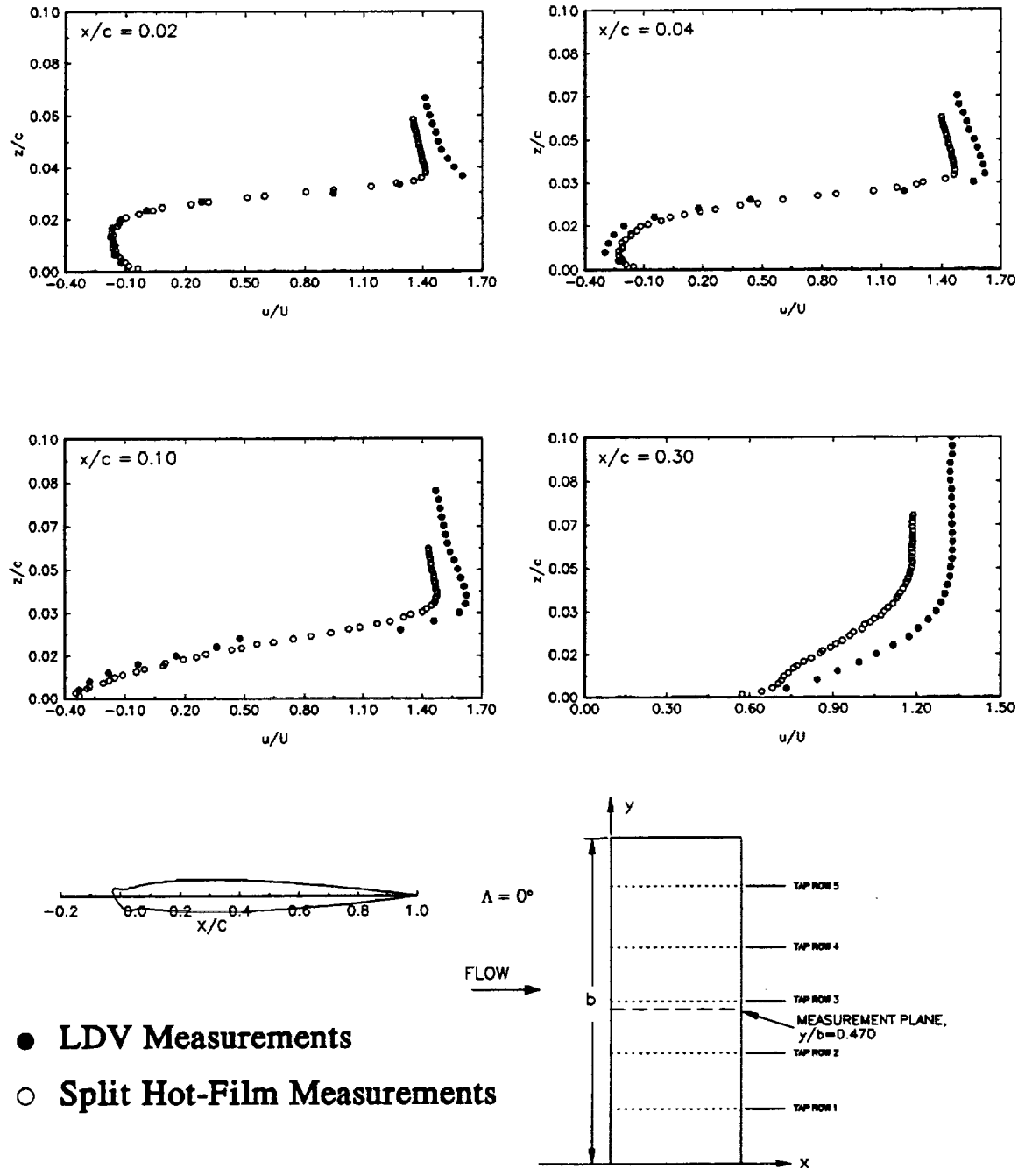

Figure 57. Comparison of Velocity Profiles from Split Hot-Film Measurements [6-9] and LDV Measurements, α =4.7, Re=1.5 Million, y/b=0.470.

PAGE 190 INTENTIONALLY BLANK
PRECEDING PAGE BLANK NOT FILMED

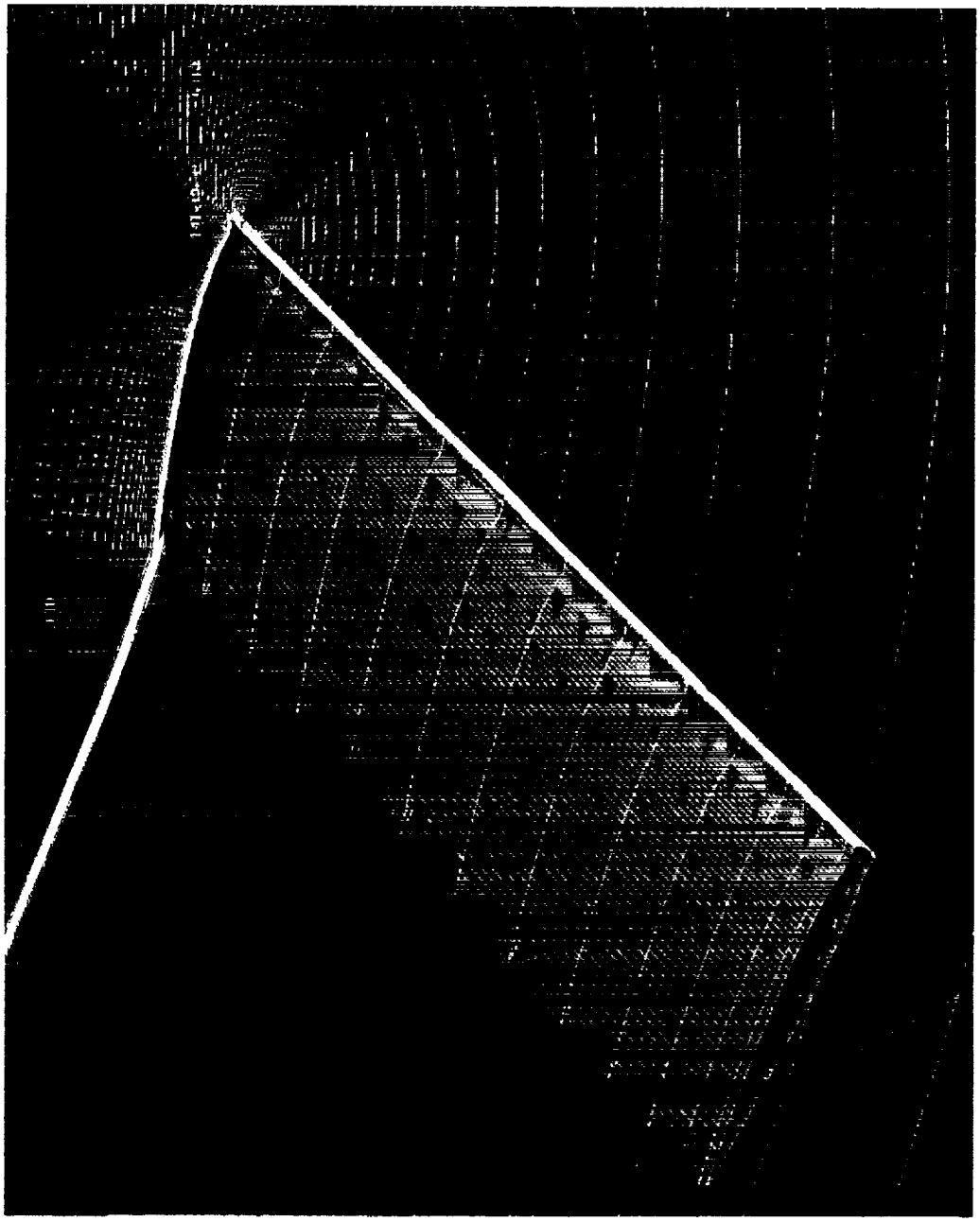

Figure 58. Surface Grid Locations for the Computational Rectangular Wing with Iced Leading Edge[37].

PRECEDING PAGE BLANK NOT FILMED

PAGE 192 INTENTIONALLY BLANK

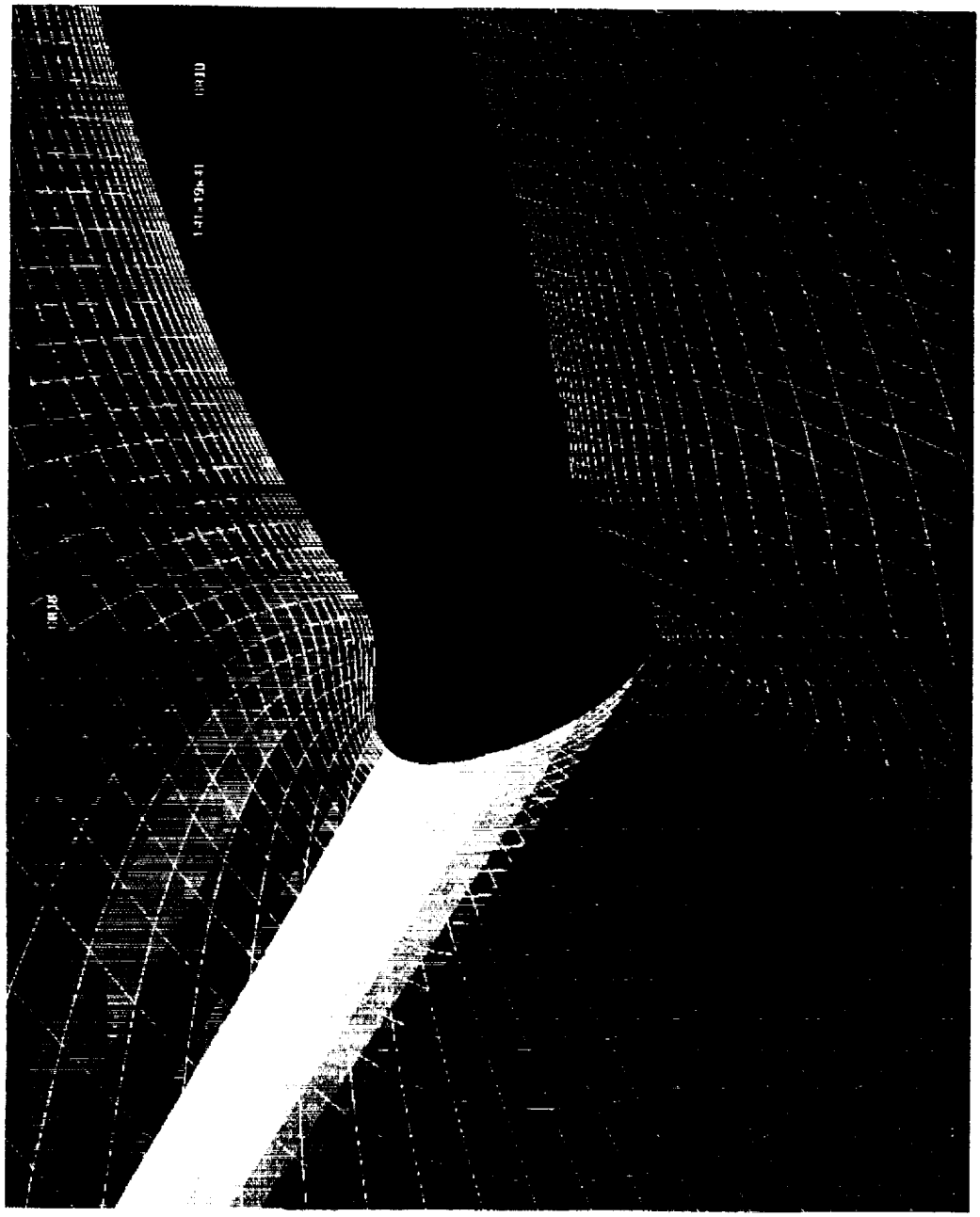

Figure 59. Computational Grid Points Normal to the Surface on the Rectangular Wing with Iced Leading Edge[37].

PRECEDING PAGE BLANK NOT FILMED
PAGE 194 INTENTIONALLY BLANK

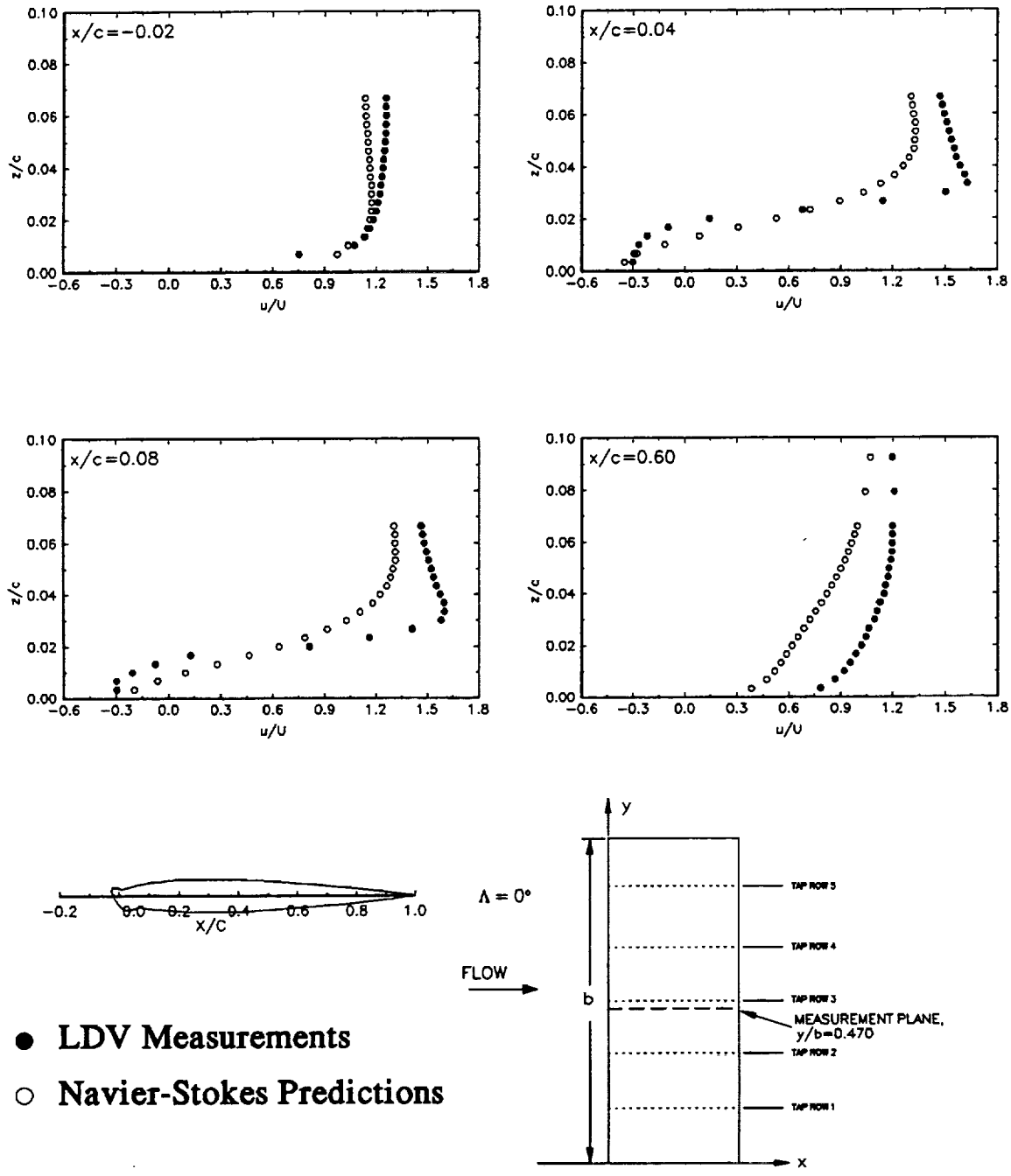

Figure 60. Comparison of Velocity Profiles from LDV Measurements and Navier-Stokes Computations[137], $\alpha = 4$, Re = 1.5 Million, y/b = 0.470.

PAGE 196 INTENTIONALLY BLANK

PRECEDING PAGE BLANK NOT FILMED

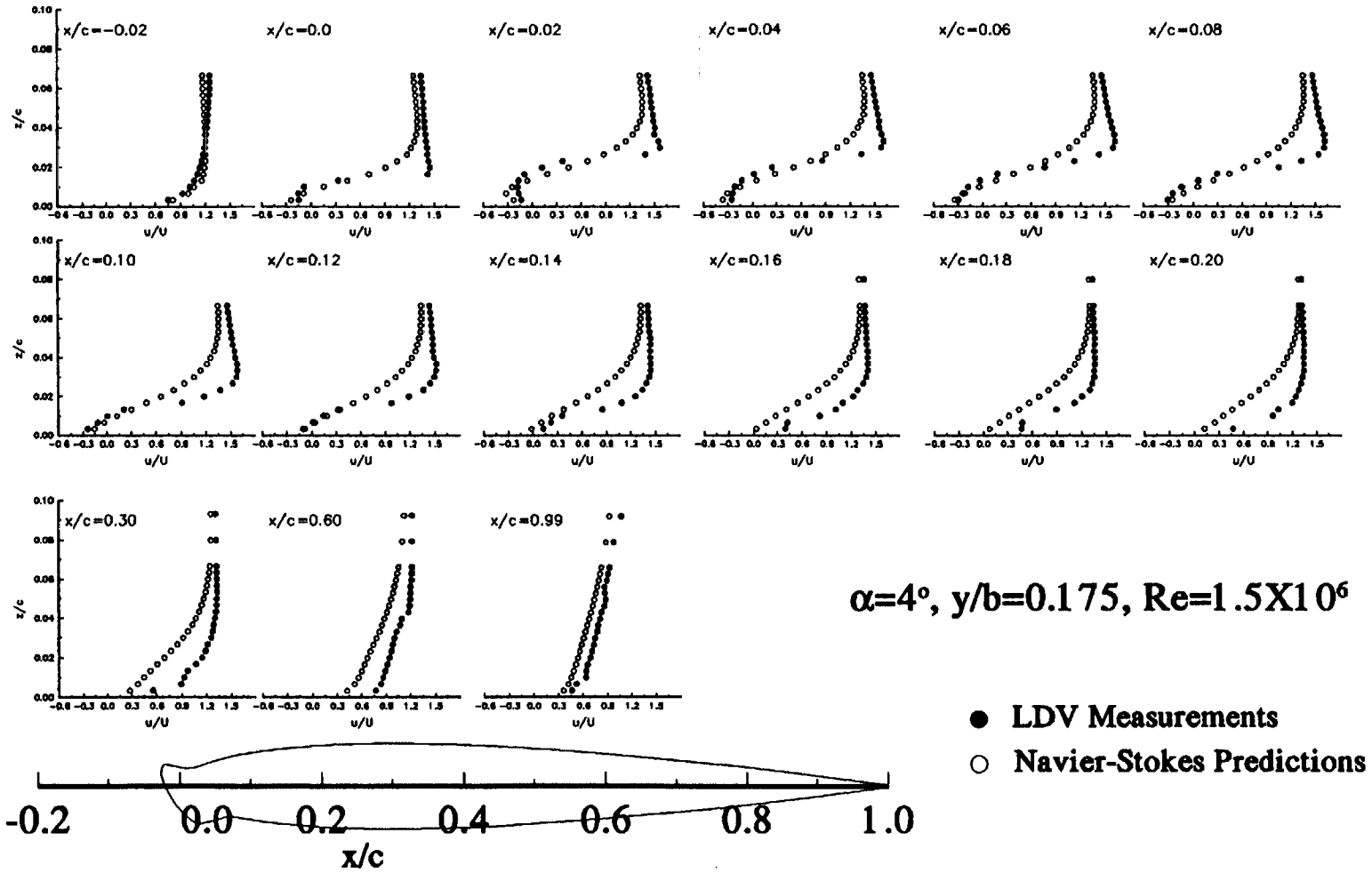

Figure 61. (u) Velocity Profiles on the Iced Wing Upper Surface at α=4, y/b=0.175, Re=1.5 Million.

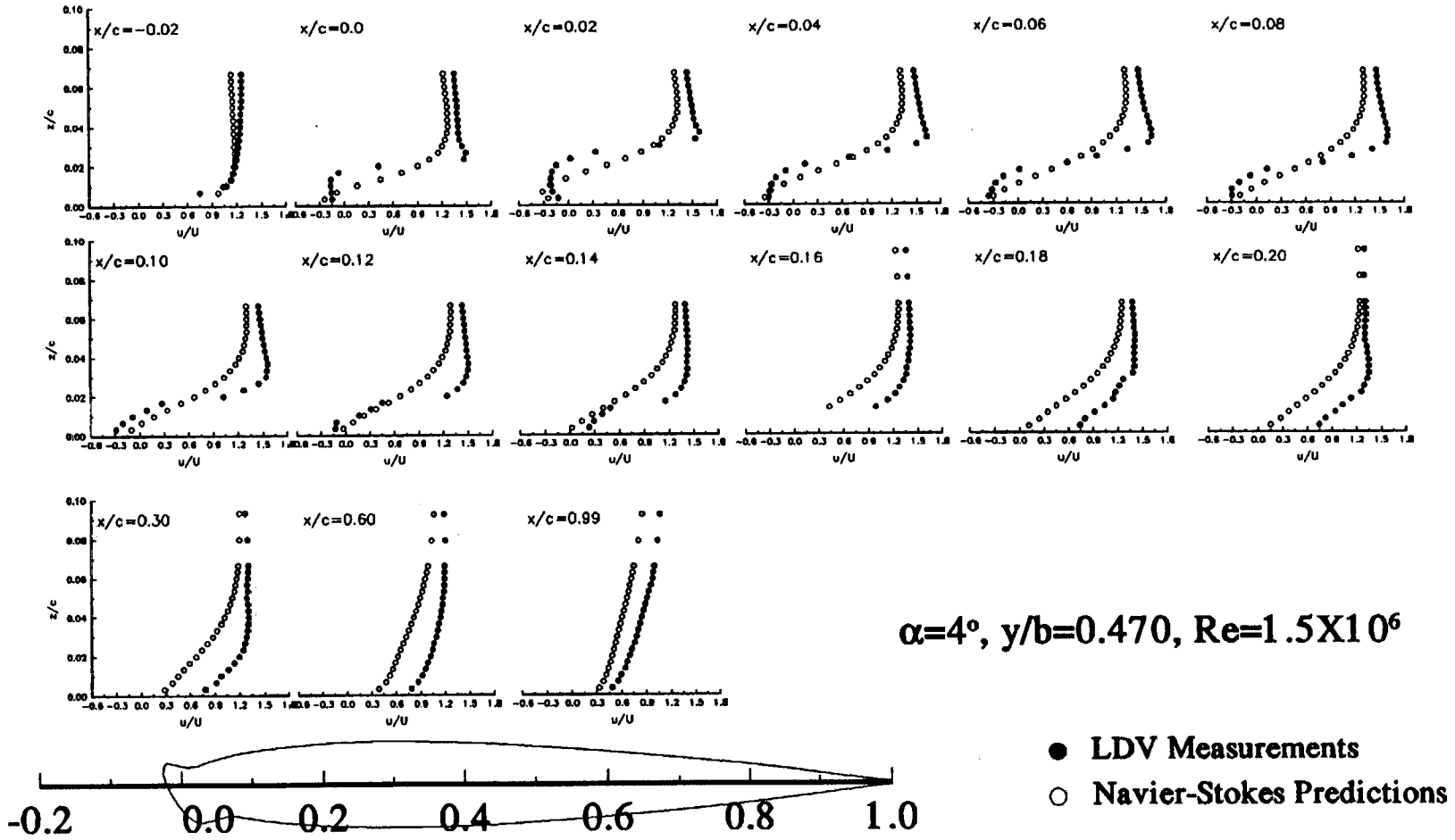

Figure 62. (u) Velocity Profiles on the Iced Wing Upper Surface at α=4, y/b=0.470, Re=1.5 Million.

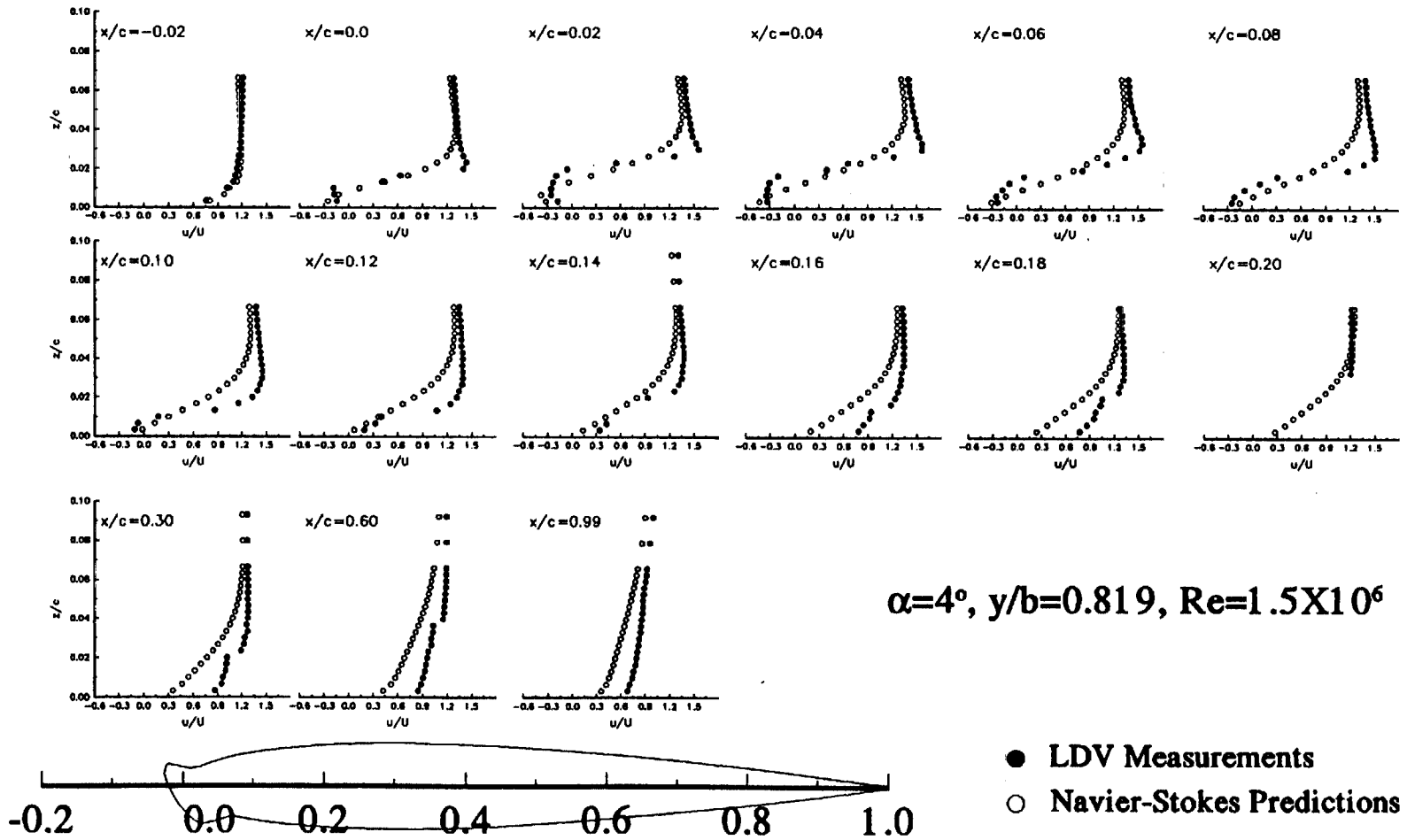

Figure 63. (u) Velocity Profiles on the Iced Wing Upper Surface at α=4, y/b=0.819, Re=1.5 Million.

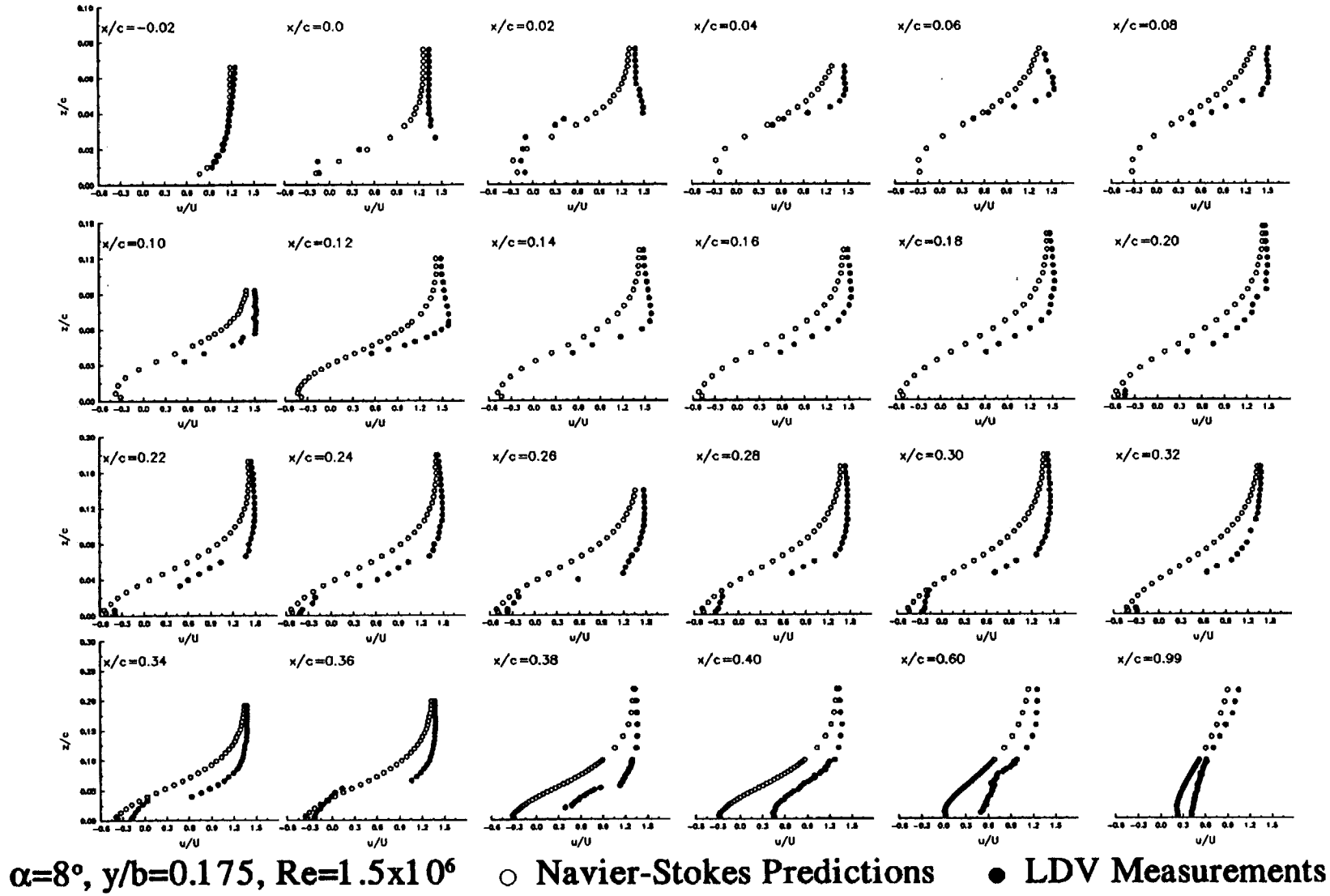

Figure 64. (u) Velocity Profiles on the Iced Wing Upper Surface at α=8, y/b=0.175, Re=1.5 Million.

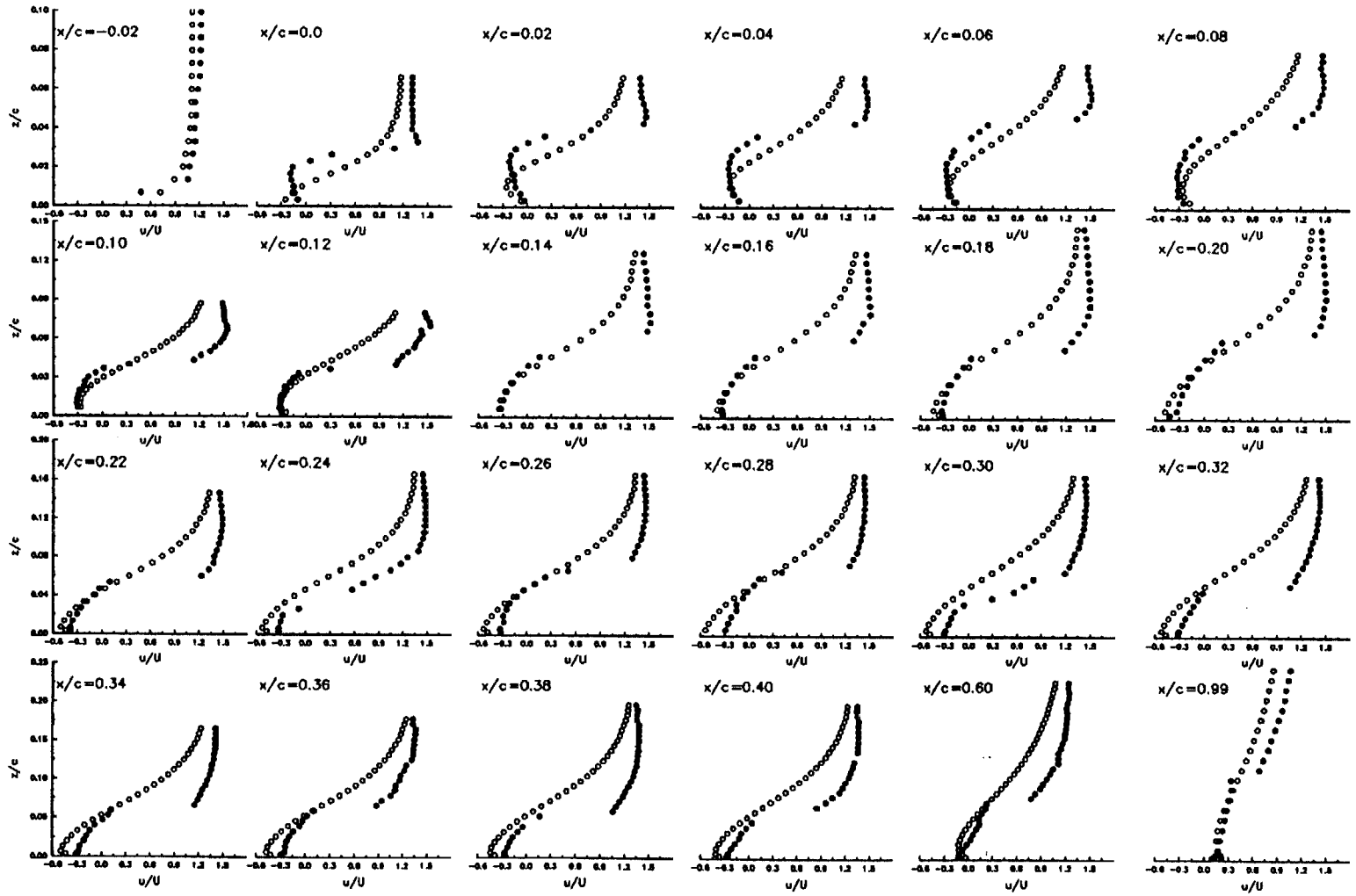

Figure 65. (u) Velocity Profiles on the Iced Wing Upper Surface at α=8, y/b=0.470, Re=1.5 Million.

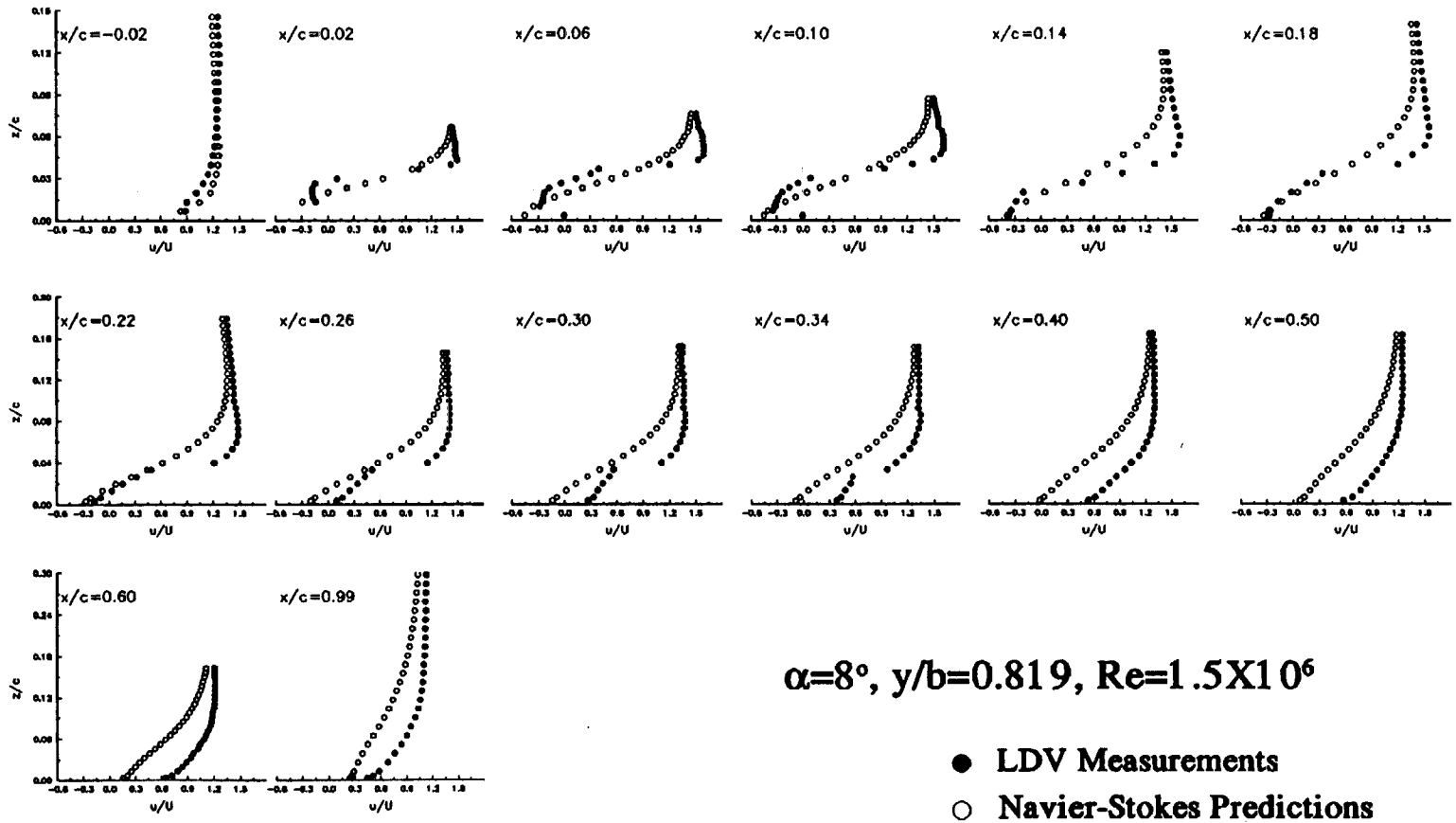

Figure 66. (u) Velocity Profiles on the Iced Wing Upper Surface at α=8, y/b=0.819, Re=1.5 Million.

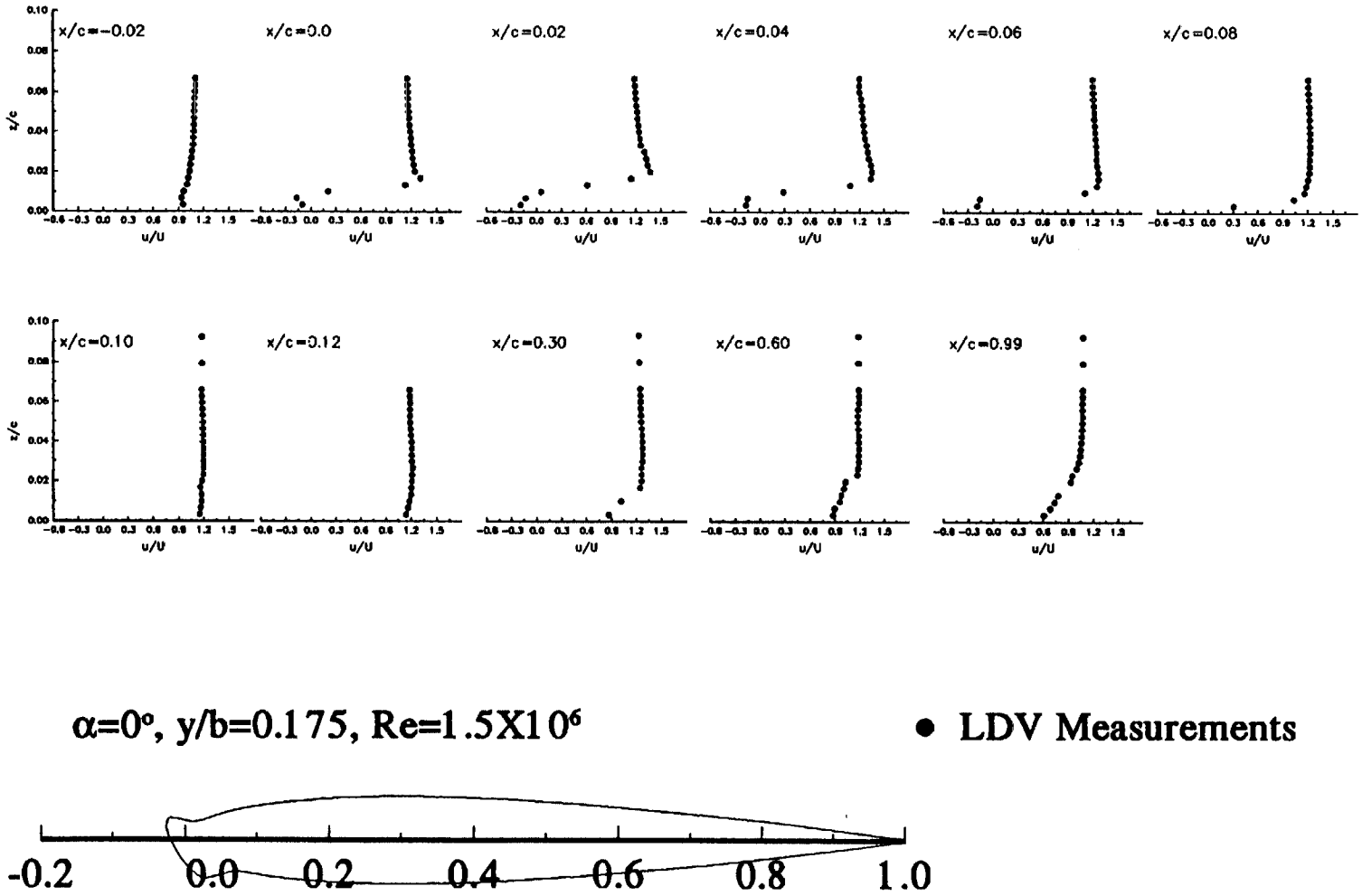

Figure 67. (u) Velocity Profiles on the Iced Wing Upper Surface at α=0, y/b=0.175, Re=1.5 Million.

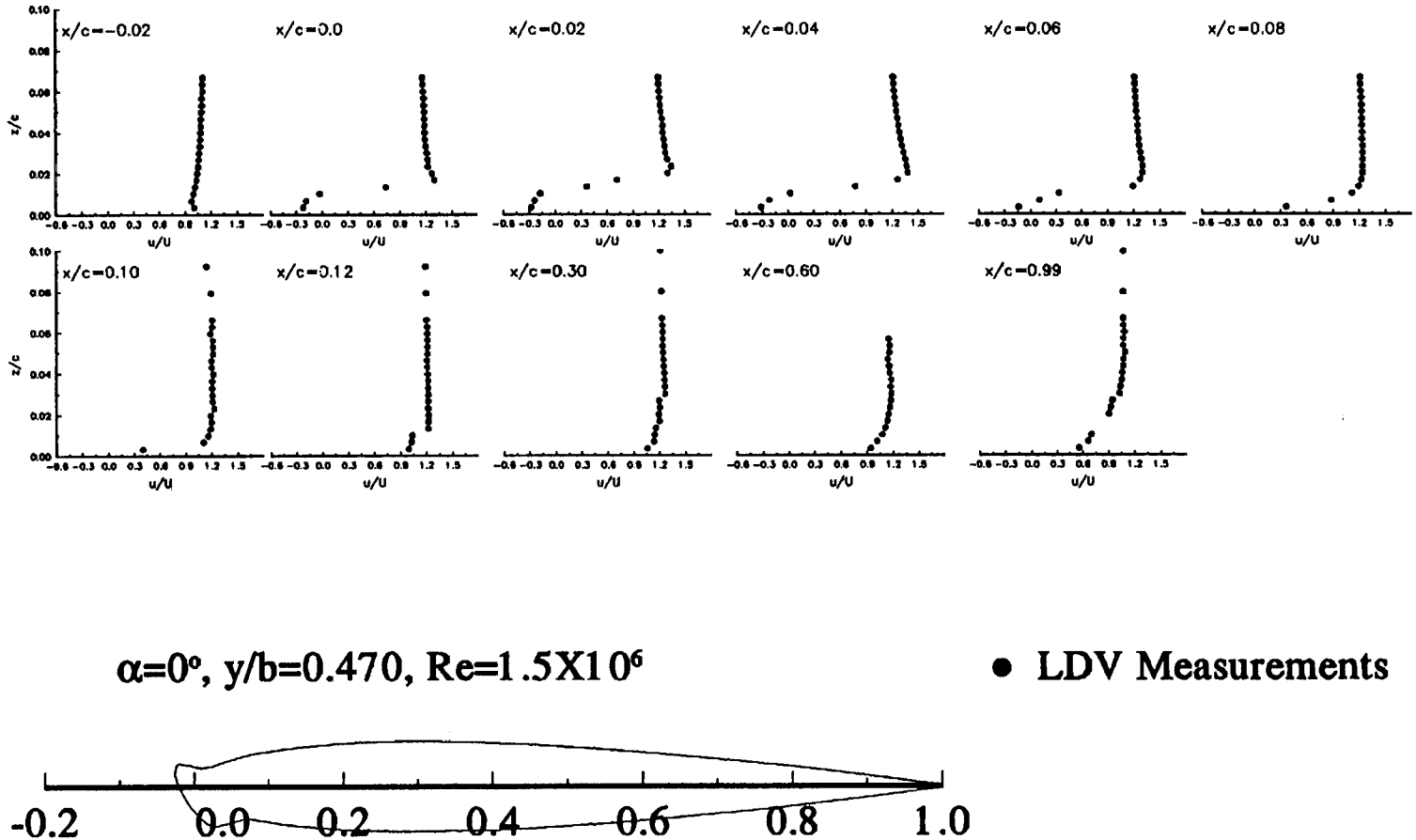

Figure 68. (u) Velocity Profiles on the Iced Wing Upper Surface at α=0, y/b=0.470, Re=1.5 Million.

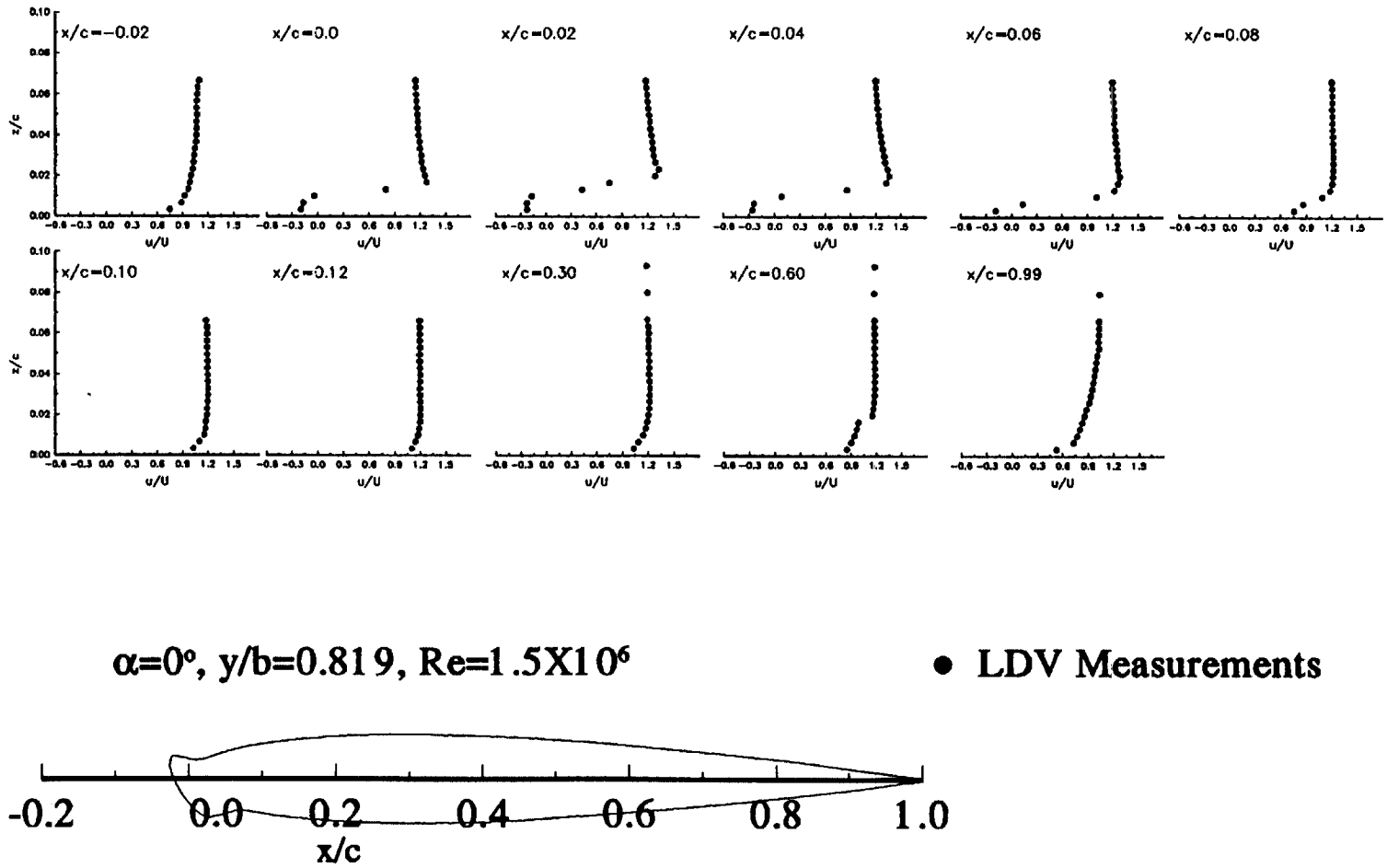

Figure 69. (u) Velocity Profiles on the Iced Wing Upper Surface at α=0, y/b=0.819, Re=1.5 Million.

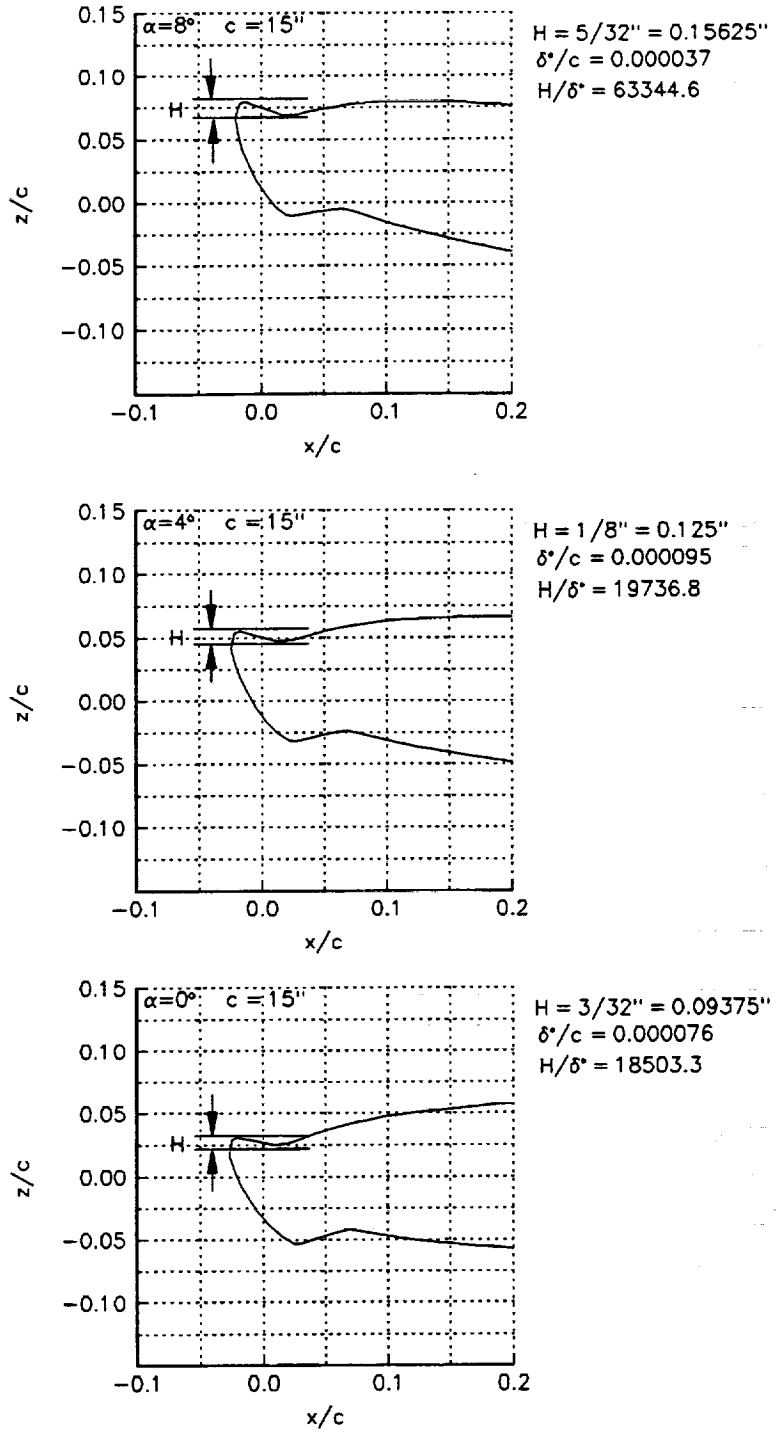

Figure 70. Typical Representative Step Height, H, for the Leading Edge Ice Shape at $\alpha = 0$, 4, and 8.

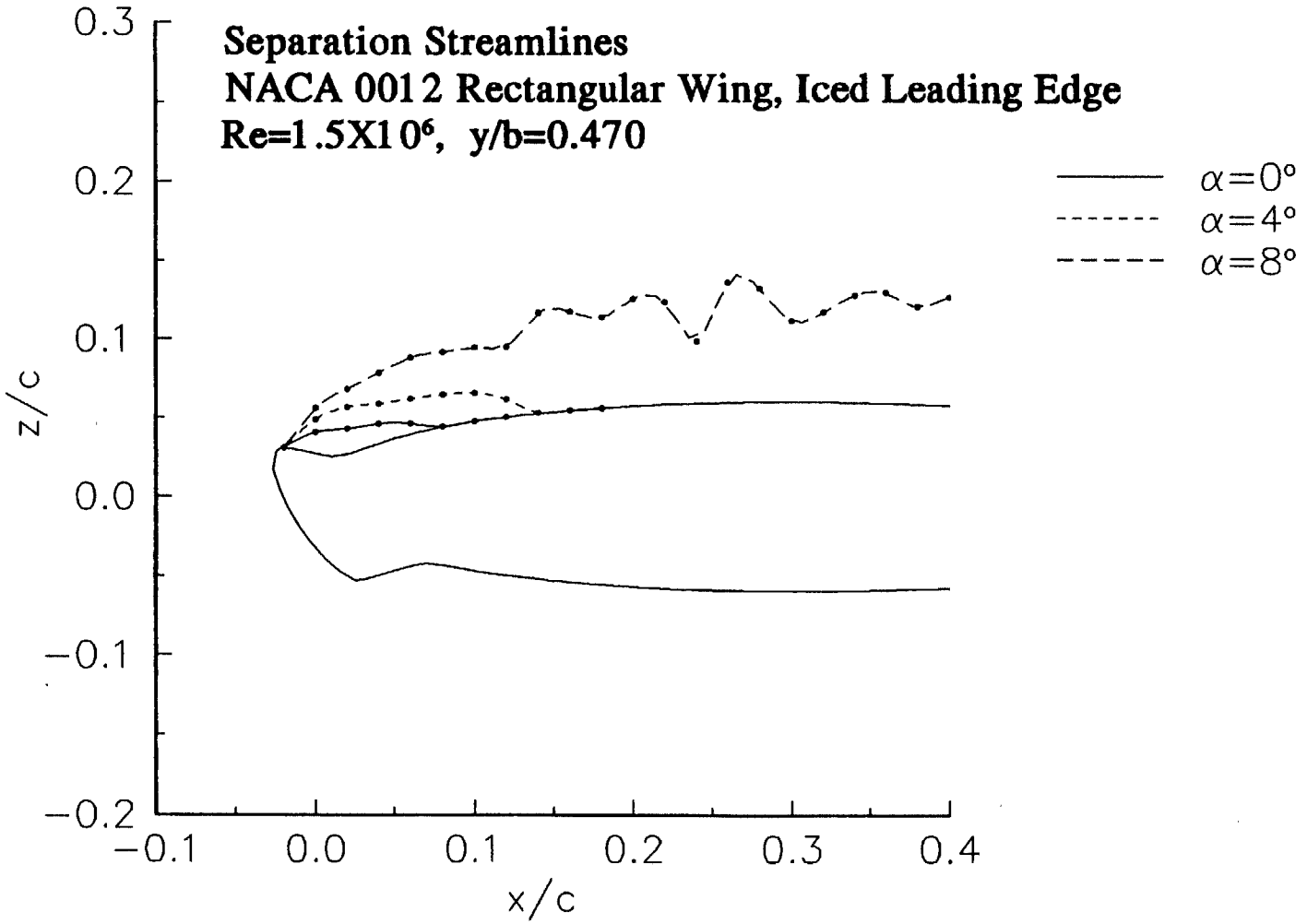

Figure 71. Separation Streamlines on the Iced Wing at y/b=0.470.

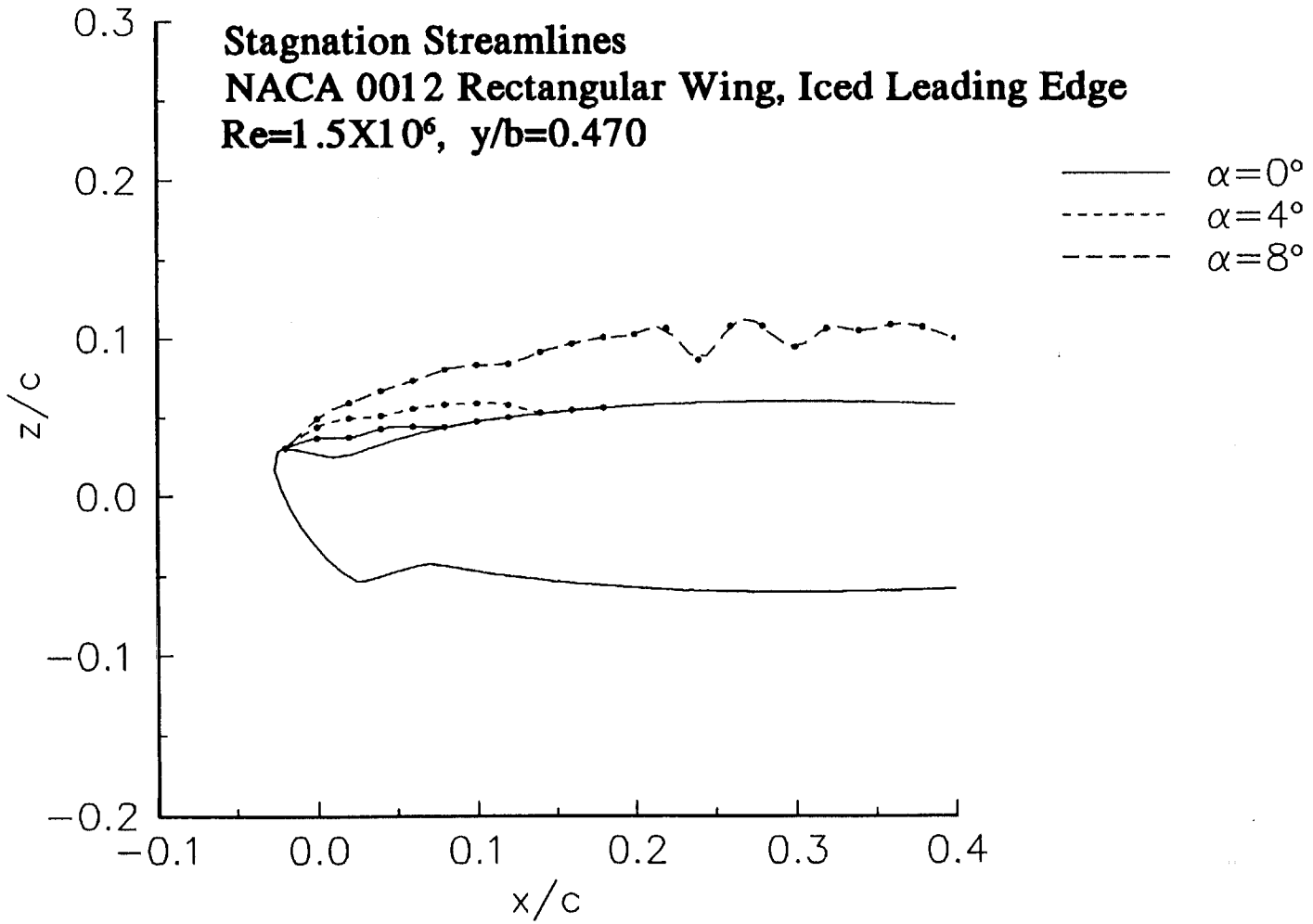

Figure 72. Stagnation Streamlines on the Iced Wing at y/b=0.470.

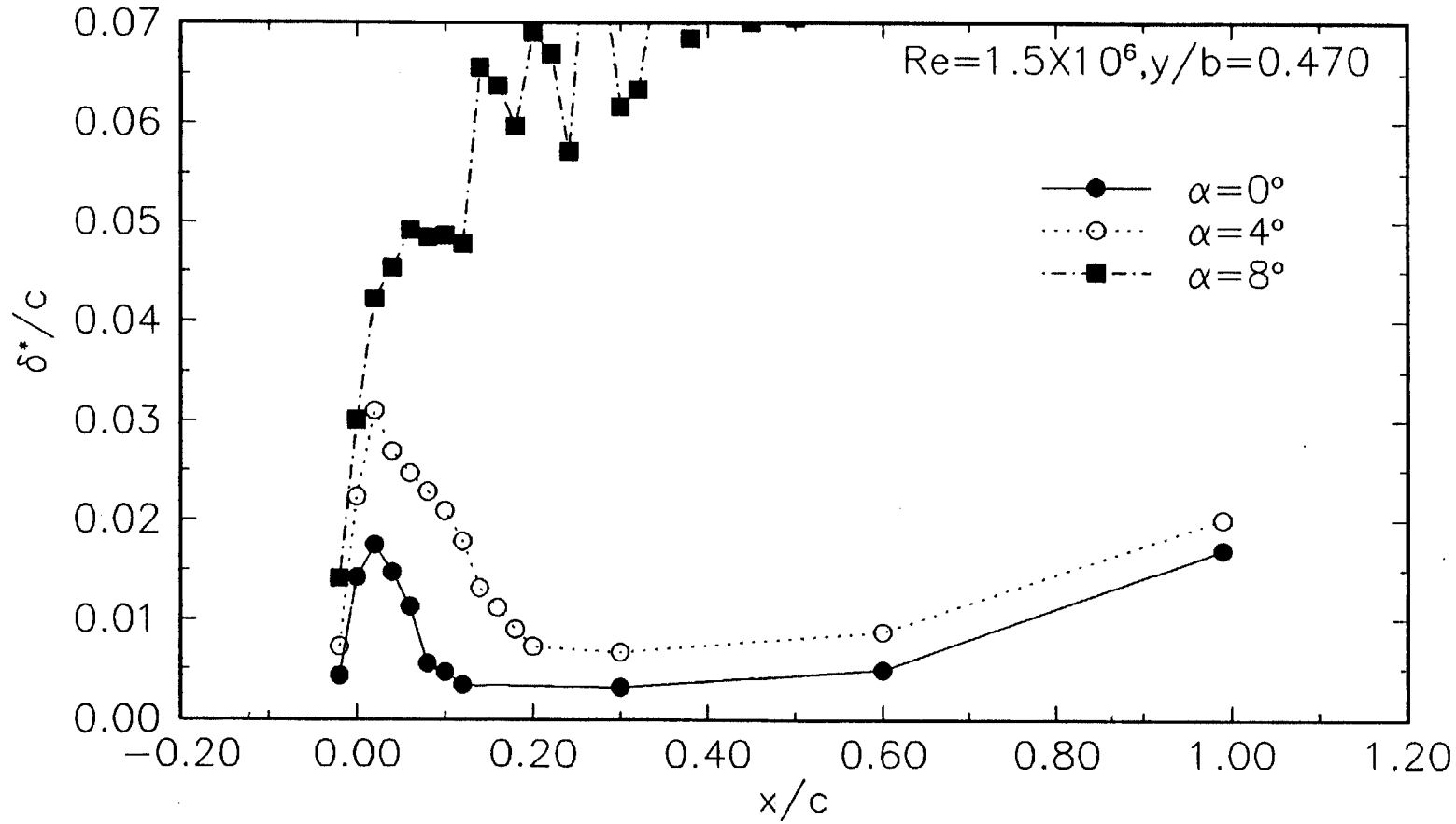

Figure 73. Distribution of Displacement Thickness on the Iced Wing at y/b=0.470.

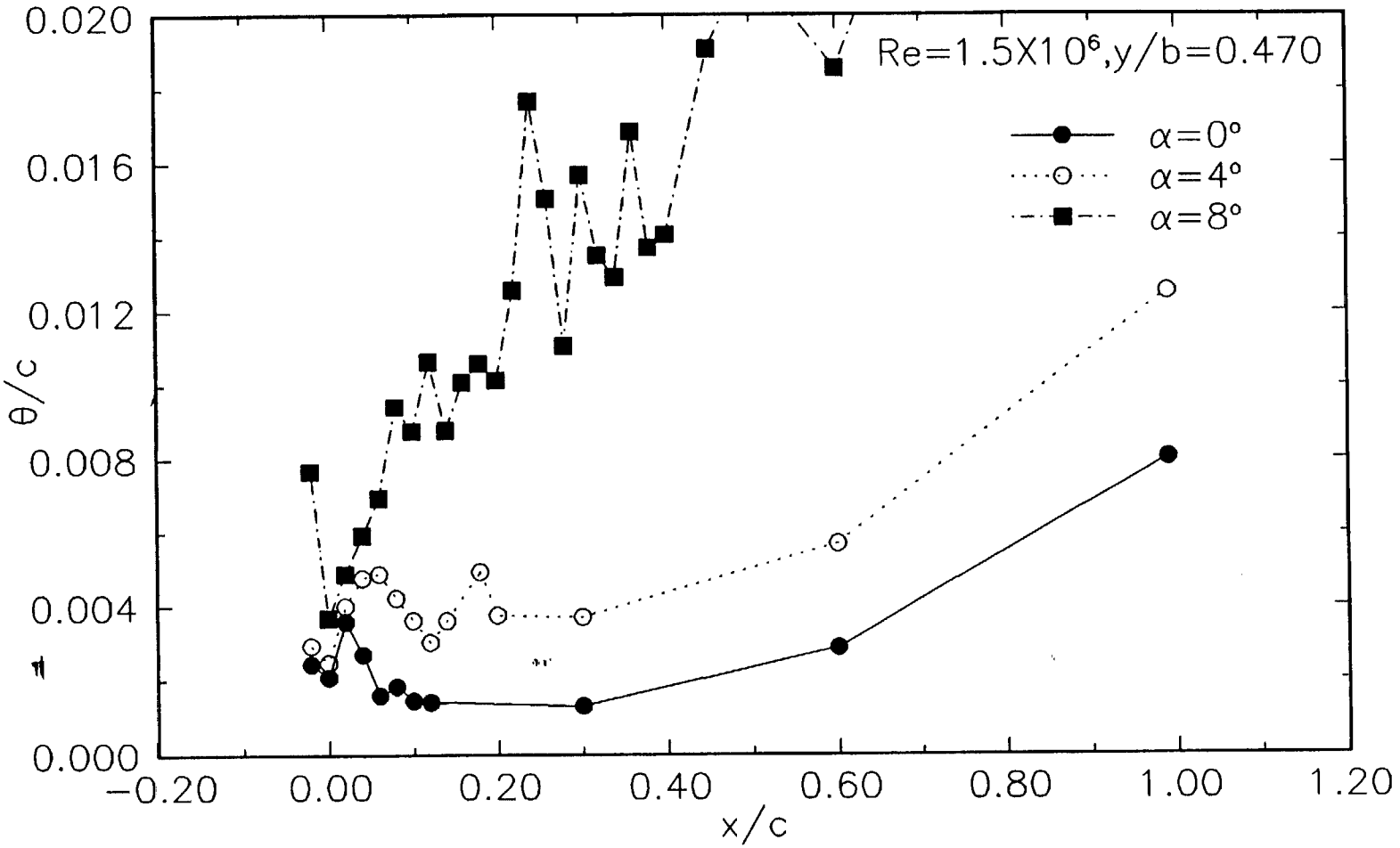

Figure 74. Distribution of Momentum Thickness on the Iced Wing at y/b=0.470.

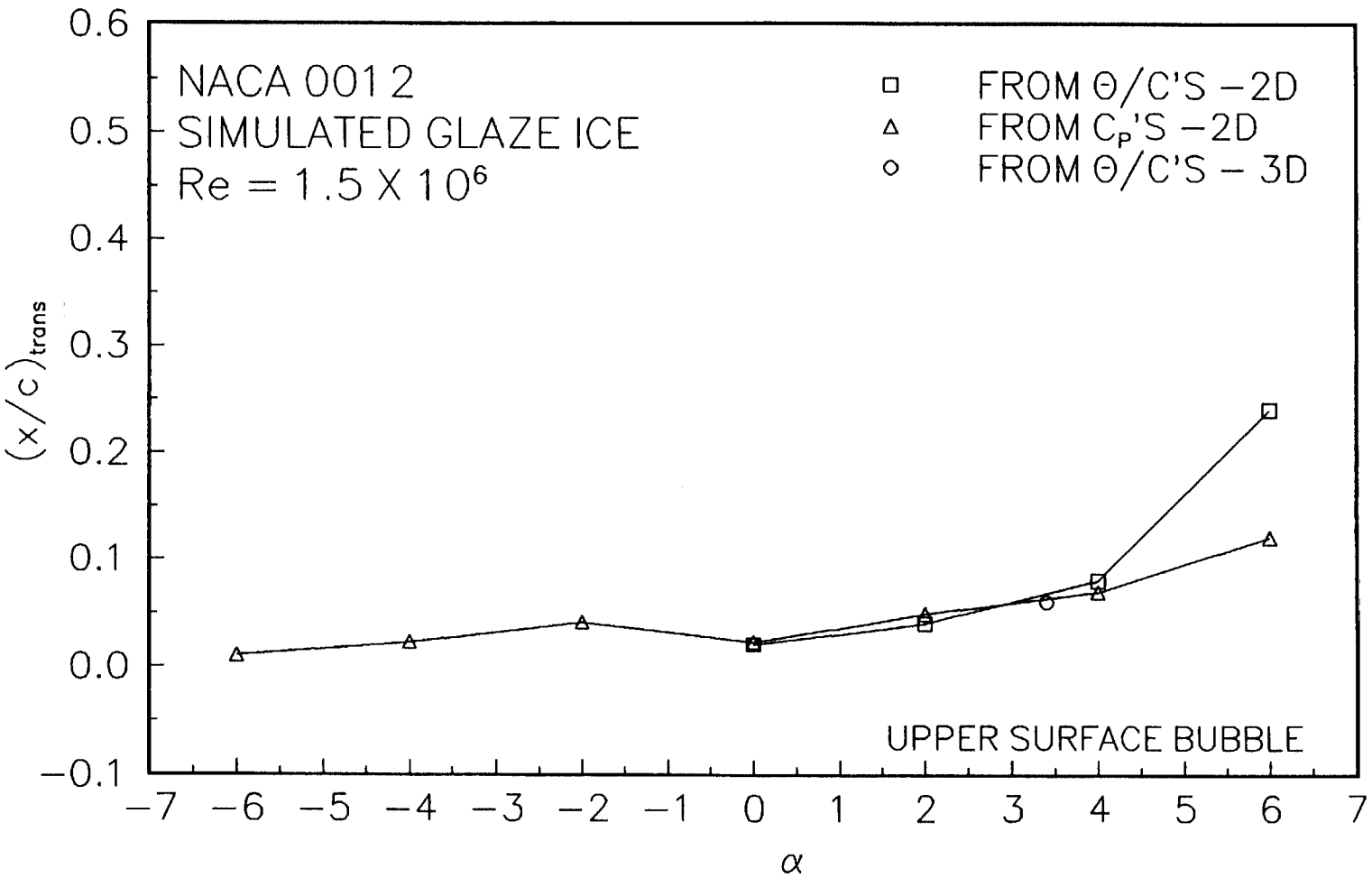

Figure 75. Comparison of the Estimated Upper-Surface Bubble Transition Locations, from 2-D Measurements and LDV Measurements.

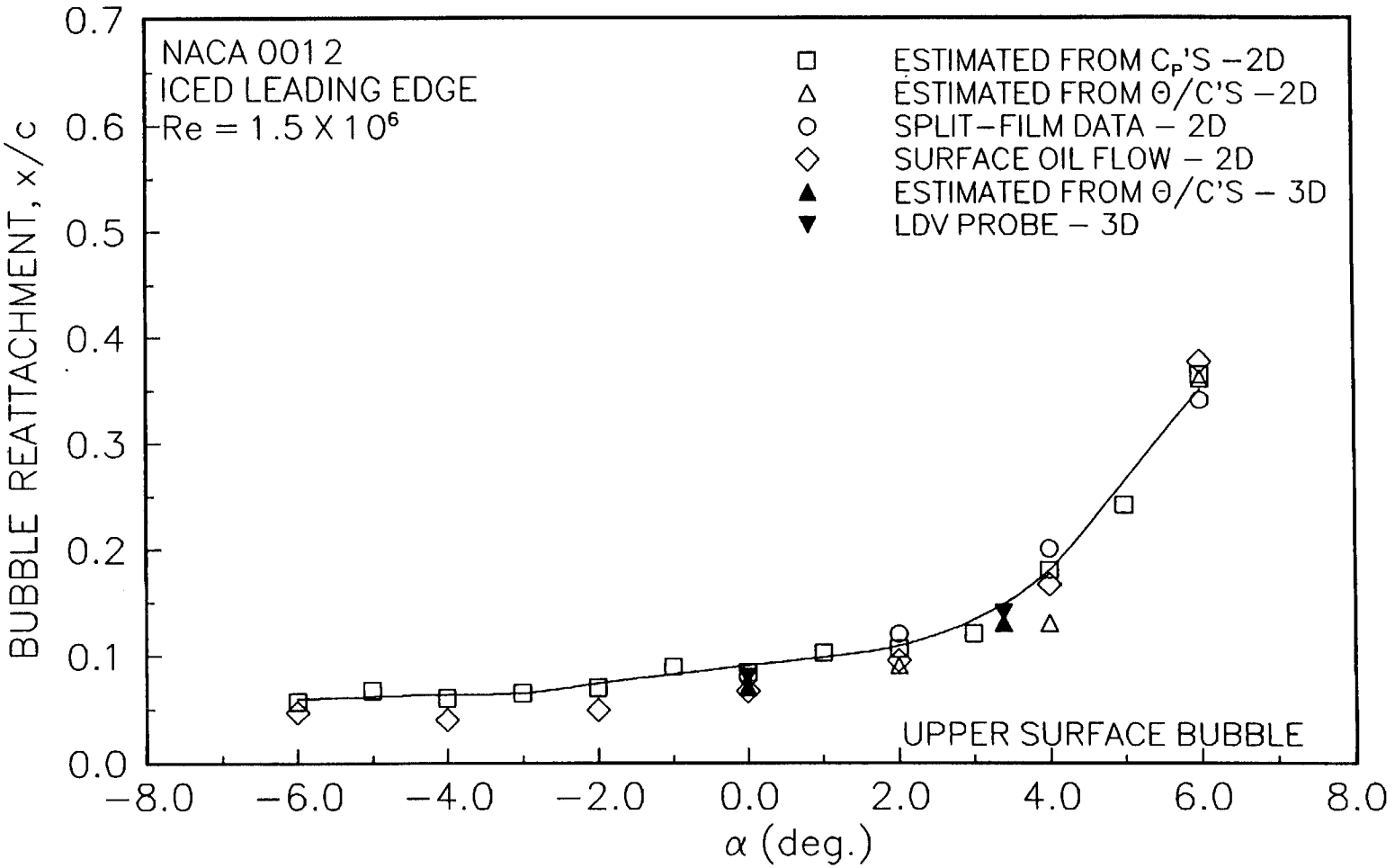

Figure 76. Comparison of the Estimated Upper-Surface Bubble Reattachment Locations, from 2-D Measurements and LDV Measurements.

PAGE 214 INTENTIONALLY BLANK

PRECEDING PAGE BLANK NOT FILMED

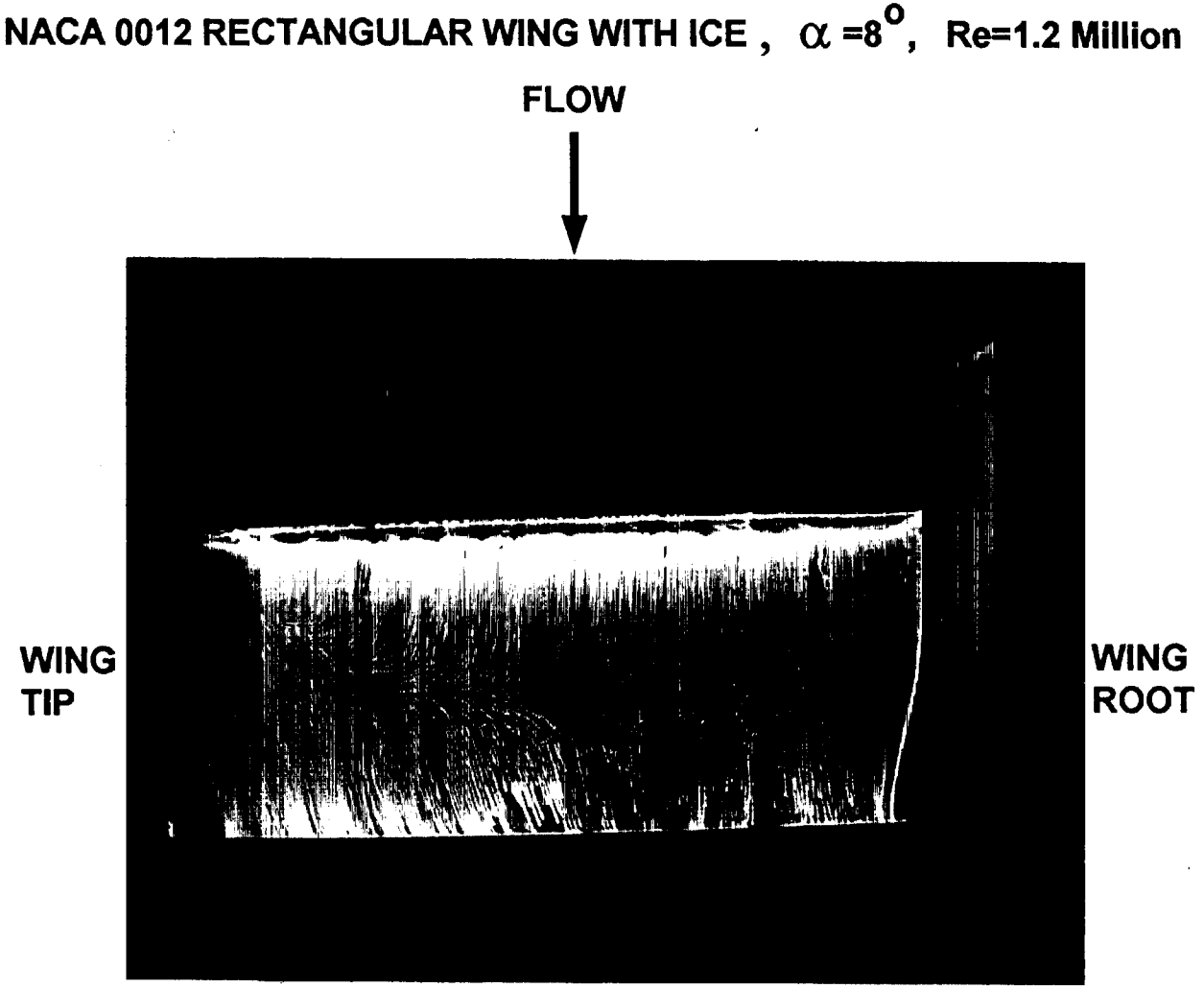

Figure 77. Flourescent Oil Flow Visualization on the Upper Surface of the Iced Wing, Re=1.2 Million, $\alpha = 8$.

PAGE BLANK NOT FILMED

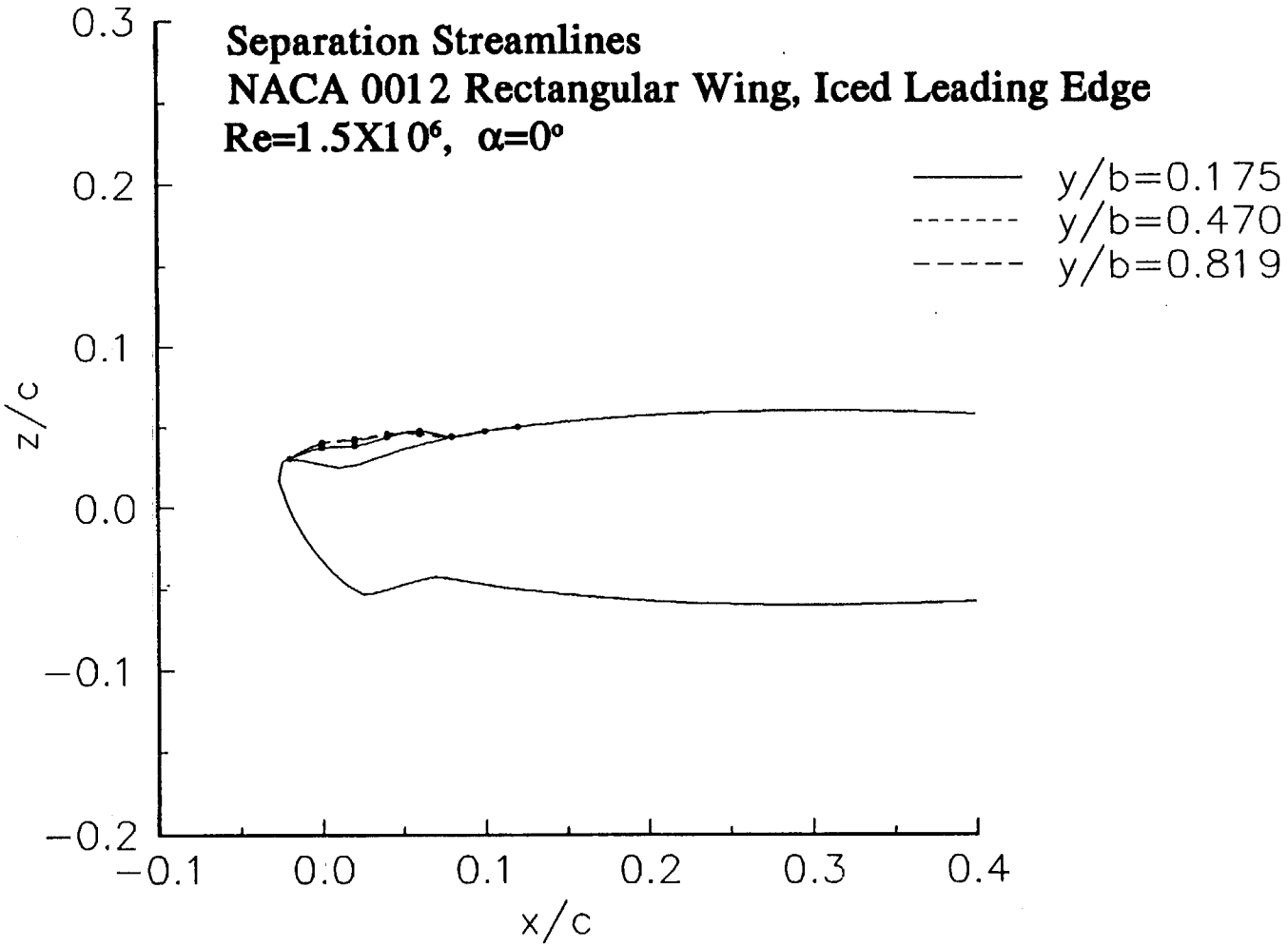

Figure 78. Separation Streamlines on the Iced Wing Upper Surface at α=0.

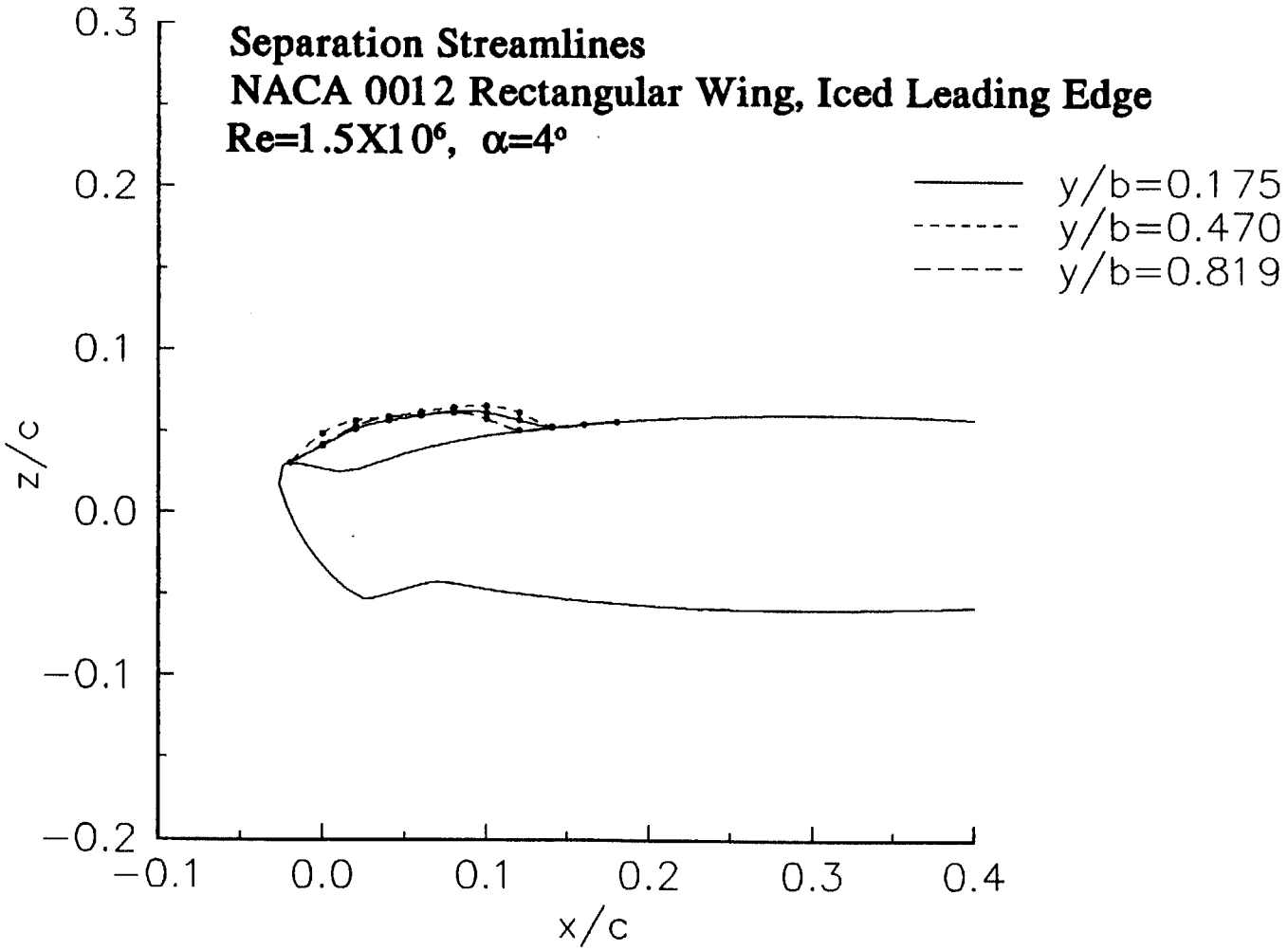

Figure 79. Separation Streamlines on the Iced Wing Upper Surface at α=4.

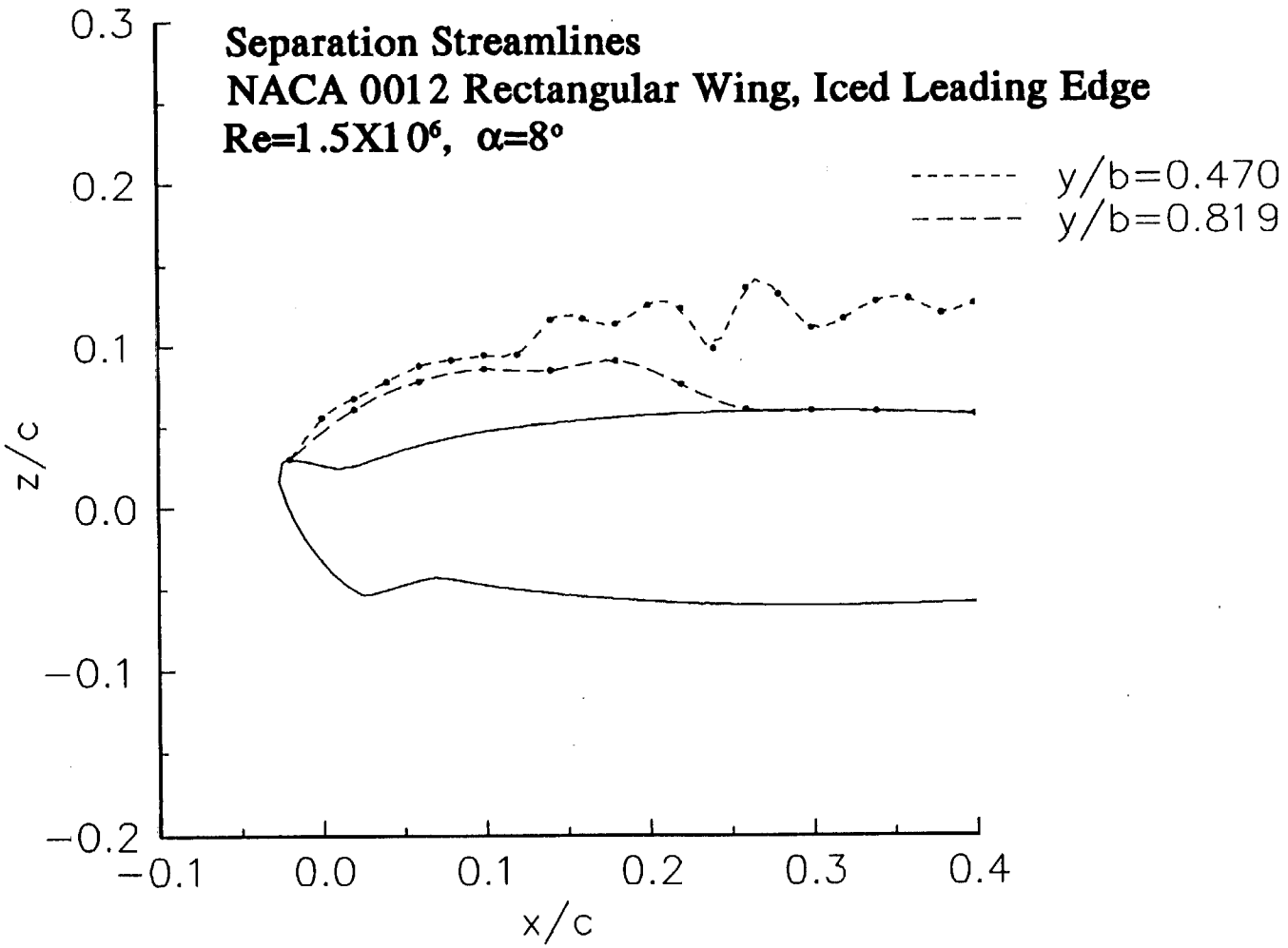

Figure 80. Separation Streamlines on the Iced Wing Upper Surface at α=8.

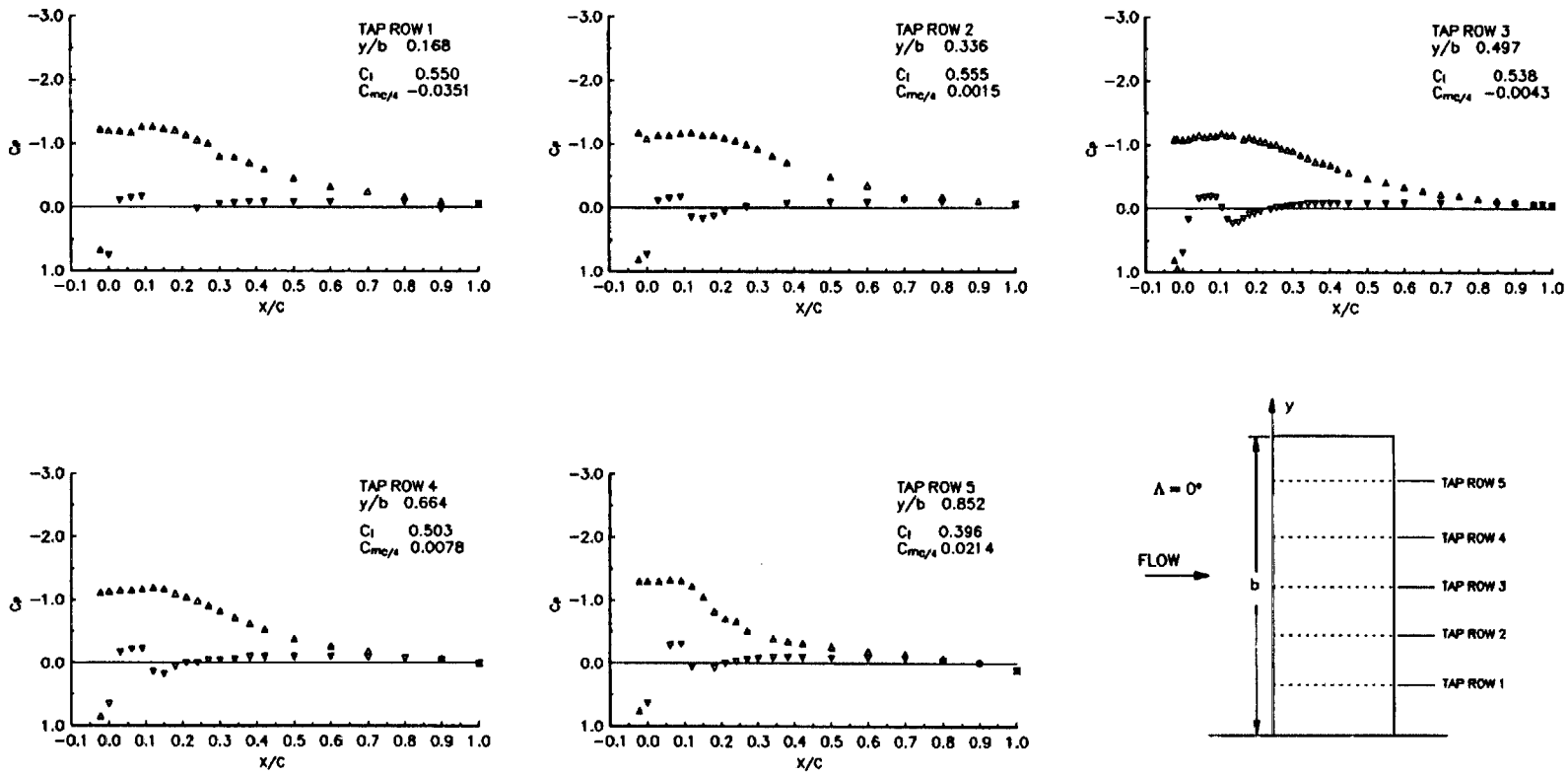

Figure 81. Pressure Distribution on the Iced Wing at α=8.

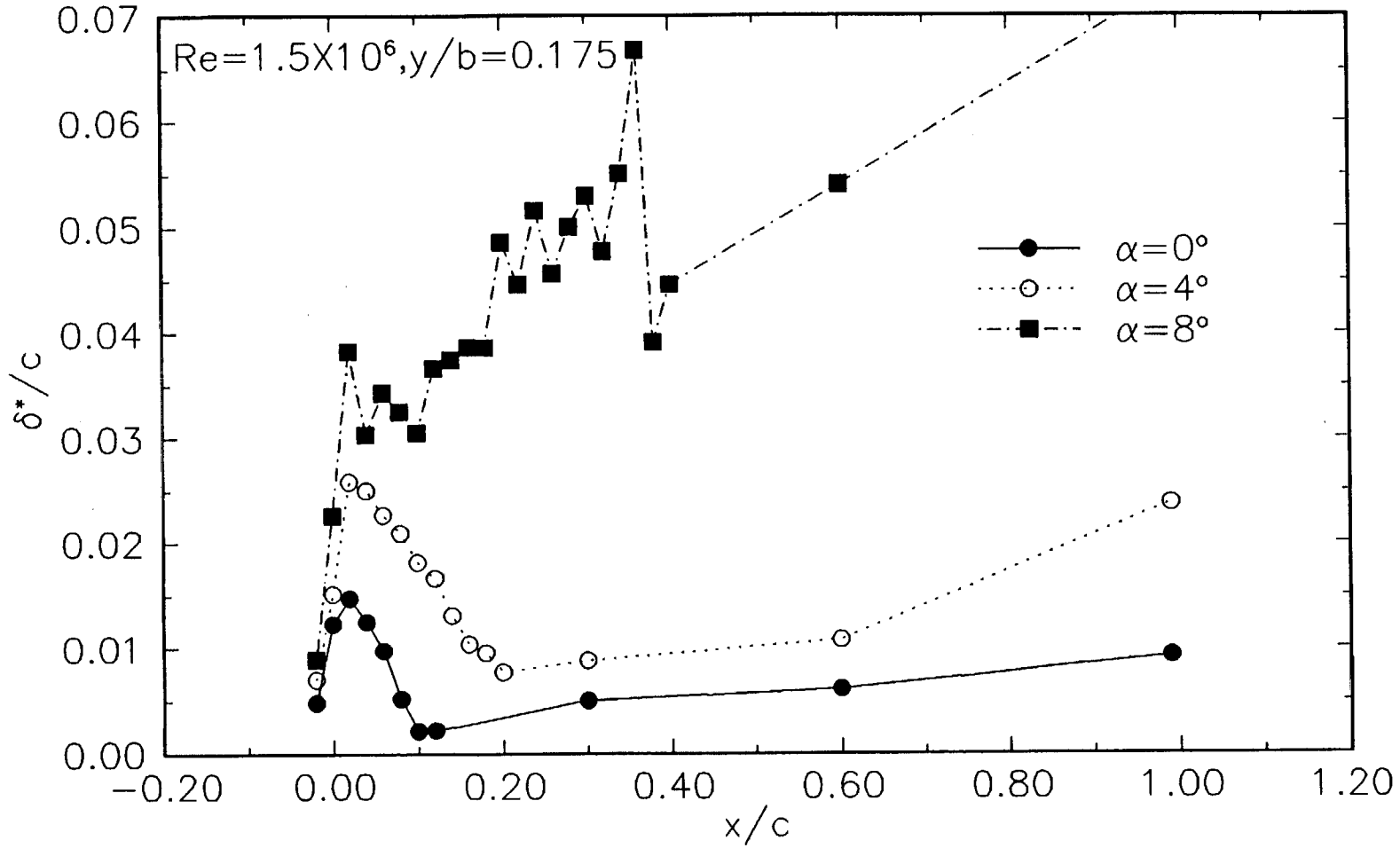

Figure 82. Distribution of Displacement Thickness on the Iced Wing at y/b=0.175.

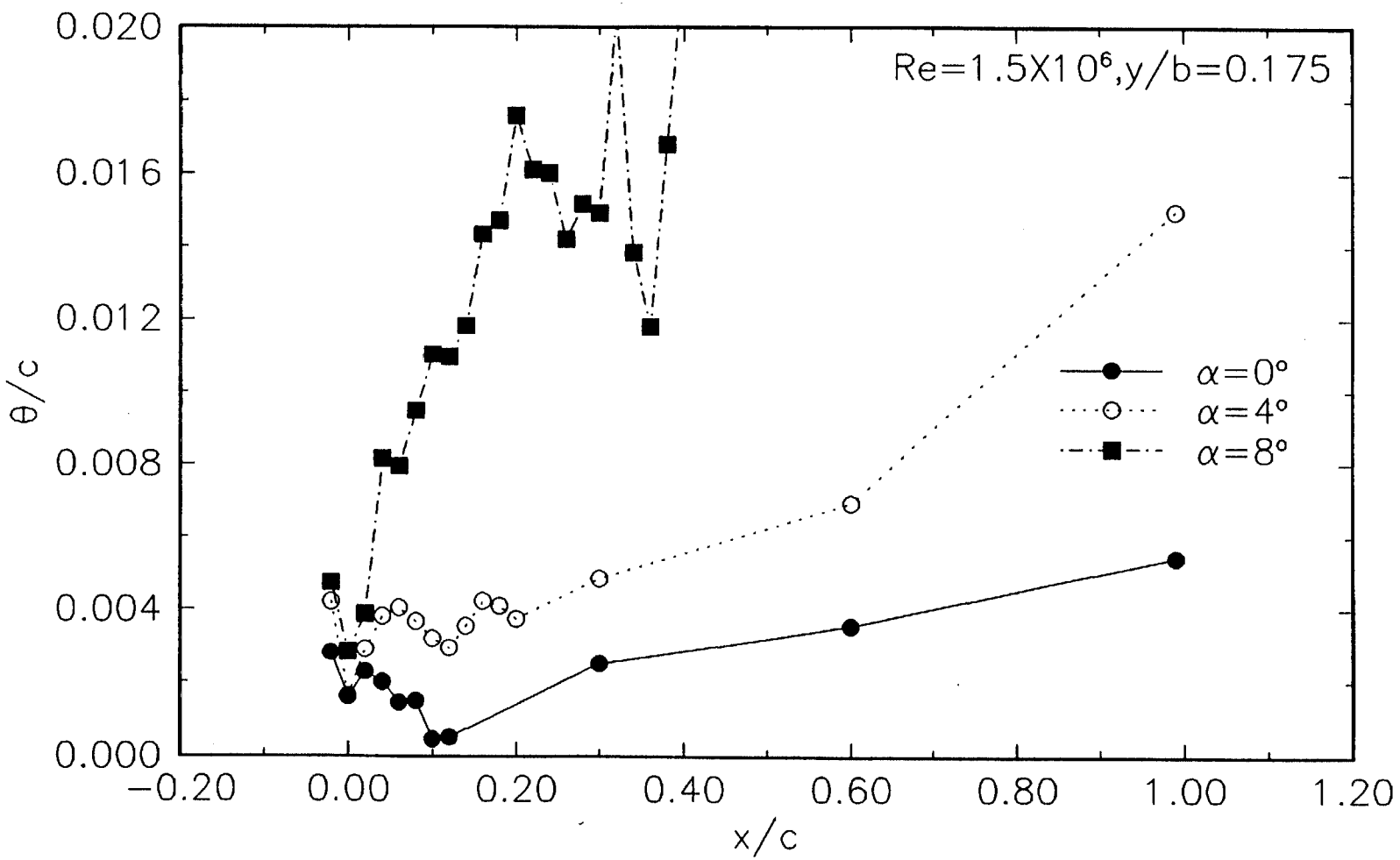

Figure 83. Distribution of Momentum Thickness on the Iced Wing at y/b=0.175.

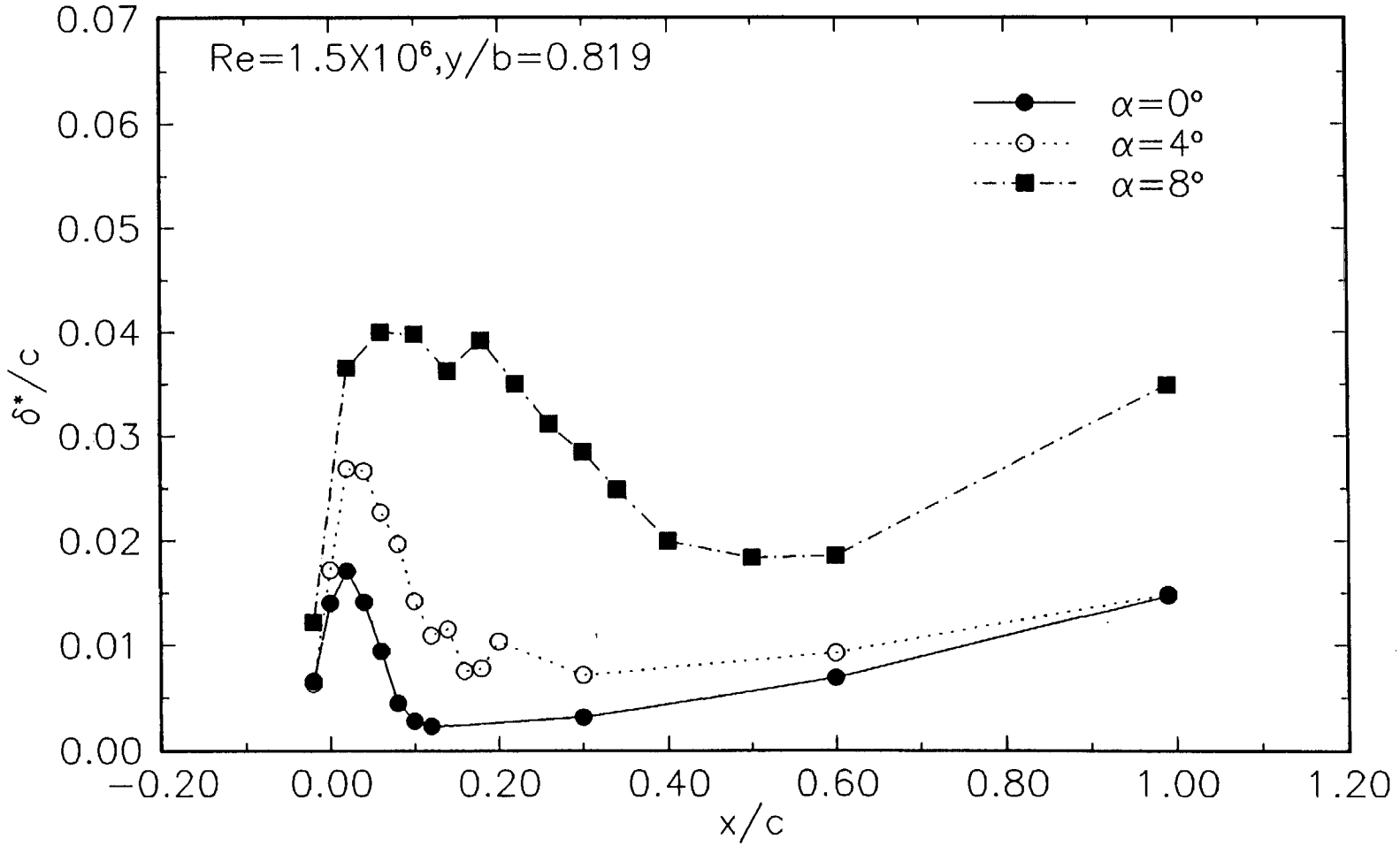

Figure 84. Distribution of Displacement Thickness on the Iced Wing at y/b=0.819.

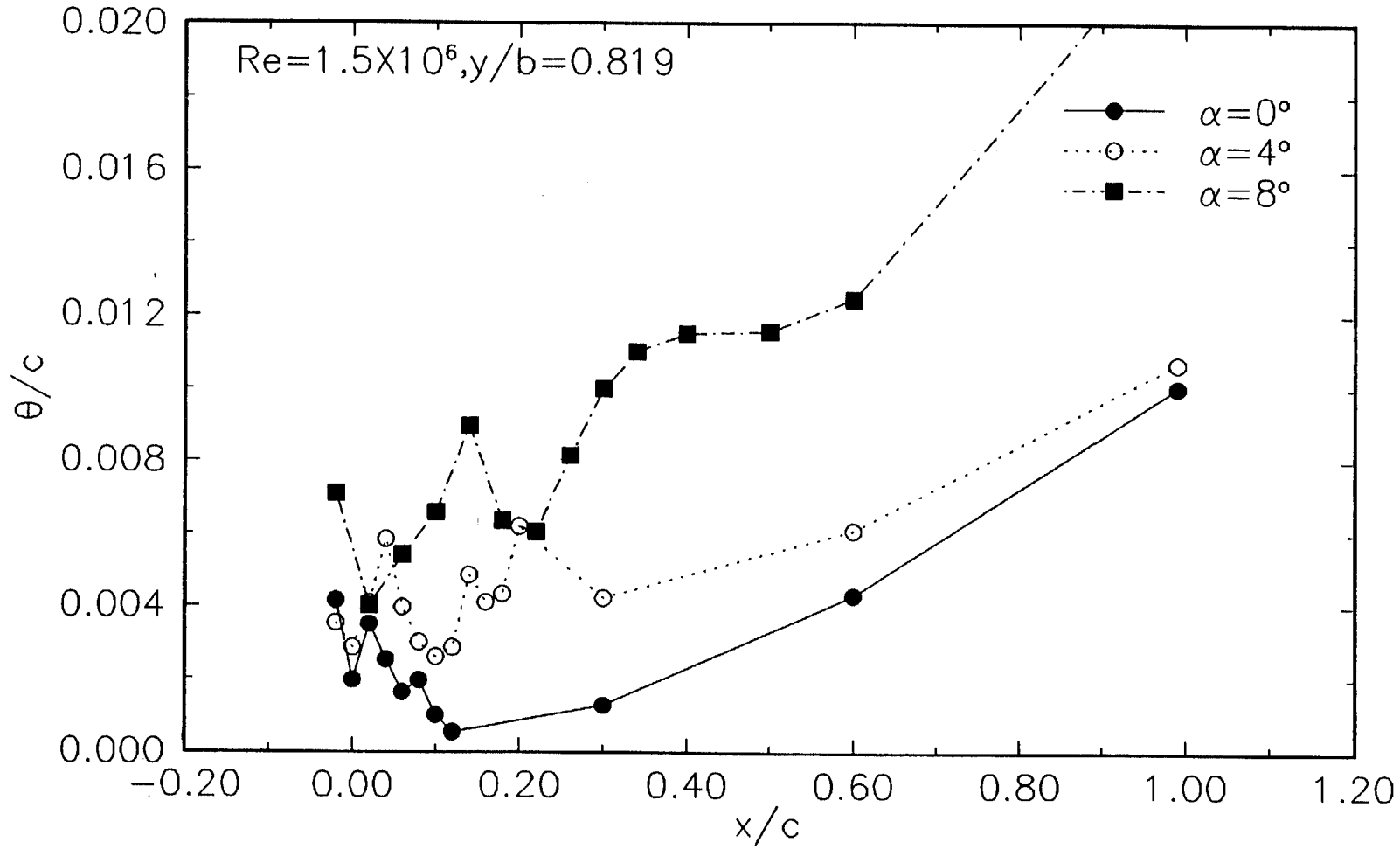

Figure 85. Distribution of Momentum Thickness on the Iced Wing at y/b=0.819.

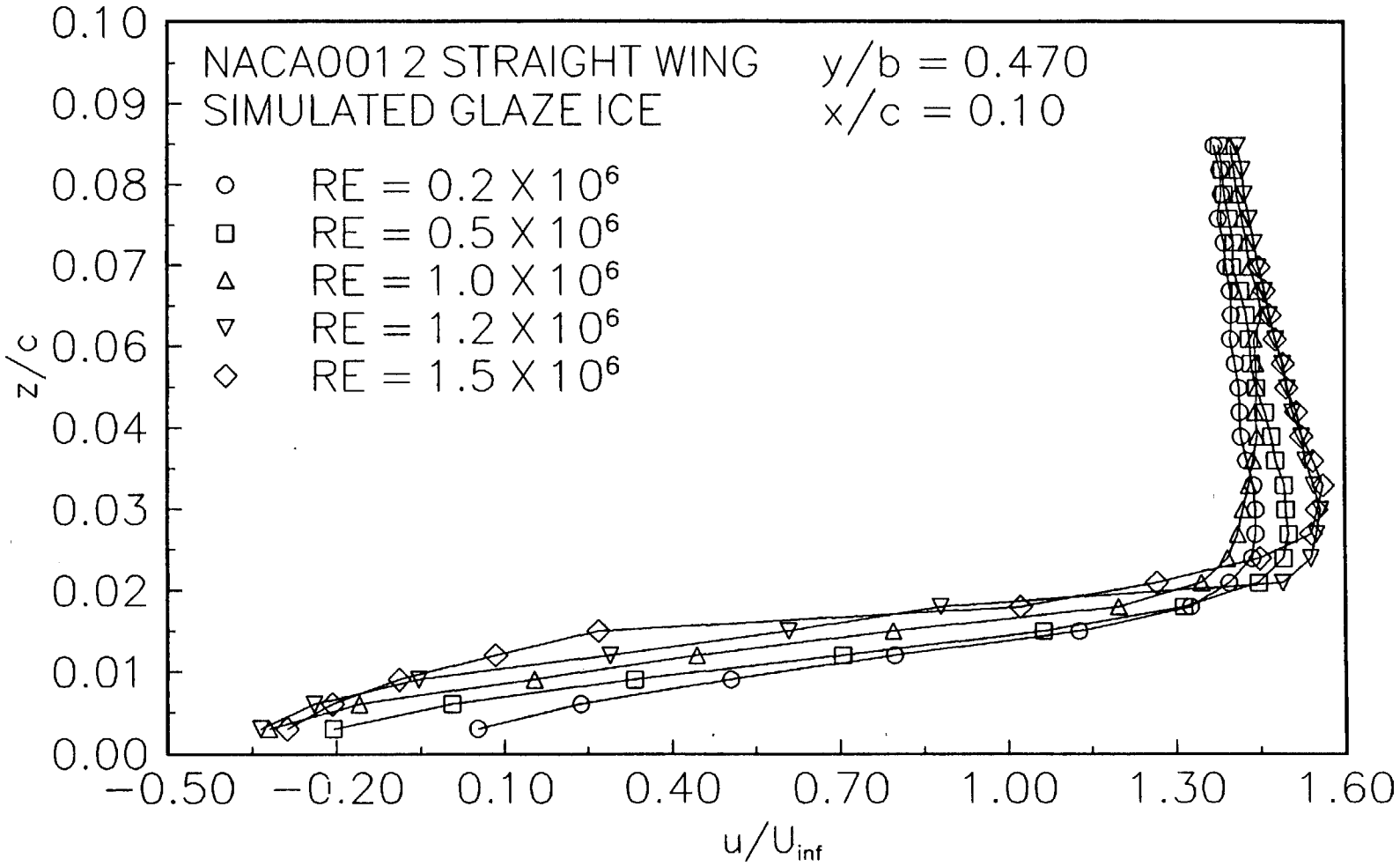

Figure 86. Effect of Reynolds Number on the (u) Velocity Profile, α=4.

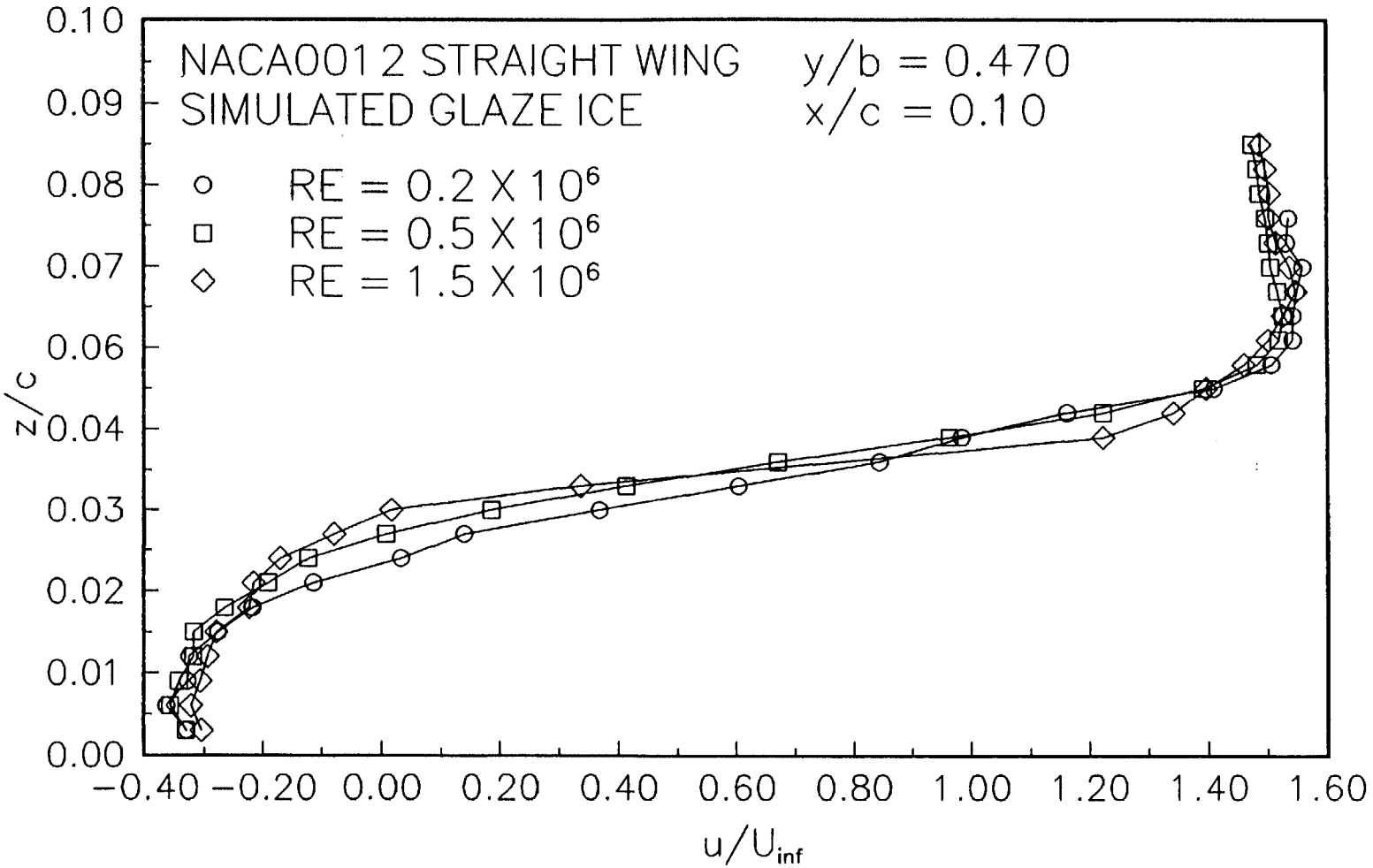

Figure 87. Effect of Reynolds Number on the (u) Velocity Profile, α=8.

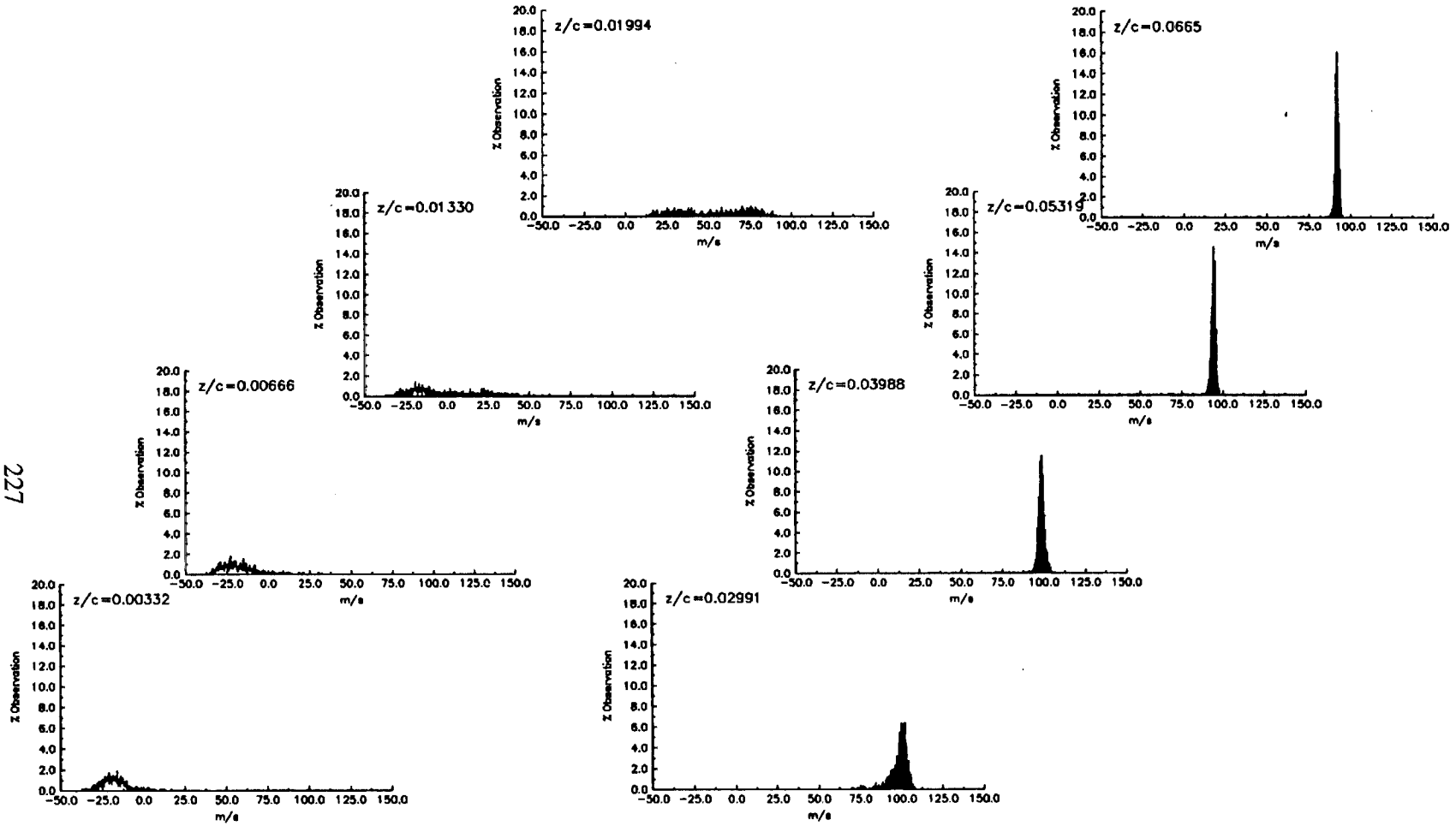

Figure 88. Velocity Histograms for the (u) Velocity on the Iced Wing at x/c=0.08, y/b=0.470, α=4, Re=1.5 Million.

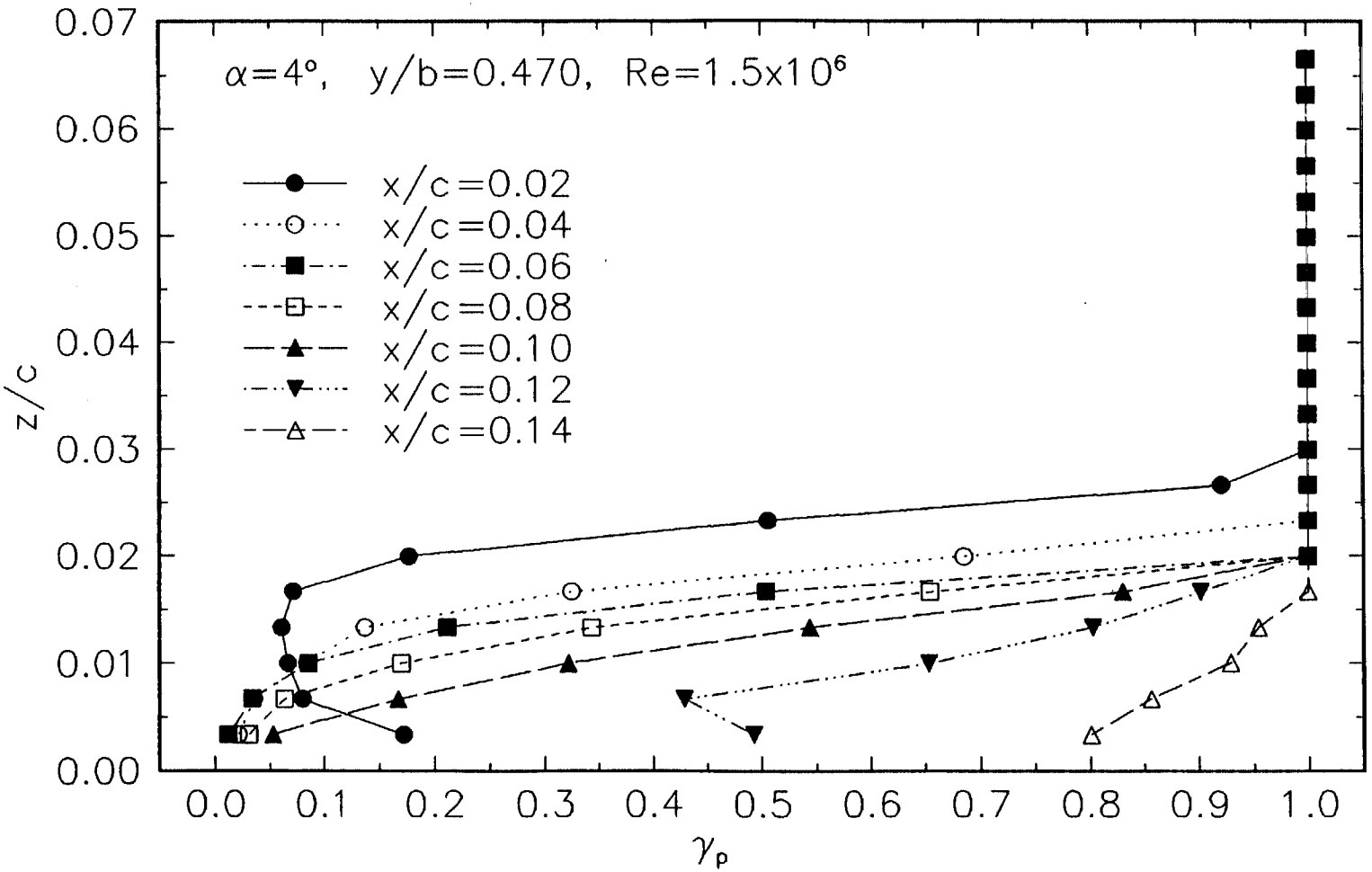

Figure 89. Intermittency Factor on the Upper Surface of the Iced Wing at y/b=0.470, α=4, Re=1.5 Million.

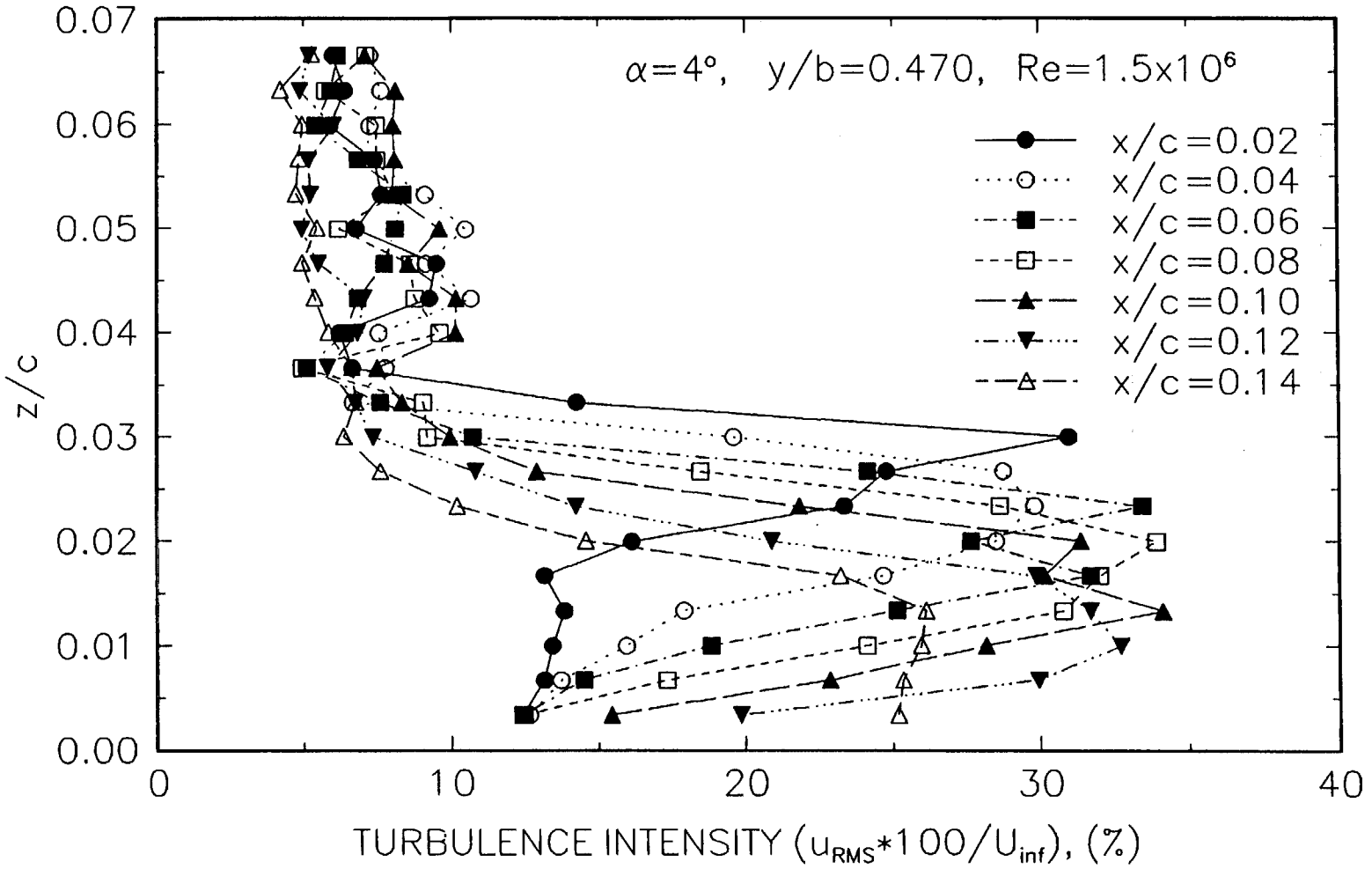

Figure 90. Turbulence Intensity on the Upper Surface of the Iced Wing at y/b=0.470, α=4, Re=1.5 Million.

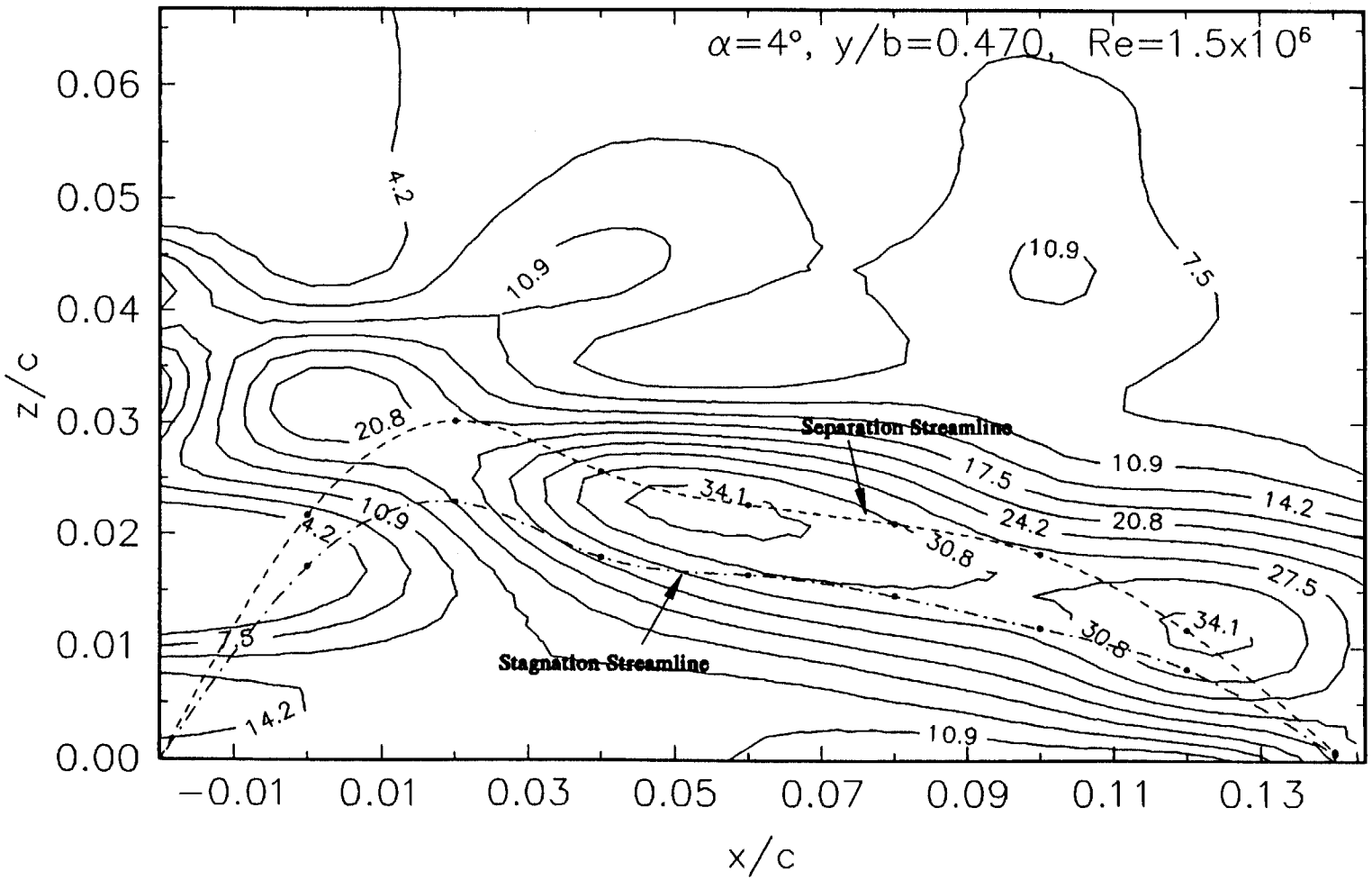

Figure 91. Turbulence Intensity Contours on the Upper Surface of the Iced Wing at y/b=0.470, α=4, Re=1.5 Million.

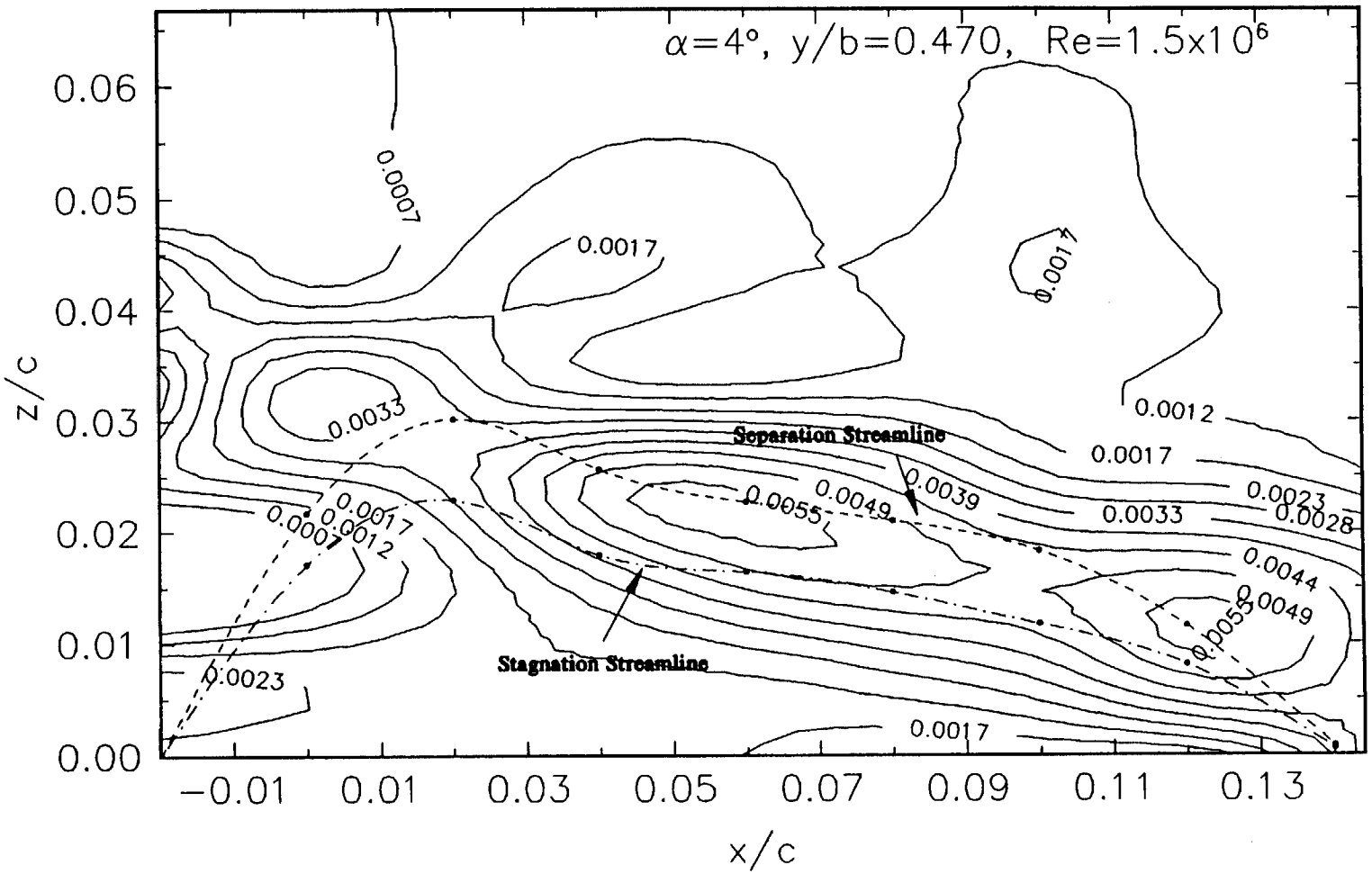

Figure 92. Reynolds Normal Stress Contours on the Upper Surface of the Iced Wing at y/b=0.470, α=4, Re=1.5 Million.

APPENDIX 1

EQUATIONS USED FOR CALCULATION OF VARIOUS FLOW MOMENTS

Equations used for signal processor statistics and flow variables[91]

individual realization ..... $V = d_f \times [\frac{N}{T_n} \times 1000 - f_s]$

velocity mean ..... $(\overline{V}) = \frac{\Sigma(V\tau)}{\Sigma\tau}$

standard deviation ..... $(\sigma_v) = \sqrt{\frac{\Sigma V^2\tau}{\Sigma\tau} - \overline{V}^2}$

turbulence ..... $(\%) = \frac{\sigma_v \times 100}{\overline{V}}$

3rd moment ..... $\frac{\Sigma V^3\tau}{\Sigma\tau} - [3 \times \frac{\Sigma V^2\tau}{\Sigma\tau} \times \overline{V}] + 2\overline{V}^3$

skewness coefficient ..... $\frac{3rd\ moment}{2\sigma_v^3}$

4th moment ..... $\frac{\Sigma V^4\tau}{\Sigma\tau} - [4 \times \frac{\Sigma V^3\tau}{\Sigma\tau} \times \overline{V}] + [6 \times \overline{V}^2 \times \frac{\Sigma V^2\tau}{\Sigma\tau}] + 3\overline{V}^4$

flatness coefficient ..... $\frac{4th\ moment}{\sigma_v^4}$

velocity vector magnitude ..... $\sqrt{(u^2 + v^2)}$

flow angle α ..... $\alpha = \arccos \frac{u}{\sqrt{(u^2 + v^2)}}$

flow angle ß ..... $\beta = \arccos \frac{v}{\sqrt{(u^2 + v^2)}}$

Reynolds stress ..... $\overline{u'v'} = \overline{uv} - \overline{u} \times \overline{v}$

APPENDIX 2

MEAN VELOCITY PROFILES FROM LDV MEASUREMENTS ON THE CLEAN RECTANGUALR WING

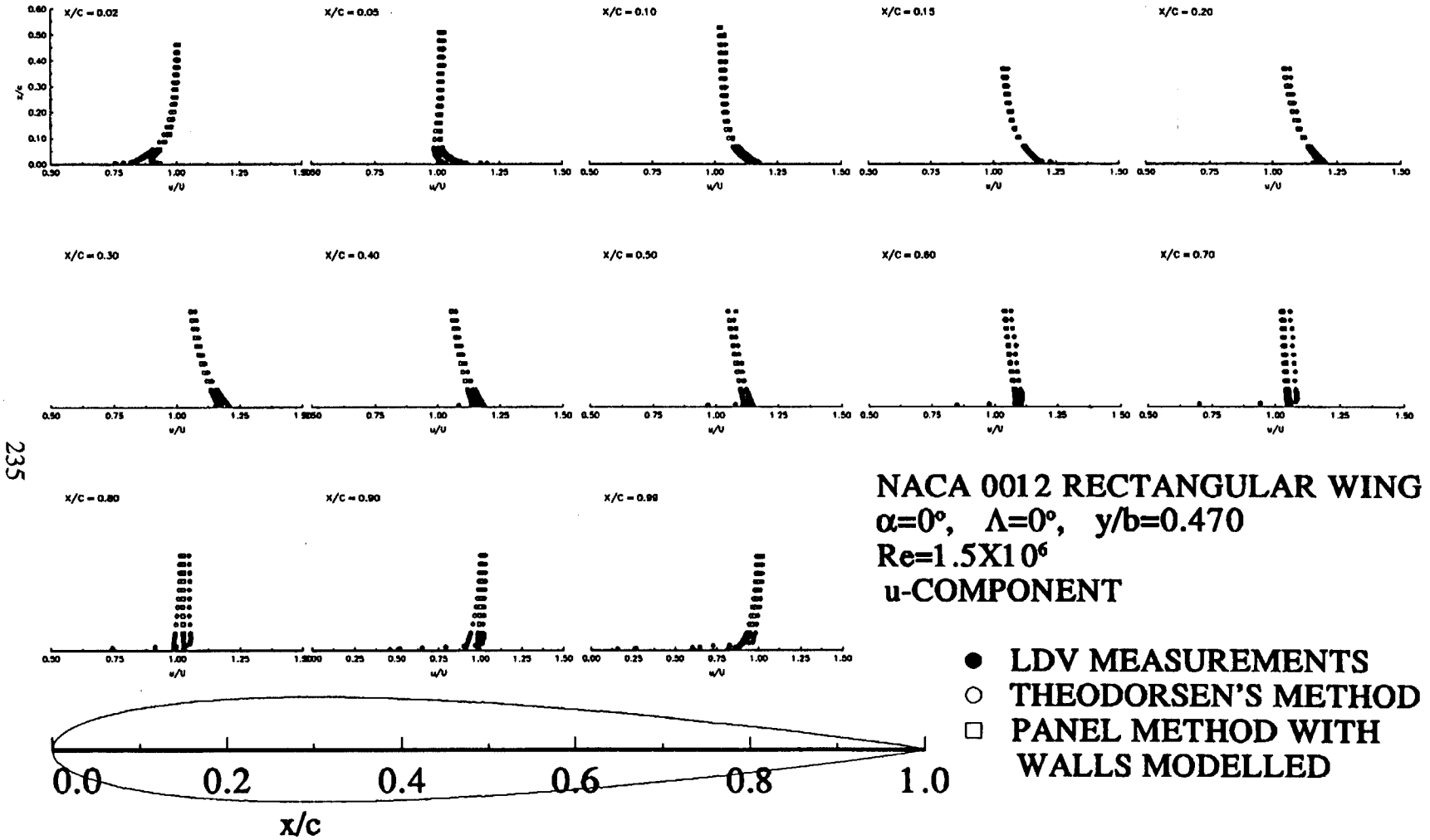

Figure 2.1. (u) Velocity Profiles on the Upper Surface of the Clean Wing at α=0, y/b=0.470, Re=1.5 Million, from LDV Measurements and Computation.

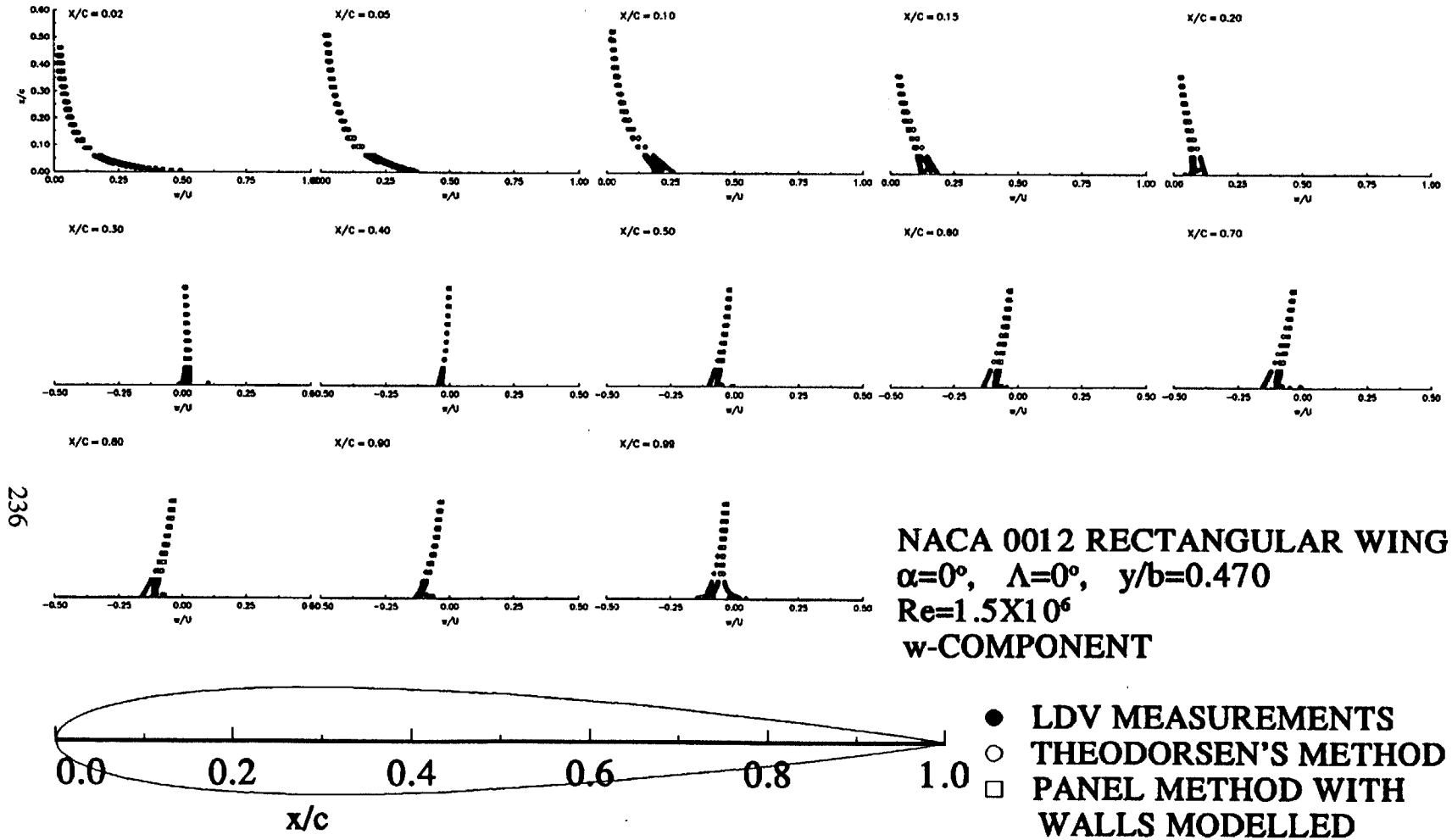

Figure 2.2. (w) Velocity Profiles on the Upper Surface of the Clean Wing at α=0, y/b=0.470, Re=1.5 Million, from LDV Measurements and Computation.

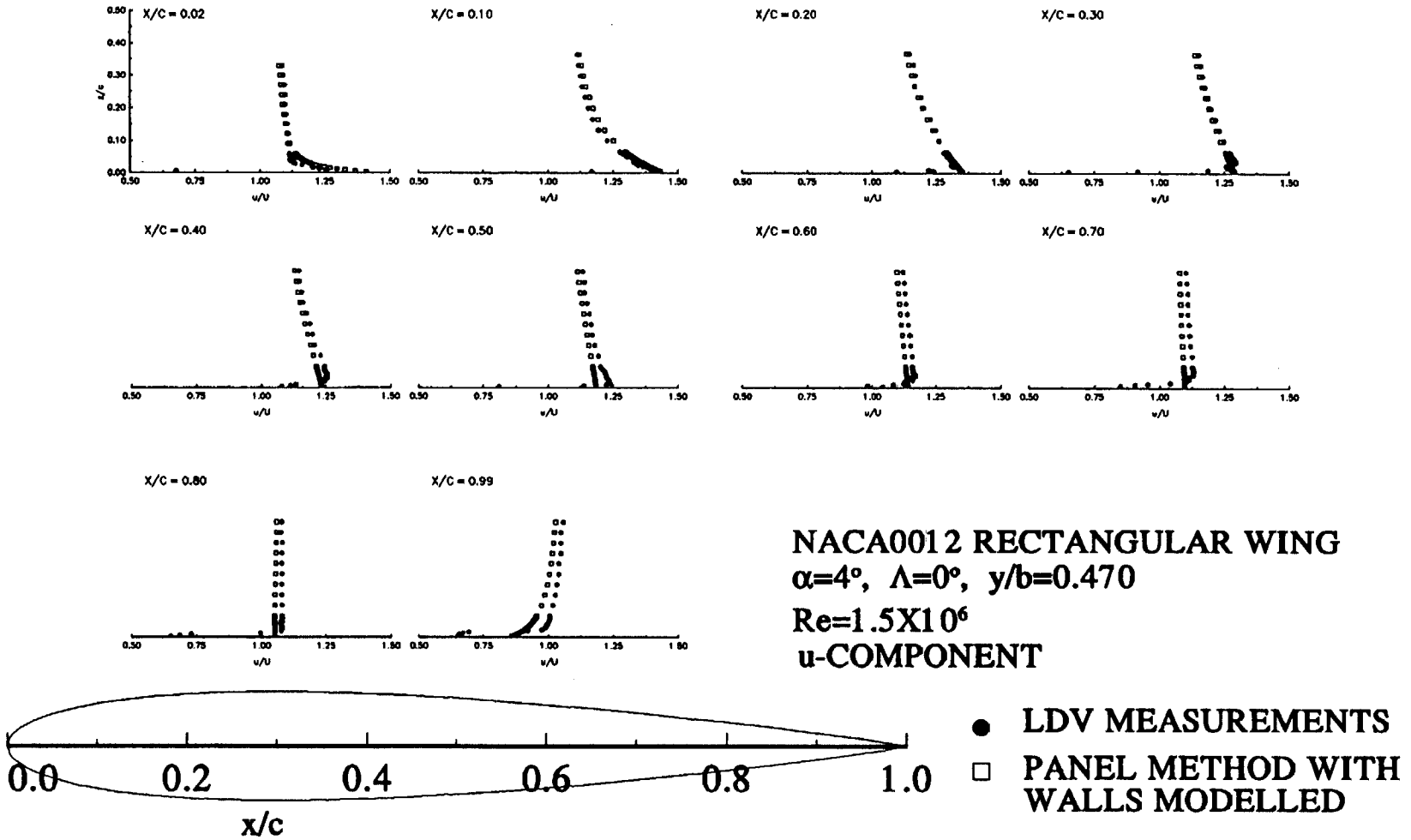

Figure 2.3. (u) Velocity Profiles on the Upper Surface of the Clean Wing at α=4, y/b=0.470, Re=1.5 Million, from LDV Measurements and Computation.

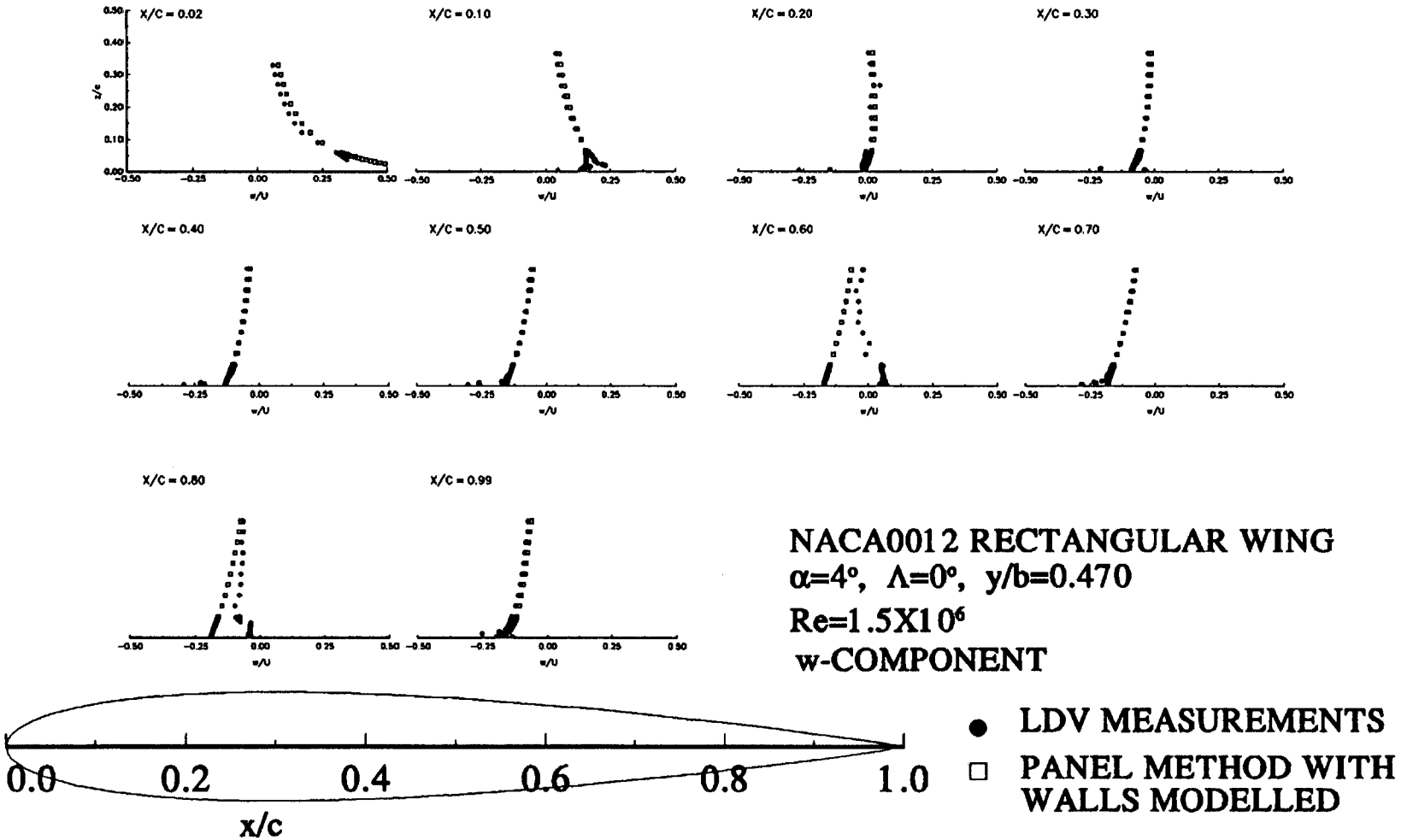

Figure 2.4. (w) Velocity Profiles on the Upper Surface of the Clean Wing at α=4, y/b=0.470, Re=1.5 Million, from LDV Measurements and Computation.

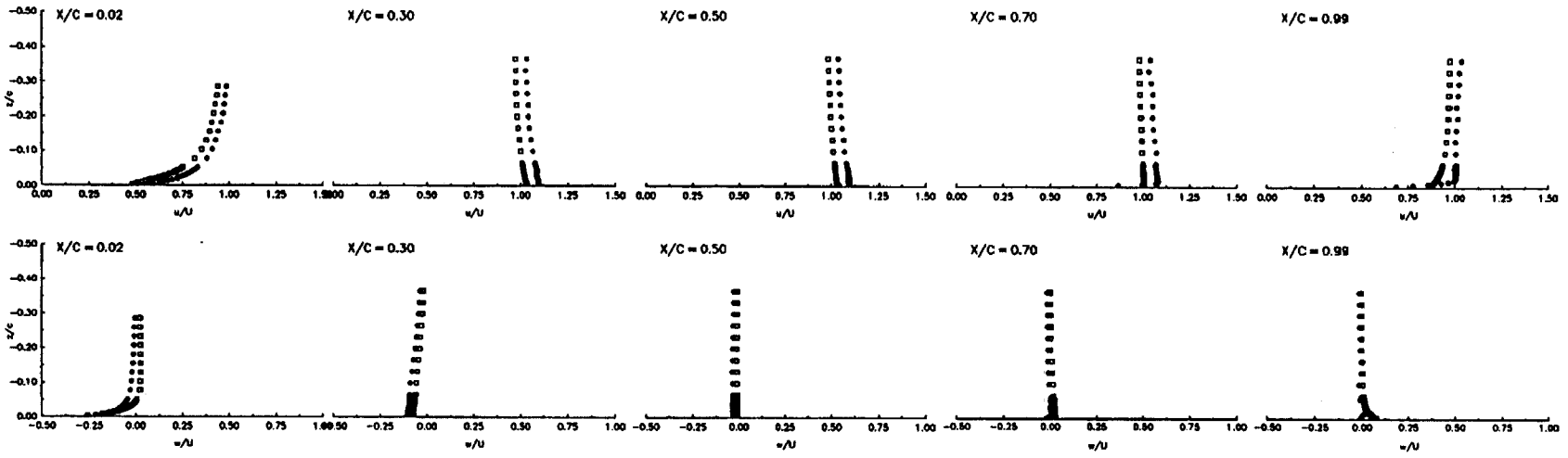

LOWER SURFACE
u- & w-COMPONENT

NACA 0012 RECTANGULAR WING
α=4°, Λ=0°, y/b=0.470
Re=1.5X10^6

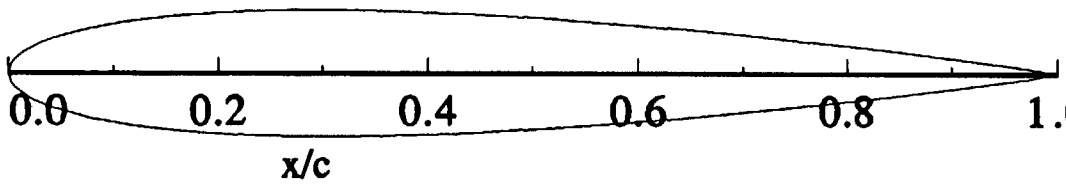

● LDV MEASUREMENTS
□ PANEL METHOD WITH WALLS MODELLED

Figure 2.5. (u) and (w) Velocity Profiles on the Lower Surface of the Clean Wing at α=4, y/b=0.470, Re=1.5 Million, from LDV Measurements and Computation.

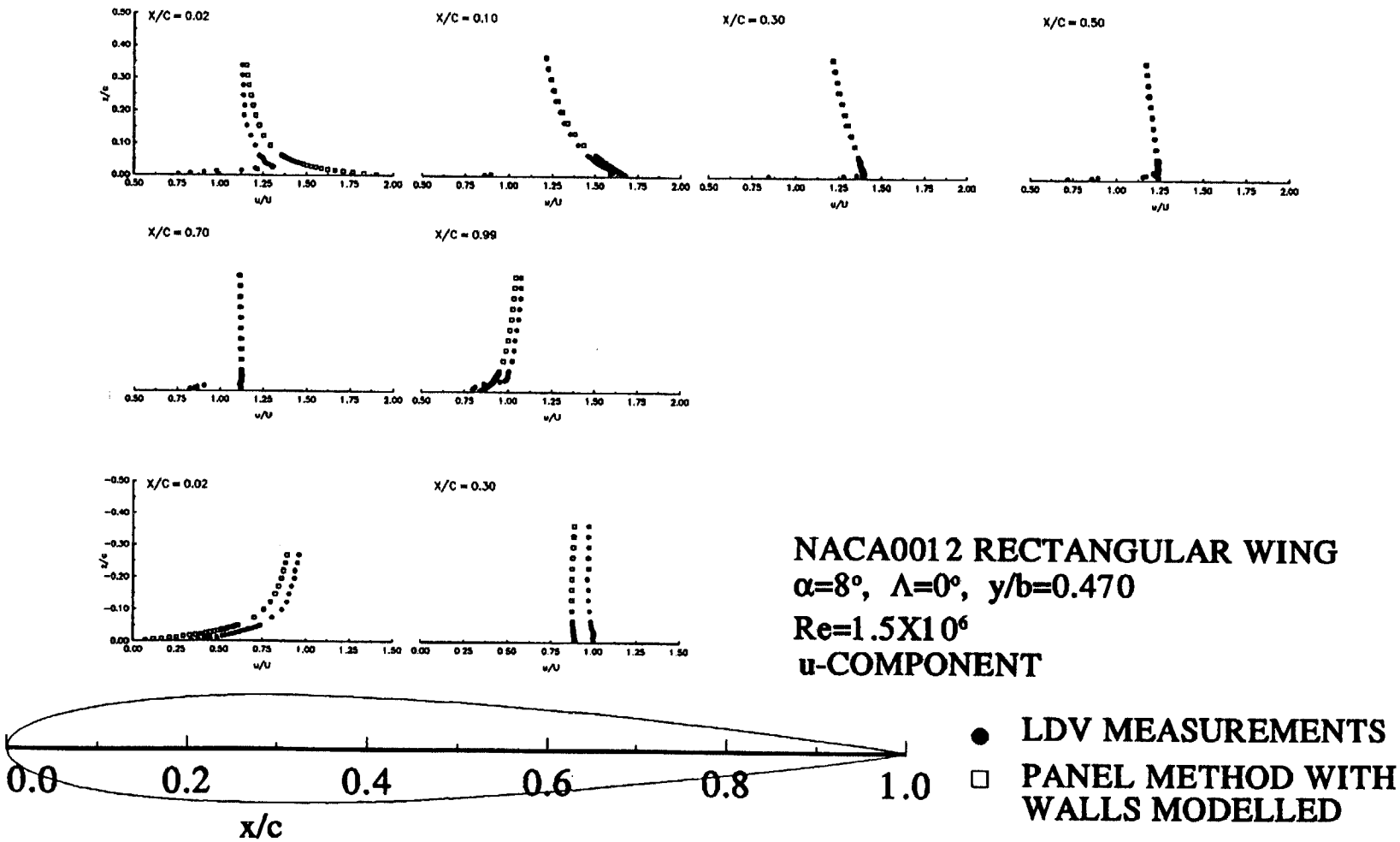

Figure 2.6. (u) Velocity Profiles on the Upper and Lower Surfaces of the Clean Wing at α=8, y/b=0.470, Re=1.5 Million, from LDV Measurements and Computation.

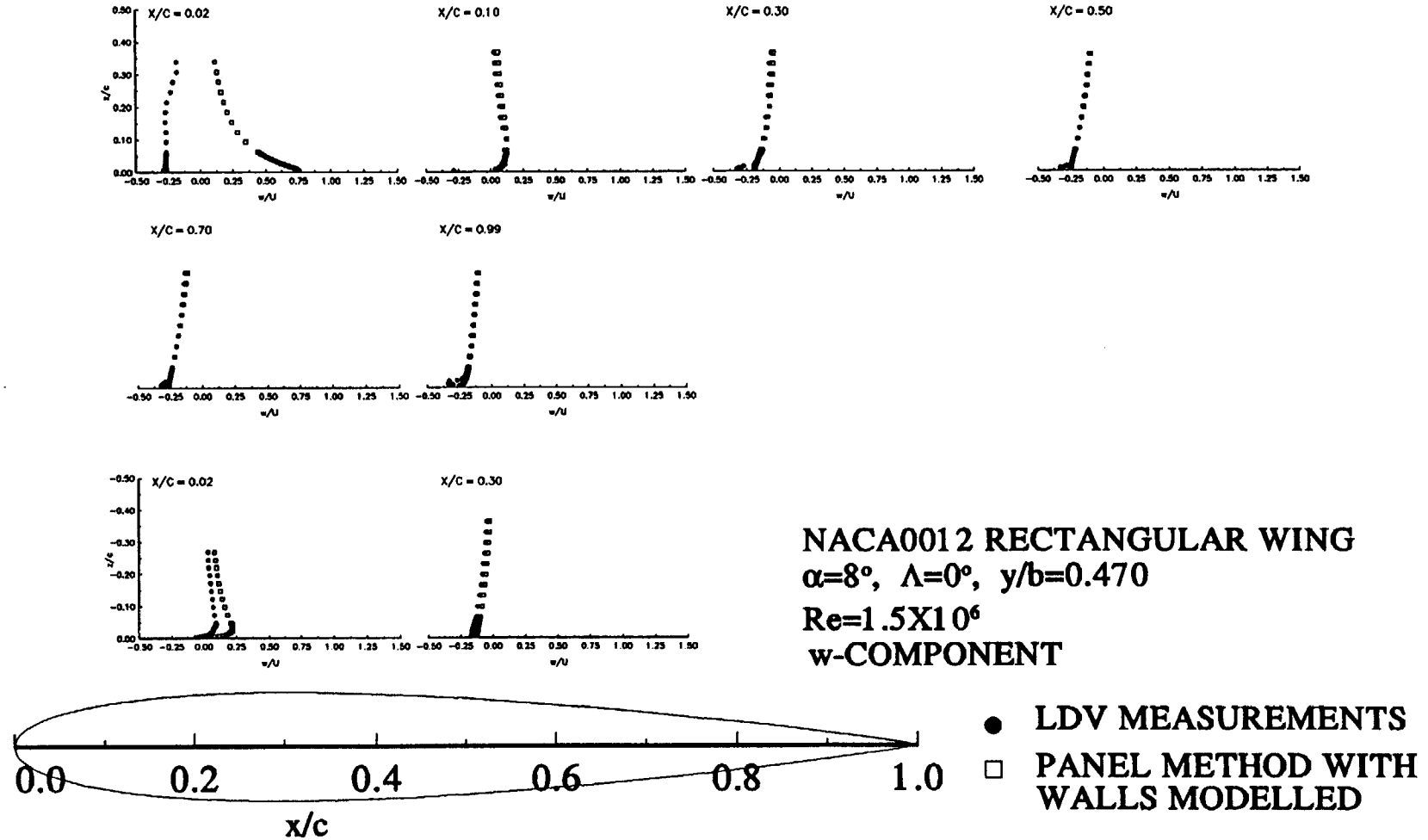

Figure 2.7. (w) Velocity Profiles on the Upper and Lower Surfaces of the Clean Wing at α=8, y/b=0.470, Re=1.5 Million, from LDV Measurements and Computation.

APPENDIX 3

COMPARISON OF SPLIT HOT-FILM MEASUREMENTS[9] WITH LDV MEASUREMENTS ON THE ICED RECTANGULAR WING

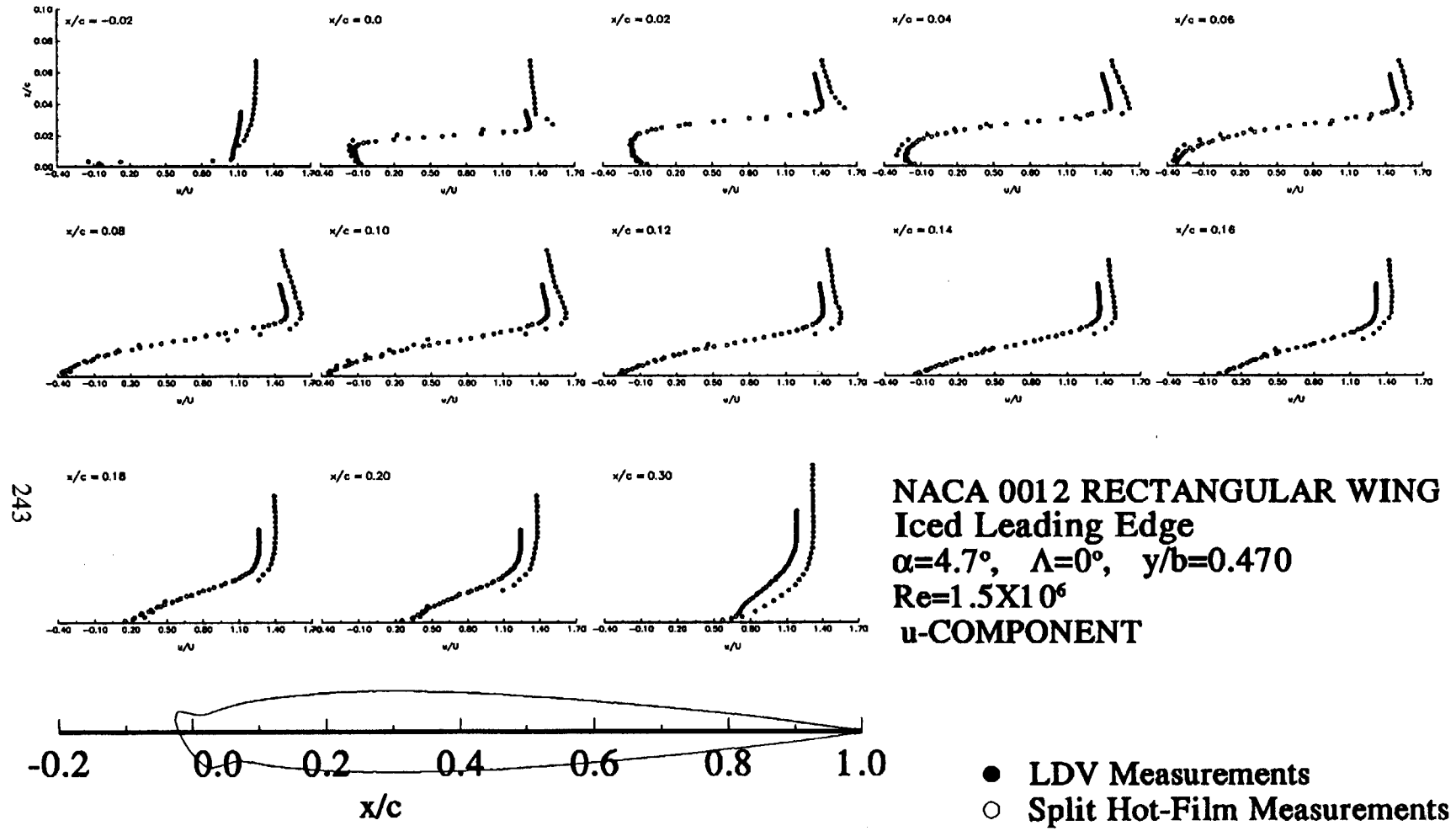

Figure 3.1. Comparison of (u) Velocity Profiles on the Upper Surface of the NACA 0012 at Matched Lift Coefficient, from Split Hot-Film Measurements (α=4), and LDV Measurements (α=4.7).

VITA

Date & Place of Birth:
[redacted]

Education:
The Ohio State University, B.S., Aero. & Astro. Engineering, December 1984.
M.S., Aero. & Astro. Engineering, June 1987.

Awards:
3rd Place, 1984 AIAA/Bendix Aircraft Design Competition.
1st Place, 1992 AIAA Ground Testing Committee National Student Engineering Contest, Graduate Division.

Experience:

University of Illinois	Graduate Research Assistant Dept. of Aero. & Astro. Engineering Jan. 1990 - Dec. 1992
The Ohio State University	Graduate Research Assistant Dept. of Aero. & Astro. Engineering May 1987 - Dec. 1989

Areas of Research:
Basic and Applied Aerodynamics
Separated Flows
Low-Speed Aerodynamics
Aerodynamics of Two- and Three-Dimensional Wings with Simulated Glaze Ice Shape

Presentations and Publications:

Bragg, M. B., Kerho, M. F., and Khodadoust, A., "LDV Flowfield Measurements on a Straight and Swept Wing with a Simulated Ice Accretion," AIAA-93-300, paper presented at the 31st Aerospace Sciences Meeting, Reno, Nevada, Jan. 11-14, 1993.

Bragg, M. B., Heinrich, D. C., and Khodadoust, A., "A Low-Frequency Flow Oscillation Over Airfoils Near Stall," submitted for publication to AIAA Journal, November 1992.

Khodadoust, A., "Effect of a Simulated Glaze Ice Shape on the Aerodynamic Performance of a Rectangular Wing," AIAA paper 92-4042, paper presented at the 17th Ground Testing Conference, Nashville, TN, July 6-8, 1992.

Bragg, M. B. ,Khodadoust, A., and Spring, S. A., "Experimental Measurements in a Large Leading-Edge Separation Bubble Due to a Simulated Airfoil Ice Accretion," *AIAA Journal*, Vol. 30, No. 6 June 1992, pp. 1462-1467.

Khodadoust, A., Bragg, M., and Kerho, M., "LDV Measurements on a Rectangular Wing with a Simulated Glaze Ice Accretion," AIAA-92-2690, paper presented at the 10th Applied Aerodynamics Meeting, Palo Alto, California, June 22-24, 1992.

Bragg, M. B., Khodadoust, A., Kerho, M., "Aerodynamics of a Finite Wing With Simulated Ice," paper presented at the 5th Symposium on Computational and Physical Aspects of Aerodynamic Flows, Cebeci, T., ed., Long Beach, California, January 1992.

Khodadoust, A., Bragg, M., Kerho, M., Wells, S., and Soltani, M., "Finite Wing Aerodynamics with Simulated Glaze Ice," AIAA-92-0414, paper presented at the 30th Aerospace Sciences Meeting, Reno, Nevada, Jan. 6-9, 1992.

Bragg, M., Khodadoust, A., Soltani, R., Wells, S., and Kerho, M., "Aerodynamic Measurements on a Finite Wing With Simulated Ice", AIAA-91-3217, paper presented at the 9th Applied Aerodynamics Meeting, Baltimore, Maryland, Sep. 23-25, 1991.

Bragg, M., Khodadoust, A., Soltani, R., Wells, S., and Kerho, M., "Effect of Simulated Ice Accretion on the Aerodynamics of a Swept Wing," AIAA-91-0442, paper presented at the 29th Aerospace Sciences Meeting, Reno, Nevada, Jan. 7-10, 1991.

Khodadoust, A., and Bragg, M. B., "Measured Aerodynamic Performance of a Swept Wing With a Simulated Glaze Ice Accretion," AIAA Paper 90-0490, paper presented at the 28th Aerospace Sciences Meeting, Reno, Nevada, Jan. 8-11, 1990.

Presentations and Publications (Cont'd):

Bragg, M. B., and Khodadoust, A., "Effect of Simulated Glaze Ice On a Rectangular Wing," AIAA-89-0750, paper presented at the 27th Aerospace Sciences Meeting, Reno, Nevada, January 9-12, 1989.

Bragg, M. B., and Khodadoust, A., "Experimental Measurements in a Large Separation Bubble Due to a Simulated Glaze Ice Accretion," AIAA-88-0116, paper presented at the 26th Aerospace Sciences Meeting, Reno, Nevada, January 11-14, 1988.

Khodadoust, A., "A Flow Visualization Study of the Leading Edge Separation Bubble on a NACA 0012 Airfoil with Simulated Glaze Ice," M.S. Thesis, Ohio State University, June 1987, also NASA CR-180846.

REPORT DOCUMENTATION PAGE

Form Approved
OMB No. 0704-0188

Public reporting burden for this collection of information is estimated to average 1 hour per response, including the time for reviewing instructions, searching existing data sources, gathering and maintaining the data needed, and completing and reviewing the collection of information. Send comments regarding this burden estimate or any other aspect of this collection of information, including suggestions for reducing this burden, to Washington Headquarters Services, Directorate for Information Operations and Reports, 1215 Jefferson Davis Highway, Suite 1204, Arlington, VA 22202-4302, and to the Office of Management and Budget, Paperwork Reduction Project (0704-0188), Washington, DC 20503.

1. AGENCY USE ONLY (*Leave blank*)	2. REPORT DATE	3. REPORT TYPE AND DATES COVERED
	April 1994	Final Contractor Report

4. TITLE AND SUBTITLE

An Experimental Study of the Flowfield on a Semispan Rectangular Wing With a Simulated Glaze Ice Accretion

5. FUNDING NUMBERS

WU–505–68–10
G–NAG3–1134

6. AUTHOR(S)

Abdollah Khodadoust

7. PERFORMING ORGANIZATION NAME(S) AND ADDRESS(ES)

University of Illinois
Urbana, Illinois 61801

8. PERFORMING ORGANIZATION REPORT NUMBER

E–8693

9. SPONSORING/MONITORING AGENCY NAME(S) AND ADDRESS(ES)

National Aeronautics and Space Administration
Lewis Research Center
Cleveland, Ohio 44135–3191

10. SPONSORING/MONITORING AGENCY REPORT NUMBER

NASA CR–195301

11. SUPPLEMENTARY NOTES

This report was submitted as a dissertation in partial fulfillment of the requirements for the degree Doctor of Philosophy to the University of Illinois, Urbana, Illinois, 1993. Project Manager, Jaiwon Shin, Propulsion Systems Division, organization code 2720, NASA Lewis Research Center, (216) 433–8714.

12a. DISTRIBUTION/AVAILABILITY STATEMENT

Unclassified - Unlimited
Subject Category 02

12b. DISTRIBUTION CODE

13. ABSTRACT ***(Maximum 200 words)***

Wind-tunnel experiments were conducted in order to study the effect of a simulated glaze ice accretion on the flowfield of a semispan, reflection-plane, rectangular wing at Re=1.5 million and M=0.12. A laser Doppler velocimeter was used to map the flowfield on the upper surface of the model in both the clean and iced configurations at α=0,4, and 8 degrees angle of attack. At low angles of attack, the massive separation bubble aft of the leading edge ice horn was found to behave in a manner similar to laminar separation bubbles. At α=0° and 4°, the locations of transition and reattachment, as deduced from momentum thickness distributions, were found to be in good agreement with transition and reattachment locations in laminar separation bubbles. These values at y/b=0.470, the centerline measurement location, matched well with data obtained on a similar but 2-D model. The measured velocity profiles on the iced wing compared reasonably with the predicted profiles from Navier-Stokes computations. The iced-induced separation bubble was also found to have features similar to the recirculating region aft of rearward-facing steps. At α=0° and 4°, reverse flow magnitudes and turbulence intensity levels were typical of those found in the recirculating region aft of rearward-facing steps. The calculated separation streamline aft of the ice horn at α=4°,y/b=0.470 coincided with the locus of the maximum Reynolds normal stress. The maximum Reynolds normal stress peaked at two locations along the separation streamline. The location of the first peak-value coincided with the transition location, as deduced from the momentum thickness distributions. The location of the second peak was just upstream of reattachment, in good agreement with measurements of flows over similar obstacles. The intermittency factor in the vicinity of reattachment at α=4°,y/b=0.470, revealed the time-dependent nature of the reattachment process. The size and extent of the separation bubble were found to be a function of angle of attack and the spanwise location. Three dimensional effects were found to be strongest at α=8°. The calculated separation and stagnation streamlines were found to vary little with spanwise location at α=0°. The calculated separation streamlines at α=4° revealed that the bubble was largest near the centerline measurement plane, whereas the tip-induced vortex flow and the model root-tunnel wall boundary-layer interaction reduced the size of the bubble. These effects were found to be most dramatic at α=8°.

14. SUBJECT TERMS

Simulated ice accretion; Laser doppler velocimeter measurements

15. NUMBER OF PAGES
248

16. PRICE CODE
A11

17. SECURITY CLASSIFICATION OF REPORT	18. SECURITY CLASSIFICATION OF THIS PAGE	19. SECURITY CLASSIFICATION OF ABSTRACT	20. LIMITATION OF ABSTRACT
Unclassified	Unclassified	Unclassified	